

Aus dem
Lehrstuhl für Medizinische Physik
Ludwig-Maximilians-Universität München
Leitung: Prof. Dr. Katia Parodi

**Investigations on Multilateration of Sonoacoustic Signals
for Localisation of the Bragg peak in Pre-clinical Research**

Dissertation
zum Erwerb des Doktorgrades der Naturwissenschaften
an der Medizinischen Fakultät der
Ludwig-Maximilians-Universität München

vorgelegt von
Ronaldo Dos Anjos Macondo Kalunga

aus
Luena

Jahr
2024

Mit Genehmigung der Medizinischen Fakultät
der Ludwig-Maximilians-Universität München

Betreuerin: Prof. Dr. Katia Parodi

Zweitgutachter: Prof. Dr. Guillaume Landry

Dekan: Prof. Dr. med. Thomas Gudermann

Tag der mündlichen Prüfung: 30. April 2025

Per aspera ad astra...

Contents

	Page
Zusammenfassung	8
Abstract	11
List of Figures	13
List of Tables	15
List of Abbreviations	16
1 Introduction	20
1.1 Context	21
1.2 External Radiotherapy	22
1.2.1 Sources of Range Uncertainties	26
1.3 In Vivo Range Verification Methods	27
1.4 Ionoacoustics	27
1.5 The SIRMIO Project	28
1.6 Thesis Objective	30
2 Ionoacoustics and Multilateration Theory	32
2.1 Principle and Derivation	33
2.1.1 Ionoacoustic Initial Pressure Derivation	37
2.1.2 Shape and Features of Ionoacoustic Signals	39
2.2 Multilateration State-of-The-Art	43
2.2.1 Multilateration Optimisation TOA and TDOA	48
2.2.2 Levenberg–Marquardt Algorithm	50
2.2.3 Nelder-Mead Simplex Algorithm	50
2.3 State of the Art on Ionoacoustic Reconstruction Methods	54
2.3.1 Source Localisation Based on Multilateration	54
2.4 Pressure Reconstruction	55
3 Material and Methods	57
3.1 Simulation Studies	58
3.1.1 TDOA Optimal Reference Sensor	58
3.1.2 Optimisation Failure and Acceptance Rate	58
3.1.3 Robustness Evaluation in Ideal Conditions (TOA, TDOA)	60
3.1.4 Ionoacoustic Simulations	61
3.2 Experimental Studies	62
3.2.1 Setup 1: 3-Sensors Configuration	62
3.2.2 Transducer’s Spatial Localisation Setup 1	64
3.2.3 Setup 2: 5-Sensors Configuration	67
3.2.4 Transducer’s Spatial Localisation Setup 2	67
3.3 SIRMIO Case Study	69
3.4 Data Analysis	71

3.4.1	Multilateration Robustness Assessment	71
3.4.2	Multilateration Workflow for BP localisation	73
3.4.3	Ionoacoustic Time-of-Flight Extraction	74
4	Results	76
4.1	Multilateration and Optimisation Methods Robustness	77
4.1.1	Nelder-Mead Simplex vs Levenberg–Marquardt	77
4.1.2	Multilateration Robustness Assessment in Ideal 2D Scenarios	80
4.1.3	Multilateration Robustness Assessment in Ideal 3D Scenarios	87
4.1.4	Comparison of 2D and 3D Multilateration in Ideal Scenarios	90
4.2	Ionoacoustic Simulation Studies at Pre-clinical Beam Energies	91
4.2.1	ToF Extraction Depending on the Sensor Position	91
4.2.2	Optimal Sensor Selection Based on ToF Error Analysis	93
4.3	Multilateration Experimental Studies	94
4.3.1	IA Experiments with 3 Sensors	94
4.3.2	IA Experiments with 5 Sensors	99
4.3.3	Improvement of the ToF extraction using a Gaussian fit	102
4.4	SIRMIO Case Study	104
4.4.1	Error on ToF Depending on the Proton Time Profile	104
4.4.2	Multilateration Accuracy Depending on the Proton Time Profile	106
4.4.3	Multilateration for Different Beam Spatial Locations	108
5	Discussion and Prospects	112
5.1	Numerical Optimisation Methods	113
5.2	Intrinsic Performances of TOA and TDOA	113
5.3	Signal Acquisition Start Time	114
5.4	Bragg Peak Localisation in Homogeneous Media	114
5.5	Bragg Peak Localisation in Heterogeneous Media	116
5.6	Multilateration in Small Animals	116
5.7	Towards Real-time Applications	118
5.8	IA Range Verification in Clinical Applications	118
5.9	Multilateration and TRR Reconstruction	119
	Appendices	121
	Appendix A Heterogeneity’s Silicone Setup	122
	Appendix B Multilateration 3D Setup	122
	Appendix C 3D I-BEAT Experimental Setup	123
	Appendix D FR Simplex and Levenberg algorithms	124
	Appendix E Multilateration and Optimisation Robustness	125
E.1	2D Multilateration Robustness Random Uncertainties	125
E.2	2D Multilateration Robustness Systematic Uncertainties	125
E.3	2D Multilateration Robustness Random and Systematic Uncertainties	125
E.4	3D Multilateration Robustness Random Uncertainties	126

E.5 3D Multilateration Robustness Systematic Uncertainties	126
E.6 3D Multilateration Robustness Random and Systematic Uncertainties	126
Appendix F TOA/TDOA Cost Function Computation	127
Appendix G Analytical Numerical Gradient	129
G.1 TOA Analytical Gradient	129
G.2 TDOA Analytical Gradient	130
G.3 Multilateration Time Performance	131
Appendix H Pulse-echo Measurement Between the Lateral Sensors	132
Appendix I TDOA Fixed Beam Position and Varying the Reference Sensor	133
Appendix J TOA/TDOA Beam Offsets & Localisation Using Multiple Sensors	134
List of Publications	136
A Bibliography	138
Affidavit	155
Confirmation of Congruency	156
Acknowledgements	157

This work is licensed under CC BY 4.0.

<https://creativecommons.org/licenses/by/4.0/>

Zusammenfassung

Strahlentherapie ist eine der am häufigsten verwendeten Behandlungen in der Krebstherapie und wird bei etwa 60 % der Patienten angewandt. Während Röntgen- und Gammastrahlen (Photonentherapie) den Standardverfahren darstellen, hat sich die Protonentherapie als wertvolle Alternative erwiesen. Die Protonentherapie ist für ihren Vorzug bekannt, eine konformalere Dosisabgabe zu ermöglichen. Die Überlegenheit der Protonentherapie gegenüber der Photonentherapie beruht darauf, dass Protonen ihre maximale Energie direkt im Tumor abgeben und dabei das umliegende gesunde Gewebe geschont wird. Allerdings ist die Protonentherapie sehr empfindlich gegenüber Reichweitenunsicherheiten. Reichweitenunsicherheiten in der Protonentherapie entstehen hauptsächlich, weil nicht genau bestimmt werden kann, wo der Protonenstrahl zum Stillstand kommt, was zum Risiko eines Überschießens oder Unterschreitens des Ziels führt. Daher besteht der Bedarf an *in vivo*-Reichweitenverifikationsmethoden, um diese Unsicherheiten zu reduzieren. Die beiden Methoden, die kurz vor dem routinemäßigen klinischen Einsatz stehen, sind die Positronen-Emissions-Tomographie (PET) und die Prompt-Gamma-Bildgebung (PGI). Die Reichweitenverifikation beruht bei diesen Methoden auf der Überwachung nuklearer Reaktionsprodukte entlang der Protonenstrahlen. Allerdings korrelieren die PET- und PGI-Methoden das messbare Signal nicht direkt mit der Reichweite des Strahls oder der Position des Bragg-Peaks (BP). Zudem sind die hierfür benötigten Gerätschaften sperrig und nicht kosteneffektiv. Daher schlägt die in dieser Arbeit durchgeführte Forschung eine kosteneffiziente Reichweitenverifikationsmethode vor, die eine direkte Korrelation zwischen dem Protonenstrahl und ionoakustischen (IA) Signalen herstellt.

Derzeit unterstützen nur zwei kommerzielle Plattformen die Photonentherapie bei Kleintieren, obwohl ihre Bildgebungssysteme für Forschungsstrahllinien angepasst werden können. Protonentherapie bietet gegenüber der Photonentherapie deutliche Vorteile, was zur Entwicklung des “Small Animal Proton Irradiator for Research in Molecular Image-guided Radiation-Oncology (SIRMIO)”-Projekts führte. Dieses Projekt wurde von Prof. Dr. Katia Parodi an der Ludwig-Maximilians-Universität (LMU) München geleitet und durch den Europäischen Forschungsrat (ERC) im Rahmen der Fördervereinbarung 725539 finanziert. SIRMIO zielte darauf ab, die erste tragbare, bildgeführte Forschungsplattform für die Protonentherapie bei Kleintieren zu entwickeln. Im Zuge dieses Vorhabens wurden verschiedene Reichweitenverifikationsmethoden untersucht. Eine dieser Methoden, die auf der Lokalisierung des BP mittels IA-Signalen basiert, wird in dieser Arbeit untersucht.

Die hier vorgestellte Forschung untersucht die Lokalisierung des BP unter Verwendung von IA-Signalen mit dem Ziel, die BP-Position sowohl im zwei-dimensionalen (2D) als auch drei-dimensionalen (3D) Raum zu bestimmen. Die Lokalisierung wurde in homogenen und heterogenen Medien mittels Laufzeitschätzung (Time-of-Flight, ToF) von verschiedenen Sensorpositionen durchgeführt. Die Lokalisierung des BP wurde mithilfe einer Technik namens Multilateration bewertet. Die ersten Studien wurden *in silico* durchgeführt, wobei ideale Punktquellen verwendet wurden, die die BP-Position emulierten und die Robustheit von zwei numerischen Optimierungsalgorithmen evaluierten: Nelder-Mead-Simplex und Levenberg-Marquardt. Daraufhin wurde die Robustheit der Multilaterationstechnik für zwei Lokalisierungsmethoden bewertet: Time-of-Arrival (TOA) und Time-Difference-of-Arrival (TDOA). Durch die Modellierung von zufälligen und systematischen Unsicherheiten in der geometrischen ToF wurde die Robustheit von TOA und TDOA untersucht. Die Zufälligen Unsicherheiten zielten darauf ab, Schwankungen der Schallgeschwindigkeit, ungenaue Kenntnisse der Sensorposition und Fehler bei der ToF zu modellieren. Die Systematischen Unsicherheiten dienten dazu, die ungenaue Kenntnis der Messstartzeit eines Protonenstrahlbeschleunigers zu simulieren.

Nach einem umfassenden Verständnis der numerischen Optimierungsmethoden und der Auswirkungen von Unsicherheiten auf TOA und TDOA wurde der Fokus auf einen realistischen Simulationsfall mit einem vorklinischen Strahl von 20 MeV gerichtet. Die Multilateration der BP-Position wurde mit einem Sensornetzwerk von 843 idealen Punktquellen in einer halbkreisförmigen Konfiguration mit einem Durchmesser von 60 mm durchgeführt. Ebenso wurde der Einfluss verschiedener ToF-Extraktionsmethoden auf die BP-Lokalisierung bewertet. Die Untersuchungen wurden auch darauf erweitert, den Einfluss der Anzahl der Sensoren auf die ToF-Schätzung und damit auf die Genauigkeit der BP-Lokalisierung zu analysieren.

Experimentelle Kampagnen wurden durchgeführt, um die Lokalisierung des BP anhand des in den Simulationsstudien gewonnenen Vorwissens zu validieren. Diese experimentellen Studien ermittelten die BP-Position im Tandem-Beschleuniger bei zwei verschiedenen Strahlenergien (20 und 22 MeV). Die erste experimentelle Kampagne zielte darauf ab, den BP mit drei Wandlern zu lokalisieren. Darüber hinaus wurden zwei verschiedene Techniken implementiert, um die räumliche Position der Wandler zu bestimmen. Die zweite experimentelle Kampagne hatte das Ziel, den BP mit 5 Wandlern zu lokalisieren. Zudem wurden die räumlichen Positionen der Wandler experimentell mithilfe eines Ansatzes bestimmt, der auf Messungen mit einem optischen Trackingsystem basierte. Für den SIRMIO-Fall wurde ein dediziertes Lokalisierungssetup mit einer Strahlenergie von 50 MeV in Betracht gezogen. Dieses Setup hatte das Ziel, den BP unter verschiedenen Bedingungen zu lokalisieren, einschließlich unterschiedlicher Protonenstrahlzeitprofile, Strahlpositionen und Sensoranzahlen. Der erste Schritt bestand darin, den Fehler in der ToF als Funktion der Protonenstrahlzeitprofile zu untersuchen und dann die Multilaterationsgenauigkeit basierend auf denselben Protonenstrahlzeitprofilen zu bewerten. Nachdem das optimale Protonenstrahlzeitprofil identifiziert worden war, wurde der BP durch konstantes Protonenstrahlzeitprofil und variable Sensoranzahlen lokalisiert.

Für die numerischen Methoden zeigte die Levenberg-Marquardt-Methode eine größere Robustheit im Vergleich zur Nelder-Mead-Simplex-Methode, mit Ausfallraten (FR) von 0.22 % und 0% bei der Lokalisierung der emulierten BP-Positionen mit TOA bzw. 1.12% und 4.85% bei der Lokalisierung der Quelle mit TDOA. Bei idealen Punktquellen waren beide Lokalisierungsmethoden in 2D äquivalent. Ein mittlerer Lokalisierungsfehler von 7.4×10^{-4} mm und 7.8×10^{-4} mm wurde für TOA und TDOA ermittelt. In 3D variierte der Lokalisierungsfehler zwischen 7.8×10^{-4} mm und 1.0×10^{-3} mm für TOA und TDOA. Die Schallgeschwindigkeit variiert *in vivo* je nach Gewebetyp, was die Genauigkeit der BP-Lokalisierung verringern dürfte. Bei einer konservativen Annahme eines Fehlers von 5% in der durchschnittlichen Schallgeschwindigkeit entlang des akustischen Pfads (modelliert durch zufällige Unsicherheiten) wurde festgestellt, dass der Lokalisierungsfehler nach der Multilateration um etwa 2 mm für die untersuchte Geometrie zunahm. Der geringste Fehler bei der ToF-Schätzung wird bei der Maximalhüllkurven-Extraktionsmethode erzielt, wenn IA-Signale betrachtet werden. Daher könnte der BP durch optimale Sensorpositionierung, um ToF-Fehler zu minimieren, *in silico* mit einer Genauigkeit von über 90 μ m (entspricht einem Fehler von 2%) lokalisiert werden.

Der BP wurde für das erste experimentelle Setup mit Fehlern im Bereich von 0.43 mm bis 0.48 mm lokalisiert, abhängig von der Anordnung der Sensoren. Die Lokalisierung erfolgte mit einer Gesamtdosis von 1.69 Gy in einem einzigen Schuss. Im zweiten experimentellen Setup wurde die Lokalisierung mit 50 IA-Signalen und einer Gesamtdosis von 29 Gy durchgeführt, wobei ein Lokalisierungsfehler von 1 mm erzielt wurde. In beiden Setups waren die Hauptursachen für die Lokalisierungsfehler Ungenauigkeiten in der Sensorpositionierung und ein niedriges Signal-Rausch-Verhältnis (SNR) aufgrund der schwachen und gerichteten Natur der IA-Emissionen. Die Studien für

die SIRMIO-Strahllinie zeigten, dass das Protonenzeitprofil einen erheblichen Einfluss auf die ToF-Schätzung hat, was sich wiederum auf die Genauigkeit der BP-Lokalisierung auswirkt. Die optimale Lokalisierungsgenauigkeit wurde bei Protonenzeitprofilen im Bereich von $1 \mu\text{s}$ bis $4 \mu\text{s}$ erreicht. In diesem Setup wurde der BP für verschiedene Strahlverschiebungen entlang der x-, y- und z-Achse lokalisiert. Bei Verschiebungen entlang der Strahlachse (x-Achse) betrug der maximale Fehler 0.48 mm. Im Gegensatz dazu wurde ein maximaler Fehler von 1.23 mm bei einer Querstrahlverschiebung (z-Achse) erzielt.

Zusammenfassend wird in dieser Arbeit eine Methode zur Reichweitenverifikation unter Verwendung von IA-Signalen im Rahmen des SIRMIO-Projekts vorgestellt. Darüber hinaus wird in weiteren Diskussionen das Potenzial der in dieser Arbeit vorgestellten Studien für Echtzeit-Anwendungen untersucht.

Abstract

Radiation therapy is one of the most typically used treatments in cancer care, with around 60% of patients undergoing this form of treatment. While X-rays and gamma rays (photon therapy) are the standard approach, proton therapy has emerged as a valuable alternative. Proton therapy is renowned for its ability to provide a more conformal dose delivery. Proton therapy's superiority over photon therapy is due to protons depositing their maximum energy directly within the tumour while sparing surrounding healthy tissues. However, proton therapy is highly sensitive to range uncertainties. Range uncertainties in proton therapy arise primarily because we cannot precisely determine where the proton beam will stop, leading to the risk of overshooting or undershooting the target. Thus, there is a need for *in vivo* range verification methods to reduce range uncertainties. The two methods nearing routine clinical use are positron emission tomography (PET) and prompt gamma imaging (PGI). Range verification relies on monitoring nuclear reaction products along proton beams for these methods. However, PET and PGI methods do not directly correlate the measurable signal, beam range, or Bragg peak (BP) position. Additionally, their equipment is bulky and not cost-effective. Therefore, the research conducted during this work proposes a range verification method that is both cost-effective and establishes a direct correlation between the proton beam and ionoacoustic (IA) signals.

At present, only two commercial platforms support small animal photon radiotherapy, though their imaging systems can be adapted for research beamlines. Proton therapy offers distinct advantages over photon therapy, which led to the development of the Small Animal Proton Irradiator for Research in Molecular Image-guided Radiation-Oncology (SIRMIO) project. It was led by Prof. Dr. Katia Parodi at Ludwig Maximilians-Universität (LMU) Munich and funded by the European Research Council (ERC) under grant agreement 725539. SIRMIO aimed to create the first portable, image-guided research platform for small animal proton therapy. As part of this effort, different range verification methods are investigated. One of these methods is the one studied in this thesis, which is based on localising the BP using IA signals.

The research presented here investigates BP localisation using IA signals, aiming to determine the BP position in both two-dimensional (2D) and three-dimensional (3D) space. The localisation was performed in homogenous and heterogenous media via time-of-flight (ToF) estimation from different sensor spatial locations. The localisation of the BP was assessed using a technique called multilateration. The initial studies were performed *in-silico*, using ideal point sources that emulated the BP position and evaluated the robustness of two numerical optimisation algorithms: Nelder-Mead Simplex and Levenberg Marquardt. Secondly, the robustness of the multilateration technique was assessed for two localisation methods: time-of-arrival (TOA) and time-difference-of-arrival (TDOA). By modelling random and systematic uncertainties in the geometrical ToF, the robustness of both TOA and TDOA was evaluated. Random uncertainties aimed to model the speed of sound variations, inaccurate knowledge of the sensor spatial location and errors on the ToF. On the other hand, the objective of modelling systematic uncertainties was to simulate the inaccurate knowledge of the measurement starting time from a proton beam accelerator.

After fully understanding the numerical optimisation methods and the impact of uncertainties on TOA and TDOA, the localisation focus was addressed to a realistic simulation case using a pre-clinical beam with an energy of 20 MeV. The multilateration of the BP position was performed with a sensor network of 843 ideal point sensors arranged in a semi-circular configuration with a diameter of 60 mm. Similarly, the impact of different ToF extraction methods on BP localisation was evaluated.

Moreover, the studies were further expanded to investigate the impact of the number of sensors on the ToF estimation and, consequently, their impact on the accuracy of the BP localisation.

Experimental campaigns were conducted to benchmark the localisation of the BP using pre-knowledge gained from the simulation studies. These experimental studies retrieved the BP position in the Tandem accelerator with two different beam energies (20 and 22 MeV). The first experimental campaign aimed to localise the BP using 3 transducers. Furthermore, two different techniques were implemented to localise the spatial location of the transducers. The second experimental campaign aimed to localise the BP using 5 transducers. Moreover, the spatial locations of the transducers were estimated experimentally using a single approach based on the measurement performed with an optical tracking system.

For the SIRMIO case, a dedicated localisation setup with a 50 MeV beam energy was considered. This setup aimed to localise the BP under various conditions, including different proton beam time profiles, beam spatial locations, and numbers of sensors. The first step involved studying the error in ToF as a function of the proton time profiles and then assessing multilateration accuracy based on the same proton time profiles. After identifying the optimal proton time profile, the BP was localised by keeping the proton time profile constant while varying the number of sensors.

For the numerical methods, the Levenberg-Marquardt method demonstrated greater robustness compared to the Nelder-Mead Simplex method, with failure rates (FR) of 0.22% and 0% when localising the emulated BP positions with TOA and 1.12% and 4.85% when localising the source with TDOA, respectively. Considering ideal point sources, both localisation methods were equivalent in 2D. A mean error in localisation of 7.4×10^{-4} mm and 7.8×10^{-4} mm for TOA and TDOA was obtained. In 3D, the localisation error varied from 7.8×10^{-4} mm and 1.0×10^{-3} mm for TOA and TDOA. The speed of sound varies *in vivo* depending on the tissue type, which is expected to reduce the BP localisation accuracy. With a conservative assumption of a 5% error in the average speed of sound along the acoustic path (modelled by random uncertainties), it was observed that the localisation error after multilateration increased by around 2 mm for the examined geometry. The lowest error on the ToF estimation is obtained for the maximum-envelope extraction method when considering IA signals. Therefore, through optimal sensor positioning to minimise ToF errors, the BP could be localised *in-silico* with an accuracy exceeding 90 μm (equivalent to a 2% error).

The BP was localised for the first experimental setup with errors ranging from 0.43 mm to 0.48 mm, depending on the sensor arrangement. The localisation was performed with a total dose of 1.69 Gy with a single shot. In the second experimental setup, the localisation was performed with 50 IA signals and a total dose of 29 Gy, achieving a localisation error of 1 mm. For both setups, the primary sources of localisation errors were inaccuracies in sensor positioning and low signal-to-noise ratio (SNR) due to the weak and directional nature of the IA emissions.

The studies conducted for the SIRMIO beamline demonstrated that the proton time profile significantly impacts the ToF estimation, influencing the accuracy of BP localisation. The optimal localisation accuracy was achieved with proton time profiles ranging from 1 μs to 4 μs . In this setup, the BP was localised for different beam offsets along the x, y, and z axes. When applying offsets along the beam axis (x-axis), the maximum error was found to be 0.48 mm. Conversely, a maximum error of 1.23 mm was obtained for a transverse beam offset (z-axis).

In conclusion, this work introduces a range verification method using IA signals within the framework of the SIRMIO project. Additionally, further discussions explore the potential for transitioning the studies presented in this thesis toward real-time range verification applications.

List of Figures

1	Depth-dose curves for photon and proton beams	22
2	Overview and comparison between two treatment modalities	25
3	Distinct treatment planning strategies for proton therapy	25
4	SIRMIO workflow setup including different planning strategies	30
5	Ionoacoustic setup with only one axial single element piezoelectric (PZT)	41
6	Ionoacoustic signal obtained in the presence of heterogeneities	42
7	Angle of arrival schematic setup in 2D with n sensors	44
8	2D geometrical interpretation of the TOA algorithm	46
9	Geometrical interpretation of the TDOA in 2D	47
10	Simplex algorithm starting point.	51
11	Simplex algorithm, reflection including computation of the centroid (O)	52
12	Simplex algorithm expansion step	52
13	Simplex algorithm, contraction step	53
14	Simplex algorithm shrink step	53
15	Time reversal reconstruction workflow.	55
16	Time reversal and iterative time reversal reconstruction	56
17	2D and 3D initial guess setup	59
18	Multilateration setups used for robustness analysis in ideal scenarios	60
19	The experimental setup comprised three sensors	63
20	Transducer's spatial localisation setup	65
21	Transducer central position estimation for the cylinder target alignment	66
22	3D Multilateration experimental setup	68
23	Schematic representation of the procedure used to estimate the centre of the transducers	68
24	3D Rigid co-registration between the sensor template and the output from the optical tracking	69
25	Multilateration setup of BP position for the beam at a fixed spatial location	70
26	Schematic representation of multilateration workflow	74
27	Simulated ionoacoustic signals and ToF extraction for various sensor locations	75
28	TOA multilateration varying the initial guess position	78
29	TDOA multilateration varying the initial guess position	78
30	Error on the 2D Multilateration of ideal point sources without uncertainties	80
31	Error distribution for ideal point source localisation performed with TOA and TDOA	81
32	Error on the 2D Multilateration of ideal point sources located in the sensor array FOV	82
33	Error on the 2D Multilateration of ideal point sources located in the sensor array FOV in the presence of systematic	84
34	Error on the 2D Multilateration of ideal point sources located in the sensor array FOV in presence of random and systematic uncertainties	86
35	RMSE of the multilateration in ideal 3D scenarios depending on the source location	87
36	RMSE of the multilateration in 3D in the presence of random uncertainties depending on the source location	88
37	RMSE of the multilateration in 3D in the presence of systematic uncertainties depending on the source location	89
38	RMSE of the multilateration in 3D in the presence of random and systematic uncertainties depending on the source location	89

39	Comparison of the performance of TOA and TDOA multilateration in 2D and 3D in the presence of random and systematic uncertainties	90
40	Error in the ToF and accuracy of the BP localisation depending on the sensor positioning	92
41	IA signal in time-domain recorded with the sensor $B_{S_{319}}$	93
42	2D experimental study, the multilateration of the Bragg peak	96
43	2D Reconstructed BP position, for the transducer spatial locations estimated from the technical drawings	97
44	Transducer localisation before and after the registration	100
45	The recorded ionoacoustic signals were obtained from various sensor locations	100
46	3D BP Multilateration performed by the horseshoes transducer array with (a) TOA and (b) TDOA	101
47	ToF fitting horseshoes experiments.	102
48	Error on ToF estimation (converted to distance) of the IA signal produced by a SIRMIO beam of 50 MeV stopped	105
49	Error in position for TOA and TDOA multilateration, varying the number of sensors and proton pulse widths	106
50	Assessment of the ToF at clinical energy	119
51	Dose reconstruction and BP localisation using TRR algorithm	120
52	Initial setup showing both silicone layers positioned near the entrance window	122
53	3D Setup with ideal source localisation, (a) sensor B_{S_1} , B_{S_2} , B_{S_3} and B_{S_4} sensor configuration, (b) setup including all the point sources inside the FOV.	122
54	The experimental setup for the 3D I-BEAT detector consists of three sensors (denoted as B_{S_1} , B_{S_2} , and B_{S_3}) and a silicon target. The silicon target was removed for the experiments discussed in this thesis, and all measurements were conducted without it. The 3D I-BEAT detector is mounted on a 3D linear stage to ensure precise and secure positioning and alignment.	123
55	FR multilateration performed with TOA using Simplex and Levenberg algorithms	124
56	FR multilateration performed with TDOA using Simplex and Levenberg algorithms	124
57	Multilateration performance with and without the analytical-numerical gradient	131
58	Pulse-echo measurement between the two lateral sensors.	132
59	Multilateration using TDOA for different proton widths.	133
60	TOA, BP localised with multiple beam offsets	134
61	TDOA, BP localised with multiple beam offsets	135

List of Tables

1	FR of TOA and TDOA for optimisations performed with the Simplex and Levenberg algorithms	79
2	Summary and comparison of the performance of 2D multilateration using TOA and TDOA without uncertainties	81
3	2D Multilateration comparison between TOA and TDOA in the presence of random uncertainties	82
4	2D Multilateration comparison between TOA and TDOA in the presence of systematic uncertainties	84
5	2D Multilateration comparison between TOA and TDOA in the presence of random and systematic uncertainties	86
6	Summary of the errors obtained using 3D Multilateration without modelling uncertainties	87
7	3D Multilateration comparison between TOA and TDOA in the presence of random uncertainties	88
8	3D Multilateration comparison between TOA and TDOA in the presence of systematic uncertainties	89
9	3D Multilateration comparison between TOA and TDOA in the presence of random and systematic uncertainties	89
10	Multilateration comparison between 2D TDOA vs 3D TDOA with random and systematic uncertainties	90
11	Multilateration of the BP position in 2D for different ToF extraction methods	92
12	Evaluation of the multilateration of the BP position using three different ToF extraction methods	94
13	Error in position reconstruction for multilateration performed in 2D	98
14	SNR estimation for single proton pulse measurements (1.69 Gy)	98
15	The mean and standard deviation of ToF for all transducers in the network	101
16	SNR estimated from all the transducers with 50 acquisitions	101
17	Multilateration error in BP position for different proton time profile widths	107
18	Multilateration error in BP position for different proton time profile widths	108
19	TOA Multilateration of the BP position for different beam offsets along the y-axis	110
20	TOA Multilateration of the BP position for different beam offsets along the x-axis	110
21	TOA Multilateration of the BP position for different beam offsets along the z-axis	110
22	TDOA Multilateration of the BP position for different beam offsets along the x-axis	111
23	TDOA Multilateration of the BP position for different beam offsets along the y-axis	111
24	TDOA Multilateration of the BP position for different beam offsets along the z-axis	111
25	Comparison of the performance of 2D multilateration using TOA and TDOA considering random uncertainties	125
26	Comparison of the performance of 2D multilateration using TOA and TDOA considering systematic uncertainties	125
27	Comparison of the performance of 2D multilateration using TOA and TDOA, random and systematic uncertainties modelled simultaneously	125
28	Comparison of the performance of 3D multilateration using TOA and TDOA considering random uncertainties	126
29	Comparison of the performance of 2D multilateration using TOA and TDOA considering systematic uncertainties	126

30	Comparison of the performance of 3D multilateration using TOA and TDOA, random and systematic uncertainties modelled simultaneously	126
----	---	-----

List of Abbreviations

AOA	Angle of arrival
AR	Acceptance rate
BP	Bragg peak
BP_{FWHM}	Bragg peak full width at half maximum
CT	Computed tomography
DECT	Dual-energy computed tomography
ew	Entrance window
FOV	Field-of-view
FWHM	Full width at half maximum
GPS	Global Positioning System
HU	Hounsfield Units
I-BEAT	Ion-Bunch Energy Acoustic Tracing
IA	Ionoacoustics
IDD	Integral depth dose
IVP	Initial value problem
LLS	Linear least squares
MC	Monte Carlo simulation
MDS	Multidimensional scaling
ML	Maximum likelihood
MRI	Magnetic resonance imaging
NLS	Nonlinear least squares
OAR	Organs at risk
pCT	Proton computed tomography

PET	Positron emission tomography
PGI	Prompt gamma imaging
RMSE	Root mean square error
RSP	Relative stopping power
RSS	Received signal strength
SIRMIO	Small Animal Proton Irradiator for Research in Molecular Image-guided Radiation-Oncology
SOBP	Spread Out Bragg Peak
Tandem	Research electrostatic accelerator
TDOA	Time-difference-of-arrival
TOA	Time-of-arrival
ToF	Time-of-flight
TPS	Treatment planning system
TRR	Time-reversal image reconstruction
US	Ultrasound
WET	Water equivalent thickness
WLLS	Weighted linear least squares

1 Introduction

*“Until suddenly one day I felt
beautiful and holy for having had
the courage to hold on to my sanity
after all I’d seen and been through,
body and soul, in too loud a
solitude...”*

Bohumil Hrabal

1.1 Context

Cancer is one of the leading causes of mortality worldwide, mostly in more industrialised countries. Deaths in those countries are increasing each year [1, 2, 3, 4]. Cancer cases in low and middle-income countries are also growing exponentially [5, 6, 7], bringing awareness about the pathology among governments and healthcare providers. In places like Sub-Saharan Africa, the most active focus was on the mortality caused by malaria [8, 9]. But in recent years, due to the rapid increase in deaths caused by cancer, many health policies have been implemented specifically to fight cancer or to support the fight against cancer. Moreover, with increasing curing options for mortality caused by malaria, cancer comes into focus. A worldwide consciousness exists regarding various forms of cancer, accompanied by robust efforts in preventive education [10, 11, 12]. One reason for the increasing number of cancers is that life expectancy is also increasing, and the incidence of some cancers is also increasing, e.g., breast and prostate cancer [13, 4]. Indeed, other factors go behind this work's scope, like cancers related to HIV/AIDS¹, obesity, decreasing physical activity, and a lifestyle more westernised [14, 15, 16]. On average, the number of cancer deaths in industrialised countries is still higher than in low and middle-income countries [16, 17]. However, we must consider that more reliable statistics coming from some low or middle-income countries is still an issue [7, 18]. This factor may also be a bias of the overall death incidence caused by cancer in industrialised versus low and middle-income countries. On this note, it is also important to mention that some low and middle-income countries are working closely with the World Health Organization to have more robust epidemiological and bio-statistics facilities to enable more reliable statistics and epidemiological data collection. The effort to fight cancer is being addressed globally with medical training, technological advancement, new drug discoveries, etc. However, besides technological advancement, it is also crucial to increase our awareness that we should rethink our lifestyle since some cancers are caused by substances we consume daily, like tobacco and alcohol.

There are currently three primary treatment options for patients diagnosed with cancer: surgery, chemotherapy and radiation therapy. The choice of the treatment modality and combination thereof depends on the disease's stage, among other factors. The surgery aims to remove the tumour or incise a significant portion of it. For cancer that is likely to spread or has already spread, chemotherapy is a preferable choice. Chemotherapy uses specific drugs (i.e., chemotherapeutic agents) to kill the tumour cells. The other technique, often used in combination with surgery and/or chemotherapy, is based on radiation therapy, subdivided into radiation therapy using internal radiation (e.g., brachytherapy) and radiation therapy using an external beam. Brachytherapy involves implanting radioactive sources into or near the tumour, delivering high doses of radiation locally while minimising exposure to healthy tissues. External radiation therapy uses high amounts of radiation originating from a particle accelerator (i.e., linear accelerator, synchrotron, cyclotron, and synchrocyclotron). Particle accelerators propel charged particles using electromagnetic fields. As relevant to the context of this work, proton therapy employs two common beam types: continuous and pulsed beams [19].

Radiation therapy is the primary modality for cancer treatment; almost 60% of cancer patients are treated with this modality. In many cases, radiation therapy can be combined with chemotherapy or surgery or other systemic therapies, depending on the oncologist's prescription [20, 21]. Among all the techniques listed before, the objective of this work is centred on radiation therapy, particularly proton therapy. In radiation therapy, photon therapy is the most widespread treatment modality. Photon therapy uses primarily X-rays (or to a less extent gamma rays) to deliver radiation locally to tumour-target cells and break their DNA in a complex way, such that cell repair is almost impossible.

¹Immunodeficiency Virus/Acquired Immunodeficiency Syndrome.

The energy deposited by photons in matter decreases almost exponentially with the penetration depth, as shown in Fig.(1). Another technique increasingly used for external radiation therapy is based on particle therapy (i.e., protons or other heavier positively charged ions), which may offer advantages over photon therapy, e.g., due to a more conformal dose delivery (see Fig.(1) next sections). The main focus of this thesis will be exclusively on proton therapy.

1.2 External Radiotherapy

External radiotherapy uses external sources of ionising radiation to damage tumour cells. To this end, doctors can recommend the radiation quality, typically photons or protons, for deep-seated tumours. However, as shown in Fig.(1), even if both modalities use an external radiation source, one could notice that photon therapy and proton therapy are entirely different. The dose, which is the energy per unit of mass, refers to the amount of radiation energy delivered to a specific target volume or tissue in the body. It quantifies the energy deposited per mass by the ionizing radiation in the treated volume and is typically measured in units such as Gray (Gy) or centigray (cGy), where 1 Gy is equivalent to 1 J/kg. In Fig.(1), one can note that when normalizing to the same maximum, the entrance dose for photons is higher than for protons for a single radiation field. As seen, the photon dose decreases almost exponentially after an initial maximum when passing through the body, i.e., proximal tissues are exposed to high radiation doses. Deep-seated tissues are also exposed to a specific dose that decreases almost exponentially with the depth. Conversely, the maximum energy for protons is deposited near the end of their range, also known as the BP . Almost no dose is deposited beyond the BP. Due to its unique depth-dose characteristic, proton therapy can deliver high conformal dose distributions to target volumes with only a few treatment fields.

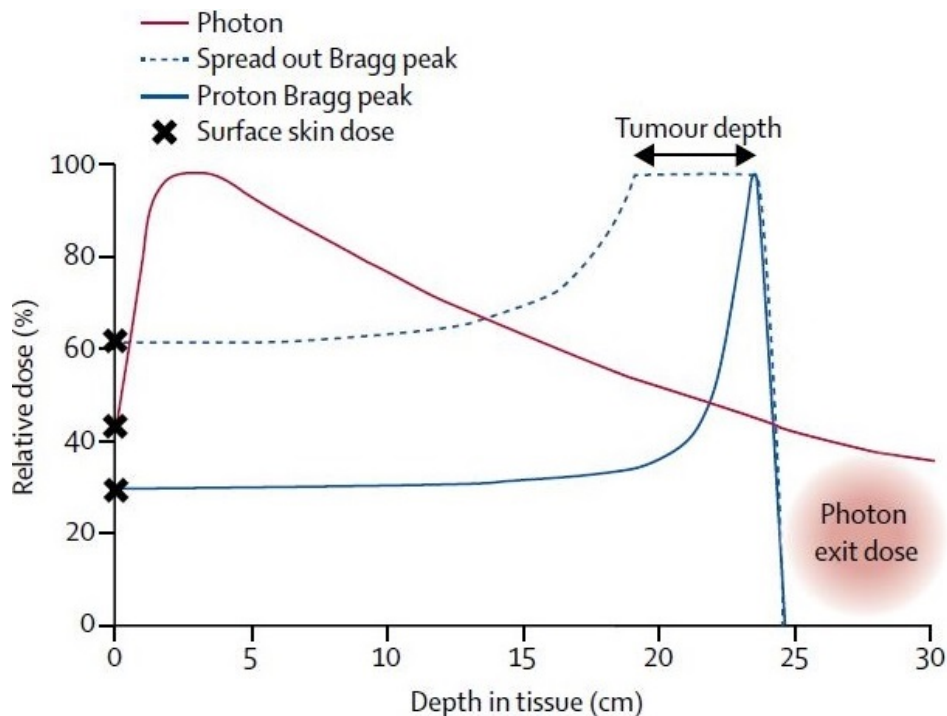


Figure 1: Depth-dose curves for photon and proton beams for a single treatment field, illustrating the cases of a single proton pencil beam (solid blue line), an Spread Out Bragg Peak (SOBP) (in dashed blue line), and a photon curve (solid red), figure extracted from [22].

However, proton therapy is more sensitive to uncertainties in the treatment planning phase and dose delivery. This chapter will discuss the source of uncertainties during the treatment planning phase in more detail. Uncertainties in proton therapy are more critical than uncertainties in photon therapy due to the steep gradient of the dose fall-off at the BP region. Understanding uncertainties in proton therapy is crucial to have a complete picture of the challenges of proton therapy compared to photon therapy. This will be concisely addressed in section 1.2.1. Multiple proton pencil beams (i.e., narrow, quasi mono-energetic beams) are commonly used to treat extended tumour volumes. An energy modulated approach called SOBPs produces an extended high dose distribution encompassing the entire tumour volume, utilizing several individual pencil beams with varying initial energies (see Fig.(1)). Protons undergo various interactions with matter, resulting in energy loss through inelastic Coulomb interactions, deflection of proton trajectory via repulsive Coulomb elastic scattering with the nucleus, removal of primary protons, and generation of secondary particles through non-elastic nuclear interactions. The Bethe-Bloch equation defines the mean energy loss (dE) per distance travelled (dx) of a charged particle, as shown below (neglecting corrective terms):

$$-\frac{dE}{dx} = \frac{4\pi n_d e^4 z_{eff}^2}{m_e c^2 \xi^2} \cdot \left[\ln \left(\frac{2m_e c^2 \xi^2}{I \cdot (1 - \xi^2)} \right) - \xi^2 \right] \quad (1.1)$$

Eq.(1.1) describes the mean energy loss per distance travelled of swift charged particles (protons, alpha particles, ions) passing through matter (or the linear stopping power of the material). The linear stopping power is given in MeV/cm, and there are some parameters in eq.(1.1) worth defining, n_d is the electron density of the material, ξ is the ratio between the speed of the particle and the speed of light in a vacuum (c_γ), z_{eff} is the charge of the projectile, I the mean excitation potential of the atoms in the absorbing medium, e is the electron charge, and m_e is the electron rest mass.

Proton imaging systems measure proton energy loss to calculate water equivalent thickness (WET), which represents the integrated stopping power relative to water. The WET measurement is used to determine the relative stopping power (RSP) of different tissues, which is crucial, for example, in reconstructing patient anatomy in proton computed tomography (pCT) and determining proton ranges based on how protons interact with tissues compared to water [23, 24, 25, 26].

The resting point of protons is defined as the range, which is nothing else than the expectation value of the distance of a proton with a given incident energy achieved in matter. The range can be described mathematically using the continuous slowing down approximation (CSDA), as reported in eq.(1.2). In eq.(1.2) \mathfrak{R}_{CSDA} is the range of a charged particle; for more details see [24].

$$\mathfrak{R}_{CSDA} \equiv \int_0^{E_0} \left(\frac{dE}{dx} \right)^{-1} dE \quad (1.2)$$

A clinically more relevant definition of the proton range is the commonly named R_{80} , which is the depth of the 80% of the maximum dose in the fall-off of the BP [27].

In proton therapy, range uncertainty refers to the case of either under-shooting or over-shooting the target volume. Under-shooting happens when the distal part of the target volume does not receive enough radiation due to a shorter range, while over-shooting occurs when a longer range delivers excessive radiation beyond the target (distally) and not enough coverage to the proximal part of the tumour. Range uncertainties can be critical when dealing with tumours close to *organs at risk* (OAR).

The OAR refers to any anatomical structure that should be spared during radiation, and one example of OAR is the heart. Therefore, a more conservative beam arrangement avoiding stopping the beam in front of OARs might be required for critical anatomical structures, as will be apparent during the discussion in this section. Fig.(2) illustrates the intricacies of a proton pencil beam traversing tissue in two scenarios: an ideal scenario² and a scenario where the pencil beam is affected by range errors. In the *nominal situation*, the pencil beam passes through different tissues and stops in the target tumour, with almost no extra dose deposited in the distal OAR. In this particular case of a single treatment field, the superiority of proton therapy over photon is evident because the maximum energy is deposited in the tumour volume while optimally sparing healthy tissues. The second case is the so-called *uncertain situation*, as illustrated in Fig.2(b). Regardless of uncertainties, for individual photon beams, the maximum dose deposition will always happen in healthy tissue for deep-seated tumours. A distal OAR will only be subject to a portion of the dose, which will always be lower than the entrance dose, as shown in Fig.(1). On the contrary, range errors are more crucial for protons, as shown in Fig.2(b). In the presence of an over-shooting, the BP will stop in the OAR, which may lead to a risky situation. In synthesis, the most significant limitation of proton therapy compared to photon therapy is the uncertainty in the range estimation, which will be addressed in section 1.2.1.

The ideal scenario for proton therapy is when the desired dose delivery is entirely confined to the tumour target volume without providing any extra dose to the OAR. Fig.(3) illustrates different planning strategies for proton therapy and their inherent sensitivity regarding range uncertainties [28]. The desired radiation plan is the so-called *single field plan*, as shown in Fig.3(a). In this radiation planning configuration, the healthy tissue, i.e., lung³ is exposed to a minimal dose. Ideally, the target tumour volume should receive the maximum dose deposition. However, range uncertainties in proton beams can result in unintended irradiation of OARs or, in the worst-case scenario, the beam stopping directly at the OAR. This situation of the beam stopping at an OAR can have disastrous consequences. Therefore, the *single field plan* would be the ideal irradiation planning strategy for cases without systematic or random uncertainties during treatment planning and treatment delivery. Another treatment plan, the *multi-field plan*, shown in Fig.3(b), involves irradiating the tumour volume from different angles to minimize the risk of range uncertainties. In this configuration, the OAR is less sensitive to range uncertainties because there is no BP directly placed in front of it. Therefore, this is a more conservative treatment plan because there will be no extra dose in the distal OAR in case of over-shoot. However, this comes with the cost of more healthy tissues being exposed to radiation and, consequently, a higher probability of side effects or secondary cancer. The last irradiation strategy is the so-called *patched-field plan*, as shown in Fig.3(c). Compared to the other treatment planning strategies, in this one, the number of beam angles is limited to reduce the dose to healthy tissue, taking the risk that some pencil beams could be misplaced at the patch line, resulting in cold or hot spots in the tumour. Therefore, as one can see, strategic treatment planning is of the highest importance. That is because we do not have the luxury of irradiating a given tumour volume at the expense of an OAR.

²In this case, assuming no range uncertainties and complete dose delivery to the target tumour.

³The healthy tissue could have been something different than the lung. However, in this particular case, the tumour volume is in the left lung.

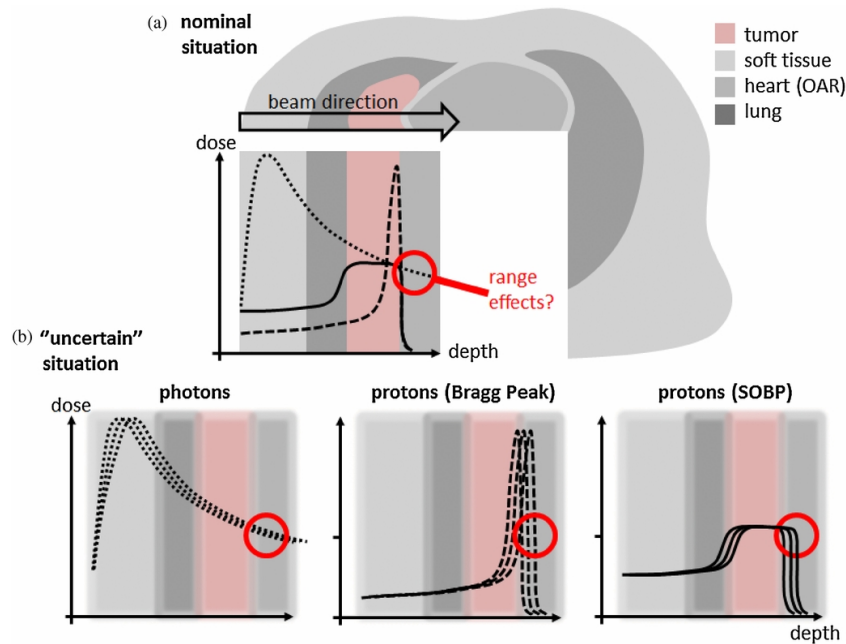


Figure 2: Overview and comparison between two treatment modalities: proton and photon therapy. (a) Potential advantage of proton therapy compared to photon therapy, ideal case without uncertainties. The dotted line is the photon depth-dose curve; the dashed line is the dose deposited by a pristine pencil beam; the solid line is the SOBP, which aims to cover the whole tumour volume. (b) Influence of range uncertainties on the respective depth-dose curves, figure extracted from [28].

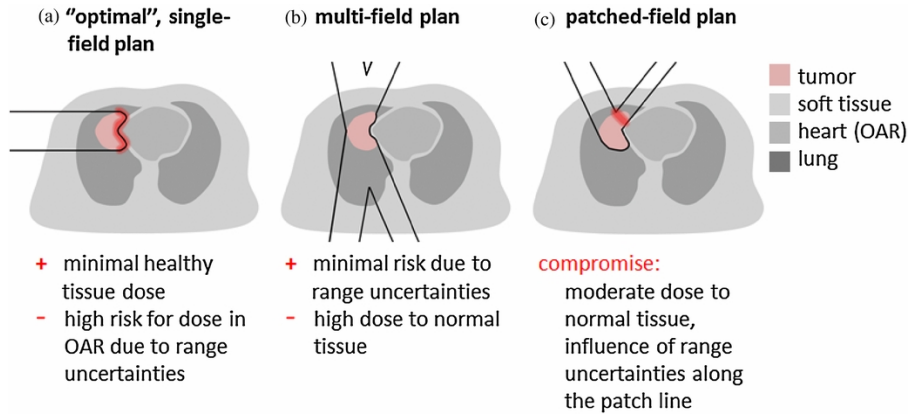


Figure 3: Distinct treatment planning strategies for proton therapy and their potential sensitivity towards range uncertainties, figure extracted from [28].

1.2.1 Sources of Range Uncertainties

Once the clinicians agree that the patient should be treated with proton therapy, the patient goes through two critical stages: treatment planning and delivery. The treatment plan is defined in a treatment planning system (TPS) that optimises the parameters of the treatment delivery (for pencil beam scanning: different energy layers, spot positions and irradiation angles) to maximise the tumour coverage and minimise the dose in the OARs. The TPS phase is mainly performed with volumetric images obtained from X-ray computed tomography (CT) scans, which can be eventually supplemented by additional image modalities such as magnetic resonance imaging (MRI) and positron emission tomography (PET) for better tumour visualisation. Last is the treatment phase; in this particular stage, the patient is treated according to the specifications defined by the TPS. The treatment is typically divided into several fractions, and one could easily imagine that this repetitive process is not error-free because uncertainties arise at the treatment planning and delivery stage.

- **Treatment Planning Phase:** a patient is referred to a CT scan already in the eventual treatment position during the treatment planning phase. After data acquisition and reconstruction, the X-ray attenuation coefficients are converted into Hounsfield Units (HU), which describes the attenuation coefficient of tissue relative to water. The conversion from HU to proton stopping power relative to water, which is needed for the computation of the treatment plan, is one of the largest causes of uncertainties in calculating the proton beam stopping position *in vivo*. Besides that, uncertainties may also arise from the CT imaging acquisition system (i.e., artefacts, resolution, noise); all these factors are discussed in depth in the literature [29, 30, 28, 31].
- **Treatment Delivery Phase:** The treatment delivery phase is repetitive, i.e., the patient goes under more than one treatment fraction in typically a few weeks [32, 33], with schedules that may change from one proton facility to another and strongly depend on the tumour entity and stage. During this phase, uncertainties may arise from patient setup errors with respect to the proton beam. Furthermore, organs in motion, e.g., due to respiration or other physiological processes, may also be a source of uncertainties. In addition, during the treatment fractions, the patient's anatomy can change; for example, the patient may gain or lose weight; hence, this fluctuation in the weight causes changes in the amount of tissue traversed by the beam, i.e., wadding of inner cavities and reduction of tissue mass, which translates into changes of the beam range and thus a source of treatment delivery uncertainties.

Efforts are being made to properly deal with range uncertainties during the treatment planning and delivery phase to fully use the potential of proton therapy. One possibility to reduce range uncertainties at the planning stage is by implementing robust treatment planning [34, 35]. Robust treatment planning is an optimisation method explicitly developed for protons. It incorporates physical (e.g. patient setup and range errors) and anatomical/biological uncertainties (e.g., tumour shrinkage) directly into the treatment plan optimisation. The aim is to simultaneously optimise the plan considering all error scenarios and worst-case deposited dose values. These optimisation techniques do not eliminate the uncertainties but are typically used to minimise the dosimetric consequences of range and other sources of uncertainties [36]. Moreover, the current clinical practice to deal with range uncertainty is to use the so-called safety margins, which can be quantified a priori during the treatment planning phase. These margins vary from facility to facility, as well as tumour type, location, and irradiation strategy. Nonetheless, a commonly used approach is to assume an uncertainty in the proton beam range of $3.5\% + 1$ or 2 mm [30, 37].

State-of-the-art imaging technologies like dual-energy computed tomography (DECT) and pCT can improve the accuracy of treatment planning, replacing the traditionally used single energy X-ray CT [38]. DECT uses two X-ray energy spectra and can provide more accurate determination of stopping power ratio, besides tissue composition information [39, 40]. pCT directly measures the proton stopping power of tissues, offering an even more precise method for treatment planning in proton therapy [41, 42, 43]. These technologies can improve targeting accuracy, dose delivery, and treatment outcomes while minimising side effects.

1.3 In Vivo Range Verification Methods

The aim of *in vivo* range verification is to be able to pinpoint the range of charged particles losing their energy within a material. The initial goal is to be able to perform *in vivo* range verification during the treatment fraction and then correct it or adapt the treatment for the following treatment fractions. The end game would be to have the capability of performing *in vivo* range verification in real-time. Several range verification methods have been studied. However, the two methods close to routine clinical implementation are PET [44] and PGI [45]. Both range verification methods (PET and PGI) are based on monitoring the reaction products of nuclear interaction along the proton beams.

- PET: the working principle of PET relies on the coincidence detection of electron-positron annihilation photons (i.e., 511 keV photons) emitted side by side. The positrons are produced by β^+ decay of positron emitters (e.g., ^{11}C , ^{15}O) created via inelastic nuclear interaction of the proton beam with target nuclei, for more details see [46, 47, 48, 49].
- PGI: it relies on the detection of prompt gamma photons released in the de-excitation stage after nuclear interactions of the proton beam with the tissue nuclei of a patient. The majority of such prompt gamma is generated from nuclear reactions of protons with ^{12}C and ^{16}O isotopes⁴ and the range verification is assessed by their spatial, temporal or energy distributions; for more detail, see [50, 51, 52].

Notwithstanding the significant advances in PET and PGI techniques for *in vivo* range verification, these techniques do not provide a forthright relationship between the measurable signal and the beam range or BP position. Moreover, the instrumentation required for PET and PGI is bulky and not cost-effective. This might be an issue for large-scale production, especially if we consider that implementing proton therapy facilities is much more expensive than photon therapy facilities. Therefore, range verification methods such as PET or PGI scale up the overall cost of proton therapy facilities. An alternative to the aforementioned techniques is range verification based on IA. In the next section, the rationale and the potential benefits of the IA range verification method compared to PET and PGI will be discussed.

1.4 Ionoacoustics

When a pulsed proton beam deposits energy in a medium, it produces thermoacoustic waves, also known as IA. Using a set of multiple ultrasound (US) transducers placed at different spatial locations makes it possible to pinpoint the proton beam stopping position in the medium. The feasibility of IA was initially proven for a clinical proton therapy treatment of a patient with hepatic cancer,

⁴Carbon-12 is the most abundant of the two stable isotopes of carbon and oxygen-16 is a stable isotope of oxygen. Both isotopes are the main components in the of human tissue.

where the authors of the study suggested that the technique could be used for range verification by improving the hardware (i.e., transducers sensitivity), also offering the possibility of co-registration with anatomical structures [53]. For tumours that can be easily imaged using ultrasound probes (i.e., liver, prostate), IA could play a significant role for *in vivo* range verification. IA range verification has many potential advantages compared to the previously mentioned techniques; the ultrasound probes could be designed to be as compact as possible, cost-effective, and can be used in real-time, providing almost direct range verification. Furthermore, combining IA and US can allow for anatomical confirmation (i.e., the localised BP position can be directly linked to the anatomical imaging when using the same US probe). All these aspects make IA a promising technique for the future of *in vivo* range verification. However, there are some drawbacks compared to PET and PGI, the first one being the fact that IA is accelerator dependent (i.e., for IA, the proton beam must be pulsed with a specific proton time profile usually between 3.5–10 μ s). Furthermore, for tumours that are not easily accessible using US imaging, IA as a range verification method will most likely not be feasible. One reason is that, by imaging complex anatomical structures, the acoustic wave will propagate through different tissues having multiple reflections and be attenuated; besides the attenuation, the acoustic wave will be subject to varying sound speeds (i.e., different tissues will have different sound speeds). Therefore, tumours in less complex anatomies such as the liver and prostate, will be less sensitive to the speed of sound variation along the US/IA beam path, making it ideal for US/IA image co-registration. Moreover, the IA signals will be less susceptible to attenuation for tissues such as the liver and prostate since the speed of sound will be almost constant compared to other anatomical locations. For this reason, *in vivo* range verification with IA for these tumours might be more easily implementable.

1.5 The SIRMIO Project

The main objective of this thesis is to localise the BP position in the context of the SIRMIO project [54]. Currently, only two commercial platforms for small animal radiotherapy are for photon radiotherapy, although their image guidance cabinet is also offered for usage in dedicated and facility-dependent research beamlines. However, as discussed in section 1.1, proton therapy has some benefits over photon therapy. Therefore, the SIRMIO project aimed at developing the first portable small animal image-guided research platform for proton therapy. The aim was to have a small animal radiotherapy platform that can be integrated into the beamlines of existing proton therapy facilities. The components are a beamline dedicated to small animals, multiple imaging modalities, and a mouse holding system to have a complete system for precision, image-guided small animal proton irradiation. One of the project's main features is combining pre-treatment imaging modalities, treatment planning and *in vivo* range verification. There have been many challenges to overcome for the project feasibility. These challenges include designing the dedicated small animal beamline, mouse holder, pre-treatment imaging system, treatment planning and *in vivo* range verification modalities. Different work packages were created to develop and eventually integrate highly complex sub-packages for each individual work package, which constitute the SIRMIO research platform. The integration of these work packages brings with it many challenges, which are listed below.

- WP1 (Beam degradation, focusing and monitoring): In proton therapy facilities, the energy used for human treatment typically varies between 70 to 250 MeV [55]. This energy spectrum is not feasible for small animal treatment because the energies required for small animals are normally lower (i.e., for a mouse treatment, it can vary from 20 to 50 MeV [56]). That is why beam energy degradation is required. The goal of beam energy degradation is to reduce the energies used for human treatment to energies for small animal treatment. In the SIRMIO

platform, the beam goes through the process of energy degradation, collimation and focusing using permanent magnets to achieve beam spot sizes appropriate for small animal treatment. The main task of this work package is to build the SIRMIO beamline able to degrade a 70 MeV beam energy to a range of 20 to 50 MeV, with a beam spot size (σ) within 1 mm [57]. To be able to design and build the beamline, several simulations were conducted using Monte Carlo simulation (MC). This work package also coordinates the mouse holder design. The mouse holder is not a single work package but the intersection of all work packages. The mouse holder main task is to keep the mouse in a sterile environment during the pre-treatment and irradiation phases.

- WP2-a (Ion radiography/tomography): Proton radiographic and tomographic imaging is sought for anatomical image guidance for target definition and 3D maps of the RSP for treatment planning as well as positioning for treatment delivery. The preference for proton over X-ray imaging is that the range calculation using this imaging technique is more accurate. The pre-treatment planning phase comprises proton tomography, while proton radiography is employed for the alignment. This work package aims to image the tumour properly and target it precisely. For both imaging modalities, a sub-millimetre resolution is expected.
- WP2-b (Ionoacoustics/ultrasound): This work package focuses on detecting ionoacoustic signals for *in vivo* range verification, along with US imaging pre-treatment and its co-registration with IA and any additional pre-treatment imaging (pCT or available X-ray CT). Additionally, the work package is responsible for developing sensitive ultrasonic detectors (i.e., able to detect acoustic signals with an amplitude $\ll 1$ Pa) capable of detecting acoustic signals with a frequency content ≤ 100 kHz as typical for IA. This work package aims to develop algorithms to localise the BP position for real-time *in vivo* range verification. The two investigated methods are based on image reconstruction (i.e., time-reversal image reconstruction (TRR)) and multilateration technique; both ways output the coordinates of the BP position in space. Nevertheless, the TRR can also output the reconstructed dose in 2D/3D.
- WP2-c (PET): This work package is responsible for *in vivo* range verification based on PET, as discussed in the section 1.2.1. The PET approach is suited for continuous-wave cyclotrons and slow-cycling synchrotrons. Therefore, this work package is responsible for designing and building high resolution and depth-of-interaction PET detectors, a prototype spherical in-beam PET scanner and image reconstruction algorithms and analysis for *in vivo* range verification. For more detail on PET designing in the context of SIRMIO see [58].
- WP3 (Adaptive treatment workflows and system integration/testing): This work package is responsible for the TPS. The workflow used for the human TPS was discussed in section 1.2.1, and it is a bit different to small animal TPS due to the need for daily imaging and replanning. From the computational point of view, a significant difference is the very low beam energies and small beam sizes used during the treatment phase, which require a well-validated dose engine tailored to this unconventional small animal application.

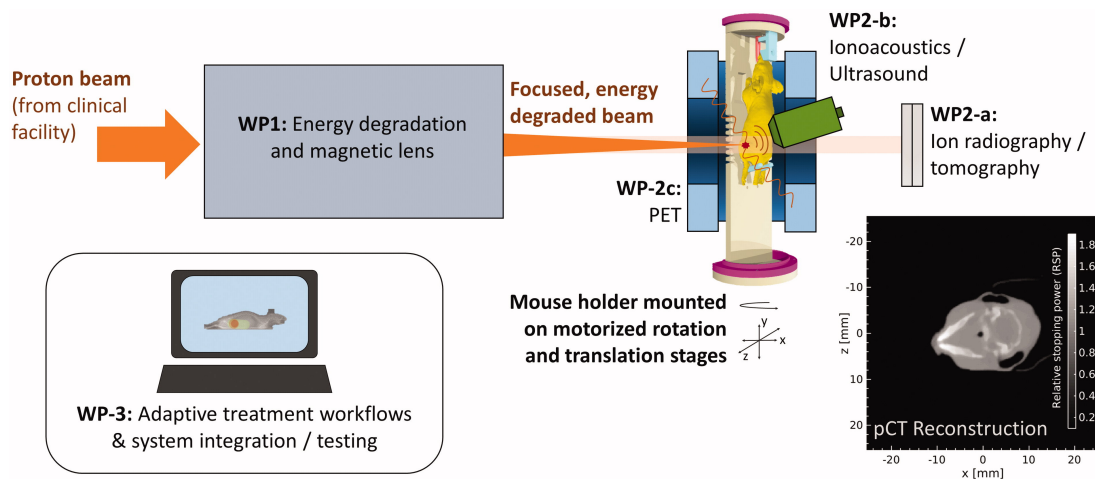


Figure 4: SIRMIO workflow setup including different work packages, figure extracted from [54].

1.6 Thesis Objective

The main aim of this thesis is to investigate IA multilateration for reliable *in vivo* range verification in small animals within the SIRMIO framework. SIRMIO focuses on low-energy proton beams, and our goal was to achieve sub-millimetre accuracy in quasi-real time while considering space limitations for the positioning of the sensors and using a minimal number of sensors. The investigation explored two numerical optimisation methods and two multilateration techniques within ideal scenarios. The objective was to evaluate the performance of two different algorithms in achieving the desired outcomes. The primary aims were to assess the impact of source position relative to sensor configuration on localisation accuracy and understand how errors in ToF estimation affected the results. By analysing various source positions in relation to sensor configuration, we gained insights into the factors influencing localisation accuracy. Additionally, we studied the effects of ToF estimation errors on overall multilateration accuracy.

The findings of this first study offer a valuable understanding of the performance and limitations of the multilateration algorithms, highlighting the importance of source position and ToF estimation errors for achieving accurate localisation. Moreover, the results contribute to optimising and refining multilateration techniques for *in vivo* range verification, particularly in the context of SIRMIO and its emphasis on low-energy proton beams.

Via a follow-up analysis, simulated IA signals were analysed to investigate various methods of extracting ToF and to assess how the sensor position relative to BP impacted ToF estimation. The objectives were twofold: first, to assess the accuracy of each ToF extraction method, and second, to evaluate its impact on BP localisation.

Through comprehensive analysis and comparison, this thesis aimed to identify the most accurate technique for extracting ToF from IA signals. Furthermore, by examining different sensor configurations, it was investigated how variations in sensor placement affect the accuracy and reliability of ToF estimation. These findings provide valuable insights into optimal sensor positioning strategies for achieving accurate BP localisation. The IA simulation studies were also cross-referenced with experimental observations, presenting their own challenges. These challenges predominantly included accurately determining the transducer spatial location and mitigating signal degradation caused by the limited SNR due to dose limitations and filtering imposed by the detectors.

Lastly, the gathered knowledge was used to support the development of a sensor array designed explicitly for multilateration in the context of the SIRMIO project. In this context, the impact of clinical proton pulse shape on ToF estimation and multilateration error was thoroughly examined. The evaluation encompassed various arc arrangements, allowing for the variation of sensor numbers while aiming to minimise their quantity. Furthermore, the beam position within the arc array was considered to mimic the delivery of a treatment plan, providing comprehensive insights into the performance of the sensor array in realistic scenarios. The implications of this study are noteworthy for developing *in vivo* range verification techniques in proton therapy, particularly in small animal studies conducted in SIRMIO. Accurate localisation with sub-millimetre precision is crucial for effective treatment planning and monitoring, and the findings of this study contribute to advancing these techniques in the field.

2 Ionoacoustics and Multilateration Theory

*Primo segno di un animo
equilibrato è la capacità
di starsene tranquilli in un posto
e in compagnia di sé stessi.*

Lucius Annaeus Seneca

2.1 Principle and Derivation

The derivation of the acoustic wave that follows is based on Kinsley's work [59, p. 113-120]. The theoretical IA principles are derived from the general acoustic wave equations. The acoustic pressure (p) is given by the difference between instantaneous acoustic pressure (\mathcal{P}) and equilibrium pressure (\mathcal{P}_0), as described in eq.(2.1). Before discussing the derivation of the acoustic pressure, it is worth defining another important parameter: condensation (s). It describes the change in density between the instantaneous density (ρ) and equilibrium density (ρ_0) for a given ambient fluid, as described in eq.(2.2). Considering adiabatic process (i.e., $\mathcal{P}/\mathcal{P}_0 = (\rho/\rho_0)^\chi$, where χ is the quotient of specific heats), the relationship between pressure and density can be described in the equation below:

$$p = \mathcal{P} - \mathcal{P}_0 \quad (2.1)$$

$$s = \frac{(\rho - \rho_0)}{\rho_0} \quad (2.2)$$

The instantaneous acoustic pressure can be expanded using Taylor's series, as described below:

$$\mathcal{P} = \mathcal{P}_0 + \left(\frac{\partial \mathcal{P}}{\partial \rho} \right)_{\rho_0} (\rho - \rho_0) + \frac{1}{2} \left(\frac{\partial^2 \mathcal{P}}{\partial \rho^2} \right)_{\rho_0} (\rho - \rho_0)^2 + \dots \quad (2.3)$$

Assuming small fluctuation, the acoustic pressure can be approximated by:

$$p \approx \mathcal{B} \left(\frac{\rho - \rho_0}{\rho_0} \right) \quad (2.4)$$

In eq.(2.4), \mathcal{B} is the adiabatic bulk modulus which describes the infinitesimal pressure change in a medium and it is defined as:

$$\mathcal{B} = \rho_0 \left(\frac{\partial \mathcal{P}}{\partial \rho} \right)_{\rho_0} \quad (2.5)$$

The equation of continuity⁵, which describes the conservation of mass is defined as follows:

$$\frac{\partial \rho}{\partial t} + \nabla \cdot (\rho \mathbf{u}) = 0 \quad (2.6)$$

⁵The continuity equation equates the shifting of the fluid with its compression or expansion, as discussed by Azhari, Haim in "Basics of biomedical ultrasound for engineers" and by John Wiley & Sons, 56-115 (2010), and Kinsler, Lawrence E., et al., in "Fundamentals of acoustics. John Wiley & sons, 116-117 (2000)."

Where \mathbf{u} represents the particle velocity of the fluid. The continuity equation can be further expanded as follows:

$$\rho_0 \frac{\partial}{\partial t} (1 + s) + \nabla \cdot [\rho_0 \cdot (1 + s) \cdot \mathbf{u}] = 0 \quad (2.7)$$

It is worth noting that eq.(2.7) was obtained by rewriting the instantaneous density in eq.(2.2) as $\rho = \rho_0(1 + s)$.

Assuming weak time and space dependence of ρ_0 and small variations of s , the continuity equation can be simplified⁶ and described as follows:

$$\frac{\partial s}{\partial t} + \nabla \cdot \mathbf{u} = 0 \quad (2.8)$$

The relationship between the acoustic pressure, particle velocity, and medium density at equilibrium can be described by Euler's equation⁷, which is expressed as follows:

$$\rho_0 \frac{\partial \mathbf{u}}{\partial t} = -\nabla p \quad (2.9)$$

Eq.(2.9) can be expanded as follows:

$$\nabla \cdot \left(\rho_0 \frac{\partial \mathbf{u}}{\partial t} \right) = -\nabla^2 p \quad (2.10)$$

The continuity equation can be expressed as follows:

$$\frac{\partial}{\partial t} \cdot \left(\frac{\partial s}{\partial t} + \nabla \cdot \mathbf{u} \right) = 0 \quad (2.11)$$

Combining eqs.(2.4,2.6,2.8 and 2.11), the wave equation at a given position (\mathbf{r}) and time instant (t) for a medium with a speed of sound (v_s), and without any external source is obtained as described below:

$$\nabla^2 p(\mathbf{r}, t) = \frac{1}{v_s^2} \left(\frac{\partial^2 p(\mathbf{r}, t)}{\partial t^2} \right) \quad (2.12)$$

⁶The initial density has no dependency on time, which can be rewritten as $\frac{\partial \rho_0}{\partial t} = 0$ and $\nabla \cdot (s \cdot \mathbf{u}) = 0$.

⁷The Euler's equation describes the simple force equation for acoustic processes of small amplitudes [59, p. 110].

Where the speed of the sound in the medium is defined as follows:

$$v_s^2 = \mathcal{B}/\rho_0 \quad (2.13)$$

Previously, the pressure wave equation was derived irrespective of any external source. However, acoustic waves can also be generated using an external source, i.e., a pulsed proton beam, which is the main acoustic source used in this thesis. The energy deposition of a pulsed proton beam generates rapid heating, resulting in a temperature increase and expansion of the medium. Therefore, if the external source describes the initial temperature rise in a given confined volume, then eq.(2.12) can be rewritten as:

$$\left(\nabla^2 - \frac{1}{v_s^2} \frac{\partial^2}{\partial t^2} \right) p(\mathbf{r}, t) = -\frac{b}{C_p} \left(\frac{\partial H(\mathbf{r}, t)}{\partial t} \right) \quad (2.14)$$

Eq.(2.14) holds only under the stress and thermal confinement conditions. The stress and thermal confinement time are discussed in section 2.1.1. In eq.(2.14), $H(\mathbf{r}, t)$ is the heating function derived from the temperature rise in the medium ($T(\mathbf{r}, t)$) [60]. $H(\mathbf{r}, t)$ can be described as follows:

$$H(\mathbf{r}, t) = \rho C_v \frac{\partial T(\mathbf{r}, t)}{\partial t} \quad (2.15)$$

In eqs.(2.14,2.15), C_p and C_v denote the specific heat capacities at constant pressure and volume, b is the volume thermal expansion coefficient. For eq.(2.14), a unique solution can be formulated in the presence of an external source using the Green function approach. Therefore, the first step is to simplify the source (heating function) located at a given position (\mathbf{r}') at a time instant (t') to a new generalised variable⁸ and considering the Green's function operator⁹. For this reason, eq.(2.14) can be rewritten as:

$$\left(\nabla'^2 - \frac{1}{v_s^2} \frac{\partial^2}{\partial t'^2} \right) p(\mathbf{r}', t') = -q(\mathbf{r}', t') \quad (2.16)$$

If we consider that a Dirac delta distribution gives the initial source, eq.(2.16) can be rewritten as follows:

$$\left(\nabla'^2 - \frac{1}{v_s^2} \frac{\partial^2}{\partial t'^2} \right) G(\mathbf{r}, t; \mathbf{r}', t') = -\delta(\mathbf{r} - \mathbf{r}') \delta(t - t') \quad (2.17)$$

⁸Generalized source variable $q(\mathbf{r}', t') = \frac{b}{C_p} \frac{\partial H(\mathbf{r}, t)}{\partial t}$.

⁹Green's function operator $G(\mathbf{r}, t; \mathbf{r}', t')$. Which has reciprocal properties i.e., $G(\mathbf{r}, t; \mathbf{r}', t') = G(\mathbf{r}', t'; \mathbf{r}, t)$. A more detailed and interesting discussion of Green's function approach for acoustic field calculations can be found in [61, p. 98-109].

For simplicity and compactness, the equations are solved without considering the time and space dependencies for $G(\mathbf{r}, t; \mathbf{r}', t')$, $q(\mathbf{r}', t')$ and $p(\mathbf{r}', t')$. However, the dependencies will be reinserted in eq.(2.22). The wave equation can be expanded further by combining eq.(2.16) and eq.(2.17), which leads to the equation described below:

$$p(\mathbf{r}, t) = \underbrace{\int_0^{t^+} \int_{V'} G q dt' d\mathbf{r}'}_{\text{I. source term}} + \underbrace{\int_0^{t^+} \int_{V'} \left(G \nabla'^2 p - p \nabla'^2 G \right) dt' d\mathbf{r}'}_{\text{II. boundary condition term}} + \underbrace{\int_0^{t^+} \int_{V'} \left(p \frac{\partial^2 G}{\partial t'^2} - G \frac{\partial^2 p}{\partial t'^2} \right) \frac{dt' d\mathbf{r}'}{v_s^2}}_{\text{III. initial condition term}} \quad (2.18)$$

Where the integration is from time instant 0 to t^+ in a volume of interest V' . The wave equation described in eq.(2.18) includes three terms¹⁰: the source term, the boundary condition term, and the initial condition term. The boundary and initial conditions can be simplified under the condition that $t' \rightarrow +\infty$ and $t' = t^+$, as described in eq.(2.19) and eq.(2.20).

$$\underbrace{\int_0^{t^+} \int_{V'} \left(G \nabla'^2 p - p \nabla'^2 G \right) dt' d\mathbf{r}'}_{\text{II. boundary condition term}} = 0; \quad t' \rightarrow +\infty; \quad (2.19)$$

$$\underbrace{\int_0^{t^+} \int_{V'} \left(p \frac{\partial^2 G}{\partial t'^2} - G \frac{\partial^2 p}{\partial t'^2} \right) dt' d\mathbf{r}'}_{\text{III. initial condition term}} = 0; \quad t' = t^+ \quad (2.20)$$

We can rewrite eq.(2.18) accounting only for the source term, and it can be described as:

$$p(\mathbf{r}, t) = \int_0^{t^+} \int_{V'} G(\mathbf{r}, t; \mathbf{r}', t') q(\mathbf{r}', t') dt' d\mathbf{r}' \quad (2.21)$$

In eq.(2.21), we assumed that the source is located in a given position (\mathbf{r}') at a given time instant (t'). The equation can be further expanded considering the heating function as follows:

$$p(\mathbf{r}, t) = \frac{b}{C_p} \int_0^{t^+} \int_{V'} G(\mathbf{r}, t; \mathbf{r}', t') \frac{\partial H(\mathbf{r}', t')}{\partial t} dt' d\mathbf{r}' \quad (2.22)$$

In an infinite space, without boundary conditions, the Green function is provided by:

¹⁰The reader can refer to [62, p. 316-317], where all the details on the eq.(2.18) are reported step by step.

$$G(\mathbf{r}, t; \mathbf{r}', t') = \frac{\delta\left(t - t' - \frac{|\mathbf{r} - \mathbf{r}'|}{v_s}\right)}{4\pi |\mathbf{r} - \mathbf{r}'|} \quad (2.23)$$

Combining eq.(2.22) and eq.(2.23), the pressure response at a given ultrasonic sensor can be written as:

$$p(\mathbf{r}, t) = \frac{b}{4\pi C_p} \frac{\partial}{\partial t} \left[\int d\mathbf{r}' \frac{1}{|\mathbf{r} - \mathbf{r}'|} H\left(\mathbf{r}', t - \frac{|\mathbf{r} - \mathbf{r}'|}{v_s}\right) \right] \quad (2.24)$$

2.1.1 Ionoacoustic Initial Pressure Derivation

To derive the IA initial pressure, it is important to define two parameters. The first one is the thermal relaxation time (τ_{th}) which characterises the thermal diffusion. The thermal relaxation time quantifies the heat transfer rate from one point to another in a given material. Thermal relaxation time can be mathematically described as below:

$$\tau_{th} = \frac{d_c^2}{\alpha_{th}} \quad (2.25)$$

Where α_{th} describes the thermal diffusivity in [m^2/s] and d_c is the specific dimension of the heated region in (m).

The second important parameter is the stress relaxation time (τ_s), which is the time needed for an acoustic wave to travel through the heated region, and it is defined as:

$$\tau_s = \frac{d_c}{v_s} \quad (2.26)$$

Consequently, for a pulse excitation, the fraction volume expansion of the heated region (dV/V) can be described as:

$$\frac{dV}{V} = -\kappa p + b\Delta T \quad (2.27)$$

In the above equation, κ is the isothermal compressibility (Pa^{-1}), p is the change in pressure, b is the thermal coefficient of volume expansion (K^{-1}), and ΔT is the change in temperature (K). Under isothermal conditions, the coefficient of compressibility for a fluid is defined as:

$$\kappa = -\frac{1}{V} \left(\frac{\partial V}{\partial p} \right)_{\Delta T} = \frac{C_p}{\rho v_s^2 C_v} \quad (2.28)$$

The excitation satisfies the thermal and stress confinement condition if the proton pulse is much shorter than the thermal and stress confinement times, meaning the heating time is short enough to ignore thermal diffusion and faster than the time it takes for an acoustic wave to pass through, the irradiated area heats up quickly due to the proton beam's energy loss. The energy loss is caused mainly by Coulomb inelastic interactions with electrons in matter. Consequently, the fractional volume expansion describe in eq.(2.27) is negligible ($dV/V = 0$), and the local pressure rise (p_0) can be expressed as:

$$p_0 = \frac{b \cdot \eta}{\kappa} \Delta T = \left(\frac{b}{\kappa \rho C_v} \right) \rho D = \Gamma \rho D \quad (2.29)$$

In eq.(2.29), p_0 was expressed in function of the Grüneisen parameter (Γ) and the deposited dose (D), which is the amount of energy (E) deposited in a volume of mass (m) and η denotes the efficiency of converting energy into heat, which is considered to be equal to one for IA applications [63, p. 22]. Furthermore, Γ is a dimensionless¹¹ material-specific constant that indicates the conversion efficiency between the deposited heat energy and pressure variation [65], and it can be rewritten as:

$$\Gamma = \frac{b}{\kappa \rho C_v} = \frac{b}{\left(\frac{C_p}{\rho v_s^2 C_v} \right) \rho C_v} \implies \Gamma = \frac{b v_s^2}{C_p} \quad (2.30)$$

The heating function can be decomposed into two parts, one spatial $H_s(\mathbf{r}')$ and one temporal component $H_t(t')$, and it can be expressed as:

$$H(\mathbf{r}', t') = H_s(\mathbf{r}') H_t(t') \quad (2.31)$$

The decomposition of the heating function in eq.(2.31) can be combined with eq.(2.24). Hence, the pressure wave can be rewritten as:

$$p(\mathbf{r}, t) = \frac{b}{4\pi C_p} \frac{\partial}{\partial t} \left[\int d\mathbf{r}' \frac{H_s(\mathbf{r}')}{|\mathbf{r} - \mathbf{r}'|} H_t \left(t - \frac{|\mathbf{r} - \mathbf{r}'|}{v_s} \right) \right] \quad (2.32)$$

When the duration of any excitation pulse is shorter than the stress relaxation time (as defined in eq.(2.26)), it can be treated as instantaneous. This assumption implies that all the heat energy has been

¹¹Theorie des festen Zustandes einatomiger Elemente [64].

transferred before any change occurs in the mass density. Consequently, this simplifies the problem of instantaneous heating to an initial value problem (IVP), a well-known topic in the literature. For further elaboration, refer to [66, 67]. Thus, when in stress confinement, the temporal heating function can be approximated to a Dirac-delta function ($H_t(t') \rightarrow \delta(t')$)¹². Therefore, the acoustic pressure for an arbitrary object excited with a delta heating response can be expressed as:

$$p(\mathbf{r}, t) = \frac{b}{4\pi C_p} \frac{\partial}{\partial t} \left[\int d\mathbf{r}' \frac{H_s(\mathbf{r}')}{|\mathbf{r} - \mathbf{r}'|} \delta\left(t - \frac{|\mathbf{r} - \mathbf{r}'|}{v_s}\right) \right] \quad (2.33)$$

Furthermore, the initial pressure located at the position (\mathbf{r}') can be written as:

$$p_0(\mathbf{r}') = \Gamma H_s(\mathbf{r}') \quad (2.34)$$

$$p(\mathbf{r}, t) = \frac{\partial}{\partial t} \left[H_t \otimes \underbrace{\frac{1}{4\pi v_s^2} \int d\mathbf{r}' \frac{p_0(\mathbf{r}')}{|\mathbf{r} - \mathbf{r}'|} \delta\left(t - \frac{|\mathbf{r} - \mathbf{r}'|}{v_s}\right)}_{P_\delta(\mathbf{r}, t)} \right] = \frac{\partial}{\partial t} [H_t \otimes P_\delta(\mathbf{r}, t)] \quad (2.35)$$

The recorded pressure by an ultrasonic sensor is expressed in eq.(2.35), where it has to be noted that the time profile of the proton beam is already included. In the aforementioned equation, $P_\delta(\mathbf{r}, t)$ includes the spatial information of the acoustic pressure without accounting for the proton time profile. Hence, from eq.(2.35), the acoustic pressure at a given sensor can be computed by considering different proton time structures, which H_t describes. The final pressure equation model described in eq.(2.35), which is given by the convolution (\otimes) between H_t and $P_\delta(\mathbf{r}, t)$ can predict the IA signals for different accelerator facilities via simulation studies.

2.1.2 Shape and Features of Ionoacoustic Signals

The change in the IA signal over time relies on the part of the proton beam detected by the sensor. Conversely, depending on the sensor position, two predominant acoustic wavefronts are usually observed in homogeneous media [68, 69, 70]. A quasi-spherical wave propagating from the BP region (γ -wave) and a cylindrical wavefront (α -wave) emanating from the plateau region, which exhibit different dose spatial gradients. Both acoustic wavefronts have different frequencies because they are emitted from the BP and the plateau region. High-frequency signals are expected for γ -wave compared to α -wave for individual pencil beams. This is typical in most pre-clinical scenarios investigated in this thesis. The discussion on BP localisation using IA signals will be centred on these two wavefronts. For multilateration purposes, the ToF will be estimated from the γ -wave and α -wave. For sensors placed perpendicular to the beam axis, the recorded IA is expected to have only contributions from the γ -wave. Conversely, for sensors placed at a certain angle with respect to the beam axis, the recorded IA signal is expected to have contributions from γ -wave and α -wave. From the ionoacoustic signals, the BP position will be retrieved after estimating the ToF from different sensor locations. The classic shape of the ionoacoustic signal was measured in an experimental campaign in water using a

¹²In eq.(2.33) it was assumed $H_t(t') = \delta(t')$.

proton beam with an energy of 20 MeV as addressed by Assmann et al., in [71]. In this experimental study, a sensor was used¹³ placed perpendicular to the proton beam entrance window (also called axial sensor), as illustrated in the setup in Fig.(5a). The trace of the IA signal recorded with a 3.5 MHz transducer is illustrated in Fig.(5b).

The IA signal is composed of three main pulses, namely *direct signal* (signal originating from the BP), *entrance signal*, which is produced at the position where the proton beam enters the water phantom, and the *reflection signal* which is the reflection of the direct signal at the interface between air and water. For multilateration purposes, only the *direct signal* is relevant both for sensors placed *on-axis*¹⁴ or for sensors placed *off-axis*¹⁵. This is because the direct signal provides the most accurate information about the position of the signal source¹⁶ and the BP, which is what we want to localise. The shape of the ionoacoustic signal depends on the proton time profile. The typical proton time profile shape is rectangular (for research accelerators) or Gaussian (as normally used for clinical beam energies). Gaussian pulses come from synchrocyclotrons, the only machines providing pulsed beams clinically. In the aforementioned experimental campaign conducted by Assmann et al., at a research electrostatic accelerator (Tandem) with artificial pulsing, the IA signal was measured using multiple rectangular proton time profiles. The shape of the IA signals is expected to change for different proton pulse widths. As summarised in Fig.(5c), for a proton pulse width of 57 ns and 190 ns, the shape of the *direct signal* changes. The relative peak-to-peak amplitude and frequency also change for both proton pulse widths. The IA signal is still in stress confinement for the two mentioned proton pulse widths at the considered beam energy and time structure. In the studies conducted by Assmann et al., the BP full width at half maximum (BP_{FWHM}) was about 300 μm for the 20 MeV proton beam energy, and the speed of sound in the medium was 1507 m/s at a temperature of 29°C. Hence, the stress confinement time τ_s was estimated to be about 200 ns. For a proton beam and considering an integral depth dose (IDD¹⁷), the stress confinement can be calculated as:

$$\tau_s = \frac{BP_{FWHM}}{v_s} \quad (2.36)$$

For higher proton pulse widths, i.e., 473 ns and 1029 ns, as illustrated in Fig.(5c), the behaviour of the acquired IA signal changes. For instance, when the proton pulse width is 473 ns, the rarefaction peak begins to separate from the compression peak. The compression and rarefaction peaks are separate as the pulse width increases to 1029 ns. This separation occurs because the stress confinement condition is no longer satisfied for these pulse durations. In simple terms, the distinct separation of the compression and rarefaction peaks occurs because the waves do not sufficiently overlap in time, allowing the effects of the compression and rarefaction waves to become visible as they move through the medium. The study conducted by Assmann and co-workers also confirmed that the proton time profile should be chosen in such a way as to preserve the essential features of the IA signal. Furthermore, since the shape, amplitudes and frequency of the IA signals will depend on the proton time profile, it is also expected to influence the accuracy and precision of the ToF estimation. Therefore, the ToF accuracy and precision are expected to directly impact the BP position localisation.

¹³In this experimental study, two axial sensors with central frequencies of 3.5MHz and 10 MHz were used.

¹⁴Axial sensor aligned with respect to the proton exit beam. It is sometimes the optimal sensor position to record the acoustic pressure trace.

¹⁵Axial sensor not aligned with respect to the proton exit beam. Some features of the recorded acoustic pressure trace are expected to change, i.e., signal amplitude and shape.

¹⁶i.e., the spatial location of the proton beam.

¹⁷The IDD is the total dose on an infinite plane normal to the central axis of a beam, beamlet or an infinitesimal pencil beam [72].

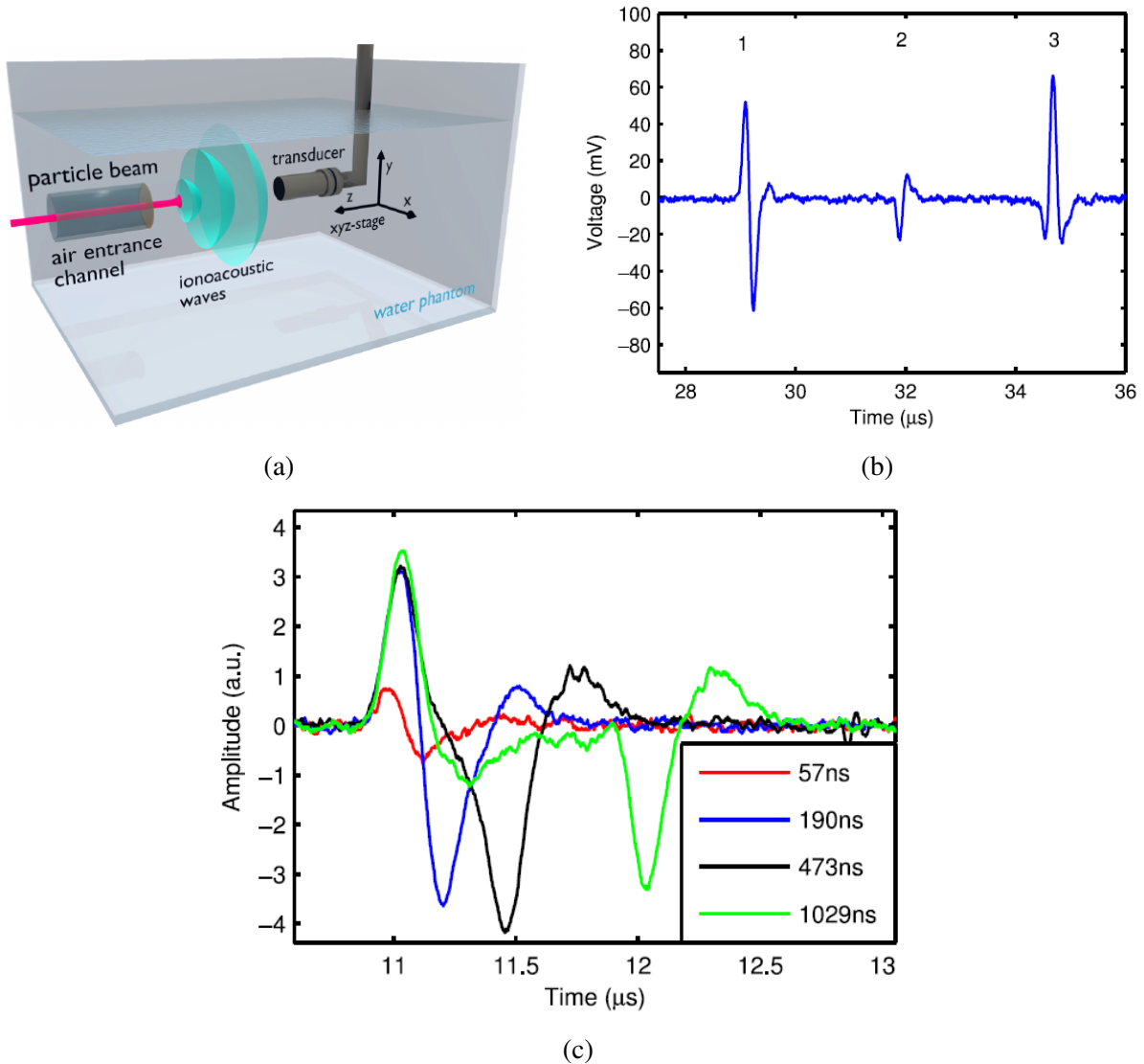


Figure 5: Ionoacoustic setup with only one axial single element piezoelectric (PZT) transducer. The single element transducer is in water distal to the expected BP. The experiments were conducted in water using a pulsed monoenergetic proton beam at an energy of 20 MeV. (a) Schematics of the water tank setup with a single-element sensor. (b) Illustrates the three main pulses (1-*direct signal*, 2-*entrance signal* and 3-*reflection signal*). (c) Recorded IA signal with different proton time profile widths (57 ns, 190 ns, 473 ns and 1029 ns).

So far, the IA signal shape has only been discussed in homogeneous media. Tissue heterogeneities, due to differences in acoustic impedances and speed of sound, are expected to affect the shape of the IA signal. The differences in tissue acoustic impedances result in multiple reflections along the beam path, which impact the ToF and pressure shape. Furthermore, variations in the medium cause changes in Grüneisen parameters and mass density, affecting the pressure magnitude associated with the absorbed dose. This poses a challenge for accurately estimating ToF. Additionally, peak-to-peak amplitude and signal frequency changes may occur, further complicating ToF estimation. Fig.(6) depicts a recorded IA signal in the presence of heterogeneities along the beam path, with water and silicone having different acoustic impedances. The changes in the signal shape can make it challenging to estimate ToF accurately and identify different tissues when the signal is composed of multiple

reflection peaks. The tissue properties will typically be determined from prior imaging data, such as X-ray CT scans, and tissue identification will help perform the BP localisation by considering the respective tissue speed of sound. Analysing IA signals for silicone and other simple materials is relatively straightforward¹⁸. Despite these challenges, this study aims to localise the BP position in water and account for heterogeneities through uncertainty models, as described in chapter 3.

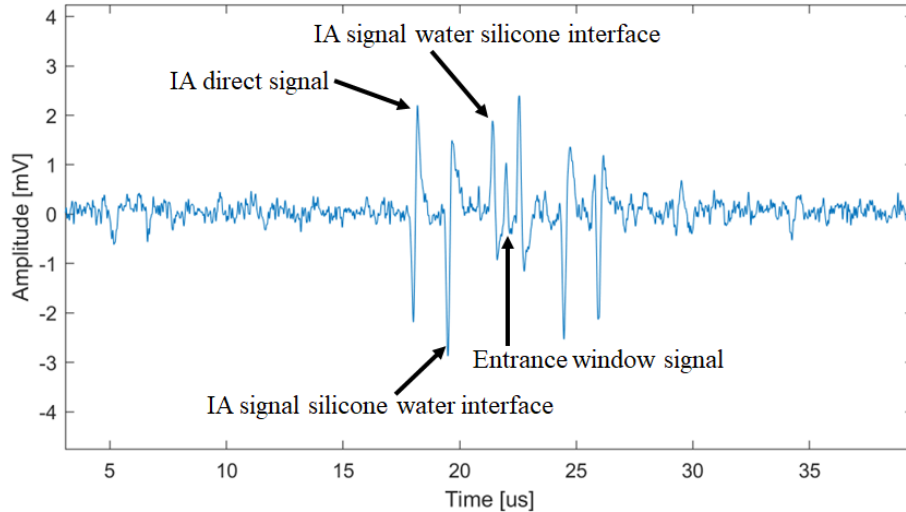


Figure 6: Ionoacoustic signal obtained in the presence of heterogeneities along the proton beam path. The experiment was performed using a phantom consisting of two silicon layers, with thicknesses of 1 mm and 2 mm, positioned near the entrance window of the water tank (shown in Fig.(5a)) such that the BP stopped between the two layers. The signal shape was significantly altered due to the multiple reflections along the beam path caused by the different tissue acoustic impedances. For more information on the experimental setup, see appendix A.

In the scope of this thesis, the BP position was localised primarily¹⁹ for pencil beams using pre-clinical beam energies of 20 and 22 MeV, as well as 50 MeV, which produce ionoacoustic signals in the range of hundreds of kHz to several MHz with magnitudes estimated to span from a few mPa to a few Pa²⁰[71, 73, 74]. However, clinical beam energies typically fall between 70 and 230 MeV, resulting in lower signal amplitudes of a few hundred mPa and a centre frequency between 10 and 100 kHz [75, 76]. The dependence of the IA signal on proton beam energy has important implications for detecting ionoacoustic signals in both pre-clinical and clinical settings. The decrease in IA signal amplitude with increasing beam energy is due to increased range straggling and scattering, which cause a broadening of the BP and an overall lower peak dose in the BP for the same number of particles per pulse. Detecting ionoacoustic signals can be challenging, requiring sensors with high sensitivity and broad frequency bandwidth. These challenges are even more pronounced due to the low signal amplitudes and lower frequency range associated with clinical beam energies. Currently, there is a lack of commercial solutions highlighting the need to develop new sensing technologies. Despite these challenges, the potential benefits of using ionoacoustic methods to monitor proton therapy delivery and verify the BP location make developing appropriate detection systems an active area of research.

¹⁸In this particular case, the acoustic impedances of silicone and water are relatively close to each other. Hence, we call it a case of simple heterogeneities. However, tissues with significantly different acoustic impedances, attenuation, and absorption, such as muscle and bone, are expected to produce a more complex signal pattern.

¹⁹For IA signals, the BP localisation was predominantly investigated in the time domain, while investigations were also conducted in the space domain for idealised sources.

²⁰Sebastian Lehrack, in [63, p. 97-99], demonstrated experimentally for a 20 MeV proton beam stopped in water (same setup as Fig.(5a)), an ionoacoustic signal could be detected with an absolute pressure of 12 Pa.

2.2 Multilateration State-of-The-Art

Multilateration is a mature technique in the following areas: wireless sensor networks, satellites using Global Positioning System (GPS), radar, wireless capsule endoscopy, and indoor localisation. The most notorious application outside of the telecommunications field is the application of multilateration for wireless capsule endoscopy [77, 78, 79, 80, 81, 82]. The algorithms used in capsule endoscopy are mainly angle of arrival (AOA), which determines angular directions (i.e., azimuth and elevation) of a propagated signal [83], and received signal strength (RSS), which measures the strength of a given propagated source signal at each sensor [84, 85]. The other two most used algorithms are the time of arrival (TOA) and the time difference of arrival (TDOA) [86]. The capsule endoscopy localisation relies on a signal emitted by a transmitter embedded in the capsule. After the ToFs estimations, the Euclidean distances between the source (i.e., capsule to be localised) and the sensors are estimated, accounting for the dielectric constant of the medium (ϵ_{med}) and the speed of light ($v_{light} \simeq 3 \cdot 10^{10}$ cm/s). The Euclidean distance can be written as: $d_i = ToF_i \cdot v_{light} / \sqrt{\epsilon_{med}}$. The dielectric constant is required to estimate the Euclidean distance because the capsule travels through different tissues. It is also shown in the literature that different tissues will have different dielectric constants [87, 88, 89], hence different tissue's speed of light. Therefore, tracking a capsule that travels from the colon to the end of the small intestine in real time is feasible. That is because the dielectric constant of blood, colon and small intestine are known [90, 91, 92, 93]. Hence, considering the tissue dielectric properties makes the Euclidean distance calculations between the sensor and source position more accurate. Furthermore, the tissues where the endoscopic capsule travels to are well known and adequately characterised, making capsule endoscopy localisation a relatively straightforward problem in non-homogeneous media. This precise understanding of tissue properties allows for more accurate predictions of the capsule path and position within the human body.

However, we also aim at non-homogenous media, starting from investigations in water. Differently from the previous example, instead of considering the speed of light as medium velocity, we will consider the speed of sound. The latter depends on medium compressibility, which is affected by temperature²¹ and medium density. Still, it is not solely reliant on them. Likewise, the Euclidean distance between the source (i.e., BP position) and the sensors in the network configuration will be in function²² of the ToF, sensor, and unknown source positions. Notably, the BP position can also be localised with AOA and RSS, which are not “completely²³” distance-based algorithms.

AOA is an angle-based source localisation approach, defined as the angle between an incident source propagation direction and a reference direction, also called orientation. Orientation is the angle (θ_i) between the emitted source at a position x_s, y_s and the received signals at sensors located at x_i, y_i , as shown in Fig.(7). The AOA in 2D can be formulated as follows:

$$\tilde{\theta}_i = \theta_i + \Upsilon_i; \quad i = 1, 2, \dots, n \quad (2.37)$$

The orientation can be computed as:

$$\tan(\theta_i) = \frac{y_s - y_i}{x_s - x_i} \implies \theta_i = \arctan\left(\frac{y_s - y_i}{x_s - x_i}\right) \quad (2.38)$$

²¹ $v_s \approx 1.402 \cdot 10^3 + 5.038 \times T - 5.799 \cdot 10^{-2} \cdot T^2 \dots$, the equation holds for the speed of sound estimated in water, where T is the temperature in °C, for a complete formalism here [94, 95].

²²Here we do not have a self-localisation problem [96], technically the only unknown variables are the source positions (x_s, y_s, z_s) to be estimated. We assume that the transducer spatial locations (x_i, y_i, z_i) and the ToF are known.

²³Both algorithms use distances but not as straightforward estimation compared to distance-based algorithms.

Where $\tilde{\theta}_i$ is the initial AOA estimated for each sensor. One way of estimating $\tilde{\theta}_i$ is to approximate it to a ratio²⁴ which accounts for the speed of sound in the medium, ToF and the distance between each sensor (l) [97]. In eq.(2.37), Υ_i accounts for the uncertainties on the angle between sensors and source estimation. An advantage of AOA is that they do not require precise time synchronisation between the emitted source and sensors. At least two sensors are required to localise the source in two-dimensional space. The main drawback of this algorithm is that it is highly θ_i dependent. Small errors in θ_i imply substantial errors in the source position localisation [98]. Hence, an accurate estimation of the angles between the source and sensors is required to retrieve the source position accurately. Another drawback is that it can be a computationally expensive algorithm for a sensor network with many sensors. The aim is to solve eq.(2.37) to retrieve x_s and y_s ; the problem could be easily expanded in 3D by considering the third coordinate for the source and sensors. For more details on the AOA, the reader is invited to see [99, 100, 101, 102, 97, 98].

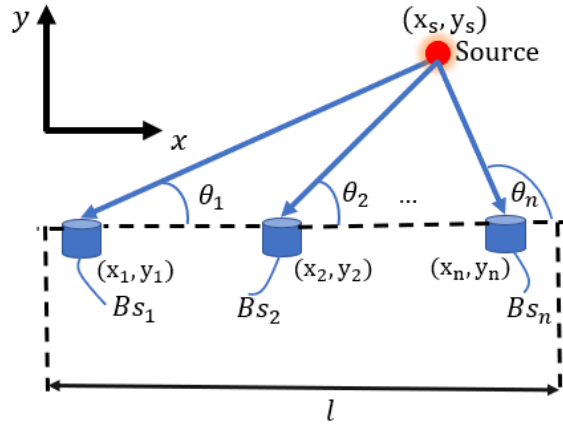


Figure 7: Angle of arrival schematic setup in 2D with n sensors. $\theta_1, \theta_2 \dots \theta_n$ are the orientation angles between the source and the sensors. The sensors BS_1, BS_2, \dots, BS_n are located at positions (x_i, y_i) for $i = 1, \dots, n$. The source is located at a position x_s, y_s .

Another localisation method is the RSS, which is the average power received at a sensor originating from the emitted source, where the average power is the signal strength at each sensor. It is one of the most used localisation methods in wireless sensor networking due to its cost-effective hardware implementation [103]. The RSS received power $P_{r,i}$ at a sensor i -th, can be modelled as:

$$P_{r,i} = K_i \frac{P_t}{d_i^\alpha}; \quad i = 1, 2, \dots, n \quad (2.39)$$

The averaged power received at i -th sensor, where it is measured in decibel meters (dBm), P_t is the emitted source power, α is a power factor which depends on the propagation media, and it can vary from 2 to 5, whereby for an $\alpha = 2$ the source is considered to be in free space, K_i is a parameter accounting for some factors like sensor geometry, which may affect the received signal strength. Normally, P_t and K_i are known a priori. However, So et al., proposed a relaxation procedure to estimate α when it is unknown [104]. In eq.(2.39), d_i is the Euclidean distance between the sensors and the source. To find a given source position using the RSS approach, the mentioned equation is

²⁴ $\tilde{\theta}_i \approx \arcsin\left(\frac{ToF_i \cdot v_s}{l}\right)$. Here, l denotes the distance/pitch between BS_1 and BS_n ; the distance can also be calculated for each pair of sensors in the network.

solved using the log-normal path loss model [105, 104]. In other words, eq.(2.39) can be expanded to:

$$-\alpha \cdot \ln(d_i) = \ln(P_{r,i}) - \ln(K_i) - \ln(P_t) \quad (2.40)$$

The received signal strength (r_{ss_i}) measured in (dBm), at any sensor, can be approximated to the product between power factor (α) and $\ln(d_i)$. Hence, the source position can be localised by solving the following equation:

$$r_{ss_i} = -\alpha \cdot \ln(d_i) + \Upsilon_i \quad (2.41)$$

For ideal scenarios, i.e., without any uncertainties $\Upsilon_i = 0$, eq.(2.41) is solved in function of the source position, which is encoded in the Euclidean distance (d_i). For the RSS, the strength of the received signal is the approximation of the distance travelled by the signal to each sensor in the network configuration. The accuracy of this localisation method will depend on factors like K_i , α and P_t . At least three sensors are required for the RSS to localise a given source position, and exact time synchronization between the emitted source and the sensors is not required.

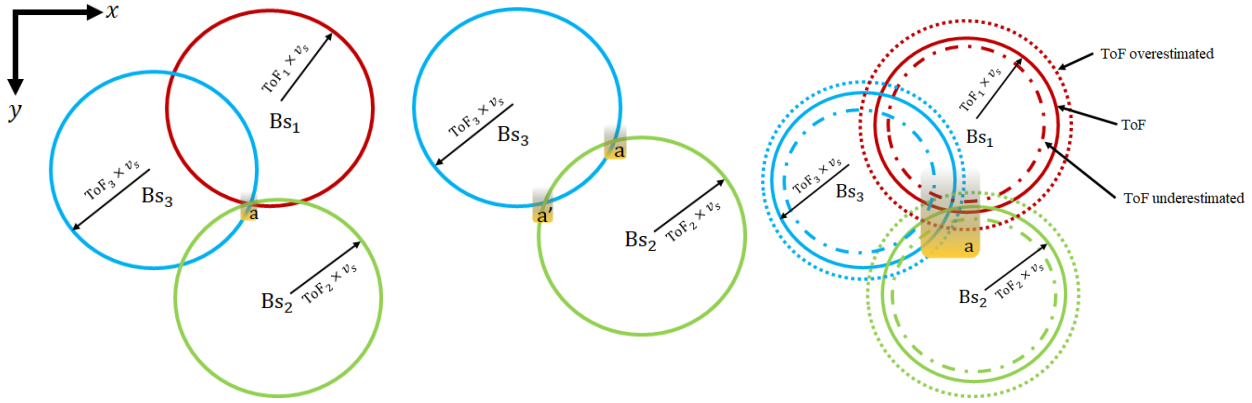
Algorithms such as AOA or RSS could also be used to localise the BP position. They have some strengths and drawbacks, as mentioned previously. For instance, AOA is highly orientation dependent, and RSS approximates the estimated received signal power in dependence on the distance and accounts for several parameters (α, K_i) to be modelled. Conversely, TOA and TDOA algorithms are uniquely distance-based and usually more accurate than AOA and RSS [106, 107, 108, 109]. For this reason, the multilateration approach used in this thesis to retrieve the BP position will be exclusively based on TOA and TDOA.

TOA is an absolute method for estimating a given position based on the difference between the wave arrival time at a given sensor and the time of emission. It requires accurate and precise time synchronisation between source emission and all receivers. Fig.(8a) illustrates the geometrical interpretation of the TOA. Each TOA can be interpreted in 2D space as a circle where the centre of each circle corresponds to the sensor position, and the radius of each circle corresponds to the distance travelled by the acoustic source to the sensor [110]. The intersection of the circles will correspond to the position where the source must lie. In the absence of uncertainties and considering that the source to be localised is contained in a 2D plane, a minimum of three sensors is required to obtain a unique solution. The location of the source is illustrated by the intersection of the three solid circles as shown Fig.(8a). On the other hand, Fig.(8b) illustrates when ambiguity could be an issue for TOA. If only two sensors are considered, the source can be located in two different spatial locations, in the mentioned figure denoted as a and a' . This ambiguity is easily solvable in many ways. One of the approaches is to increase the number of sensors, i.e., to three or more.

Fig.(8c) illustrates the multilateration outcomes in case of uncertainties on the ToF estimation (i.e., overestimation or underestimation of its value represented by the dashed lines). In that case, the circles will not intersect at a single point but will define an area where the source is likely to be. Therefore, the accuracy of the source location will decrease. Similarly, in 3D space, each TOA can be interpreted as a sphere, and the intersection of all the spheres will be the position where the source should lie. It is worth mentioning that the main advantage of TOA compared to other localisation algorithms, i.e., AOA and RSS is its high accuracy due to a straightforward implementation and fewer parameters²⁵ to include in its mathematical formulation. However, the drawback is that accurate time synchronisation between the source and all sensors is always required. In other words, if the time

²⁵In TOA, the unknowns are the source position and ToF, as speed of sound and sensor locations are known.

instant when the proton beam enters the irradiated object is not accurately estimated or not known, the BP position localisation accuracy and reproducibility will be compromised. As importantly, TOA can be a computationally expensive localisation algorithm when dealing with complex systems, i.e., localisation performed with multiple sensor configurations with a particular geometry [81, 111].



(a) TOA without uncertainties. (b) TOA, solution ambiguity. (c) TOA, in the presence of uncertainties.

Figure 8: 2D geometrical interpretation of the TOA algorithm in the absence (solid circles) and in the presence (dotted/dashed circles) of uncertainties on the ToF estimation. (a) The solid circles represent the case where the multilateration is performed in ideal conditions, i.e., no errors on the ToF estimation. Without uncertainties, the source is located at a single point given by the intersection of the three circles. (b) TOA without uncertainties but with ambiguity on the source spatial location, the two squared a and a' indicate the two possible source spatial locations. (c) The dotted/dot-dashed circles indicate the cases when the ToF is underestimated or overestimated. In the presence of uncertainties, the source is no longer located in a single point and can be located in an area defined as a .

TDOA is the difference between the wave arrival time at each sensor and that of a reference sensor. This method is also known as hyperbolic localisation because it uses time differences (refer to eq.(2.44)), to form hyperbolas²⁶ that represent possible locations of the source. By intersecting these hyperbolas from multiple sensor pairs, the location of the BP source can be determined. It is a relative localisation method which always requires a reference sensor. Nonetheless, the TDOA algorithm does not need accurate time synchronisation between the emitted source and the sensors. For the TDOA algorithm, at least three sensors are required to localise the source in 2D, and a minimum of four sensors are required to localise the source in 3D.

Fig.(9a) illustrates the geometrical interpretation of TDOA in 2D without uncertainties. The intersection of the two hyperbolas²⁷ gives the source position. However, depending on the sensor configuration, a unique TDOA solution is not always guaranteed, as illustrated in Fig.(9b). Three sensors make it possible to obtain three hyperbolas²⁸ intersecting in two different positions (i.e., a and a'). In this case, there is an ambiguity regarding the TDOA solution. This ambiguity can be easily solved by increasing the number of sensors to four. Usually, it is more than enough to localise the source in 2D, with only three sensors. However, it is essential to keep in mind that ambiguity might occur in the TDOA solution. For simplicity, in the presence of uncertainties, only the TDOA with two hyperbolas will be discussed, as shown in Fig.(9c). If the ToF is overestimated or underestimated, the hyperbolas

²⁶We can derive the general hyperbola equation using the Euclidean distances from the sensors in eq.(2.44).

²⁷The source and sensors are placed at $(x_s, y_s) \neq (0, 0)$ mm, and $Bs_1(x_1, z_1) = (0, 0)$ mm, and $Bs_i(x_i, z_i)_{i=2,3} \neq (0, 0)$ mm.

²⁸The source and sensors are placed at $(x_s, y_s) \neq (0, 0)$ mm, and $Bs_i(x_i, z_i)_{i=1,2,3} \neq (0, 0)$ mm.

will no longer intersect in a single point. Therefore, the source position to be retrieved will be located in an area (a) as illustrated in Fig.(9c).

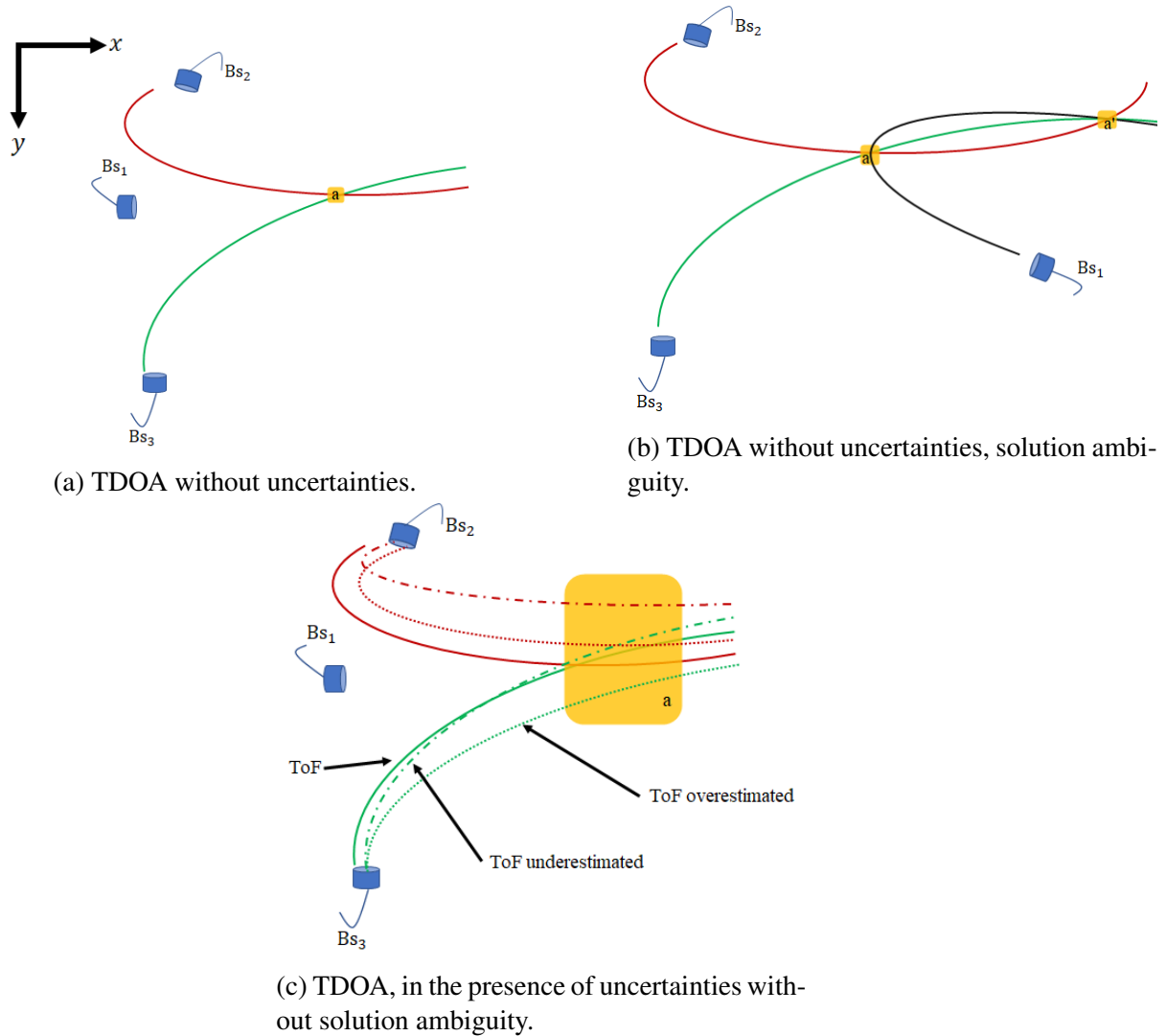


Figure 9: Geometrical interpretation of the TDOA in 2D in the absence and presence of uncertainties. (a) TDOA with three sensors without uncertainties. The intersection of the two hyperbolas gives the source position. (b) TDOA with three sensors without modelling uncertainties. The sensor configuration has changed compared to the previous figure. There is an ambiguity in the solution of the source position. The hyperbolas intersect at two different spatial locations (a and a'). (c) TDOA in the presence of uncertainties, the source is not located in a single position but in an area (a).

Both the TOA and TDOA algorithms utilise a set of nonlinear equations, detailed in section 2.2.1, that express the relationship between the sensor positions and the unknown source positions. Two approaches are used primarily to solve the nonlinear equations: the linear least squares (LLS) and weighted linear least squares (WLLS) approach [112, 113, 114]. LLS transforms the set of nonlinear equations into linear ones by introducing extra variables and using the least squares approach. However, the main drawback of this method is that the solution is suboptimal. LLS is suboptimal due to the support variables used to linearise the TOA and TDOA nonlinear equations. The support variables might have different powers or different weights, which might affect the localisation accuracy. For this reason, the weighted linear least squares approach is usually preferred. In conclusion, the LLS

and WLLS approaches linearise the nonlinear equations by not accounting for the uncertainties in the TOA and TDOA mathematical models. The linearized equations are expressed in terms of cost functions using the matrix approach. LLS will have an unimodal distribution, guaranteeing a global solution for retrieving the desired source position. The LLS method also includes the subspace approach, which decomposes the linearised equations into a multidimensional similarity matrix using multidimensional scaling (MDS) [115, 116, 117, 118].

Another common approach to locating the source position is based on nonlinear methods such as nonlinear least squares (NLS) [119, 120, 121] and maximum likelihood (ML) [122, 123]. The idea behind NLS or ML is that after expressing the TOA and TDOA equations in terms of cost functions, both NLS and ML methods attempt to minimise the cost functions by using some well-known numerical optimisation methods, i.e., Gauss-Newton, Newton-Raphson, Nonlinear Simplex, steepest descent and Levenberg–Marquardt [124, 125, 126, 127, 128]. Compared to LLS and WLLS, NLS and ML do not require the linearisation step of the cost function. Their accuracy is usually higher because they are not suboptimal²⁹ optimisation algorithms [111, 129]. For NLS or ML, a global solution is not always guaranteed, and it depends on the numerical optimisation method, among other factors, which are not the aim of this work. For more insights on global optimisation, refer to [130, 131]. The choice of NLS compared to LLS or WLS approaches is motivated by the high accuracy and the more straightforward implementation. There is no need to linearise the cost functions or use support variables compared to LLS or WLLS. However, NLS algorithms sometimes require the analytical gradients of the cost functions to increase the optimisation accuracy. The analytical gradients are calculated from the TOA and TDOA cost functions and then fed into the solver of any programming language. One drawback of NLS is that they are computationally demanding since several iterations are required to reach convergence. Another disadvantage is that a global solution, i.e., global maximum or minimum, is not always guaranteed.

2.2.1 Multilateration Optimisation TOA and TDOA

There are several multilateration methods, as already discussed in section 2.2. However, this section will only discuss the TOA and the TDOA methods in greater detail. As already defined, TOA relies on estimating the one-way propagation time of the signal travelling between a source and a receiver. To estimate a given source position, evaluating the time-of-flight and knowing when the source is emitted (t_0) is crucial. Thus, time synchronisation between source emission and all receivers is needed. The ToF is converted to distance, requiring knowledge of the speed of sound in the medium. Therefore, accurate knowledge of the speed of sound in the medium and all the sensor positions in the network is crucial for the localisation algorithm. Mathematically, the distance between the source and all sensors in the network can be computed as follows:

$$d_i = v_s \cdot (ToF_i + \Upsilon_i) = \sqrt{(x_i - x_s)^2 + (y_i - y_s)^2 + (z_i - z_s)^2}; \quad i = 1, 2, \dots, n \quad (2.42)$$

Where in eq.(2.42), d_i is the Euclidean distance between the source and the sensors, (x_i, y_i, z_i) are the sensor positions, (x_s, y_s, z_s) are the unknown source positions and Υ_i are the uncertainties on the ToF estimation. The ToF encodes a time instant t_0 , which is the starting time of any measurement. When the proton beam pulse enters the water tank, it may experience delays, such as those caused by the length of cables used in the chopping system of the particle accelerator, as observed in some cases in

²⁹There is no need to use support variables to retrieve the source position compared to the LLS and WLLS approaches.

this study. Eq.(2.42) can be expressed as a cost function and be solved using the NLS approach as described in eq.(2.43). The described cost function includes the uncertainty in the ToF estimation and synchronization error (Υ_i).

$$\min_{x_s, y_s, z_s} f_{TOA}(x_s, y_s, z_s) = \min_{x_s, y_s, z_s} \sum_{i=1}^n \left(v_s \cdot (ToF_i + \Upsilon_i) - \sqrt{(x_i - x_s)^2 + (y_i - y_s)^2 + (z_i - z_s)^2} \right)^2 \quad (2.43)$$

The second multilateration method is TDOA, which is the time difference between the arrival time estimated from each sensor and a reference sensor. The TDOA between all the sensors (Bs_i) and a given reference sensor (Bs_{ref}), can be mathematically expressed as follows:

$$d_i - d_{ref} = v_s \cdot (ToF_i + \Upsilon_i) - v_s \cdot (ToF_{ref} + \Upsilon_{ref}); \quad i = 1, 2, 3 \dots n; \quad ref \neq i \quad (2.44)$$

Eq.(2.44) can be rewritten as follows:

$$d_i - d_{ref} = v_s \cdot (ToF_i - ToF_{ref} + \Upsilon_i - \Upsilon_{ref}); \quad (2.45)$$

ToF_i and ToF_{ref} contain information about the time instant (t_0) when the proton beam pulse enters the water. While the sensors still need to be synchronized (i.e., time must evolve synchronously), the exact start signal (t_0) becomes irrelevant. From equation eq.(2.45), t_0 cancels out due to the time-of-flight difference ($ToF_i - ToF_{ref}$), eliminating the need for precise synchronization when using TDOA.

Any sensor in the network can be chosen as a reference sensor if the difference in eq.(2.45) is not zero. Using an auxiliary variable w to simplify the mathematical expression, the TDOA can be written in terms of a cost function as shown in eq.(2.46).

$$\min_{x_s, y_s, z_s} f_{TDOA}(x_s, y_s, z_s) = \min_{x_s, y_s, z_s} \sum_{i=1}^n \sum_{ref \neq i} \left(v_s \cdot w - \sqrt{(x - x_s)^2 + (y - y_s)^2 + (z - z_s)^2} + \|d_{ref}\|_2 \right)^2 \quad (2.46)$$

With :

$$w = (ToF_i + \Upsilon_i) - (ToF_{ref} + \Upsilon_{ref}); \quad (2.47)$$

$$\|d_{ref}\|_2 = \sqrt{(x_{ref} - x_s)^2 + (y_{ref} - y_s)^2 + (z_{ref} - z_s)^2} \quad (2.48)$$

During the work conducted in this thesis, the multilateration was performed using the NLS approach. In concrete, the TOA and TDOA were solved using the Levenberg and Nonlinear Simplex. This will

sometimes be referred to as Simplex and not be mistaken for the linear Simplex algorithm, commonly used in linear programming [132]. Therefore, the two mentioned algorithms to solve the cost functions described in eq.(2.43) and eq.(2.46) will be described in the section 2.2.2 and 2.2.3.

2.2.2 Levenberg–Marquardt Algorithm

The Levenberg algorithm is derived from the *least-squares* curve fitting problem, which involves minimising the sum of the squares. Mathematically, it is defined as:

$$\min_{\hat{x}_s, \hat{y}_s, \hat{z}_s} \|d_{i,j} - f_j(x)\|_2^2 \quad (2.49)$$

In eq.(2.49), $d_{i,j}$ is the distance component from the BP position and the sensor position, and $f_j(x)$ is the function encoding the TOA and TDOA information.

Another key equation is described by the *Gauss-Newton* algorithm, which is defined as:

$$(\hat{x}_s, \hat{y}_s, \hat{z}_s) = \left(J_{f,j}^T J_{f,j} \right)^{-1} J_{f,j}^T (d_{i,j} - f_j(x)) \quad (2.50)$$

From eq.(2.50), it is possible to derive the Levenberg algorithm with minor changes, as shown in eq.(2.51). The objective of this work is not in numerical optimisation. For more detail, the reader is invited to see [127, 133, 134]. However, it is worth noting that the Levenberg algorithm employs a trust-region strategy. The trust region method offers better convergence than the line search method, especially in cases where the Jacobian is rank-deficient or nearly rank-deficient [131, p. 258].

The initialisation of the Levenberg comes from an initial guess set by the user (i.e., setting $\hat{x}_s, \hat{y}_s, \hat{z}_s$ to a value), which will later allow us to discuss the choice and impact of the initial guess on the multilateration of the BP position outcome.

$$(\hat{x}_s, \hat{y}_s, \hat{z}_s) = \left(J_{f,j}^T J_{f,j} + \lambda^D \text{diag}(J_{f,j}^T J_{f,j}) \right)^{-1} J_{f,j}^T (d_{i,j} - f_j(x)); \quad \begin{cases} J_{f,j} = \left(\nabla f_j^T(x_s, y_s, z_s) \right); \\ d_{i,j} = v_s \cdot \text{ToF}_i \\ j = (\text{TOA}, \text{TDOA}) \end{cases} \quad (2.51)$$

In eq.(2.51), $J_{f,j}^T$ is the Jacobian matrix of $f(x)_j$, and λ^D is the damping factor of the Levenberg algorithm. The choice of the damping factor can increase or decrease the convergence of the method.

2.2.3 Nelder-Mead Simplex Algorithm

The *Nelder-Mead* algorithm, also called nonlinear Simplex, is a gradient-free algorithm that relies on simplices (i.e., polytopes of dimension $n + 1$). The algorithm is commonly used for NLS problems, especially acoustic source localisation problems, for nondestructive testing [110]. The Simplex Algorithm is based on six steps: order, centroid, reflection, expansion, contraction, and shrink, as

illustrated in Fig.(10) to Fig.(13). The algorithm objective in a single iteration is to pull out the vertex with the worst function value and restore it with another point with a better value. The algorithm will iterate on a simplex, with dimension $n + 1$; in 2D, it is a triangle, and in 3D, it is a tetrahedron. For simplicity, only the 2D case will be considered. The Simplex algorithm starts by considering the vertices of a triangle, as illustrated in Fig.(10). Each vertex of the triangle corresponds to a specific point and number. The points are named; first, $x_h \rightarrow$ worst, second $x_s \rightarrow$ next to worst, last $x_l \rightarrow$ best, as illustrated in Fig.(10). All the steps performed by the algorithm are listed below.

1. Sort the values of the cost function $f(x)$, according to the values at the vertices³⁰:

$$f(x)^{(1)} < f(x)^{(2)} < f(x)^{(3)} \leq \dots \leq f(x)^{(n+1)} \quad (2.52)$$

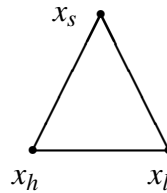


Figure 10: Simplex algorithm starting point.

2. Compute the centroid of all points except x_h :

$$O = \frac{1}{n} \sum_{i \neq h} x_i \quad (2.53)$$

3. Reflection :

$$x_r = O + a_R(O - x_h); \quad a_R > 0; \quad \text{where } a_R \text{ is the reflection factor} \quad (2.54)$$

(a) If $f(x_s) < f(x_r) \leq f(x_l) \rightarrow x_r$ is better than x_s

(b) x_s is replaced by x_r , and the next iteration is computed

³⁰The function $f(x)$ representing the cost function for TOA or TDOA algorithms can be thought as $f(x) = f_j(x)$ were $j = (TOA, TDOA)$. However, even if the Simplex Algorithm is being applied to both TOA and TDOA, we will keep the notation of the cost function as $f(x)$, only for simplicity.

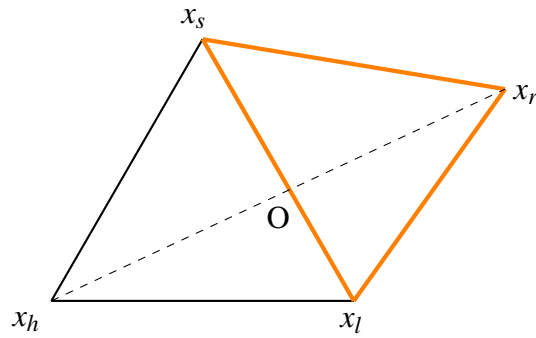


Figure 11: Simplex algorithm, reflection including computation of the centroid (O).

4. Expansion :

- (a) If $f(x_r) > f(x_l) \rightarrow x_e = O + g(x_r - O)$; $g > 1$; where g is the expansion parameter
- (b) If $f(x_e) < f(x_r) \rightarrow x_h$ is replaced by x_e
- (c) x_s is computed by x_r , and the next iteration is computed

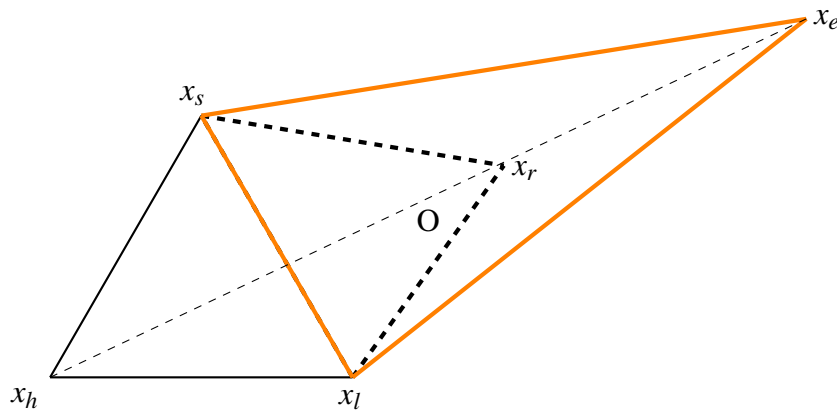


Figure 12: Simplex algorithm expansion step.

5. Contraction:

$$x_c = O + k(x_h - O); \quad a_R > 0 \text{ where } k \text{ is the contraction factor} \quad (2.55)$$

- (a) If $f(x_c) > f(x_h) \rightarrow x_h$ is replaced by x_c
- (b) If the condition above is not verified, the contraction is shrunk

6. Shrink:

The Shrink phase is defined by the j -th new point in the triangle. These points are defined as:

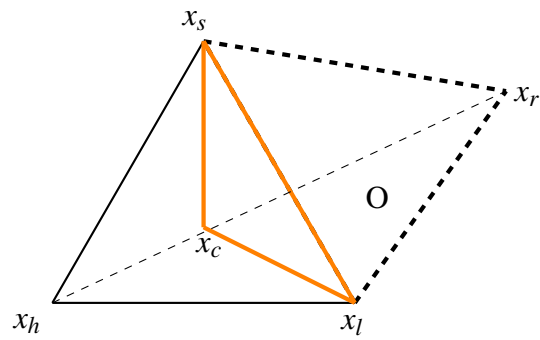


Figure 13: Simplex algorithm, contraction step.

$$x_j = x_l + \sigma(x_j - x_l); \text{ where } \sigma \text{ is the shrinking factor} \quad (2.56)$$

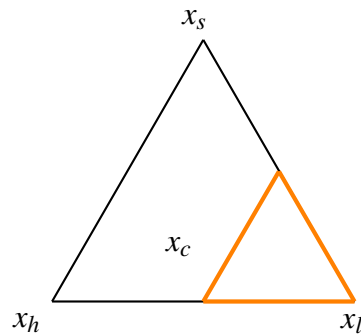


Figure 14: Simplex algorithm shrink step.

2.3 State of the Art on Ionoacoustic Reconstruction Methods

This section discusses the two primary algorithmic approaches utilised to reconstruct the BP position using acoustic signals in this thesis. Both algorithms aim to reconstruct the BP position by leveraging the unique properties of ionoacoustic signals. The first approach utilises multilateration to output the spatial coordinates of the reconstructed source, which spatially localises the strongest position of the acoustic emission (source). The second algorithm relies on pressure reconstruction, which relies for instance on using time reversal and iterative time reversal techniques to reconstruct the BP position. The key difference between the first and second approaches is that the first pinpoints the position of the source, while the latter reconstructs the 3D pressure distribution correlated to the dose. By comparing the two techniques, we can determine which algorithm yields the most reliable and accurate results for BP localisation.

2.3.1 Source Localisation Based on Multilateration

Recently, acoustic BP localisation using the TOA algorithm with LLS has been suggested as a method for range verification [135, 136]. The localisation of the BP position was estimated using triangulation. The triangulation technique uses angles afterwards converted into distance to retrieve the unknown source position [137, 110]. In the simulation studies conducted by Patch et al., the BP position was localised for prostate cancer using four sensors. The ToF was estimated using the Fourier shift theorem algorithm [138]. Meanwhile, in the simulation studies conducted by Jones et al., the BP was localised with twelve sensors for liver cancer and nine sensors for prostate cancer. For both cases, the ToF was estimated from the maximum signal amplitude [70]. These preliminary investigations showed the first evidence of acoustic source localisation feasibility for *in vivo* range verification. Acoustic BP localisation in a homogeneous medium based on NLS optimisation and the TDOA algorithm has been proposed recently [139]. In the studies conducted by Otero et al., the optimisation was performed using the Newtown-Rapson method, which is one of the most used algorithms in acoustic source localisation. The study involved both simulations and experiments to emulate the BP position. In the simulations, a 100 MeV proton beam with a 50 μs Gaussian proton time profile was used. For the experimental study, a hydrophone served as a source to replicate the BP. In the mentioned study, the source was localised with multiple sensors. The acoustic source was placed in the centre of the phantom for all the sensor configurations. The phantom volume was changed to assess the time performance for the multilateration [139]. The conclusion reached by Otero and co-workers was that the accuracy of the source localisation improves by increasing the number of sensors (i.e., localisation with 12 sensors) and for source localisation with only four sensors it is preferable to have the source inside the volume covered by the sensors. Another introductory remark by Otero and co-workers is that multilateration can be used for real-time *in vivo* range verification. Their study demonstrated that the multilateration computational time does not increase considerably by increasing the volume of interest. With a volume of interest of 0.35 m³, the time required to localise the source position with four sensors was around 450 μs . In the same study, there was room for improvement for the computational resources³¹ used to retrieve the BP position. A complementary *in-silico* study from the same authors [140] showed that BP could be located in the brain with an accuracy of 1 mm using a 100 MeV proton beam with a 10 μs Gaussian proton time profile. For all investigations conducted by Otero and co-workers, the ToF was estimated based on the generalised cross-correlation [141]. Still, the effect of the ToF estimation method on the localisation accuracy was not discussed.

³¹The calculations were not performed using the most recent computer processors. With modern processors, it is expected to decrease the 450 μs further.

Most studies on the BP position localisation using multilateration presented in the literature were based on simulation studies. The only exceptions were those performed by Otero and co-workers [139]. Nonetheless, the experimental studies conducted by the mentioned author did not use a proton beam. Furthermore, the source used to emulate the BP positions had a frequency bandwidth of 50 kHz to 800 kHz. However, for an ion beam, the expected ionoacoustic frequency bandwidth goes from hundreds of kHz to a few MHz depending on beam energy and time pulsing structure [75, 76, 73].

2.4 Pressure Reconstruction

In recent years, there has been significant work on BP range verification using image reconstruction [142, 143, 74, 144, 145]. One of the most interesting algorithms is the so-called time reversal reconstruction (TRR³²). In chapter 5, we will briefly discuss about the implementation of multilateration and TRR into pre/clinical applications. The conceptual idea behind TRR is quite simple; it is based on the re-transmission of the measured acoustic pressure waves into the medium (i.e., homogeneous or heterogeneous) in inverted temporal order ($t \rightarrow t^-$). The time reversal reconstruction workflow is illustrated in Fig.(51)³³, the initial reconstruction step consists on the recorded $p(\mathbf{r}, t)$ by a set of sensors ($\mathbf{B}s_i$), it is then inverted in temporal order $p(\mathbf{r}, t \rightarrow t^-)$, and then re-propagated into the medium from the sensor locations. This additional step is normally called *backward propagation*. After the re-propagation of the inverted pressure, the initial pressure is finally reconstructed (the reconstructed pressure here is denoted as $p_0^R(\mathbf{r}, t)$). An interesting feature of the TRR is the ability to visualise the initial pressure distribution and at the same time the spatial location of the BP (i.e., intended as the coordinates in space x, y, z).

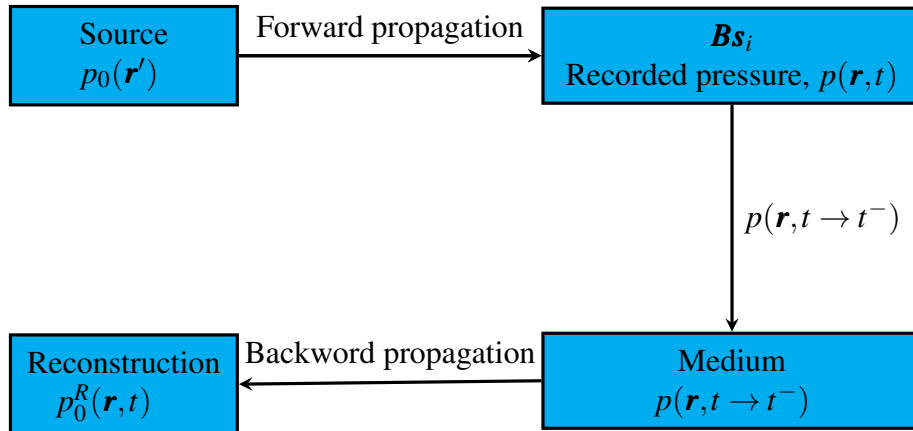


Figure 15: Time reversal reconstruction workflow.

The literature demonstrates that TRR is sensitive to the number of sensors and their respective geometry [142, 148, 149]. In other words, the accuracy of the reconstruction will depend on the sensor placement (i.e., covering the irradiated volume) and the capability of the sensors to capture the ionoacoustic wavefront³⁴. It is also important to note that in the context of ionoacoustic, TRR provides

³²French physicist Mathias Fink conducted one of the most notorious works in the field of time reversal in acoustics. Most of his initial work focused on time-reversal mirrors [146], and time-reversed acoustics [147].

³³The *forward propagation* step does not belong to the TRR reconstruction algorithm, is only the acoustic simulation step generating the initial source $p_0(\mathbf{r}')$ which is propagated in the medium and then recorded by a set of ultrasound sensors.

³⁴Pratik Kumar Dash conducted extensive studies on various sensor geometries and their impact on final BP position reconstruction using TRR. For more details, refer to [148]. Additionally, all the work on TRR presented in this thesis is part of Pratik Dash's PhD research within the context of the SIRMIO project.

the pressure associated with the energy deposition density. To determine the dose, the Grüneisen parameter must also be known, as it links pressure to energy deposition. When the sensors cannot fully grasp the ionoacoustic wavefront, the TRR would be compromised, which implies an inaccurate reconstruction of the initial pressure and, consequently, the BP position. Therefore, the accuracy of the reconstructed BP position will be lower. To improve the accuracy and mitigate the discrepancies between the initial pressure and the reconstructed one, iterative time reversal reconstruction (ITRR³⁵) it is usually considered. The ITRR steps are illustrated in Fig.(16); the ITRR adds an iterative process to the reconstruction step. Each iteration will perform the difference between the initial and reconstructed pressure, followed by an update of the pressure.

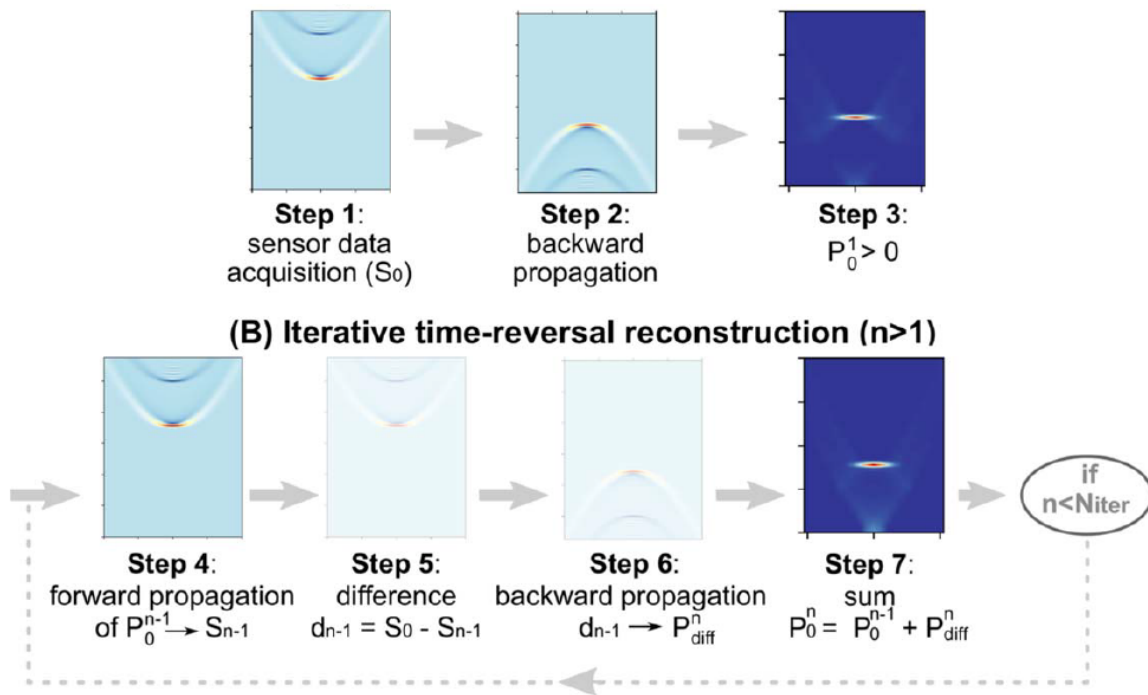


Figure 16: Time reversal and iterative time reversal reconstruction, figure extracted from [74]. The reconstruction workflow is performed in two stages. First, the TRR is performed, and then the ITRR is performed for a certain number of iterations. For more details, refer to the mentioned publication.

In the following sections, more will be discussed on BP localisation using multilateration, from simulation to experimental studies. It is essential to mention that both algorithms share a common source of uncertainties. Such as sensor position with respect to BP position, proton accelerator synchronisation time (i.e., the exact time that the protons start irradiating a given tissue) and speed of sound, to cite a few sources of uncertainties. Therefore, for multilateration studies, we will model and discuss the source of uncertainties and their impact on BP localisation.

³⁵Discussed intensively in the work of the French physicist Mathias Fink, “Time-reversal mirrors”, [146].

3 Material and Methods

Your purpose... should always be
to know...the whole that was
intended to be known.

Maimonides

3.1 Simulation Studies

This section presents the simulation setup used in this thesis, except for the simulations conducted for the SIRMIO beamline, which will be discussed in section 3.3. The aim is to localise the BP position using a dedicated beamline for small animals. To start with, the optimal reference sensor selection for multilateration using the TDOA algorithm will be introduced. Then, the multilateration will be performed in two sets of simulations. In the first simulation, the aim will be to assess the dependency of the initial guess condition on the Levenberg and Simplex algorithms based on the outcome of the multilateration results. This simulation will use an ideal point source to emulate the spatial locations of the BP positions. In another localisation setup, the accuracy and precision of the multilateration, where the BP will be localised only considering the ideal point sources, will be evaluated. Afterwards, the localisation will be performed by modelling random and systematic errors on the ToF estimation. The studies that consider ideal point sources will be conducted in 2D and 3D. After an extensive study considering ideal point sources, a realistic scenario will be considered where the BP position will be localised using simulated ionoacoustic signals with pre-clinical beam energies of 20 and 22 MeV. The knowledge gained during the localisation of the BP position, considering ideal point sources, will be used to properly understand and contextualise some of the results of the BP localisation, considering realistic ionoacoustic signals.

3.1.1 TDOA Optimal Reference Sensor

With performing the multilateration with the TDOA, a selection of a reference sensor is required. The reference sensor selection might influence the outcome of the multilateration. Eq.(2.45) describes the mathematical formulation of the TDOA assuming any reference sensor. Therefore, as mentioned earlier, the equation does not consider any specifications about the reference sensor. Hence, two reference sensor sets were considered for the study based on ideal scenarios (point sources at different spatial locations) using TDOA. The study aimed to determine the optimal reference sensor selection. The first set was labelled as static, and the second one was referred to as a dynamic reference sensor. The static reference sensor is used independently of the source location; i.e., estimating the ToF to select a reference sensor is unnecessary. Instead, the reference sensor is selected based on prior knowledge of the number of sensors, sensor arrangement and expected source position. The static selection of the reference sensor may require precise and accurate knowledge of the overall localisation setup. In the dynamic sensor scenario, the reference sensor was modified in accordance with the ToF data captured by each sensor in the network. Three dynamic partitioning strategies were utilised to define the reference sensor set: the minimum ToF, the maximum ToF, and the average ToF. In the latter instance, the reference sensor was chosen to match the sensor whose ToF measurement was the closest (with the minimum difference) to the average ToF measurement across all sensors. For a compact and concise notation, all the reference sensors based on the minimum, maximum and average ToF estimation will be labelled as $l^{Ref,min}$, $l^{Ref,max}$ and $l^{Ref,mean}$.

3.1.2 Optimisation Failure and Acceptance Rate

As discussed at the beginning of this thesis, it is known that different NLS optimisation methods are sensitive to the initialisation value because they are mainly based on search algorithms. The initial guess is a mathematical condition that sets the algorithm's starting condition, and several iterations are performed till the solution is reached. Different approaches are used to define an optimal initial guess condition; it is a common practice to use the solution of LLS methods as an initial guess condition for the NLS algorithms. We conducted a study on the algorithm's performance between the Simplex and

Levenberg algorithms in the presence of different initial guess positions. The aim was to assess and compare the influence of the initial guess on the multilateration results (convergence and accuracy) of the Simplex and Levenberg algorithms. For that, a 2D setup with an area of $30 \times 50.5 \text{ mm}^2$, with three ideal point sensors, was considered, as shown in Fig.(17a). The setup dimension illustrated in Fig.(17a) was chosen to have a comparable size with the setup used for the experimental studies, as shown in Fig.(19a) and discussed in the section 3.2.1. In this particular setup, the initial guess was sampled from a uniform pseudorandom integers distribution once and kept constant for all the multilateration cases. The sample intervals along the x and y-axis were given by the width and length of the 2D simulation setup. For this particular setup, only the ideal point source varied in space. The number of initial guesses was set to be equal to the number of source positions; in total, 66 initial guesses and source positions. Fig.(17a) illustrates the setup used for the robustness analysis of the Simplex and Levenberg algorithms for a fixed source position.

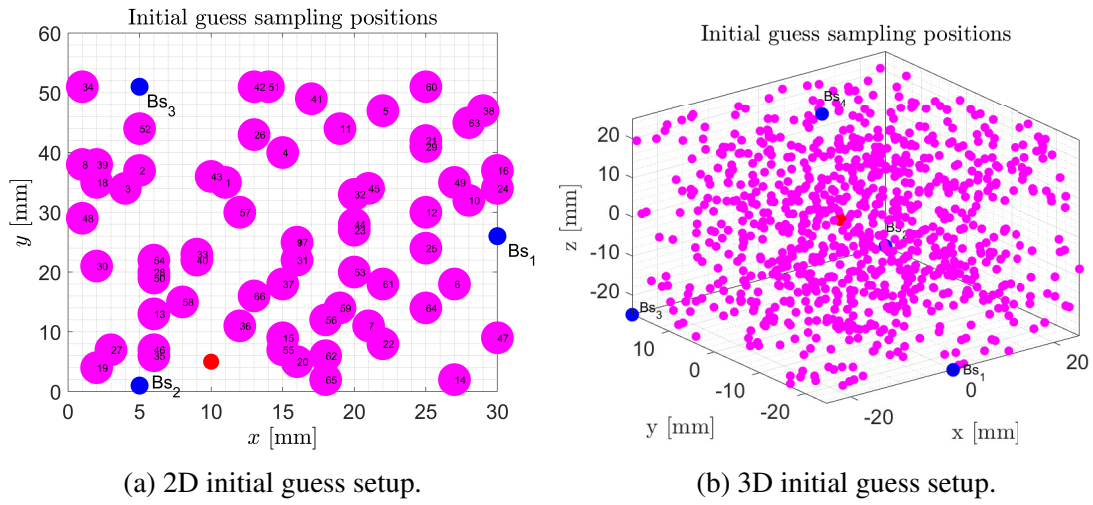


Figure 17: 2D and 3D initial guess setup, sampled from uniformly distributed pseudorandom integers. (a) 2D Initial guess position (in magenta) with three sensor positions (in blue), B_{S_1} and B_{S_2} , B_{S_3} , with a given source position (in red). For this particular setup, different source locations were considered. However, for simplicity, only one source position is illustrated. (b) 3D initial guess position (in magenta) with four sensor positions (in blue) B_{S_1} , B_{S_2} , B_{S_3} and B_{S_4} , and with a given source position (in red).

The same study between the Levenberg and Simplex was conducted in 3D. The main difference now is that the source was not scanned along the x,y and z-axis. The source position was placed in the centre of the grid. In this setup, the dimension was expanded to $50 \times 43 \times 50 \text{ mm}^3$, as described in Fig.(17b). For the 3D setup, chosen to be similar to the one discussed in the section 3.2.1, a coplanarity check was performed to have the sensors not lie on the same plane. The coplanarity was performed by calculating the determinant of the sensor's volume. Here the volume is given by the coordinates of the sensors ($x_i, y_i, z_i, i = 1, 2, \dots, 4$), as shown in eq.(3.1), and in this case, $\det(\text{volume}) \neq 0$ means that the sensors are not coplanar.

$$\text{volume} = \begin{pmatrix} x_1 & y_1 & z_1 & 1 \\ x_2 & y_2 & z_2 & 1 \\ x_3 & y_3 & z_3 & 1 \\ x_4 & y_4 & z_4 & 1 \end{pmatrix} \implies \text{if} \begin{cases} \det(\text{volume}) = 0 & \text{sensors are coplanar} \\ \det(\text{volume}) \neq 0 & \text{sensors are not coplanar} \end{cases} \quad (3.1)$$

The same sampling procedure as for the 2D case was used. However, in this case, the source location was kept fixed inside the cuboid because we would expect to have a similar result between the 2D and 3D. Hence, the point source emulating the BP position was placed in the centre of the cuboid to assess the failure and acceptance rate between Levenberg and Simplex only for a central source position. Two metrics (in 2D and 3D) were used for both algorithms to assess convergence and accuracy. The first metric was the failure rate (FR), which refers to the percentage of the reconstructed source positions above a certain threshold. The second metric was the acceptance rate (AR), which refers to the percentage of reconstructed source positions below a given threshold. The two described metrics will be mathematically defined in section 3.4.1.

3.1.3 Robustness Evaluation in Ideal Conditions (TOA, TDOA)

To assess the robustness of multilateration localisation outputs in ideal scenarios, two geometries were employed for the purpose of investigating the effect of ToF error. These geometries are illustrated in Fig.(18). For these studies, the localisation of the BP in the spatial domain was performed in the absence and presence of uncertainties. Multilateration algorithms were first analysed in a two-dimensional context. The spatial BP position was mimicked by an ideal point source, which was subsequently moved to 126 positions on a $56 \times 36 \text{ mm}^2$ orthogonal grid with 4 mm increments (see Fig.18a). The setup is close to the previous 2D setup, but the volume was increased by a factor of 1.33. The geometrical ToFs were assessed from the Euclidean distance between every single source and the sensor positions, assuming a speed of sound of 1500 m/s, which is relatively close to the speed of sound in water. As shown in Fig.(18a), only three sensors (B_{S_1} , B_{S_2} , and B_{S_3}) were utilised. The selection of sensor positions was determined by the ionoacoustic experiment setup, which is introduced in section 3.2.1. The simulation geometry was further expanded to three dimensions, as shown in Fig.(18b). In this configuration, a fourth sensor (B_{S_4}) was added on top, and the grid size was increased to $56 \times 36 \times 48 \text{ mm}^3$ with a 4 mm spacing. To streamline the analysis of the results and focus on a realistic configuration, the concept of the field-of-view (FOV) of the sensor network was defined as the surface³⁶ encompassed by the sensors, as shown in Fig(18).

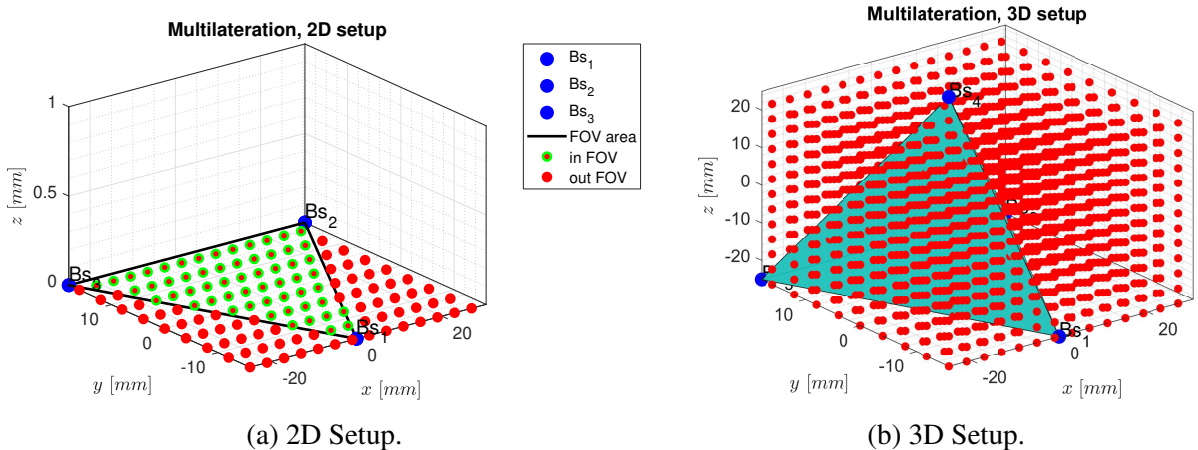


Figure 18: Multilateration setups used for robustness analysis in ideal conditions: (a) 2D setup with three sensors B_{S_1} , B_{S_2} , and B_{S_3} ; (b) 3D setup with four sensors B_{S_1} , B_{S_2} , B_{S_3} , and B_{S_4} . The blue points represent the sensor positions, and the red points indicate the source positions. The FOVs of the sensor networks are shown in green (triangle in 2D and tetrahedron in 3D). For more details on the 3D setup configuration, see Figs. (54,53b) in appendix B. Plots extracted from [150].

³⁶It can also be defined as the 3D volume.

Second, random uncertainties in the geometrical ToF computation were considered to assess the robustness of the localisation. The purpose behind modelling this type of uncertainty was to evaluate the influence of the speed of sound variations, incorrect knowledge of the detector's spatial location and error on the ToF and to determine how they affect the multilateration performance. Therefore, the ToF error for each sensor was sampled from a multivariate normal distribution $\mathcal{N}(\boldsymbol{\mu}, \boldsymbol{\Sigma})$ with a mean of zero and a standard deviation (σ_{random}) set to 5% of the absolute ToF, to replicate the *in vivo* variability in the speed of sound. It should be emphasised that the random uncertainties of individual sensors were uncorrelated, so the off-diagonal elements in $\mathcal{N}(\boldsymbol{\mu}, \boldsymbol{\Sigma})$ were zero. The multilateration was performed in 2D and 3D, as was the case when uncertainties were not modelled.

As a third step, systematic uncertainties were included in the study. The focus was on modelling uncertainties related to the imprecise determination of the measurement start time. Especially the time instant when the proton beam irradiates the target. A multivariate Normal distribution modelled systematic uncertainties. Based on studies previously conducted on our chair³⁷, a standard deviation (σ_{syst}) of 1 μs was chosen accordingly [76, 151]. The assumption made in the study was that there existed a perfect correlation between the systematic uncertainties on the ToF for all sensors considered (off-diagonal elements in $\mathcal{N}(\boldsymbol{\mu}, \boldsymbol{\Sigma})$ were > 0).

Lastly, in order to reproduce realistic scenarios, the study incorporated both random and systematic uncertainties simultaneously to account for variations in the speed of sound, imprecise knowledge of the sensor spatial location, error on the ToF, imprecise determination of the measurement start time. As a result, 150 samples were selected for each type of uncertainty, with N_{rand} and N_{syst} both set to 150, resulting in a total of 22500 samples for every source position. The number of samples was chosen to ensure enough samples to represent the multilateration error distribution comprehensively. Throughout this thesis, the word robustness will be used frequently, especially for both algorithms (TOA and TDOA). Therefore, the two algorithms are defined as robust based on accuracy and precision. This definition is valid for either the case of an ideal point source in the absence of uncertainties or when uncertainties are modelled.

3.1.4 Ionoacoustic Simulations³⁸

In a homogeneous water phantom, the performance of multilateration algorithms (TOA and TDOA) was assessed through *in-silico* evaluation of realistic ionoacoustic signals. The study aimed to analyse the impact of sensor positioning on the ToF error. The three-dimensional dose distribution, $D(\mathbf{r})$, for a 20 MeV monoenergetic proton beam was generated using the FLUKA Monte Carlo code (version 2020.0.4, with PRECISION defaults) [152, 153]. Further details regarding the simulation setup can be found in the supplementary material in Lascaud et al. [154]. The initial pressure ($p_0(\mathbf{r})$) was derived from the deposited energy ($D(\mathbf{r}) \cdot \rho$, where ρ represents the density of water, which is equivalent to 998 kg m^{-3} at the considered temperature), which is then multiplied by the Grüneisen parameter ($\Gamma = 0.11$ in water, see eq.(2.30)). The propagation of the initial pressure in three dimensions was performed on an anisotropic grid. The grid resolution along the propagation axis was 75 μm , and a lateral grid resolution of 150 μm . The acoustic simulation was performed using the MATLAB k-Wave toolbox (MATLAB R2019a, MathWorks, Natick, MA) [155]. It is worth noting that due to the sharpness of the BP (300 μm BP_{FWHM}) relative to the lateral beam dimensions (2.5 mm BP_{FWHM}

³⁷Chair of Medical Physics (LMU). For more details see <https://www.med.physik.uni-muenchen.de/research/range-verification/ionoacoustics/index.html>

³⁸FLUKA and k-wave simulations courtesy of Dr Julie Lascaud and Dr Hans-Peter Wieser.

at the phantom entrance, as estimated experimentally from a Gafchromic film measurement), higher frequencies are transmitted along the proton beam axis, thus requiring the finer grid in this direction. To accurately simulate the acoustic emission at the interface between air and water, a 1 mm-thick air gap was included downstream of the proton beam in the k-Wave simulation setup³⁹ (Fig.(19b)). The pressure waves were captured using 843 ideal point sensors arranged in a semi-circular configuration with a diameter of 60 mm. The sensor network was placed such that the centre of the arc coincided with the maximum of the proton dose, and the arc dimension was chosen to match the experimental setup depicted in Fig.(19a). Lastly, each ionoacoustic signal recorded was convolved with a 200 ns square pulse to account for the proton pulse shape from the accelerator configuration used in the measurements (refer to section 3.2).

3.2 Experimental Studies

Throughout this study, multiple experimental investigations were carried out to determine the location of the BP position. The two most relevant experiments will be presented in sections 3.2.1 and 3.2.3. Experimental campaigns aimed to benchmark the multilateration experimentally with simulation studies, meaning to localise the BP position under realistic scenarios. The first experiment was performed using the 3D I-BEAT detector [156], and only considering the sensors located in the same plane⁴⁰; for this particular setup, the multilateration was assessed in 2D with three sensors, as described in section 3.2.1. For the second setup, a specific sensor housing was designed in this thesis work to be able to localise the BP in 3D with five sensors configured in such a way as to record the ionoacoustic signal from different spatial locations and at different angles. The complete setup is discussed in more detail in section 3.2.3. For both experimental studies, particular attention was paid to defining a suitable method to localise the transducer's spatial location. As discussed in section 3.2.1, two methods for the transducer's spatial location were proposed for the BP localised with only three sensors and in a two-dimensional plane. For the second setup described in section 3.2.3, transducers were localized using an optical tracking system, a widely-used technique in various clinical practices such as transrectal ultrasound-guided prostate biopsy and image-guided transcranial ultrasound [157, 158, 159]. However, this localisation technique carries some constraints that will be further discussed.

3.2.1 Setup 1: 3-Sensors Configuration

The experiments were carried out at the Maier-Leibnitz-Laboratory in Munich, Germany, using a 20 MeV monoenergetic pulsed proton beam impinging in a water-filled aluminium box. The proton beam entered the setup through an air channel, which was terminated by a 50 μm -thick polyimide foil acting as the entrance window, as illustrated in Fig.(19a). During this first experiment, the beam was transmitted in pulses lasting 200 ns and occurring at a rate of 4.9 kHz. In addition, the beam's current was set to 3 nA, causing a dose of 1.69 Gy to be deposited at the BP with each pulse. To record the ionoacoustic wavefront, three detectors were positioned on the proton beam axis (z-axis, axial sensor) and on an axis perpendicular to it (lateral sensors). The detectors were chosen based on the expected frequency spectrum at the respective positions and were directly mounted into the aluminium box. Water-sealed apertures in the box wall ensured that the detectors were at the focus of the beam profile (BP) and maintained a fixed position relative to the entrance window throughout the experimental campaign. Notably, all the single-element detectors were focused piezoelectric

³⁹k-Wave simulations courtesy Dr Hans-Peter Wieser.

⁴⁰See the experimental setup of the 3D-IBEAT in appendix C.

transducers manufactured by Olympus-Parametric (3.5 MHz centre frequency with a 73 % fractional bandwidth and a diameter of 12.7 mm). The experimental setup was placed on a motorised three-axis stage for alignment. For this purpose, ionoacoustic measurements were taken by moving the setup to various positions along the x- and y-axes, as shown in Fig.(19a), in 1 mm increments. The position where the maximum signal amplitude was recorded on Bs_1 was considered the *on-axis* position, aligned with the proton beam. The phantom was shifted 5 mm along the x-axis to acquire additional measurements, resulting in an *off-axis* position.

The ionoacoustic signals were amplified by 60 dB using a low-noise amplifier (HVA-10M-60-B, FEMTO Messtechnik GmbH, Germany) before being acquired with a digital oscilloscope (6404D PicoScope, Pico Technology Ltd., GB) at a sampling frequency of 156.25 MHz. A synchronisation signal delivered by the chopping system of the Tandem was employed to initiate the signal acquisition. As a result of this trigger, there was a time delay of 1.43 μs between the beginning of the measurement and the time when the first protons collided with the target, which had been previously characterised [76, 151], and was later subtracted from the time of arrival to estimate the ToF. To perform the measurements, 1000 consecutive acquisitions were systematically made, with each acquisition consisting of 1000 proton pulses. Throughout the experiment, the temperature of the water was monitored with a PT1000 probe submerged in it. The average temperature recorded was 21.92 $^{\circ}\text{C}$, which was then used to calculate the speed of sound in the water as 1488.1 ms^{-1} . The speed of sound in water was later used to estimate the BP position from the signal ToF. For each acquired signal, a noise reduction technique was implemented in post-processing using the Daubechies wavelet family with 5 decomposition levels [160, 161, 162, 163]. The location of the Bragg Peak was identified with a single shot, resulting in a peak dose of 1.69 Gy deposited precisely at the Bragg Peak.

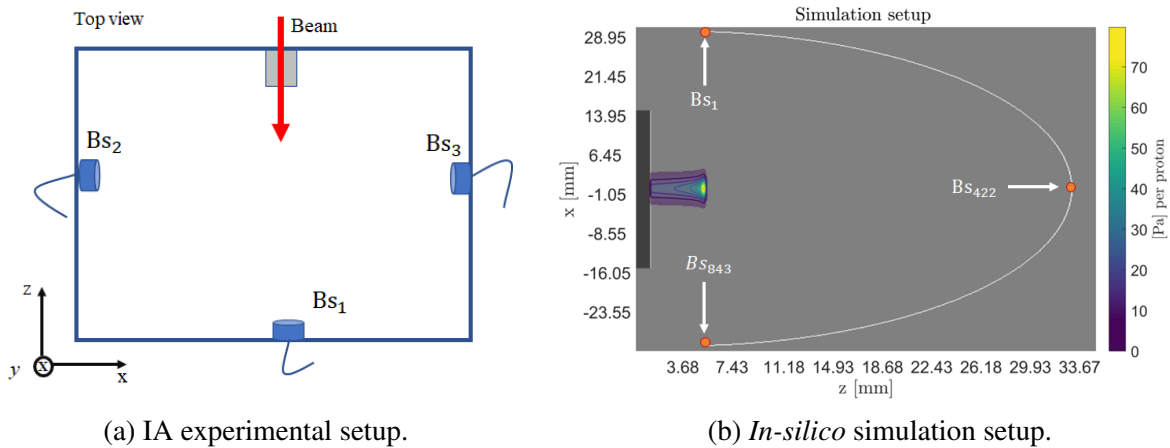


Figure 19: The experimental setup comprised three sensors, as shown in the top view schematic (a). The two lateral sensors (Bs_2 and Bs_3) were positioned 54.7 mm apart, while the axial sensor (Bs_1) was situated 30 mm from the entrance window. The acoustic simulation setup, depicted in (b), involved a water-based setup with a superimposed dose. The simulation geometry consisted of a white semi-circle of 843 individual point sensors. Black represented the air in the entrance channel, and light grey indicated the water medium. In the simulation setup, the sensor indexes began at Bs_1 (the lateral sensor visible in the top view schematic in (b)) and concluded with Bs_{843} , as highlighted by the orange dots, figures extracted from [150].

3.2.2 Transducer's Spatial Localisation Setup 1

As stated in previous sections, to localise the BP position, it is crucial to know the spatial location of the transducers with a certain accuracy because, among other factors, the localisation of the BP position depends on it. The transducer's spatial location was initially determined for this experimental setup using two approaches. The first one was based on the construction drawings⁴¹ used to design the 3D I-BEAT detector. This approach estimated the distances between the sensors and the phantom entrance window, assuming that the phantom entrance window was at the origin. This geometrical approach was relatively simple. However, it is not uncertainty-free, especially if the sensors' curvature is not considered. The curvature of the sensor is accounted for by considering the depth of the sensor (h), which is calculated in eq.(3.2), where r is the sensor radius. Another important aspect is that the transducer's spatial location estimated from the drawings may differ slightly from the positions of the transducers mounted into the setup, e.g., due to the screwing of transducers, supports used to fixate the transducers into the phantom, etc.

$$h = \sqrt{r^2 + f_i^2} - f_i \quad (3.2)$$

The second approach was more elaborate, attempting to retrieve the transducer's spatial location experimentally. For this study, three transducers were mounted into the aluminium box system⁴², and an aluminium cylinder with a diameter of 4 mm was used as a target. The objective was to define the position of the sensors relative to the cylinder. That was achieved by recording the acoustic signals emitted by the sensors and reflected from the cylinder target at different spatial locations w.r.t the transducers. The cylinder target was moved by a motorised linear stage, and its position was kept constant along the y -axis. The recorded signal was then used to estimate the transducer's spatial central position, as described in eq.(3.3). In the aforementioned equation, $P(R,t)$ is the recorded pressure and $C_i(R)$ is the central position integrated into a time interval from t_0 to t_f , and R is the variable encoding the cylinder coordinates ($R=(x,y,z)$). In eq.(3.3), t_0 represents the initial time instant for the acoustic signal, while t_f corresponds to the final time instant. This temporal window was carefully chosen to eliminate artefacts associated with the integrated pressure wave. It is worth noticing that $C_i(R)$ ⁴³ corresponds to the position where the maximum recorded pressure is achieved.

$$C_i(R) = \max \left(\int_{t_0}^{t_f} P(R,t) dt \right); \quad R = (x,y,z) \quad (3.3)$$

The central position was then used to align the target inside the phantom. The complete experimental setup is depicted in Fig.(20), and the transducer's spatial location was calculated as follows:

- The first step was to turn the proton beam off, and the I-BEAT⁴⁴ entrance window (ew) was unmounted to have a wider scanning range for the cylinder target. The single-element ultrasonic detectors were securely mounted to prevent water leakage, and the cylinder target was fixed at a

⁴¹The schematic drawings were implemented in Inventor.

⁴²See the sensors mounted on the 3D-IBEAT detector in appendix C.

⁴³ i is the number of sensors ranging from 1 to 3, $i = (Bs_1, Bs_2, Bs_3)$.

⁴⁴Sometimes the names 3D I-BEAT and I-BEAT will be interchanged.

specific location on a motorized stage within the I-BEAT detector. Finally, the I-BEAT detector was loaded with distilled water, as shown in Fig.(20). Next, the target was placed at a distance (d) equal to the transducer focal length and scanned along the x -axis with a step of 0.5 mm while the transducer B_{S1} transmitted and received pulse-echo signals. Once the cylinder was fully scanned, a 2D pressure profile was recorded, as illustrated in Fig.(21a). For the recorded pressure, a post-processing technique was applied to better estimate the transducer's spatial location. Fig.(21b) illustrates the steps used in the post-processing. To begin with, the recorded pressure $P(R,t)$ was windowed to avoid unwanted reflected signals. Afterwards, the signal was detrended to have a zero mean, and consequently, the signal envelope ($H\{P(R,t)\}$) was computed, and then the transducer central position $C_i(R)$ was estimated.

- Second, the cylinder target was scanned on the z -axis while the transducer B_{S2} transmitted and received pulse-echo signals. Finally, the same procedure performed for the axial transducer B_{S1} was applied to B_{S2} and B_{S3} , and the cylinder was placed at $C_i(x,0,z)$. If the setup is perfectly aligned and there are no uncertainties on the mounting process of both lateral transducers (B_{S2} and B_{S3}), we would expect the centre spatial location of both transducers to match, i.e., $C_{B_{S2}}(x,0,z) = C_{B_{S3}}(x,0,z)$.
- Third, the cylinder target was deemed aligned for all the sensors because it was placed in a new spatial location, which is now the coordinate origin $(x,0,z) = (0,0,0)$ mm. From this new spatial location, a pulse-echo is computed with all sensors. From the recorded pulse-echo signals, the spatial location of all transducers is estimated by calculating the distance from the cylinder to each transducer.

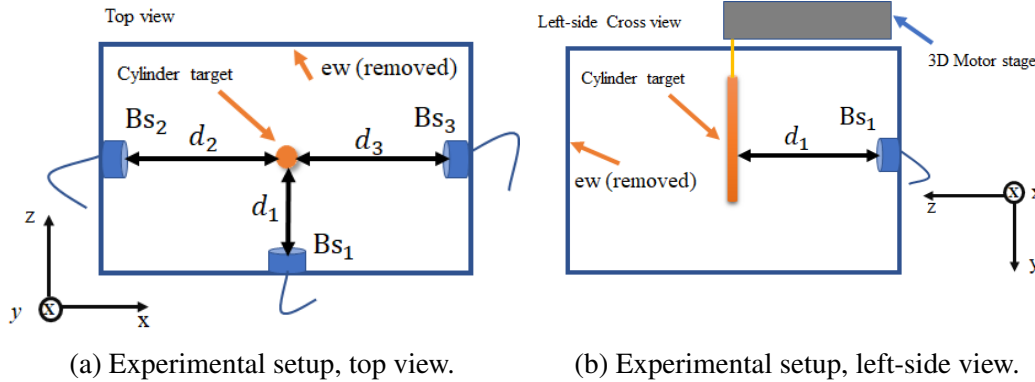
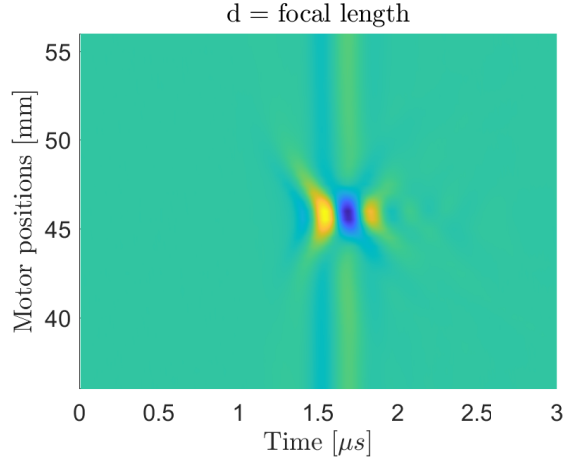


Figure 20: Transducer's spatial localisation setup. (a) Top view with three transducers B_{S1}, B_{S2} and B_{S3} , located at distances d_1, d_2 and d_3 from the centre of the cylinder target (represented by the orange circle), (ew) is the position of the beam entrance window (which was removed); (b) left-side cross view, with the axial transducer B_{S1} and the cylinder target mounted on a motor stage.

The relative distances d_1, d_2 and d_3 were computed from the recorded pressure. The calculation of the relative distances took into consideration the radius (r) of the cylindrical target. For each pulse-echo measurement, the ToF was estimated. The relative distances were calculated using the speed of sound v_s in water. The origin has been placed at the centre of the cylinder target, and the spatial location of the transducers was expressed mathematically as:

$$\begin{bmatrix} Bs_1(x,0,z) \\ Bs_2(x,0,z) \\ Bs_3(x,0,z) \end{bmatrix} = \begin{bmatrix} d_1 & 0 & 0 \\ 0 & 0 & d_2 \\ 0 & 0 & -d_3 \end{bmatrix} = \begin{bmatrix} \left(v_s \cdot \frac{ToF_1}{2} + r\right) & 0 & 0 \\ 0 & 0 & \left(v_s \cdot \frac{ToF_2}{2} + r\right) \\ 0 & 0 & -\left(v_s \cdot \frac{ToF_3}{2} + r\right) \end{bmatrix}, d_i = ToF_i \cdot \left(\frac{v_s}{2}\right) + r; i = 1, 2, 3 \quad (3.4)$$



(a) 2D raster scan pressure profile.



(b) Post-processing pipeline to retrieve the centre position.

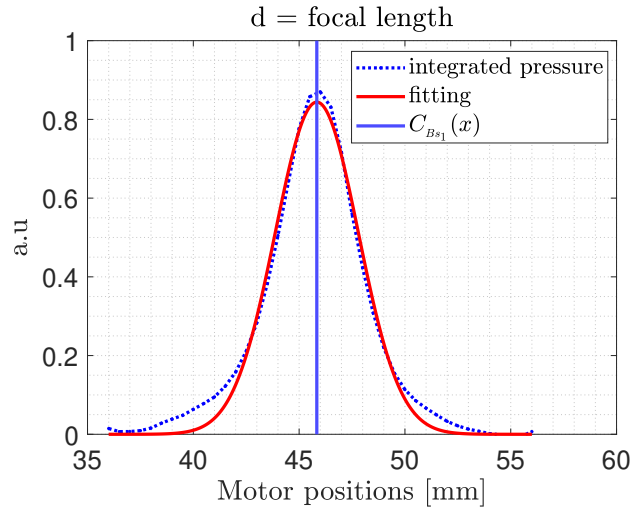
(c) Integrated pressure in the time domain for the acoustic signal recorded with the Bs_1 transducer. The cylinder was scanned along the x-axis.

Figure 21: Transducer central position estimation for the cylinder target alignment. (a) 2D raster scan pressure profile recorded with the axial transducer Bs_1 moving the cylinder along the x-axis; (b) signal post-processing technique to improve the signal quality; (c) Integrated pressure in the time domain, which enables to estimate the central position.

3.2.3 Setup 2: 5-Sensors Configuration

In a water tank, a 5-sensor arrangement was assembled using a dedicated holder (*horseshoes*) developed in this work to conduct additional experiments, as depicted in Fig.(22). In this particular configuration, the proton beam energy was raised to 22 MeV. The beam current was set to 3.5 nA with a proton pulse length of 200 ns at a repetition rate of 10 kHz, corresponding to a dose per pulse of 0.58 Gy delivered at the BP. For this setup, 12.7 mm-diameter piezoelectric single elements with a 3.5 MHz centre frequency were utilised, following a similar arrangement as in the previous experiments. Specifically, the arrangement consisted of one axial transducer (B_{S_2} ; $fl = 50.8$ mm), two transducers inclined at an angle of 28° with respect to the beam axis (B_{S_1} and B_{S_3} ; $fl = 25.4$ mm), and two lateral transducers, both of them focused (B_{S_0} and B_{S_4} ; $fl = 25.4$ mm), as shown in Fig.(22). The ionoacoustic signals were acquired sequentially due to limited channels available on the picoScope, first with B_{S_0} to B_{S_2} and then with B_{S_2} to B_{S_4} . As previously, the measurements were repeated over 1000 consecutive proton pulses, but the SNR for the IA signals recorded by the two tilted transducers (B_{S_1} and B_{S_3}) was lower than in the previous experiments due to their orientation relative to the beam axis. The signals were averaged over 50 acquisitions to address this, resulting in a total peak dose of 29 Gy deposited at the BP before performing the wavelet filtering.

3.2.4 Transducer's Spatial Localisation Setup 2

A 3D optical tracking system (Hybrid Polaris Spectra System, Northern Digital Inc., Waterloo, ON, Canada) using a passive marker tool was utilised to estimate the spatial location of the transducers (c_0 to c_4). In the case of focused transducers, the transducer location was defined as the projection of the outer rim centre onto the curved surface. The position of the rim centre was determined by locating three points on the circle, and its projection on the curved surface was obtained from a fourth measurement on the curved surface. In addition, the accuracy of transducer localisation was enhanced by performing a 3D rigid registration. The 3D rigid registration was based on the Coherent Point Drift (CPD) algorithm [164], and it was performed between a template derived from the holder drawing (moving image) and the position obtained from the optical measurements. The entry point of the proton beam into the water tank, referred to as the entrance window (c_{ew}), was determined by irradiating a Gafchromic film. Following this, a passive marker was placed at the centre of the Gafchromic film, allowing the spatial location of the beam entrance window to be recorded using an optical tracking system. Fig.(23) illustrates the step of estimating three points, p_1 , p_2 , and p_3 , on the rear surface of the ultrasound transducer using a passive optical marker to determine the transducer spatial location. Here, each point is denoted as $p_{i=1,2,3}$ and can be represented as a function of its Cartesian coordinates, x , y , and z . In the mentioned figure, the parameter h was fixed according to the transducer focal length. In other words, equal to 0 mm for B_{S_0} (unfocused), 0.78 mm for B_{S_1} , B_{S_3} , B_{S_4} and 0.39 mm for B_{S_2} . Given the position of these three points, the centre c_j of the transducer was estimated by solving eq.(3.5). The procedure was repeated for all the transducers, having their spatial locations as c_0 , c_1 , c_3 , and c_4 . Finally, the transducer location was estimated from the centre positions by accounting for the focal length of every single transducer along the sensor axis.

As mentioned previously, to increase the accuracy of the transducer spatial location of the *horseshoes* setup, the CPD registration, which is based on a probabilistic approach to align two point sets, was used. The array drawings was labelled as IV, and the 3D optical tracking system output was labelled as OT. Fig.(24) illustrates the four steps used for the rigid co-registration, as listed below:

- First, the template provided by drawing IV was initially rotated along all three axes (x, y, z).

- Second, to properly align the template IV, it was shifted by subtracting the mean value of the OT to the IV template.
- Third, the point clouds were estimated considering both inputs from IV and OT.
- Fourth, a 3D rigid co-registration between IV and OT was performed by moving IV while OT was kept fixed. From the 3D rigid co-registration output, the new transducer spatial locations c_j^1 ($j = \{0, 1, \dots, 4\}$) were estimated and considered for the multilateration of the BP position.

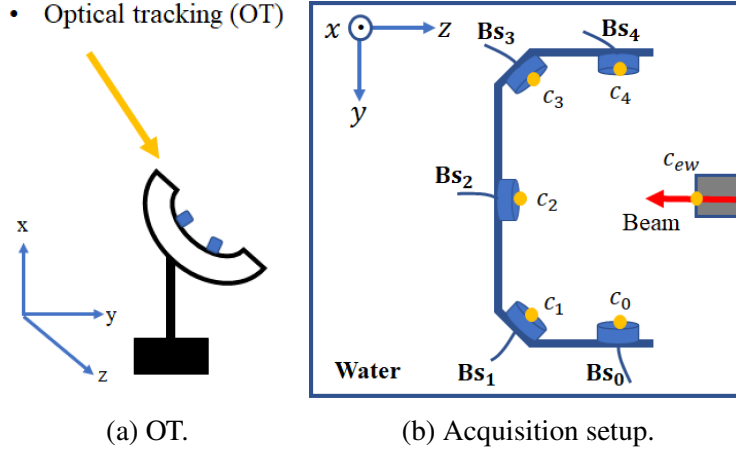


Figure 22: 3D Multilateration experimental setup. (a) 3D optical tracking is used to localise the transducer spatial locations. (b) The water tank setup illustrates the transducer centre positions (yellow dots) and the entrance window central position (orange dot on the red arrow indicating the beam entering the water phantom), figure extracted from [150].

$$(p_{i,x} - c_{j,x})^2 + (p_{i,y} - c_{j,y})^2 + (p_{i,z} - c_{j,z})^2 = r_j^2; \begin{cases} i = 1, 2, 3 \\ j = 0, \dots, 4 \end{cases} \quad (3.5)$$

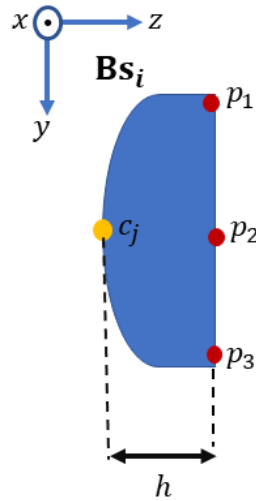


Figure 23: Schematic representation of the procedure used to estimate the centre of the transducers. The red dots show the OT measurement positions on the transducer's outer rim, and the yellow dot depicts the location of the transducer centre (projection of the rim centre on the curved surface). Figure extracted from [150].

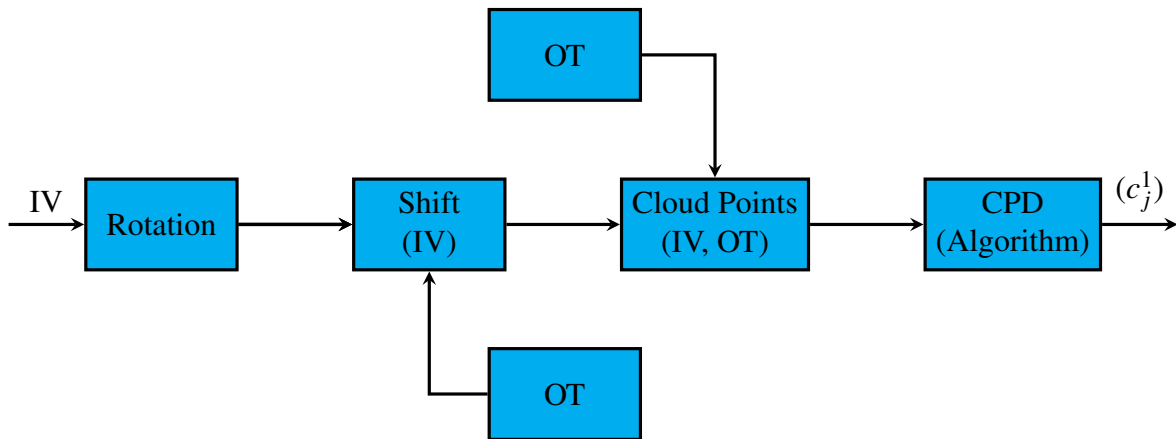


Figure 24: 3D Rigid co-registration between the sensor template and the output from the optical tracking system. (IV) is the technical drawing template, (OT) is the sensor coordinates provided by the optical tracking coordinates output.

3.3 SIRMIO Case Study ⁴⁵

The SIRMIO beamline was used to degrade and focus a low energy proton beam starting with an initial energy of 75 MeV [56], resulting in a 50 MeV proton beam in water [54]. The Geant4 Monte Carlo simulation package (version 10.06.p02) was used for the simulation. The simulation allowed obtaining a 3D dose deposition in water using a homogeneous scoring grid spacing of 50 μm . The homogeneous grid spacing was later interpolated to 200 μm for the k-Wave simulation of the acoustic pressure propagation. The simulation setup included a 1 mm thickness of air preceding the water target. From the k-Wave simulation, the aim was to evaluate multilateration in the context of SIRMIO using an arc sensor. Fig.(25) illustrates the setup arrangement with xy and xz plane views. The sensor setup included 52 sensors arranged in an arc shape with a radius of 20 mm, covering the area where the mouse was expected to be located, as shown in Fig.(25a). All the sensors in the current setup have a diameter of 1 mm, and they were all used to record the ionoacoustic signals produced by the pulsed SIRMIO beam. The axial sensor, which corresponded to the centre on the arc, was placed at a distance of 14 mm w.r.t the BP position. The simulation was performed for different lateral and distal beam offsets to evaluate the BP position for different beam spatial locations. The reason for different beam shifts was to reproduce the beam scanning. The first beam offset was applied along the x-axis. Consequently, the beam was shifted by ± 1 mm with a step of 0.5 mm while keeping the y and z-axis fixed. Subsequently, the beam was shifted along the y-axis by ± 1 mm with a step of 0.5 mm while keeping the x and z-axis fixed. Lastly, the beam was shifted along the z-axis by ± 1 mm with a step of 0.5 mm while keeping the x and y-axis fixed. Before localising the BP position, the error on the ToF was assessed considering the IVP. Afterwards, the error on ToF was evaluated by convolving the solution of the IVP⁴⁶ with a Gaussian time profiles with varying widths (FWHM) ranging from 1 to 10 μs , with a step of 1 μs . The error in the distance was computed as ground truth distance given by the BP position (x_{BP}, y_{BP}, z_{BP}) and sensors positions (x_i, y_i, z_i) minus the estimated distance given by the ToF extraction method, as described by the equation below:

⁴⁵Simulations (FLUKA and k-Wave) courtesy of Pratik Dash based on requirements of this work for multilateration purposes. Geant4 simulation courtesy of Dr Marco Pinto.

⁴⁶Pressure integrated on the sensor surface assuming an instantaneous energy deposition.

$$\varepsilon = \left| \sqrt{(x_{BP} - x_i)^2 + (y_{BP} - y_i)^2 + (z_{BP} - z_i)^2} - d_{ToF_i} \right| \quad (3.6)$$

The error assessment⁴⁷ related to the ToF was performed considering a different setup with 37 sensors (1 mm dimension) separated by 5° from each other sensors instead of 52 sensors. All the other simulation parameters were kept the same except for the number of sensors and sensor dimension. The reason for not re-assessing the ToF error studies with a new setup with 52 sensors instead of 37 sensors is that the results are expected to be the same because the error will mainly depend on the proton time profile width, among other parameters like the sensor dimension. However, a 1 mm transducer dimension is expected to not change the result significantly compared to a point transducer.

On the other hand, the motivation beyond selecting the proton time profile widths is that from a clinical synchrocyclotron facility, the time profile is expected to be between 3 to 6 μs [76]. Therefore, for the error on ToF analyses, only the beam centred w.r.t the arc sensor was considered (beam at $x, y, z = 0, 0, 0$ mm). After evaluating the impact of the ToF for different proton time profiles, the BP position was localised. Initially, it was localised without considering a proton time profile, and then the BP position was retrieved considering all the beam offsets and all the introduced proton time profile widths.

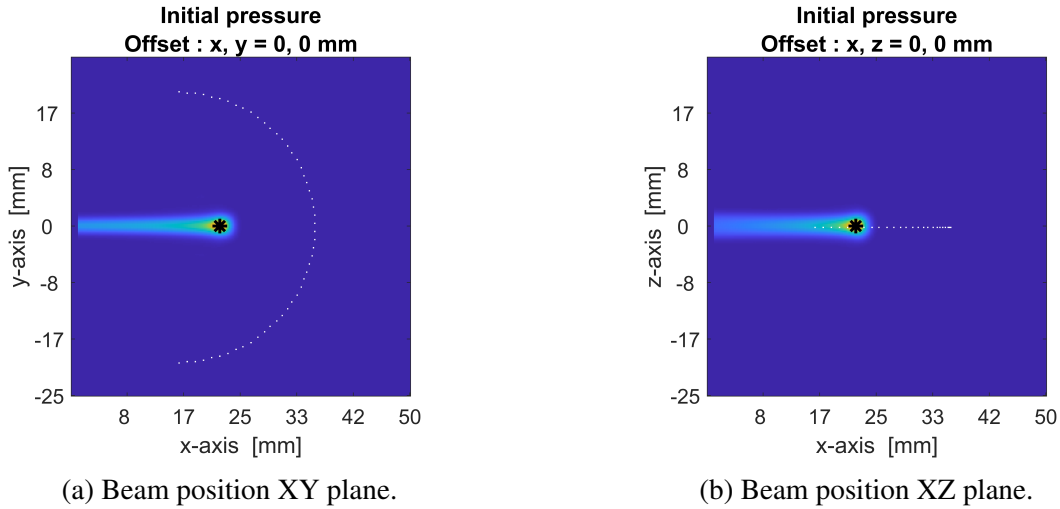


Figure 25: Multilateration setup of BP position for the beam at a fixed spatial location, no offset applied to the beam ($x, y, z = 0, 0, 0$ mm). The black asterisk corresponds to the ground truth (maximum BP position along all the axes). (a) The 52 sensors, with 1 mm dimension (x, y plane view), are the white dots in the form of an arc. (b) The same sensor is viewed from a different plane (x, z plane). Both figures are reproduced by courtesy of Pratik Dash.

⁴⁷Results were readily available for another ongoing PhD thesis project by Pratik Dash.

3.4 Data Analysis

The same metric was applied to the multilateration studies solved for ideal point sources and with ionoacoustic propagated signals to assess the performance in localisation (i.e., error in the retrieved position). However, since the robustness analysis was only conducted for the ideal point sources, on top of the error in position, the root mean square error (RMSE) was also defined as a metric, especially for the cases where random and systematic uncertainties were modelled. From these two metrics (i.e., error in position, root mean square error), another set of metrics was defined to assess the robustness of the multilateration algorithms. The other two metrics that were determined to evaluate the convergence and accuracy of the optimisation algorithms are the FR and AR, already introduced in section 3.1.2, which are based on the error in position output from the multilateration.

3.4.1 Multilateration Robustness Assessment

To assess the robustness of multilateration for both TOA and TDOA algorithms, initially, the localisation metrics were defined only for cases where uncertainties were not modelled in the ToF. Afterwards, uncertainties were accounted for, leading to defining a new set of metrics. Some metrics described here are mainly for ideal point source studies (BP localised in the space domain). However, some of these metrics will also be considered when the BP position is retrieved from a signal emanated from a proton beam (BP localised from a ToF signal). The metrics used to evaluate the performance of multilateration and numerical optimisation algorithms are listed below:

- The accuracy can be defined mathematically in terms of the position error ϵ_{xyz} . However, it should be noted that this definition does not consider any uncertainties.

$$\epsilon_{xyz} = \sqrt{(x' - x_s)^2 + (y' - y_s)^2 + (z' - z_s)^2} \quad (3.7)$$

Where x' , y' , and z' coordinates in the equation are the known source positions (e.g., the BP position ground truth). On the other hand, x_s , y_s , and z_s are the reconstructed source positions from the optimisation output. The 3D metric is reducible to 1D or 2D by cancelling the coordinate of the missing dimensions. For the BP at multiple spatial locations, i.e., when its position varies spatially as shown in Fig.(18), from the error in position a mean value $\mu_{\epsilon_{xyz}}$ and a standard deviation $\sigma_{\epsilon_{xyz}}$ of the error in position were assessed. The analyses also included unrealistic cases, i.e., cases when the BP position is outside the volume covered by the sensors network. For the more realistic cases when the sources are inside the FOV, the corresponding metrics are designated as ϵ_{xyz}^{FOV} , $\mu_{\epsilon_{xyz}}^{FOV}$ and $\sigma_{\epsilon_{xyz}}^{FOV}$.

- For the BP position localised in the presence of uncertainties, the error in position metric was replaced by the RMSE, i.e., the RMSE between the actual and retrieved source position, as described in eq.(3.8).

$$RMSE = \sqrt{\frac{1}{N} \sum_{i=1}^N \left((x'_i - x_s^i)^2 + (y'_i - y_s^i)^2 + (z'_i - z_s^i)^2 \right)} \quad (3.8)$$

Other metrics were obtained from the RMSE, such as the mean root mean square error (μ_{RMSE}) and the standard deviation of the root mean square error (σ_{RMSE}). On the other hand, when considering only source locations within the FOV and modelled the uncertainties, the metrics were renamed as $RMSE^{FOV}$, μ_{RMSE}^{FOV} and σ_{RMSE}^{FOV} .

The accuracy of various ToF extraction methods is assessed by calculating the error in ToF estimation, denoted as ε^{ToF} . This error was defined as the absolute difference between the known ToF and the ToF estimated by a particular extraction method multiplied by the speed of sound in the medium. The known ToF is the ground truth, determined during the simulation study described in section 3.4.3. For each sensor, the ground truth of the ToF was defined as the quotient of the Euclidean distance between the sensor spatial location and the known BP position, divided by the speed of sound in the medium. After calculating the ground truth for each sensor, the total error in ToF was estimated from eq.(3.9).

$$\varepsilon^{ToF} = \left| ToF_i - ToF_i^{Ground-truth} \right|; \quad i = 1, 2, \dots, n \quad (3.9)$$

On the other hand, considering the signal originated from the 20 MeV, 22 MeV and 50 MeV proton beam, the ground truth of the BP position was determined from the equivalent FLUKA Monte Carlo simulations. While the simulations for the 22 MeV proton beam setup were not directly benchmarked against an independent measurement, the strong consistency observed between the experimental and simulated IA signals instils confidence in the reliability of the utilised model. Furthermore, it is worth noting that this model had undergone prior validation in a time-of-flight spectrometry study [165].

- To assess the convergence and accuracy of two optimisation algorithms, Levenberg and Simplex, two metrics were defined based on the error in position. The first metric is the FR, and the second metric is the AR, which was evaluated using eq.(3.10) and eq.(3.11), respectively. Primarily, a localised source position was classified as an FR if its error in position was above the threshold (γ^T) of 1 mm. On the other hand, if the error in position was below or equal to the threshold, the position was classified as an AR. Both metrics were based on the error in position. The FR and AR values determine the success or failure of a particular outcome. If these values fall below or above a certain threshold, a decision is made based on that outcome.

$$\varepsilon_{xyz} > \gamma^T \rightarrow \text{FR} \quad (3.10)$$

$$\varepsilon_{xyz} \leq \gamma^T \rightarrow \text{AR} \quad (3.11)$$

The threshold can be further changed if one knows a prior maximum and minimum expected error in position. However, for the studies conducted here, a threshold of 1 mm was within the maximum acceptable error for the localisation performed without uncertainties. The motivation behind the threshold value is based on the current clinical margins of safety, typically 3.5% + 1 or 2 mm [30, 37]. However, the margin safety can also change from one clinical facility to

another. Furthermore, this work is on BP localisation for pre-clinical applications; therefore, a small margin of safety is expected.

- Another important metric is the SNR. The recorded ionoacoustic signal depends highly on the dose and sensor position w.r.t the proton beam. Hence, different sensors spatial locations are expected to have different signal quality, regardless of the number of signal averaging. Therefore, another way to understand the error in position for a given experimental setup is to estimate the SNR and put both results in context. The SNR for each sensor was defined as the ratio between the peak-to-peak amplitude and the noise standard deviation and mathematically can be described as:

$$SNR^{Bs_i} = \frac{V_{p-p}[mV]}{\sigma(Noise)[mV]}; \quad i = 1, 2, \dots, n \quad (3.12)$$

In eq(3.12) V_{p-p} is the peak-to-peak amplitude of the primary signal and $\sigma(Noise)$ is the noise standard deviation. V_{p-p} was estimated from the signal acoustic traces recorded by the digital oscilloscope. From the IA signal, V_{p-p} was calculated as the absolute difference between the compression's maximum and the rarefaction peaks' minimum. On the other hand, $\sigma(Noise)$ was estimated by looking outside the signal in the acoustic traces and from there, the standard deviation was computed. The acquisition of the noise signal was long enough to have many samples to compute $\sigma(Noise)$.

3.4.2 Multilateration Workflow for BP localisation

Fig.(26) illustrates the multilateration workflow used for BP localisation. The ToF was estimated for each sensor Bs_1 to Bs_n , where n is the number of sensors located at a spatial location c_1 to c_j ⁴⁸, respectively, and converted to a distance knowing the medium speed-of-sound (v_s). Multilateration was performed afterwards, either using TOA or TDOA algorithms⁴⁹. To this aim, the cost functions described in eq.(2.43) and eq.(2.46) for TOA and TDOA, respectively, were minimised using the Levenberg and Simplex algorithms. For the minimisation purpose, the input parameters for both algorithms were the same, i.e., 500 iterations and a termination tolerance set to 10^{-9} . The algorithms were available from the Matlab software (Matlab R2021a). The code of the cost function computation is reported in appendix F. For multilateration, the optimisation process is based on the computation of gradients by solving the TOA and TDOA equations using, for example, the Levenberg approach. Therefore, by default, Matlab software uses numerical gradient approximations based on several algorithms, i.e., finite difference method. However, this computation approach can be slow, especially in cases where uncertainties are considered. Therefore, analytical gradients were computed and implemented in the minimisation process to speed up the optimisation process for both algorithms (TOA and TDOA); see the appendix G.

As previously discussed in section 2.2.1, the TOA method is an absolute position localisation technique and does not require a reference sensor. However, the TDOA method always requires a reference sensor. Therefore, the study considered two types of reference sensors for the ideal scenario of

⁴⁸ j is defined in eq.(3.5).

⁴⁹For TOA and TDOA, the word "algorithms" and "methods" will be sometimes interchanged.

point sources at multiple locations using TDOA. These are static and dynamic reference sensors. In the case of static reference sensors, the same reference sensor is used regardless of the source location. In contrast, for dynamic reference sensors, the reference sensor is changed based on the ToF readings on each sensor of the network.

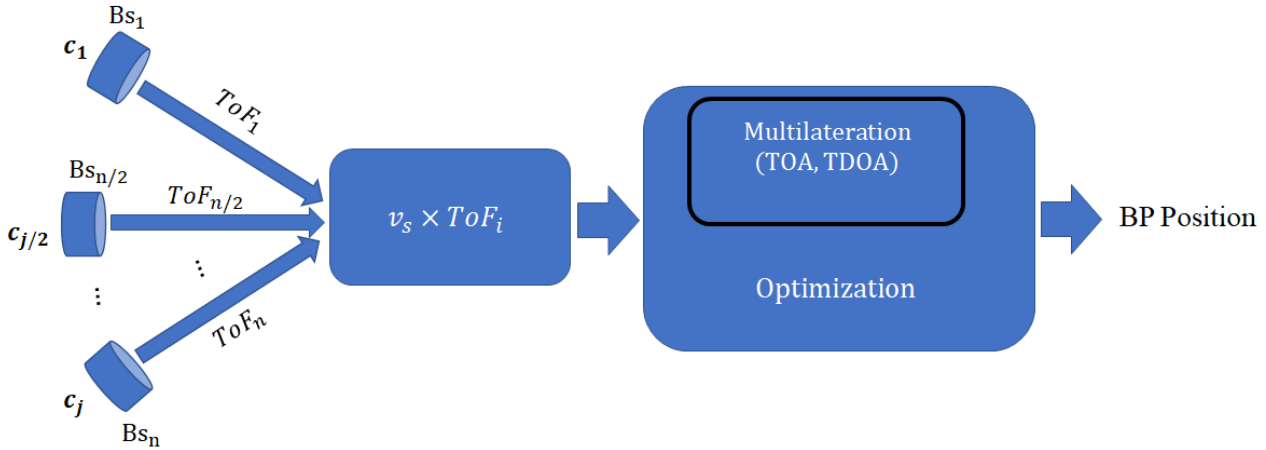


Figure 26: Schematic representation of multilateration workflow. For the multilateration localised for three or four sensors, n is always equal to j , figure extracted from [150] with slight changes.

3.4.3 Ionoacoustic Time-of-Flight Extraction

In order to localise the BP position in water within the time domain (i.e., IA signal generated by a proton beam), a study on different ToF extraction methods was assessed. The ToF was obtained from the direct signal (γ -wave) in studies involving IA signals, and various extraction methods were evaluated. Fig.(27a) and Fig.(27b) show simulated IA signals recorded at different sensor positions (axial and lateral, respectively), with annotations highlighting the signal features used for ToF extraction. From the several ToF extraction methods described in this section, only a particular method will be used to assess the accuracy of the BP position localisation for the experimental studies. So, the different ToF extraction methods are listed below:

- For axial sensors, the *zero-crossing* method identifies the time instant when the IA signal crosses zero between the compression and rarefaction pulses. This method is hereafter referred to as the *zero-crossing* method (see Fig.(27a)). As shown in Fig.(27b), lateral sensors may produce multiple zero-crossings. In such cases, the first *zero-crossing* point is typically chosen for ToF extraction.
- The *max amplitude* method identifies the time instant when the IA signal reaches its maximum amplitude. However, this method may be inaccurate when multiple peaks occur due to distortion of the pressure wave or spatial averaging effects⁵⁰.
- The *min amplitude* method is similar to the previous method; however, it aims to identify the time instant when the IA signal reaches its minimum amplitude. All the techniques suggested for the maximum amplitude method could also be applied here.

⁵⁰The latter is a well-known problem in ultrasound and acoustics, where the shape of the received acoustic wave can vary depending on the sensor position relative to the emitting source, which can affect the signal frequency content [166, 167].

- The *max envelope* approach for extracting ToF involves obtaining the signal envelope maximum value by taking the Hilbert transforms of the absolute value of the recorded IA signal. The Hilbert transform is a mathematical technique used to compute the analytic signal [168], which contains information about the signal amplitude and phase. The instantaneous amplitude (or envelope) can be extracted from the analytic signal, and the ToF can be obtained from this envelope.

For all the ToF extraction methods, except for zero-crossing, an acceptable fitting method, i.e., Gaussian fitting of the pressure wave, would be useful to estimate the time instant where the signal peaks properly. However, the fitting does not come for free because the ToF extraction can be underestimated or overestimated by doing so. The accuracy of the fitting method on the BP localisation will be discussed in the results later on, but only for the experimental studies performed with the *horseshoes* setup. Furthermore, to assess the impact of fitting on the ToF estimation and, consequently, on the localisation of the BP position, all 1000 consecutive measurements acquired using the *horseshoes* setup were averaged to reduce statistical noise. Therefore, the fitting results on the ToF and BP localisation presented in this thesis will be focused on the ToF extracted with the maximum envelope approach for reasons that will be clarified in section 4.2.1.

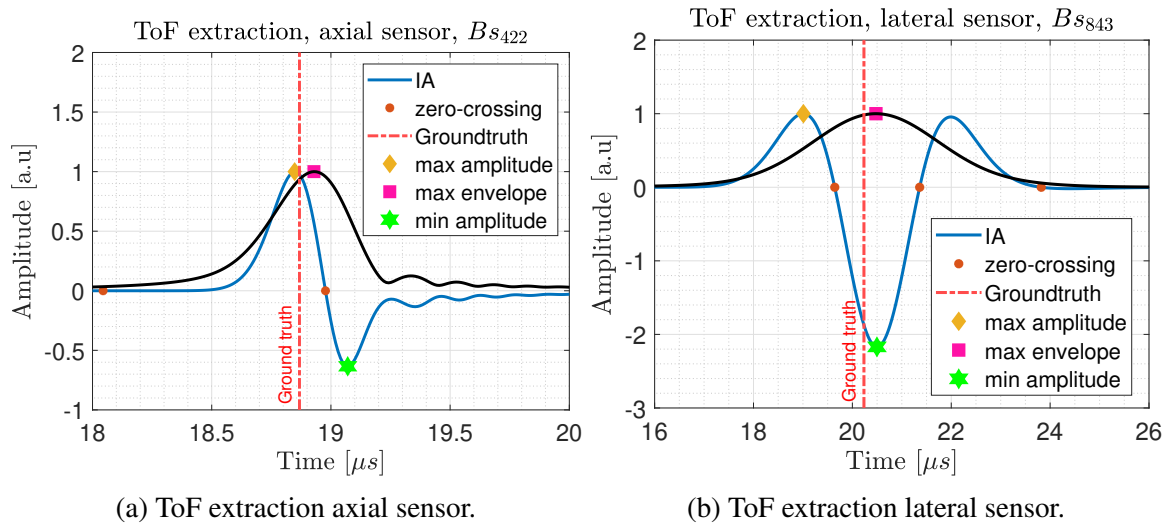


Figure 27: Simulated ionoacoustic signals and ToF extraction for different sensor positions (as introduced in the simulation setup in Fig.(19b)). The ToF was extracted using an axial sensor (a) and a lateral sensor (b). The ground truth for each sensor was established by measuring the distance from the sensor to the BP (dose maximum) defined in the simulation, which was then converted into a ToF. In the figure, the black curves represent the IA signal envelope, illustrated by the blue lines. With slight modifications, all figures were adapted from [150].

4 Results

First say to yourself what you
would be; and then do what you
have to do

Epictetus

4.1 Multilateration and Optimisation Methods Robustness

The accuracy of multilateration algorithms depends on the numerical optimisation methods used. Therefore, this section focuses on analysing the numerical optimisation algorithms and the multilateration algorithms for ideal point sources that mimic the spatial location of the BP. The performance of two numerical optimisation algorithms – the Simplex and Levenberg–Marquardt – was assessed, evaluating their sensitivity to initial guess conditions and their ability to converge to a local minimum. Following that, a comprehensive study of multilateration was conducted using ideal acoustic point sources and point sensors. The study aimed to test multilateration algorithms like TOA and TDOA with and without uncertainties. It also evaluated the accuracy and precision of localisation estimates in different conditions, examining the impact of uncertainties in both 2D and 3D scenarios.

4.1.1 Nelder-Mead Simplex vs Levenberg–Marquardt

To comprehensively analyse the multilateration results, the impact of the source location was first examined in two scenarios: when it is inside and outside the FOV. This approach identified the regions where multilateration failed and succeeded. Failure is indicated by a dark circle with magenta edges in Fig.(29a), and the regions where it succeeds are represented by a green circle with magenta edges. Subsequently, the total FR is reported based on the initial guess positions. For the first case, the influence of the initial guess on the multilateration results was assessed by localising the source with the TOA algorithm, as shown in Fig.(28). The multilateration was performed using the Simplex algorithm, as shown in Fig.(28a). The localisation was assumed to fail for localisation errors larger than 1 mm. As shown in Figs.(28a,28b), the FR for the acoustic point source located outside and inside the FOV equals 0% for the investigated scenario. Figs.(28c,28d) illustrate the FR when the acoustic point source is localised with the Levenberg algorithm. Compared to the previous case, the FR is equal to 0.22%. The results indicate that the TOA is not significantly influenced by variations in the initial guess, at least for the two cases considered.

For the second case, the influence of the initial guess on the multilateration results was assessed by localising the source with the TDOA algorithm, as shown in Fig.(29). Same as in the case for TOA, the FR was assessed for the source inside and outside the FOV. Fig.(29a) shows the FR for the multilateration optimisation performed with the Simplex algorithm. Within all the reference sensors, the dynamic reference sensor $l^{Ref,min}$ was used as an example to show the most critical initial guess positions where the multilateration fails. In these particular cases where the source is outside the FOV, the FR equals 42.42% for the source localised with TDOA and goes down to 0% when the source is located inside the FOV, as shown in Fig.(29b). On the contrary, in the case of source localisation performed using the Levenberg algorithm, the FR is 9.0% when the source is located outside the FOV, as depicted in Fig.(29c). Furthermore, when the source is located inside the FOV, the FR is 0%, as illustrated in Fig.(29d).

In summary, high FR is mostly linked to positions where the acoustic point source is outside the FOV, as demonstrated in the TDOA multilateration case. Clarification may be needed for the TOA because the FR is approximately 0% for all numerical optimisation methods, as shown in Fig.(28). This needs further validation with more statistics and initial guess positions. Notably, initial guess positions within the FOV are optimal, consistent with standard procedures for selecting the initial guess in numerical optimisation methods. Thus, choosing the centre of mass as the initial guess is commonly used. For the remainder of the thesis, the results of the multilateration are presented using the centre of mass derived from the spatial locations of the sensors as the initial guess.

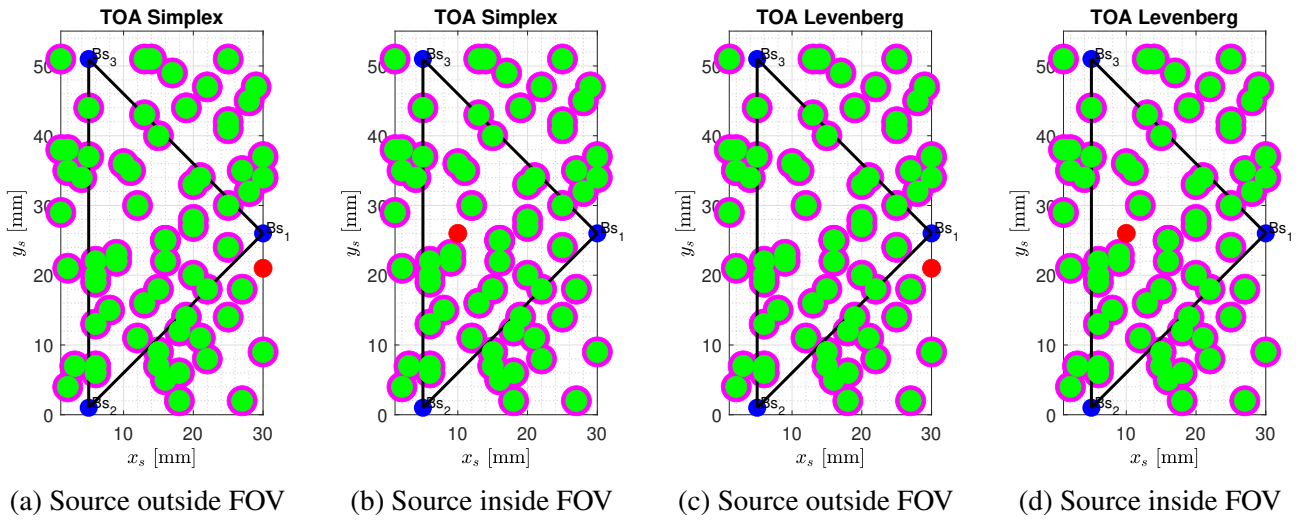


Figure 28: TOA varying the initial guess position using Simplex and Levenberg algorithms, for a total of 66 random initial guesses positions (see section 3.1.2) and 66 acoustic source positions moving in space. The red circle indicates an exemplary source position, and the blue circle indicates the point sensors. The green circles indicate the initial guess positions where the source is successfully localised (AR), which means an error below 1 mm. (a) The acoustic point source is outside the FOV and close to the sensor B_{S1} . (b) The acoustic point source is inside the FOV, and localisation is performed with the Simplex algorithm. (c) The acoustic source is outside the FOV and near B_{S1} . (d) The acoustic source is within the FOV, and localisation is done using the Levenberg algorithm

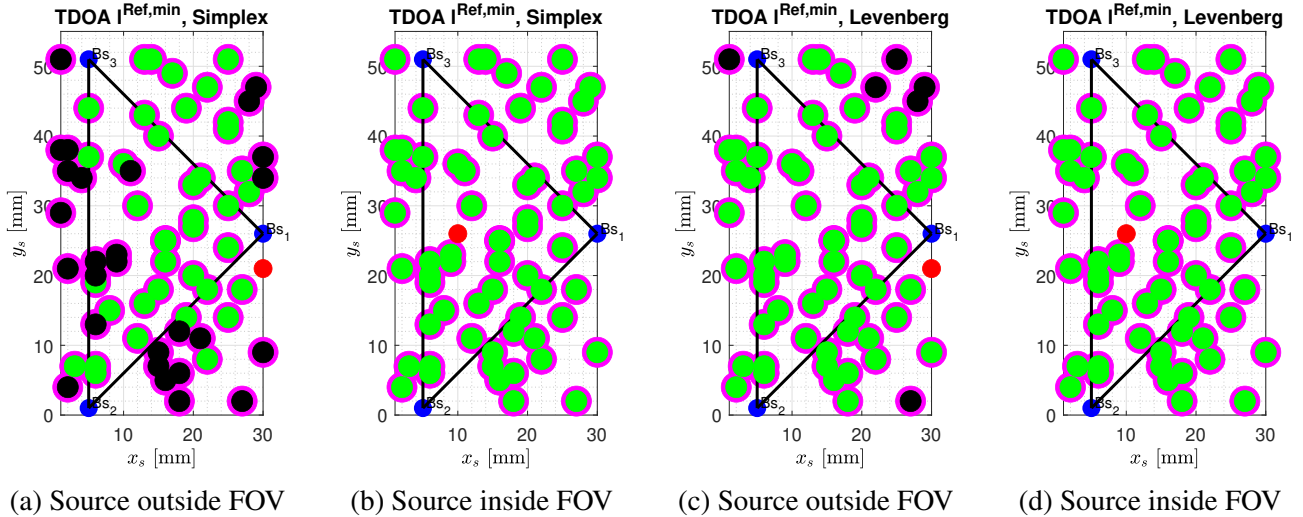


Figure 29: TDOA varying the initial guess position using Simplex and Levenberg algorithms, for a total of 66 random initial guesses positions (see section 3.1.2) and 66 acoustic source positions moving in space. The red circle indicates an exemplary source position, and the blue circle indicates the point sensors. The green circles indicate the guess positions where the source is successfully localised (AR), which means an error below 1 mm. The black circles indicate the initial guess positions where the source is not successfully localised (FR). (a) The acoustic point source is outside the FOV and close to the sensor B_{S1} . (b) The acoustic point source is inside the FOV, and localisation is performed with the Simplex algorithm. (c) The acoustic point source is outside the FOV and close to the sensor B_{S1} . (d) The acoustic point source is inside the FOV, and localisation is performed with the Levenberg algorithm.

In general, when considering the 66 source and initial guess positions, the Levenberg algorithm was less sensitive to the initial guess than the Simplex algorithm. Table(1) summarises the FR for the multilateration performed with both algorithms. For the TOA, having localised the source with the Simplex algorithm, the FR is 0% against an FR of 0.22% for the source localised with the Levenberg algorithm, indicating that the Simplex algorithm is the algorithm of choice if the source is localised uniquely with the TOA. However, when considering the TDOA, a trade-off is needed to evaluate the optimal optimisation method. For the TDOA, the FR also depends on the reference sensor. In fact, as seen in Table(1), the FRs fluctuate from a minimum of 0.55% (I^{Ref, Bs_2}) to a maximum of 1.12% (I^{Ref, Bs_1}) if the optimisation is performed with the Levenberg algorithm. On the other hand, if the optimisation is performed with Simplex, the FR fluctuates from a minimum of 4.82% (I^{Ref, Bs_1}) to a maximum of 10.76% ($I^{Ref, max}$). Furthermore, the maximum FR achieved with the Levenberg is 1.12% (I^{Ref, Bs_1}) compared to 10.76% ($I^{Ref, max}$) achieved with the Simplex algorithm.

So far, the discussion has primarily focused on the FR of 2D multilateration. The 3D multilateration studies have not been as comprehensive as the 2D. In fact, for the 3D, the FR for a source located within the FOV was 0% for both TOA and TDOA algorithms and for numerical optimisation performed with Simplex and Levenberg algorithms. Hence, it was assumed that the results for 3D multilateration are comparable to those obtained in 2D. In 3D, the magnitude of FR is expected to be higher for sources both within and outside the FOV. This is due to the increase in error output of the multilateration performed in 3D, as discussed in section 4.1.4. However, to fully conclude the FR in 3D, further detailed studies are necessary to confirm our assumptions.

The FR studies performed in 2D can be concluded with three important remarks. First, the multilateration performed with the TOA is less sensitive to the initial guess and source position than TDOA. Second, the Levenberg and Simplex algorithms yield similar results when used with TOA multilateration. However, for TDOA multilateration, the Levenberg algorithm consistently outperforms the Simplex algorithm, see Table(1). For this reason, the Levenberg algorithm will be preferred because it gives the best FR compromises for both TOA and TDOA localisation approaches. Furthermore, all the results reported in the following sections will be based on the Levenberg algorithm. Lastly, the error increases drastically when the Simplex optimisation does not converge to a local minimum. The source localisation outputs unrealistic values, with errors in the kilometre range. For more detail on the localisation error, see appendix D.

Multilateration Methods	Reference Sensor	$FR^{Levenberg}$	$FR^{Simplex}$
TDOA	Bs_1	1.12 %	4.82 %
	Bs_2	0.55 %	10.10 %
	Bs_3	0.80 %	6.31 %
	$I^{Ref, max}$	1.05 %	10.76 %
	$I^{Ref, min}$	0.57 %	5.48 %
TOA	<i>none</i>	0.22 %	0.00 %

Table 1: FR of TOA and TDOA for optimisations performed with the Simplex and Levenberg algorithms for the considered arrangement of sensors and ideal sources.

4.1.2 Multilateration Robustness Assessment in Ideal 2D Scenarios

Fig.(30) illustrates the cases considered for the 2D multilateration without uncertainties⁵¹. The error in position was initially assessed for all the source positions. Afterwards, the error in position was assessed exclusively for the source located inside the FOV (depicted as black triangle in Fig.(30)). Starting with the source located everywhere, the error obtained with TOA is nearly unaffected by variations in the source location, resulting in ϵ_{xy} equal to $0.81 \pm 0.46 \mu\text{m}$, which reduces to $0.74 \pm 0.59 \mu\text{m}$ for sources located inside the FOV. In synthesis, for the TOA, the error in position increases for the sources located outside the FOV. The TOA's localisation error is illustrated in Fig.(30a).

When considering the TDOA executed with the static reference sensors, the best multilateration performance was achieved with the BS_1 . In fact, without considering the FOV, the obtained error ϵ_{xy} equals to $2.00 \pm 1.80 \mu\text{m}$, which decreases to $0.78 \pm 0.05 \mu\text{m}$ when the source is located inside the FOV. Furthermore, the error increases for the sources located in proximity to the reference sensors, as shown in Fig.(30b) to Fig.(30d). For the multilateration performed with the second set of reference sensors (i.e., dynamic sensor $l^{Ref,max}$), the achieved error in localisation is $1.90 \pm 1.50 \mu\text{m}$ without considering the FOV. The error in localisation decreases to $0.84 \pm 0.57 \mu\text{m}$ considering the sources inside the FOV. The multilateration performed using reference sensors BS_1 and $l^{Ref,max}$ yielded a similar localisation error when the FOV was not considered. For the sources located inside the FOV, the reference sensor BS_1 gives a lower localisation error, as reported in Table(2). For the TOA and TDOA, all the multilateration results are reported and summarised in Table(2).

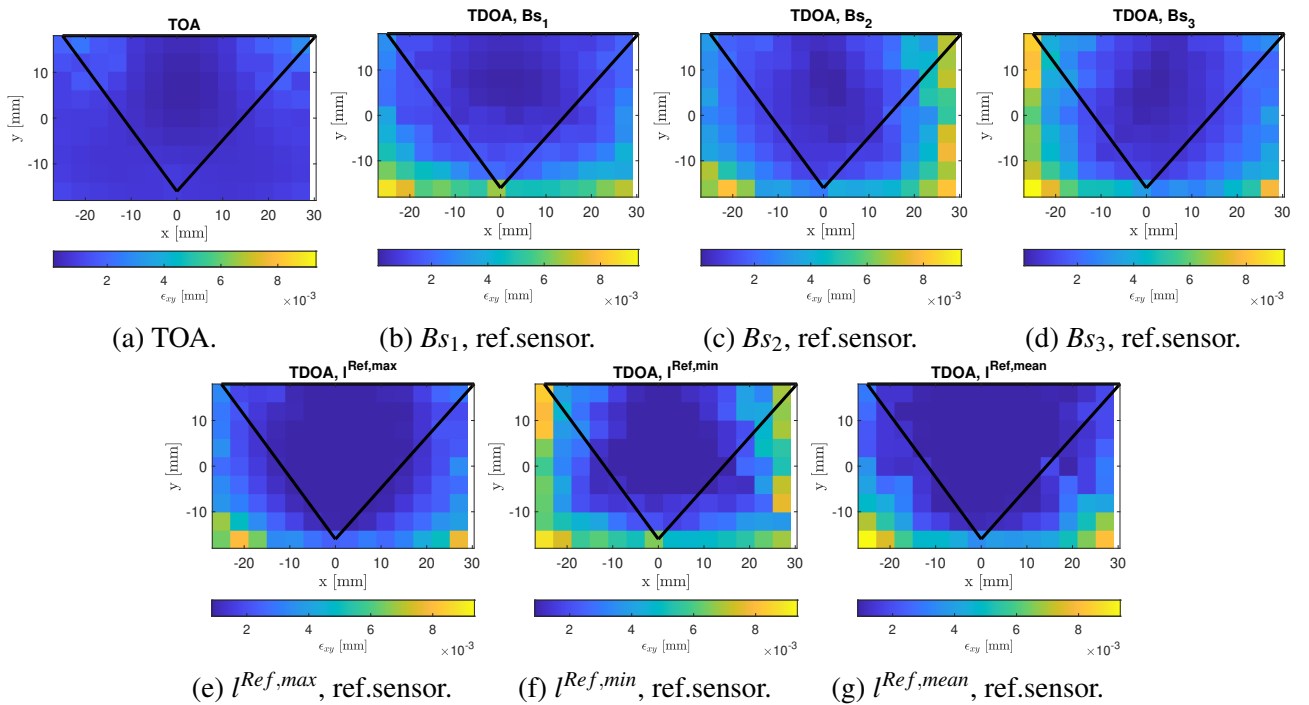


Figure 30: Error in 2D Multilateration of ideal point sources without uncertainties: (a) TOA and TDOA with (b) BS_1 , (c) BS_2 , (d) BS_3 as static reference sensors, and (e) $l^{Ref,max}$, (f) $l^{Ref,min}$, and (g) $l^{Ref,mean}$ as dynamic reference sensors. In all figures, the black triangle denotes the FOV. With slight changes, all the figures reported here were extracted from [150].

⁵¹The sensor configurations in Figs. (30, 29d) differ. For setup details, check sections 3.1.2 and 3.1.3.

In conclusion, TOA and TDOA performed similarly for sources located inside the FOV when there are no uncertainties on the geometrical ToF estimation, as illustrated in Fig.(31). Moreover, from Fig.(31), based on the distribution of the error inside the FOV for both multilateration algorithms, it can be concluded that TOA and TDOA are around equal. However, the results also demonstrate that TOA is less geometry dependent compared to TDOA (see the outlier errors for the TDOA in Figs.(31b,31c and 31d)).

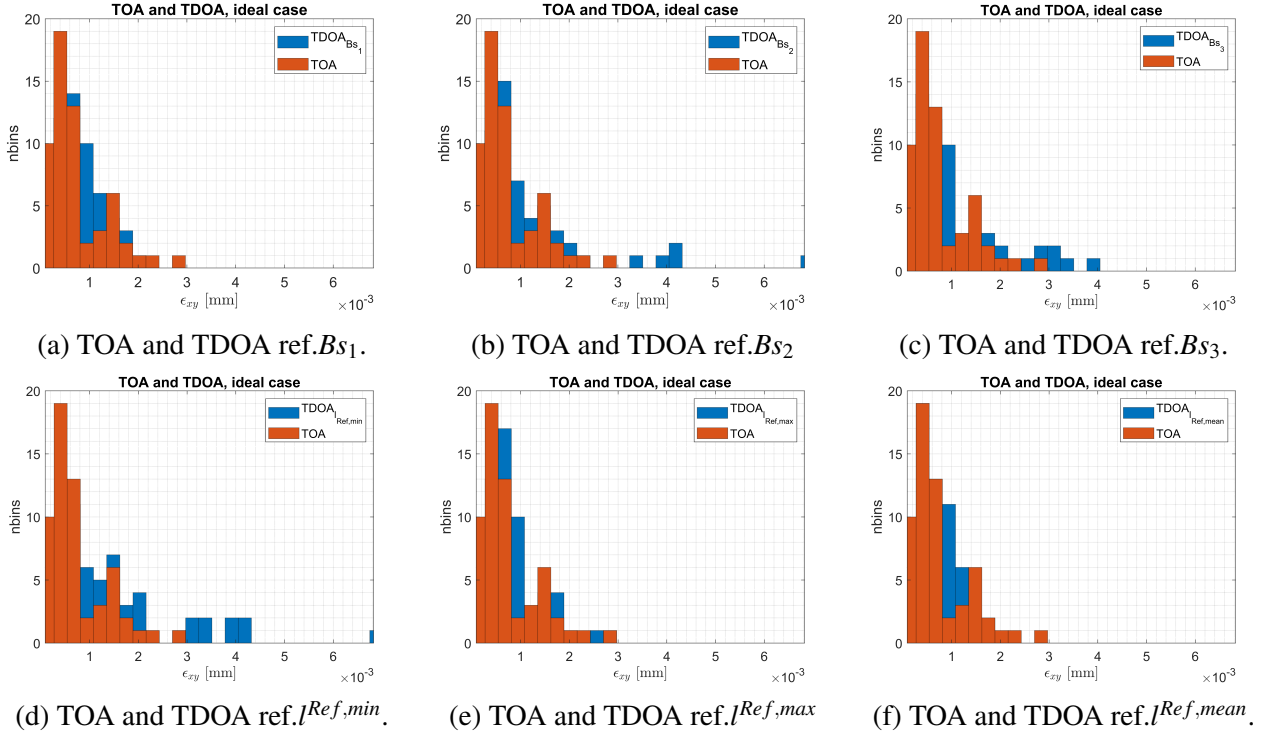


Figure 31: Error distribution for ideal point source localisation performed with TOA and TDOA without uncertainties. For TDOA, the ideal source was localised with static reference and dynamic reference sensors. (a,b,c) Comparison between multilateration performed with TOA and TDOA (static reference sensors Bs_1 , Bs_2 and Bs_3). (d,e,f) Comparison between multilateration performed with TOA and TDOA (dynamic reference sensor $l^{Ref,min}$, $l^{Ref,max}$ and $l^{Ref,mean}$). All the results reported here are for the sources located inside the FOV.

Multilateration Methods	Reference Sensor	$\mu_{\epsilon_{xy}}$ [mm]	$\mu_{\epsilon_{xy}}^{FOV}$ [mm]	$\sigma_{\epsilon_{xy}}$ [mm]	$\sigma_{\epsilon_{xy}}^{FOV}$ [mm]
TDOA	Bs_1	2.0×10^{-3}	7.8×10^{-4}	1.8×10^{-3}	4.8×10^{-5}
	Bs_2	2.4×10^{-3}	1.2×10^{-3}	2.0×10^{-3}	1.2×10^{-3}
	Bs_3	2.3×10^{-3}	1.1×10^{-3}	2.1×10^{-3}	8.9×10^{-4}
	$l^{Ref,max}$	1.9×10^{-3}	8.4×10^{-4}	1.5×10^{-3}	5.7×10^{-4}
	$l^{Ref,min}$	3.0×10^{-3}	1.5×10^{-3}	2.3×10^{-3}	1.3×10^{-3}
	$l^{Ref,mean}$	2.0×10^{-3}	6.9×10^{-3}	1.9×10^{-3}	3.8×10^{-3}
TOA	<i>none</i>	8.1×10^{-4}	7.4×10^{-4}	4.6×10^{-4}	5.9×10^{-4}

Table 2: Overview and comparison of 2D multilateration performance using TOA and TDOA in the absence of uncertainties. TDOA multilateration was conducted with various reference sensors, including static (Bs_1 , Bs_2 , Bs_3) and dynamic ($l^{Ref,max}$, $l^{Ref,min}$, $l^{Ref,mean}$).

Random and systematic uncertainties were evaluated separately before having both to better understand their individual contribution. To simplify and make the analysis more concise, the thesis will focus exclusively on localising sources inside the FOV using both multilateration algorithms. Additionally, when localising sources with TDOA, the reference sensor B_{S_1} will be preferred, as it results in the lowest error in position estimation.

When modelling random uncertainties, the source localisation is more accurate at the centre of the sensor network, independently of the method utilised. However, for the multilateration performed with TOA, the error progressively increases inside the FOV from the centre. The average RMSE is 1.60 mm, reaching 3.21 mm at the outermost edges, leading to an average RMSE of 2.19 ± 0.41 mm, for the range of uncertainty modelled as shown in Fig.(32a). The positions where the RMSE increases are correlated to the positions where the source is located at the edge of the FOV.

On the other hand, when modelling random uncertainties for the TDOA, the RMSE goes from a minimum of 1.61 mm to a steep increase near B_{S_2} and B_{S_3} , going up to 5.52 mm for the acoustic point source located close to the B_{S_2} sensor. Hence, the mean root mean square error and its standard deviation ($\mu_{RMSE}^{FOV}, \sigma_{RMSE}^{FOV}$) were found to be 2.32 ± 0.66 mm, as illustrated in Fig.(32b). The results for both algorithms are summarised in Table(3).

Through a comparison of Fig.(32a) and Fig.(32b), the plots show a higher degree of homogeneity on the error distribution for TOA compared to TDOA. This observation indicates the superior performance of TOA in the presence of random uncertainties. Furthermore, the TDOA's higher dependency on the geometry can be seen from the error that increases on the edge of the FOV.

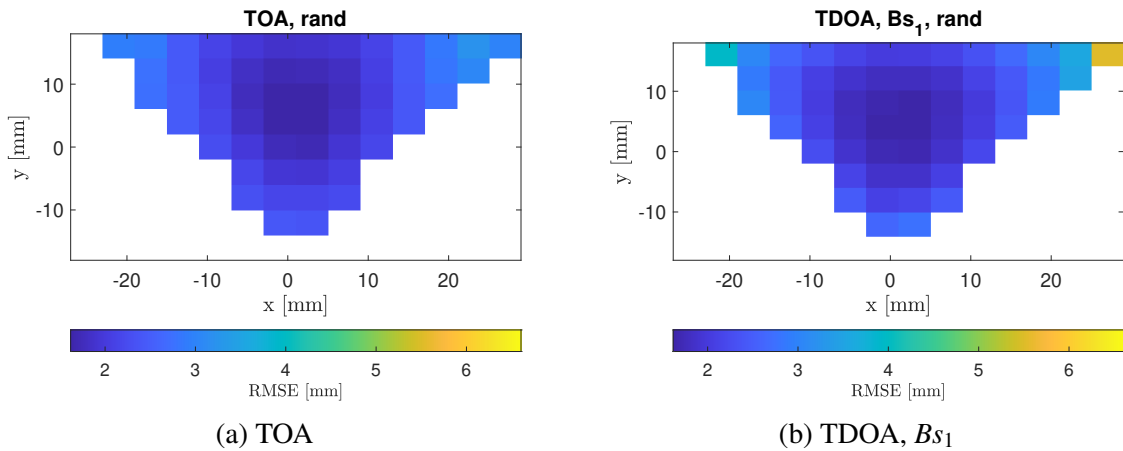


Figure 32: Error on the 2D Multilateration of ideal point sources located in the sensor array FOV in the presence of random uncertainties, $\mathcal{N}(\boldsymbol{\mu}, \boldsymbol{\Sigma})$ with mean zero and a standard deviation (σ_{random}) equal to 5% of the absolute ToF. (a) TOA multilateration and (b) TDOA multilateration with B_{S_1} as a reference. Figure extracted from [150]

Multilateration Methods	Reference Sensor	μ_{RMSE}^{FOV} [mm]	σ_{RMSE}^{FOV} [mm]
TDOA	B_{S_1}	2.32	0.66
TOA	<i>none</i>	2.19	0.41

Table 3: Comparison of 2D multilateration between TOA and TDOA in the presence of random uncertainties, $\mathcal{N}(\boldsymbol{\mu}, \boldsymbol{\Sigma})$, with a mean of zero and a standard deviation (σ_{random}) set to 5% of the absolute ToF.

The different performance between TOA and TDOA in the presence of random uncertainties can be explained mathematically from the cost function of both localisation algorithms. Starting with TDOA and considering its cost function as described below:

$$\min_{x_s, y_s} f_{TDOA}(x_s, y_s) = \min_{x_s, y_s} \sum_{i=1}^n \sum_{ref \neq i} \left(v_s \cdot ToF_i - \|d_i\|_2 - v_s \cdot ToF_{ref} + \|d_{ref}\|_2 \right)^2 \quad (4.1)$$

The cost function in eq.(4.1) can be re-written introducing the two variables Υ_i and Υ_{ref} , which accounts for random uncertainties, for the ToF estimated from sensor Bs_1 to Bs_n and for the ToF estimated with the reference sensor Bs_{ref} . So, the new formulation of the cost function follows:

$$\min_{x_s, y_s} f_{TDOA}(x_s, y_s) = \min_{x_s, y_s} \sum_{i=1}^n \sum_{ref \neq i} \left(v_s \cdot \{ (ToF_i - ToF_{ref}) + (\Upsilon_i - \Upsilon_{ref}) \} - \|d_i\|_2 + \|d_{ref}\|_2 \right)^2 \quad (4.2)$$

There was no correlation between random uncertainties of individual sensors ($\Upsilon_i \neq \Upsilon_{ref}$). Therefore, for the TDOA algorithm, the total error is proportional to the error on each sensor plus the error on the reference sensor⁵². Hence, poor performance is observed when modelling random uncertainties.

On the other hand, when considering the TOA and by re-writing its cost function as:

$$\min_{x_s, y_s} f_{TOA}(x_s, y_s) = \min_{x_s, y_s} \sum_{i=1}^n \left(v_s \cdot ToF_i - \|d_i\|_2 \right)^2 \quad (4.3)$$

Again, considering the random uncertainties introduced on the ToF extracted from sensors Bs_1 to sensor Bs_n as Υ_i , the TOA cost function can be further expanded as :

$$\min_{x_s, y_s} f_{TOA}(x_s, y_s) = \min_{x_s, y_s} \sum_{i=1}^n \left(v_s \cdot (ToF_i + \Upsilon_i) - \|d_i\|_2 \right)^2 \quad (4.4)$$

From eq.(4.3) it can be seen that only Υ_i contributes on the uncertainties introduced on the ToF. Indeed, the performance of the TOA algorithm is attributed to the fact that the total error in TOA is solely influenced by the error associated with each sensor. Consequently, the TOA algorithm demonstrates higher performance in scenarios involving random uncertainties than TDOA.

⁵² $\Upsilon_{tot} = \sum_{i=1}^n \sum_{ref \neq i} \sqrt{\Upsilon_i^2 + \Upsilon_{ref}^2}$.

Fig.(33) illustrates the RMSE for multilateration with systematic uncertainties using the TOA and TDOA algorithms. When localising the source with TOA, the $RMSE^{FOV}$ can increase up to 2.14 mm for sources located at the edge positions. The mean root mean square error and its standard deviation equal 1.03 ± 0.52 mm. The $RMSE^{FOV}$ decreases to 0.12 mm for the sources at the centre. The systematic uncertainties cancel out for the multilateration performed with TDOA as shown in Fig.(33b); in fact, the RMSE equals $0.78 \pm 0.05 \mu\text{m}$. The RMSE obtained in the presence of systematic uncertainties is equal to the error in multilateration without modelling uncertainties, with a value of $0.78 \pm 0.05 \mu\text{m}$ (see the TDOA results for B_{S_1} reported in Table(2)).

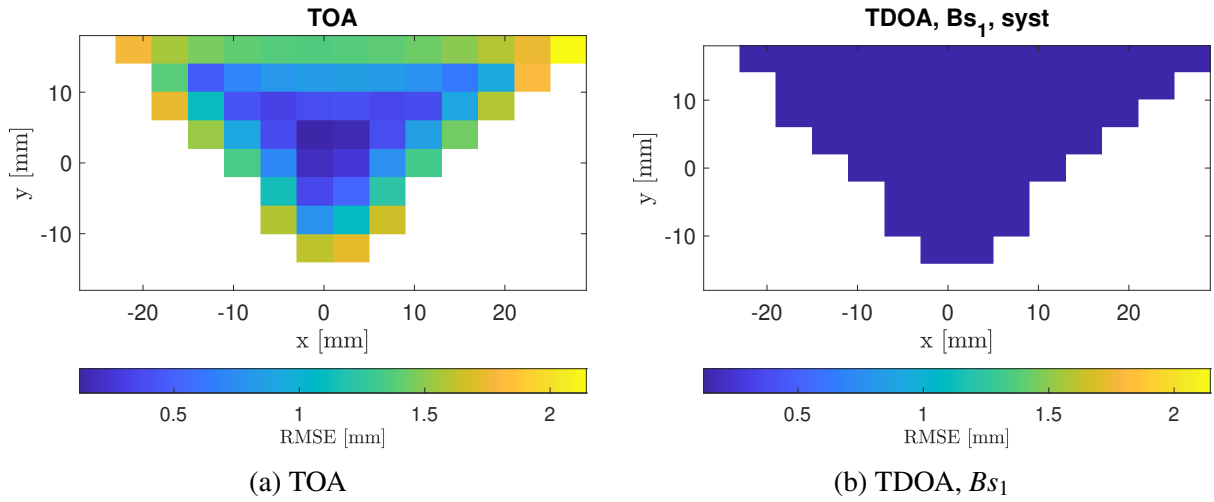


Figure 33: Error on the 2D Multilateration of ideal point sources located in the sensor array FOV in the presence of systematic uncertainties, $\mathcal{N}(\boldsymbol{\mu}, \boldsymbol{\Sigma})$, with mean zero and a standard deviation ($\sigma_{systematic}$) equal to $1 \mu\text{s}$. (a) TOA multilateration, and (b) TDOA multilateration with B_{S_1} as a reference. Figure extracted from [150].

Multilateration Methods	Reference Sensor	μ_{RMSE}^{FOV} [mm]	σ_{RMSE}^{FOV} [mm]
TDOA	B_{S_1}	7.8×10^{-4}	4.8×10^{-5}
TOA	<i>none</i>	1.03	0.52

Table 4: 2D Multilateration comparison between TOA and TDOA in the presence of systematic uncertainties, $\mathcal{N}(\boldsymbol{\mu}, \boldsymbol{\Sigma})$, with mean zero and a standard deviation ($\sigma_{systematic}$) equal to $1 \mu\text{s}$.

The cancellation of systematic uncertainties in multilateration performed with TDOA can be mathematically explained. This can be achieved by rewriting the cost function expressed in eq.(4.5) by assuming that there is a correlation among the systematic uncertainties considered for every individual sensor, which implies $\Upsilon_i = \Upsilon_{ref}$. That implies that the localisation of the acoustic point source relies exclusively on the ToF extraction method. As a result, the new cost function can be simplified as described in eq.(4.6).

$$\min_{x_s, y_s} f_{TDOA}(x_s, y_s) = \min_{x_s, y_s} \sum_{i=1}^n \sum_{ref \neq i} \left(v_s \cdot \{ (ToF_i + \Upsilon_i) - (ToF_{ref} + \Upsilon_{ref}) \} - \|d_i\|_2 + \|d_{ref}\|_2 \right)^2 \quad (4.5)$$

$$\min_{x_s, y_s} f_{TDOA}(x_s, y_s) = \min_{x_s, y_s} \sum_{i=1}^n \sum_{ref \neq i} \left(v_s \cdot (ToF_i - ToF_{ref}) - \|d_i\|_2 + \|d_{ref}\|_2 \right)^2 \quad (4.6)$$

The same analogy used to explain the TDOA can be made for the TOA by re-writing its cost function as:

$$\min_{x_s, y_s} f_{TOA}(x_s, y_s) = \min_{x_s, y_s} \sum_{i=1}^n \left(v_s \cdot ToF_i - \|d_i\|_2 \right)^2 \quad (4.7)$$

Again, considering the systematic uncertainties introduced on the ToF extracted from sensors B_{s_1} to sensor B_{s_n} as Υ_i , the TOA cost function can be further expanded as :

$$\min_{x_s, y_s} f_{TOA}(x_s, y_s) = \min_{x_s, y_s} \sum_{i=1}^n \left(v_s \cdot (ToF_i + \Upsilon_i) - \|d_i\|_2 \right)^2 \quad (4.8)$$

After analysing a case where the TDOA algorithm is applied with perfect correlation among the uncertainties of all sensors, it can be concluded that the systematic uncertainties are eliminated, as demonstrated in equation (4.6). On the opposite, the TOA algorithm is sensitive to systematic uncertainties, as demonstrated in eq.(4.8). These results are also valid for the multilateration performed in 3D. A more detailed discussion of the 3D multilateration, including the results for TOA and TDOA algorithms, will be presented in section 4.1.3.

To understand the robustness of each localisation algorithm in the presence of different types of uncertainties, we modelled random and systematic uncertainties separately as a starting point. In clinical beam facilities, both uncertainties are expected to be correlated to the IA signals, and it is crucial to study the impact of both uncertainties modelled simultaneously. The previous sections found that the TOA algorithm is less sensitive to random uncertainties, while the TDOA algorithm is not sensitive to systematic uncertainties. To examine the effect of random and systematic uncertainties on the localisation results, we performed multilateration with both algorithms. Fig.(34) presents the results of multilateration in the presence of random and systematic uncertainties.

For the multilateration performed with the TOA algorithm, the error gradually increases inside the FOV as the source moves from the centre towards the edges. The RMSE equals 1.63 mm at the centre and 4.03 mm at the edges, leading to an average RMSE of 2.68 ± 0.63 mm for the range of uncertainty modelled, as shown in Fig.(34a). The higher RMSE is correlated to the positions where the source is located at the edge of the FOV. When the uncertainties were modelled for the TDOA algorithm (B_{s_1} as reference sensor), the error rapidly increased near B_{s_2} and B_{s_3} , going up to 5.52 mm for the acoustic point source located close to the B_{s_2} sensor. The minimum RMSE was achieved for all the sources located in the centre of the FOV and was 1.61 mm. The mean root mean square error and its standard deviation were found to be 2.32 ± 0.66 mm, as illustrated in Fig.(34b). All source localisations are listed and summarised in Table(5).

To summarise, for the range of random and systematic uncertainties investigated, TDOA is more robust for all the acoustic source points in the centre of the FOV. However, it is less robust for sources located at the FOV edges than the TOA. TDOA is more sensitive to geometry, i.e., sensor arrangement. As a consequence, it might result in higher RMSE and standard deviation compared to the TOA.

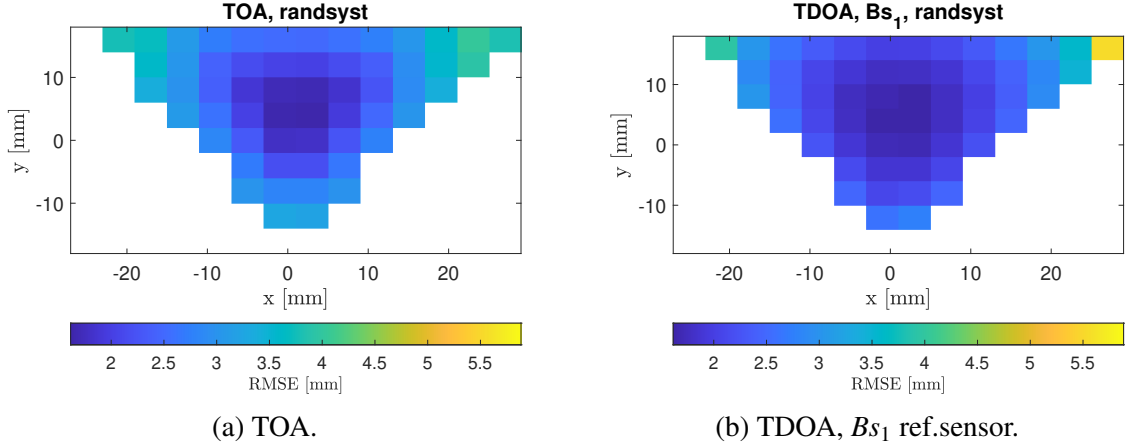


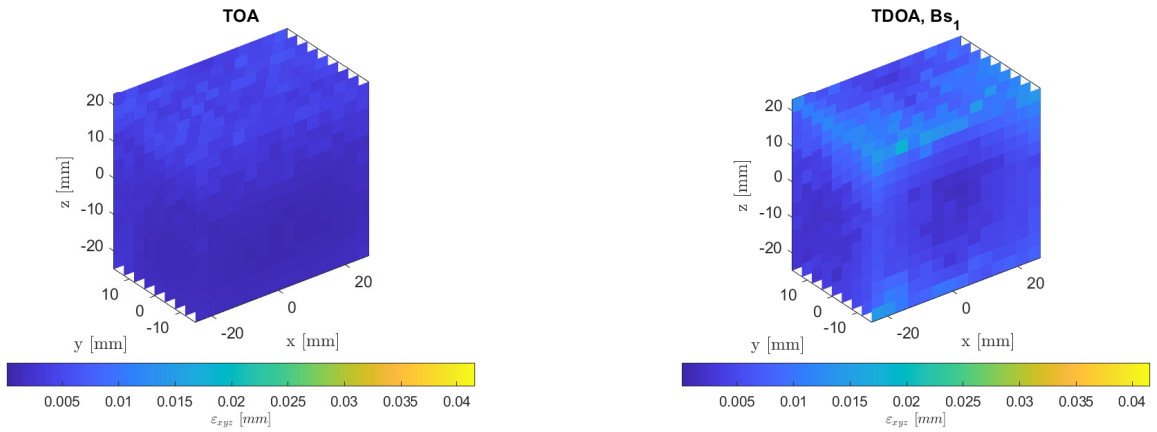
Figure 34: Error on the 2D Multilateration of ideal point sources located in the sensor array FOV in presence of random and systematic uncertainties, $\mathcal{N}(\boldsymbol{\mu}, \boldsymbol{\Sigma})$, with mean zero and a standard deviations σ_{random} equal to 5 % of the absolute ToF, and a $\sigma_{systematic}$ equal to 1 μs . using (a) TOA multilateration and (b) TDOA multilateration with B_{S_1} as a reference. Figure extracted from [150].

Multilateration Methods	Reference Sensor	μ_{RMSE}^{FOV} [mm]	σ_{RMSE}^{FOV} [mm]
TDOA	B_{S_1}	2.32	0.66
TOA	<i>none</i>	2.68	0.63

Table 5: 2D Multilateration comparison between TOA and TDOA in the presence of random and systematic uncertainties, $\mathcal{N}(\boldsymbol{\mu}, \boldsymbol{\Sigma})$, with mean zero and a standard deviations σ_{random} equal to 5 % of the absolute ToF, and a $\sigma_{systematic}$ equal to 1 μs , and v_s equal to 1500 m/s.

4.1.3 Multilateration Robustness Assessment in Ideal 3D Scenarios

Fig.(35) depicts the results of 3D multilateration. The results obtained without uncertainties are similar to the 2D multilateration without uncertainties. In fact, starting with TOA and considering the source inside the FOV, the obtained error and standard deviation were equal to $0.78 \pm 0.58 \mu\text{m}$. There is no significant change in the error magnitude for TOA. This makes the localisation performed in 3D comparable to the one performed in 2D. On the contrary, when localising the source with the TDOA having B_{s_1} as the reference sensor, the error and the standard deviation was equal to $1.00 \pm 0.62 \mu\text{m}$. The summary of the results between both multilateration algorithms is reported in Table(6).



(a) 3D TOA ideal scenario.

(b) 3D TDOA ideal scenario.

Figure 35: RMSE of the multilateration in 3D ideal scenarios depending on the source location, for (a) TOA and (b) TDOA using B_{s_1} as a reference sensor.

Multilateration Methods	Reference Sensor	$\mu_{\epsilon_{xyz}}^{FOV}$ [mm]	$\sigma_{\epsilon_{xyz}}^{FOV}$ [mm]
TDOA	B_{s_1}	1.0×10^{-3}	6.2×10^{-4}
TOA	<i>none</i>	7.8×10^{-4}	5.8×10^{-4}

Table 6: Summary of the errors obtained using 3D multilateration without modelling uncertainties.

Fig.(36) illustrates the RMSE output of localisation using multilateration in the presence of random uncertainties. When localising the source using TOA, the mean root mean square error inside the FOV and its standard deviation are 3.14 ± 0.42 mm, as shown in Fig.(36a). The minimum RMSE obtained is 2.42 mm, corresponding to source positions located in the centre of the FOV. However, when moving to the edge of the FOV, the RMSE increases to 4.49 mm. When localising the source with TDOA as shown in Fig.(36b), the mean root mean square error inside the FOV and its standard deviation (RMSE^{FOV}, $\sigma_{\epsilon_{xyz}}^{FOV}$) equal 3.35 ± 0.74 mm. The minimum RMSE of 2.45 mm is achieved for the sources in the centre of the FOV. Moreover, the RMSE increases for sources located on the edge of the FOV up to a maximum of 8.38 mm. Similar to the multilateration performed in 2D, the TOA performs better than TDOA in the presence of random uncertainties.

Fig.(37) shows the RMSE for the multilateration performed in 3D in the presence of systematic uncertainties. For the TOA algorithm, the RMSE showed a minimum of 0.21 mm, reaching a maximum

of 2.34 mm for sources located on the edge of the FOV. For all the sources located inside the FOV, the mean root mean square error and the standard deviation ($\text{RMSE}^{FOV}, \sigma^{FOV}$) equal 1.42 ± 0.41 mm, as shown in Fig.(37a) and summarised in Table(8). For the multilateration performed with TDOA, as shown in Fig.(37b), the RMSE reduces for all the source positions having the mean root mean square error and its standard deviation of 1.00 ± 0.62 μm , as summarised in Table(8).

Fig.(38) illustrates the multilateration performed in 3D with both random and systematic uncertainties. Starting with the TOA algorithm, the mean root mean square error inside the FOV and its standard deviation are equal to 3.74 ± 0.54 mm, as shown in Fig.(38a). The minimum mean square error equals 2.58 mm for the sources in the centre of the FOV. When moving outside the centre of the FOV, the mean root mean square error increases to 5.38 mm. When localising the source position with TDOA, the mean error and standard deviation equal 3.35 ± 0.74 mm, as shown in Fig.(38b). The minimum RMSE equals 2.47 mm for the source in the centre of the FOV, increasing to 8.37 mm when moving towards the edges of the FOV. It is important to note that the results obtained for the TDOA in the presence of random and systematic uncertainties are similar to the ones obtained when only random uncertainties are modelled, as systematic errors cancel out. For both algorithms, the results reported in 3D agree with those presented for the multilateration in 2D. They confirm that in the presence of random and systematic uncertainties, TDOA results are more robust than TOA, especially for sources inside the FOV due to the lower minimum RMSE (2.47 mm for TDOA, compared to 2.58 mm for TOA). However, they also exhibit a stronger dependency on the sensor arrangement due to the higher σ^{FOV} . All the results for both algorithms considering the source inside the FOV are reported in Table(9).

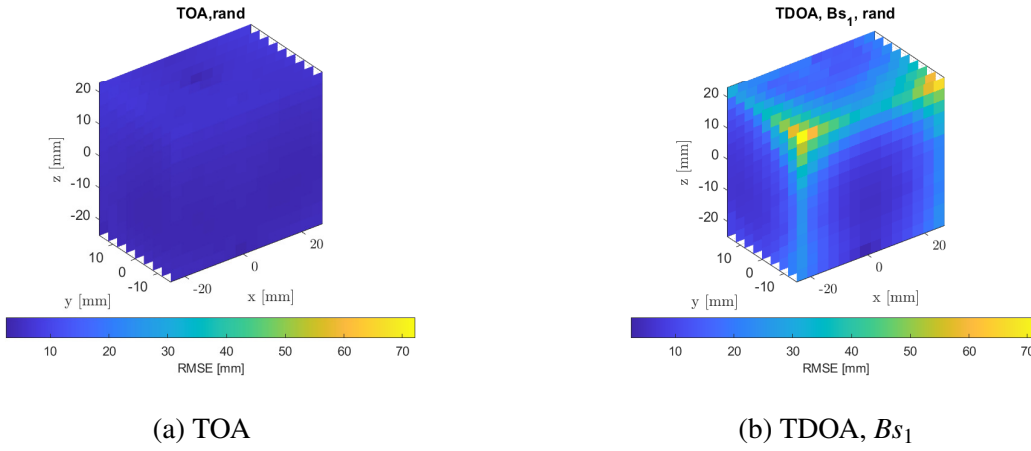


Figure 36: RMSE of the multilateration in 3D depending on the source location and in the presence of random uncertainties, $\mathcal{N}(\boldsymbol{\mu}, \boldsymbol{\Sigma})$, with mean zero and a standard deviation (σ_{random}) equal to 5 % of the absolute ToF. (a) TOA multilateration and (b) TDOA multilateration using B_{s_1} as a reference sensor. Figure extracted from [150].

Multilateration Methods	Reference Sensor	μ_{RMSE}^{FOV} [mm]	σ_{RMSE}^{FOV} [mm]
TDOA	B_{s_1}	3.35	0.74
TOA	<i>none</i>	3.14	0.42

Table 7: 3D Multilateration comparison between TOA and TDOA in the presence of random uncertainties, $\mathcal{N}(\boldsymbol{\mu}, \boldsymbol{\Sigma})$, with mean zero and a standard deviation (σ_{random}) equal to 5 % of the absolute ToF, and v_s equal to 1500 m/s.

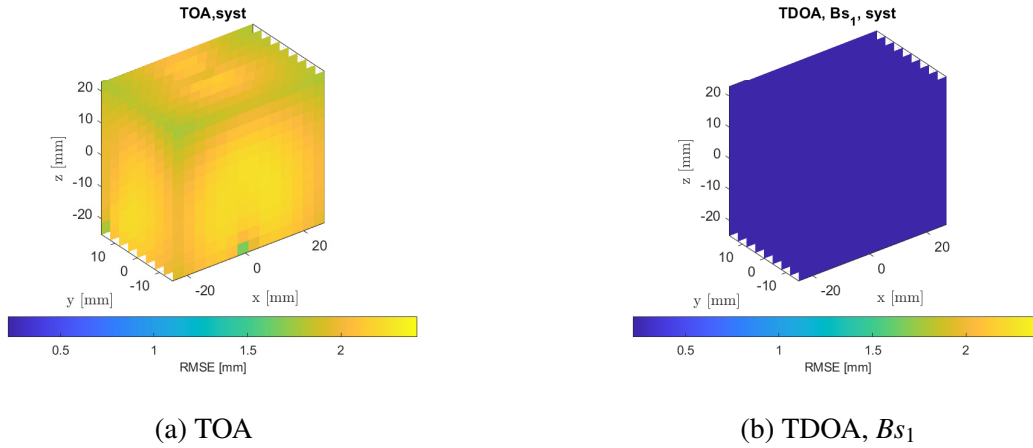


Figure 37: RMSE of the multilateration in 3D depending on the source location and in the presence of systematic uncertainties, $\mathcal{N}(\boldsymbol{\mu}, \boldsymbol{\Sigma})$, with mean zero and a standard deviation ($\sigma_{systematic}$) equal to $1 \mu s$. (a) TOA multilateration and (b) TDOA multilateration using B_{S_1} as a reference sensor. Figure extracted from [150]. Figure extracted from [150].

Multilateration Methods	Reference Sensor	μ_{RMSE}^{FOV} [mm]	σ_{RMSE}^{FOV} [mm]
TDOA	B_{S_1}	1.0×10^{-3}	6.2×10^{-4}
TOA	<i>none</i>	1.42	0.41

Table 8: 3D Multilateration comparison between TOA and TDOA in the presence of systematic uncertainties, $\mathcal{N}(\boldsymbol{\mu}, \boldsymbol{\Sigma})$, with mean zero and a standard deviation ($\sigma_{systematic}$) equal to $1 \mu s$, and v_s equal to 1500 m/s.

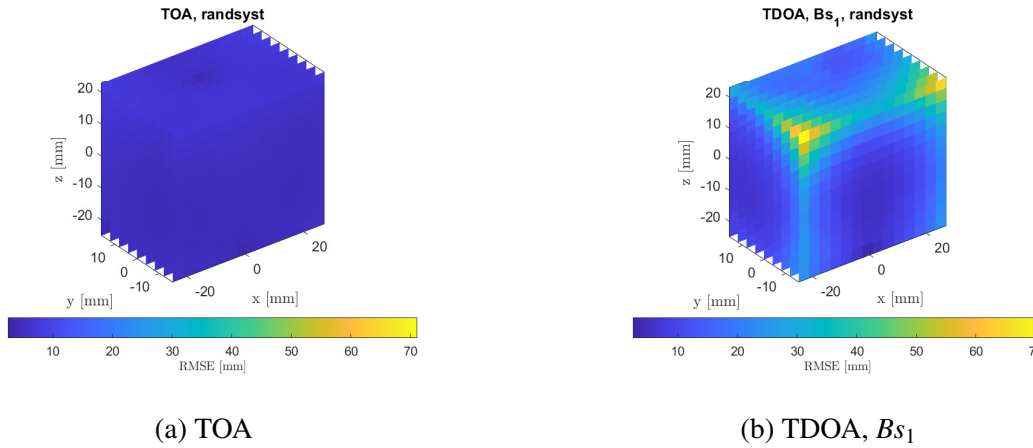


Figure 38: RMSE of the multilateration in 3D depending on the source location and in presence of random and systematic uncertainties, $\mathcal{N}(\boldsymbol{\mu}, \boldsymbol{\Sigma})$, with mean zero and a standard deviations σ_{random} equal to 5 % of the absolute ToF, and a $\sigma_{systematic}$ equal to $1 \mu s$. (a) TOA multilateration and (b) TDOA multilateration with B_{S_1} as a reference. Figure extracted from [150].

Multilateration Methods	Reference Sensor	μ_{RMSE}^{FOV} [mm]	σ_{RMSE}^{FOV} [mm]
TDOA	B_{S_1}	3.35	0.74
TOA	<i>none</i>	3.74	0.54

Table 9: 3D Multilateration comparison between TOA and TDOA in the presence of random and systematic uncertainties, $\mathcal{N}(\boldsymbol{\mu}, \boldsymbol{\Sigma})$, with mean zero and a standard deviations σ_{random} equal to 5 % of the absolute ToF and $\sigma_{systematic}$ equal to $1 \mu s$, and v_s equal to 1500 m/s.

4.1.4 Comparison of 2D and 3D Multilateration in Ideal Scenarios

For compactness, the comparison between multilateration in 2D and 3D has been performed only for the algorithm's localisation in the presence of random and systematic uncertainties. It is important to stress that, in multilateration, the source localisation accuracy can be affected by various factors, such as the geometry of the sensor network, sensor location, the number of sensors used for the localisation, and ToF estimation. For 3D multilateration using TOA, adding an extra sensor (B_{S_4}) does not always improve accuracy, especially with suboptimal sensor arrangement. However, a fourth sensor can reduce ambiguity in localisation, even though the multilateration using TOA works with just three sensors. In contrast, TDOA localisation in 3D requires four sensors and optimal arrangement. Additionally, 3D multilateration may be more computationally complex than 2D, which impacts its suitability for real-time applications.

Fig.(39) illustrates the comparison in performance of 2D and 3D multilateration for localising sources in the same plane, defined by B_{S_1} , B_{S_2} , and B_{S_3} , and limited to the sources within the sensor FOV. A minimum of three sensors is required for multilateration executed in 2D. For the 3D multilateration, at least four sensors are required. Therefore, an additional sensor (B_{S_4}) was used for 3D multilateration, resulting in higher localisation complexity as 3D multilateration is more demanding than 2D. In concrete, when performing the multilateration with the TOA algorithm, the mean root mean square error and standard deviation increased from 2.68 ± 0.63 mm in 2D to 4.03 ± 0.33 mm in 3D. Correspondingly, the mean root mean square error for the TDOA algorithm increased from 2.32 ± 0.66 mm in 2D to 3.86 ± 0.86 mm in 3D. The performance of the multilateration is better in 2D compared to the multilateration performed in 3D. For the latter, the increase in the localisation error is more likely because the multilateration is being performed in 3D (i.e., more planes to cover). The summary of the comparison between TDOA performed in 2D and 3D are reported in Table(10).

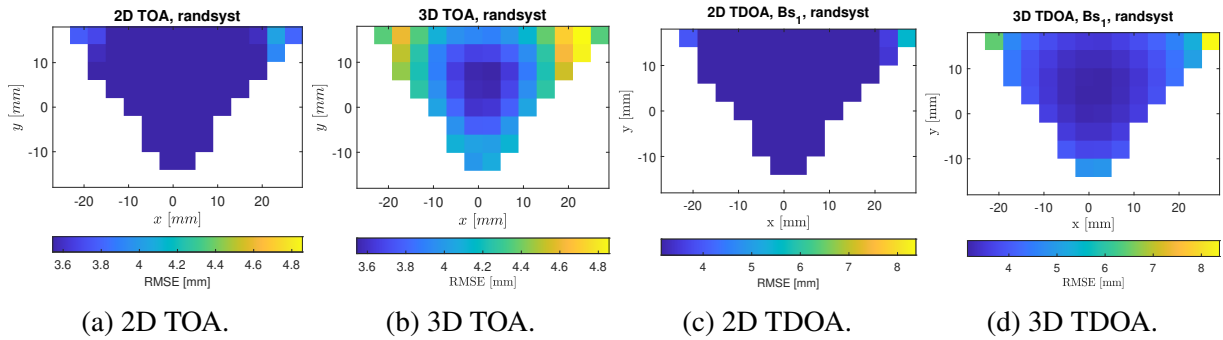


Figure 39: Comparison of the performance of TOA and TDOA multilateration in 2D and 3D in the presence of random and systematic uncertainties. For TDOA, B_{S_1} was systematically used as a reference sensor.

Multilateration Methods	Reference Sensor	μ_{RMSE}^{FOV} [mm]	σ_{RMSE}^{FOV} [mm]
2D TOA	<i>none</i>	2.68	0.63
3D TOA	<i>none</i>	4.03	0.33
2D TDOA	B_{S_1}	2.32	0.66
3D TDOA	B_{S_1}	3.87	0.86

Table 10: Multilateration comparison between 2D TDOA vs 3D TDOA with random and systematic uncertainties, $\mathcal{N}(\boldsymbol{\mu}, \boldsymbol{\Sigma})$, with mean zero and a standard deviations σ_{random} equal to 5 % and $\sigma_{systematic}$ equal to $1 \mu s$, and v_s equal to 1500 m/s.

4.2 Ionoacoustic Simulation Studies at Pre-clinical Beam Energies

This section is focused on localising the BP position using IA signals and previously introduced localisation algorithms. Firstly, we examined the impact of the ToF extraction method on the accuracy of BP position localisation. The accuracy of the ToF extraction method can significantly affect the localisation accuracy of the BP position. Different ToF extraction methods have been proposed in the literature [70, 76], and their performance can vary depending on the IA signal characteristics and the signal processing algorithms used. This work will discuss the advantages and disadvantages of different ToF extraction methods and their impact on the localisation accuracy of the BP position. Secondly, we explored the influence of the reference sensor when considering IA signals. The reference sensor is an essential component of IA signal-based localisation algorithms, as it provides a time reference for the multilateration. Therefore, the placement of the reference sensor can affect the accuracy of the BP position localisation, and its selection should be carefully considered. The impact of different reference sensor placements on localisation accuracy is examined, and methods to optimise the reference sensor selection are discussed.

4.2.1 ToF Extraction Depending on the Sensor Position

Fig.(40a) illustrates how the error in ToF determined from simulated⁵³ ionoacoustic signals depends on the extraction method and the sensor position⁵⁴ in the arc array introduced in section 3.2.1 and illustrated Fig.(19b). Independently of the extraction method used, the minimum ToF error occurs for the axial sensors (i.e., B_{S422}), and the error increases for lateral sensors such as B_{S1} and B_{S843} . The ToF extraction from the signal's *max envelope* yields the absolute lowest errors, with errors lower than $0.1 \mu\text{s}$ at four positions close to the beam axis (B_{S322} , B_{S403} , B_{S441} , B_{S523}). On average, the lowest error is obtained using the *zero-crossing* method across all analysed sensor positions.

Fig.(40b) illustrates the TDOA performance across different reference sensors, from B_{S1} to B_{S843} , during 2D multilateration using all 843 sensors and applying the *zero-crossing* method to extract the ToF. Consistent with the ToF error pattern, the localisation error is minimum when the reference sensor is on the beam axis ($\epsilon_{xz} = 0.18 \text{ mm}$ for B_{S422} as the reference sensor) and increases when selecting a lateral sensor as the reference sensor (up to $\epsilon_{xz} = 1.60 \text{ mm}$ for B_{S1} as the reference sensor). However, the minimum error in ToF estimation does not correspond to the lowest localisation error. Table(11) presents the errors in BP localisation obtained using TOA and TDOA multilateration methods (with B_{S422} as a reference sensor, similar to B_{S1} in previous ideal studies) for different ToF extraction methods. When using all 843 sensor positions, the *zero-crossing* method proved to be the most accurate for ToF extraction, yielding the lowest BP position error (0.55 mm for TOA and 0.18 mm for TDOA) as well as the lowest average ToF error. Therefore, reducing the ToF error will improve the multilateration outcomes.

For the BP localisation with three sensors, the errors were 0.09 mm and 0.35 mm for TOA and TDOA, respectively. The *max envelope* ToF extraction method showed that the lateral⁵⁵ and axial⁵⁶ sensors always had lower errors in ToF estimation than other extraction methods, as illustrated in Fig.(40a). Fig.(40a) displays several sensor positions where the ToF error estimation, based on the *max envelope* and *min amplitude*, exceeds $1.5 \mu\text{s}$. The observed discontinuities result from the shape of the IA sig-

⁵³For the simulation setup see Fig.(19b).

⁵⁴Ranging from B_{S1} to B_{S843} .

⁵⁵Lateral sensors B_{S1} and B_{S843} .

⁵⁶Axial sensor B_{S422} .

nals, where the rarefaction peak and the window signal are superimposed, as illustrated in Fig.(41a). This feature significantly impacts the ToF estimation when computing the ToF from the IA signal minimum amplitude, as several local minima may be present, making it challenging to identify the rarefaction peak. Similarly, when utilising all information of the recorded signal, i.e., by computing the signal envelope, the merging effect can still influence the position where the ToF is accurately extracted, as several peaks can be present in the signal envelope. Furthermore, due to the merging effect, the signal envelope can become spread out, leading to either an underestimation or overestimation of the ToF, as shown in Fig.(41b).

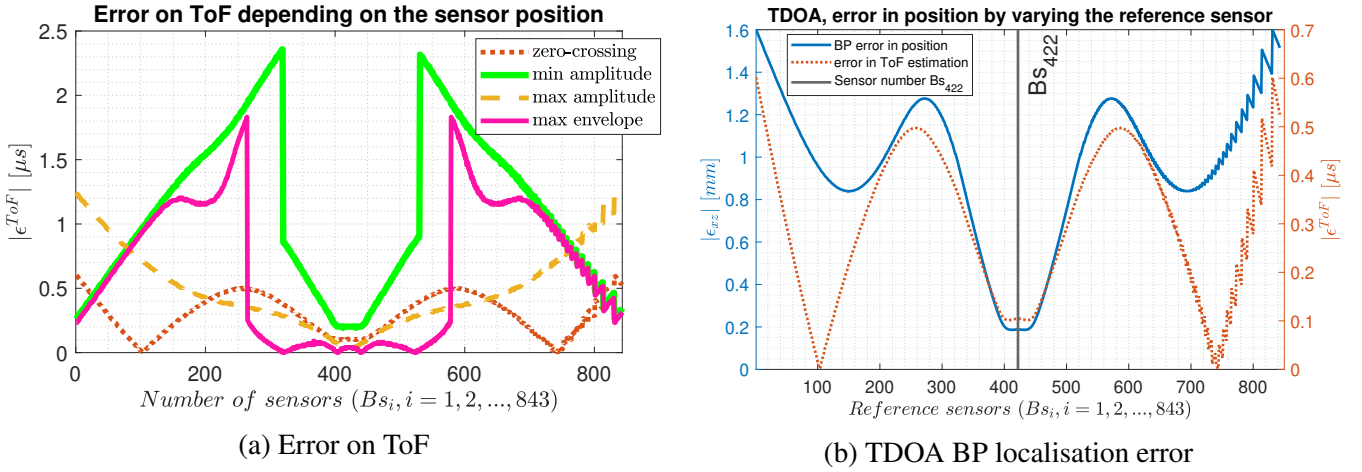


Figure 40: ToF error and BP localisation accuracy as a function of sensor positioning are presented. (a) ToF error is shown based on sensor position along the arc for four extraction methods: *zero-crossing*, *min amplitude*, *max amplitude*, and *max envelope*. (b) BP localisation error using 843 sensors with TDOA is displayed relative to the reference sensor position, with ToF extracted using *zero-crossing* in all cases. The discretised behaviour in both plots results from rounding errors in sensor placement on the computational grid and slight asymmetry in the beam position relative to the sensors. Figures adapted with minor changes from [150].

Number of sensors	ToF extraction	ϵ_{xz}^{TOA}	ϵ_{xz}^{TDOA}	mean ϵ^{ToF}
843	ground truth	0.15 μm	0.87 μm	
	<i>min amplitude</i>	3.76 mm	1.19 mm	1.09 μs
	<i>max amplitude</i>	0.62 mm	1.52 mm	0.50 μs
	<i>max envelope</i>	4.49 mm	2.49 mm	0.64 μs
	<i>zero crossing</i>	0.55 mm	0.18 mm	0.29 μs
3	ground truth	2.00 μm	3.00 μm	
	<i>max envelope</i>	0.09 mm	0.35 mm	0.19 μs

Table 11: 2D multilateration of the BP position was evaluated using different ToF extraction methods. Two scenarios were analysed: one utilising all 843 sensors and another using only three optimally selected sensors. The ground truth reflects the error in multilateration when ToF was derived from the Euclidean distance between the BP and the selected sensors.

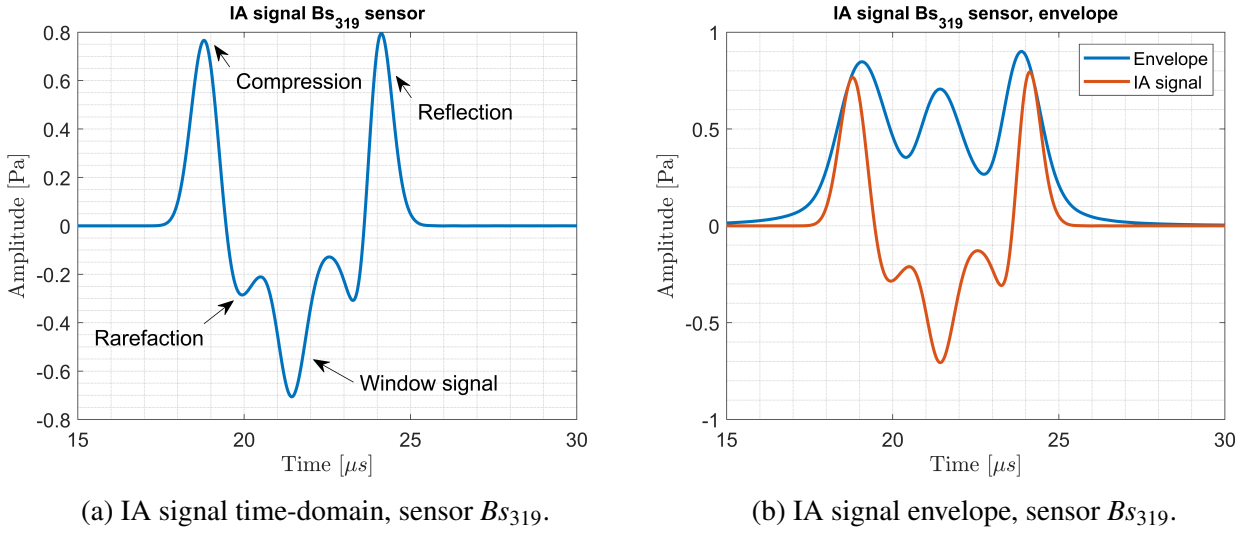


Figure 41: IA signal in time-domain recorded with the sensor $B_{S_{319}}$. (a) The figure illustrates the distorted shape of the IA signal due to the merging effect (i.e., there is no clear separation between the rarefaction peak and the window signal). (b) Overlap of the signal envelope and the IA signal, the envelope comprises three prominent peaks indicating the compression, rarefaction/window signal (merged) and the reflected signal.

4.2.2 Optimal Sensor Selection Based on ToF Error Analysis

The previous results did not include an optimal selection of the sensors for the multilateration. In other words, the BP position can be localised more accurately by selecting the sensors optimally. The results reported here are specifically for the TOA algorithm to simplify the complexity of the reference sensor choice introduced by TDOA. The only exception is for the multilateration performed with three sensors, where the results for TOA and TDOA will be reported. A more generic selection of the reference sensor to minimise the error outcome on the multilateration of the BP is described by eq.(4.9), which is defined as follows:

$$B_{S_i} = \begin{cases} B_{S_i}^{\min} \epsilon^{d_{ToF,i}}; & \epsilon^{d_{ToF,i}} < \eta^{d_{ToF,i}} \quad i = 1, \dots, n \\ B_{S_i}^{\max} \epsilon^{d_{ToF,i}}; & \epsilon^{d_{ToF,i}} > \eta^{d_{ToF,i}} \quad i = 1, \dots, n \end{cases} \quad (4.9)$$

This study is feasible in an *in-silico* scenario where there is a ground truth available, enabling the examination of the impact of ToF error on sensor selection. In eq.(4.9), B_{S_i} represents the sensors in the network, while n is the number of sensors. $\epsilon^{d_{ToF,i}}$ indicates the error on the ToF estimated from the ground truth and converted into distance using the speed of sound in water, and $\eta^{d_{ToF,i}}$ denotes the chosen threshold distance, based on the minimum desired error on the ToF. By employing this method and selecting a threshold ($\eta^{d_{ToF,i}}$) of 0.1 mm for localising the BP using TOA, an error of 46 μm is achieved when extracting the ToF with the *max amplitude* method. In this particular case, the number of sensors decreases from 843 to a total of 37 sensors. When localising the BP with ToF extracted with the *zero-crossing* method, the error equals 21.80 μm , with a total of 52 sensors. Furthermore, when localising the BP position using the *max envelope* ToF extraction method, the error in localisation

equals $6.00 \mu\text{m}$ for a total of 72 sensors. Likewise, when selecting the minimum number of sensors, for example, using only three sensors (B_{S_1} , $B_{S_{422}}$, and $B_{S_{843}}$) and extracting the ToF from the *max envelope*, which is the method that offers the lowest error for axial and the two lateral sensors, the localisation error reaches the values of 0.09 mm and 0.35 mm for TOA and TDOA with $B_{S_{422}}$ as a reference, respectively. All the multilateration results are summarised in Table(12).

The number of sensors depends on the threshold, which is why different ToF extraction methods employ different numbers of sensors. The aim is not to compare which method performs better but to point out that the sensor selection for the BP localisation can be chosen optimally. Furthermore, the results based on the ToF extracted from the *min amplitude* are not included because the average error is $1.09 \mu\text{s}$, which is about two times higher compared to the other ToF extraction methods.

Number of sensors	ToF extraction	ε_{xz}^{TOA}	Optimal sensor selection
843	ground-truth	$0.15 \mu\text{m}$	No
	zero-crossing	0.15 mm	No
	max amplitude	0.62 mm	No
37	max amplitude	$46 \mu\text{m}$	Yes
52	zero-crossing	$21.80 \mu\text{m}$	Yes
3	max envelope	0.09 mm	Yes
75	max envelope	$6.00 \mu\text{m}$	Yes

Table 12: Assessment of BP position multilateration using three distinct ToF extraction techniques: *zero-crossing*, *max amplitude*, and *max envelope*. The multilateration was carried out both with and without optimal sensor selection based on the ToF error relative to the known ground truth, applying a threshold ($\eta^{d_{ToF,i}}$) of 0.1 mm ($\varepsilon^{d_{ToF,i}} < \eta^{d_{ToF,i}}$).

4.3 Multilateration Experimental Studies

This section presents the experimental results for multilateration of the BP position from ionoacoustic signals produced in water at different pre-clinical proton beam energies (20 and 22 MeV). The localisation process involved several steps. Initially, the localisation of the BP position was performed in 2D. Next, the localisation was performed using two sets of sensor positions: one estimated from the phantom drawings and the other calculated experimentally using pulse-echo measurements; for more details, see section 3.2.2. Finally, a specially designed array⁵⁷ was used to accurately localise the BP position for the pre-clinical beam energy (for more details, see section 3.2.4). A significant portion of the study focused on accurately determining the spatial locations of the transducers for both experimental investigations.

4.3.1 IA Experiments with 3 Sensors

The IA signals detected by three sensors - an axial sensor, B_{S_1} , and two lateral sensors, B_{S_2} and B_{S_3} - are shown in Fig.(42a) to Fig.(42c). The experimental studies were conducted under two conditions: *on-axis*, where the setup was positioned on the beam axis, i.e., aligned w.r.t to beam entrance window, and *off-axis*, where the setup was shifted laterally by ± 5 mm. Here, for compactness, only the results

⁵⁷During this work, a dedicated ultrasound array was designed to capture the IA traces from different spatial locations.

of the setup shifted by +5 mm will be presented and discussed. The axial signal, shown in Fig.(42a), comprises three distinct pulses: the direct signal (used for ToF estimation), an entrance signal generated where the proton beam enters the water phantom, and a signal reflecting⁵⁸ from the interface between air and water. The axial signal has a higher frequency and amplitude than the lateral signals (as shown in Figs.(42b,42c)) due to sharper energy gradients along the proton beam axis for the considered monoenergetic scenarios. Accordingly, when the setup is shifted laterally by +5 mm, the ToF calculated from the lateral sensors⁵⁹ is primarily affected since the longitudinal shift is smaller than the transducer diameter of 12.7 mm. Consequently, the ToF measured by B_{S_2} increases, while that measured by B_{S_3} decreases. This shift in time is expected to be retrieved from the localised BP position. For all localisation results presented, the ToF was extracted using the signal *max envelope*, as it yields a lower ToF error for lateral and axial sensors (see section 4.2.1).

Initially, the BP position was retrieved using the transducer spatial location derived from the pulse-echo experiments described in section 3.2.2. The BP localisation was assessed with a total of 1000 consecutive IA measurements. When the phantom was positioned *on-axis*, the projected error along the beam axis (1D) equals 0.20 ± 0.05 mm and 0.16 ± 0.11 mm for TOA and TDOA algorithms, respectively, with B_{S_1} as the reference sensor. Furthermore, the error for the BP position localised in 2D is 0.87 ± 0.18 mm and 0.86 ± 0.22 mm for TOA and TDOA, respectively. The reconstructed lateral and axial BP positions for the phantom *on-axis* are illustrated in Figs.(42d,42e). For the phantom positioned *off-axis*, the projected error along the beam axis is 0.76 ± 0.06 mm and 0.87 ± 0.07 mm for TOA and TDOA, respectively. The total error for the BP localised in 2D equals 1.40 ± 0.12 mm and 1.46 ± 0.14 mm for TOA and TDOA, respectively.

The accurate localisation of the BP position depends on the transducer spatial locations accuracy, among the previously discussed factors. For the transducer spatial locations estimated with pulse echo, the error in BP localisation is high, approximately 0.90 mm and 1.50 mm for the phantom *on-axis* and *off-axis*. The high errors in BP localisation are primarily due to the complexity of aligning the cylinder target during pulse-echo measurements. Similarly, we conducted the spatial localisation of the transducers using the cylinder target on different days compared to the main experiment using the pre-clinical proton beam, which may have introduced additional variability. During the mounting phase of the transducers on the phantom, a misalignment of 0.10 mm was also detected between the centres of B_{S_2} and B_{S_3} (see Fig.(58) in appendix H). This misalignment was identified through acoustic pulse-echo measurements, where B_{S_2} was used to send a pulse that reflected off the surface of the B_{S_3} transducer, and vice-versa. Therefore, the sources of errors in estimating the transducer spatial location are directly linked to the error in the BP localisation, as demonstrated by the findings. In order to improve the localisation, it is crucial to decrease the error on the transducer spatial location.

⁵⁸The reflected signal is the reflection of the direct signal.

⁵⁹i.e., B_{S_2} and B_{S_3} .

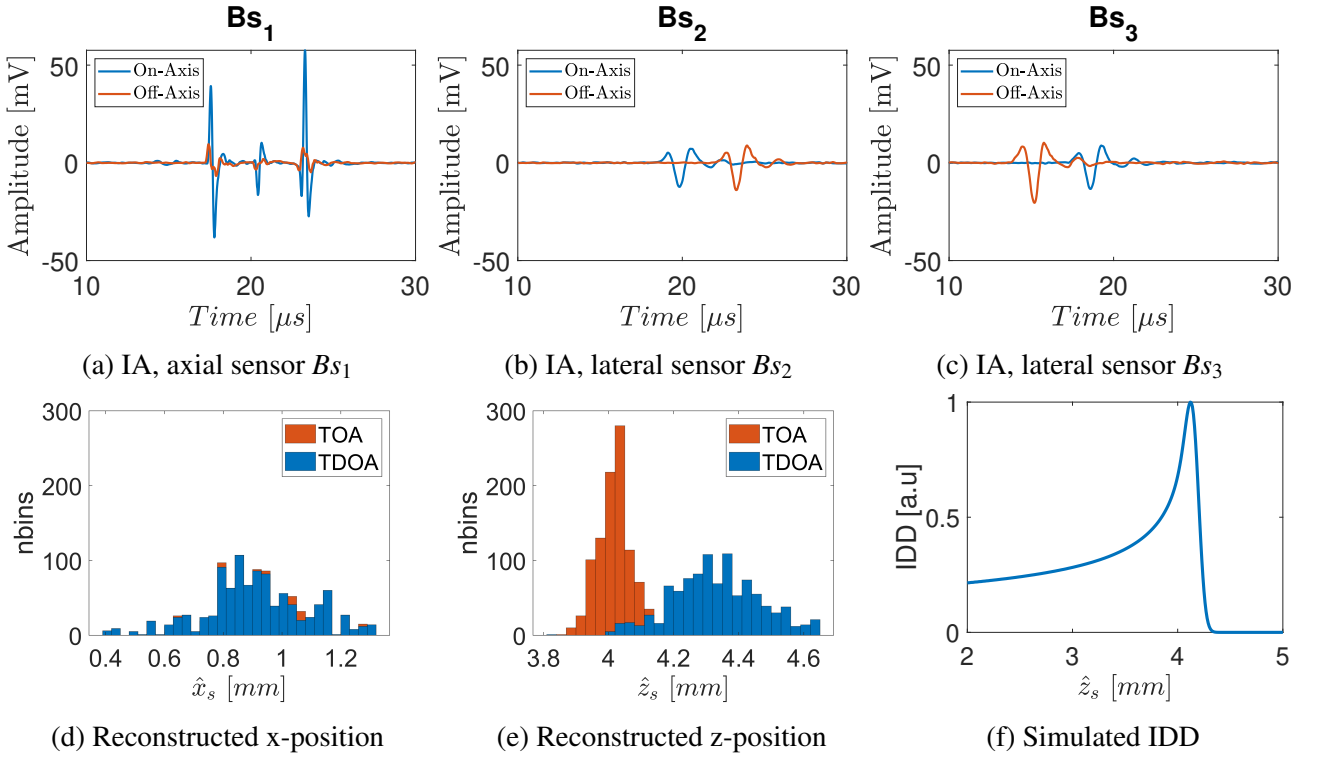


Figure 42: 2D experimental study, the multilateration of the Bragg peak (BP) was assessed, and the corresponding IA signals were recorded using (a) the axial sensor Bs_1 and the lateral sensors (b) Bs_2 and (c) Bs_3 . The BP lateral and axial positions (*on-axis*) were reconstructed and visualised in (d) and (e), using the transducer spatial locations estimated from pulse-echo measurements. Furthermore, the simulated laterally IDD distribution normalised by its maximum and displayed in (f) reveals the Bragg peak located 4.12 mm distal to the phantom entrance (simulated IDD courtesy of Dr Hans-Peter Wieser). The signals presented in figures (a) to (c) were averaged for better visualisation. Figures extracted from [150], with exception to figures (d,e).

Figs.(43a,43b) illustrate the distribution of the BP reconstructed lateral and axial positions for the phantom located *on-axis*. However, for the current reported results, the transducer spatial locations were retrieved from the technical drawings of the I-BEAT [56]. Similar to the previous localisation results, a total of 1000 consecutive IA measurements were used. When localising the BP having the phantom located *on-axis*, the estimated error projection along the beam axis equals 0.21 ± 0.08 mm and 0.30 ± 0.12 mm for TOA and TDOA (having Bs_1 as a reference sensor). Furthermore, the corresponding error on the BP position in 2D is 0.43 ± 0.20 mm and 0.48 ± 0.22 mm for TOA and TDOA. All the reconstructed errors in position are summarised in Table(13). In both multilateration cases (using TOA and TDOA), it was found that the main contribution to the total error in position ($\epsilon_{\hat{x}_s, \hat{z}_s}$) arises from the reconstruction of the lateral position ($\epsilon_{\hat{x}_s} = 0.37 \pm 0.17$ mm for TOA and TDOA, respectively), which is attributed to an inaccurate knowledge of the transducer spatial location relative to the beam entrance window.

When the phantom was positioned *off-axis*, the total error in BP position increased to 1.26 ± 0.13 mm for TOA and 1.25 ± 0.14 mm for TDOA, primarily due to inaccuracies in ToF estimation. Moreover, the error in Bs_1 was higher compared to the previous setup (i.e., when the phantom was positioned *on-axis*), which can be attributed to its nearly lateral positioning and reduced SNR. The SNR is one of the most important metrics to assess the overall IA signal quality and its transition to pre/clinical applications [169]. For this reason, the multilateration results performed with the two sets of

transducer spatial locations⁶⁰ can be contextualised by considering the estimated SNR for each transducer when the phantom is positioned *on-axis* and *off-axis*. Therefore, for the phantom positioned *on-axis*, the higher SNR is achieved for the axial transducer B_{s1} , which equals 60.66 ± 3.41 dB (for the SNR estimation, see eq.(3.12)). The high SNR leads to a stronger and more distinguishable IA signal, implying an accurate ToF estimation. In addition, for the two lateral transducers, the estimated SNR equals 19.08 ± 1.43 dB and 20.89 ± 1.38 dB for B_{s2} and B_{s3} , respectively. The difference in the SNR between both lateral sensors is about 1.81 dB, which translates to a similar IA signal strength, integrity and features (see Fig.(42b)). The slight difference in the SNR between the two lateral sensors could be due to the beam asymmetry w.r.t the sensors and uncertainties in the setup alignment. Furthermore, the ToF accuracy and precision are expected to be comparable, if not the same. For the phantom located *on-axis*, all the estimated SNR results are reported in Table(14). On the other hand, when the phantom is located *off-axis*, the estimated SNR for the axial transducer B_{s1} decreased to 14.91 ± 1.16 dB. For the lateral sensor B_{s2} , the SNR also decreased to 14.55 ± 0.73 dB because the dose deposited in water is close to the lateral sensor B_{s3} , where the SNR increased to 26.81 ± 0.85 dB. All the results on the SNR are reported in Table(14).

In summary, when localising the BP using the transducer spatial locations estimated from pulse-echo measurements, both TOA and TDOA methods exhibit a similar total error of approximately 0.90 mm (phantom *on-axis*). These increased errors compared to the drawings are attributed to uncertainties in accurately estimating the spatial location of the transducers using the cylinder target within the phantom. Furthermore, the limited space between the entrance window and the cylinder target posed challenges during the experimental studies, impacting the alignment and placement of the cylinder target within the phantom. After employing a direct transducer localisation approach, i.e., based on the phantom drawings, there was a significant improvement in localising the BP position. For the phantom *on-axis*, the BP localisation error was 0.43 mm and 0.48 mm (TOA and TDOA, respectively). For the phantom located *off-axis*, the accuracy of ToF estimation and proper knowledge of the transducer's spatial location is even more crucial due to the lower SNR for B_{s1} and B_{s2} . Both transducers have similar SNR. Therefore, for the BP localised using the two sets of the transducer spatial location, the error on the BP localisation was above 1 mm (TOA and TDOA, respectively). Hence, it can be concluded that when the sensor positions are known with high accuracy, and the IA signals are recorded with high SNR, the BP position can be retrieved with high accuracy, assuming that the error in ToF is properly estimated and the speed of sound in the medium is known.

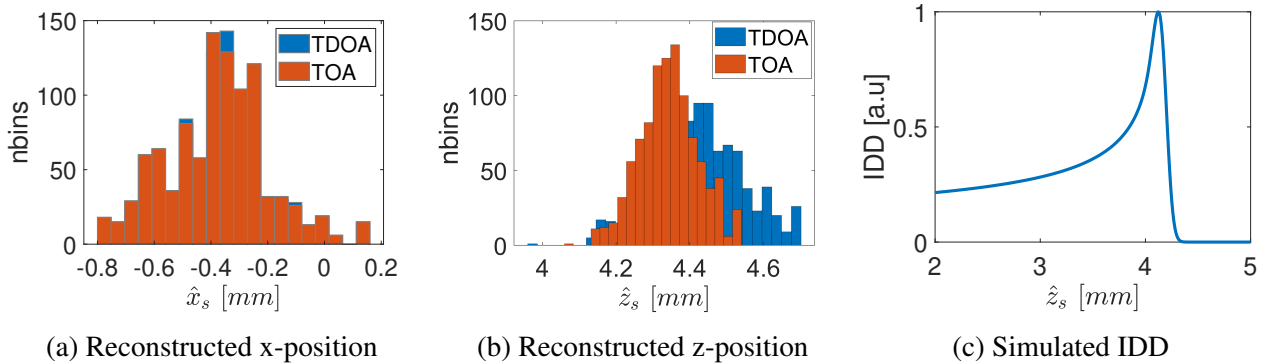


Figure 43: 2D Reconstructed BP position, for the transducer spatial locations estimated from the technical drawings. (a) reconstructed lateral BP position and (b) axial BP position, both for the phantom located *off-axis*. IDD distribution normalised by its maximum and displayed in (c) (simulated IDD courtesy of Dr Hans-Peter Wieser). Figures extracted from [150].

⁶⁰i.e., using the cylinder and technical drawings.

Phantom Position	Multilateration Methods	Reference Sensor	ToF extraction	ϵ_{z_s} [mm]	$\epsilon_{\hat{x}_s \hat{z}_s}$ [mm]
<i>On-axis</i>	$TOA^{Pulse\ echo}$	none	max envelope	0.20 ± 0.05	0.87 ± 0.18
	$TDOA^{Pulse\ echo}$	Bs_1	max envelope	0.16 ± 0.11	0.86 ± 0.22
	$TOA^{Drawings}$	none	max envelope	0.21 ± 0.08	0.43 ± 0.20
	$TDOA^{Drawings}$	Bs_1	max envelope	0.30 ± 0.12	0.48 ± 0.22
<i>Off-axis</i>	$TOA^{Pulse\ echo}$	none	max envelope	0.76 ± 0.06	1.40 ± 0.12
	$TDOA^{Pulse\ echo}$	Bs_1	max envelope	0.87 ± 0.07	1.46 ± 0.14
	$TOA^{Drawings}$	none	max envelope	0.93 ± 0.07	1.26 ± 0.13
	$TDOA^{Drawings}$	Bs_1	max envelope	0.91 ± 0.09	1.25 ± 0.14

Table 13: Position reconstruction errors for 2D multilateration are presented, comparing TOA and TDOA algorithms with the phantom in both *on-axis* and *off-axis* positions. The BP localisation was based on single-shot measurements (1.69 Gy). The reported localisation error represents the mean and standard deviation calculated from 1000 consecutive measurements. Multilateration was performed using BP with two sets of transducer spatial locations: one derived from drawings and the other from pulse-echo measurements.

Phantom Position	SNR^{Bs_1}	SNR^{Bs_2}	SNR^{Bs_3}
<i>On-axis</i>	60.66 ± 3.41	19.08 ± 1.43	20.89 ± 1.38
<i>Off-axis</i>	14.91 ± 1.16	14.55 ± 0.73	26.81 ± 0.85

Table 14: SNR estimation was conducted for single proton pulse measurements (1.69 Gy) collected by the various sensors with the phantom in both *on-axis* and *off-axis* positions. These SNR values were calculated from 1000 consecutive measurements and are presented as the mean and standard deviation.

4.3.2 IA Experiments with 5 Sensors

In real-life scenarios involving a small animal (i.e., a mouse), it becomes crucial to determine the position of the sensor array relative to the animal. In such cases, optical measurements can be used to retrieve the position of each sensor element. Furthermore, optical tracking measurements provide the advantage of precise positioning by allowing for accurate tracking (i.e., an accuracy⁶¹ of 0.35 mm [170]) and alignment of the sensor array with the beam entrance. We used an optical tracking system to deduce the transducer spatial locations. Nevertheless, the results that were obtained did not meet the required level of accuracy due to inherent challenges in the experimental setup. The inaccuracies primarily resulted from the dependence of the optical tracking system on precise marker placement on the transducer surface for accurate reconstruction of estimated points on the transducer rim surface. Moreover, accessing and ensuring the visibility of markers on all transducer surfaces posed difficulties. Accordingly, inaccuracies arise from the required rotations and translations of the pivot point in manually positioning the markers on the transducer surface. Each point on the surface had to be measured by manually holding a passive marker with a pivot point, further reducing the accuracy. Fig.(44a) shows the transducer spatial location obtained from the optical measurements. One way to assess if the transducer spatial location was accurate was to verify the *horseshoes* dimensions using the coordinates estimated with the optical tracking. The distance estimated with the axial sensor was benchmarked by computing the equation below:

$$d_{Bs_2}^{BP} \approx \sqrt{(x_2 - x_{ew})^2 + (y_2 - y_{ew})^2 + (z_2 - z_{ew})^2} - Range \implies \left| d_{Bs_2}^{BP} - d_{Bs_2}^{ToF} \right| \approx 0 \quad (4.10)$$

Eq.(4.10) compares the distance from the BP to the axial sensor estimated geometrically and based on the ToF estimation from the recorded IA signal. In the equation, $x_2, y_2,$ and z_2 are the axial transducer spatial location, $x_{ew}, y_{ew},$ and z_{ew} are the entrance window spatial location, and *Range* is the Bragg peak position in water. From the geometrical calculation, the distance from the BP position to the axial sensor ($d_{Bs_2}^{BP}$) was estimated to be 37.33 mm. The distance from the axial sensor to the BP position ($d_{Bs_2}^{ToF}$)⁶² estimated using the IA signal was 44.60 mm. The difference between both distances gave an offset of 9.27 mm. In addition, this offset was confirmed by comparing the dimension of the *horseshoes* setup estimated from the output of the optical tracking coordinates and the one estimated using the manufactured *horseshoes* drawings.

Fig.(44b) illustrates the transducer's spatial localisation after applying the CPD rigid registration and accounting for the proper matrix rotation for the sensors Bs_1 and Bs_3 defined in the template. Doing so made compensating for the transducer's spatial localisation errors possible. Therefore, after performing the CPD rigid registration, a new set of transducer's spatial locations was recalculated (i.e., c_0^1, c_1^1 to c_4^1). The distances between the BP to the axial sensor, estimated geometrically and based on the ToF estimation from the recorded IA signal, were again compared, giving an error of 0.96 mm. Before discussing the output results of the multilateration algorithm, it is essential to describe the IA signal recorded by each sensor using the *horseshoes* setup. Figs.(45a) to (45c) illustrate every recorded signal from Bs_0 to Bs_4 . Considering the sensor pairs (i.e., the lateral Bs_0 and Bs_4), it could be noticed that the shape of the IA signal changes from one sensor to another, which is due to the fact that one sensor is focused and the other is unfocused. The other pair of sensors (Bs_1 and Bs_3) are shifted in phase because of different spatial impulse response. Lastly, the IA signal recorded with the

⁶¹The accuracy also depends on the type of the optical tracking system.

⁶² $d_{Bs_2}^{ToF} = v_s \cdot ToF_{Bs_2}$.

axial sensor (Bs_2) is illustrated in Fig.(45c). From the axial sensor, the classic shape of the IA signal can be seen with the three main peaks, *direct signal*, window signal and *reflected signal*.

The ToF estimated with sensors Bs_0 to Bs_4 is reported in Table(15). The SNR was computed for every single sensor in the network, and all the results are reported in Table(16).

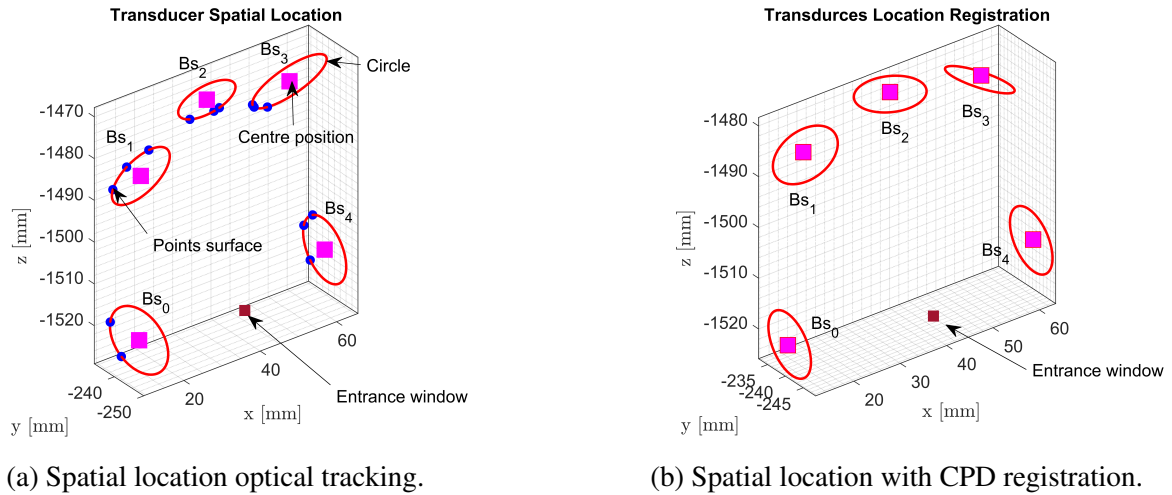


Figure 44: Transducer localisation before and after the registration. (a) Transducers spatial localisation, output directly from the optical tracking system. The orientation of sensors is illustrated by the red circles. The magenta square indicates the centre of the sensors. The three blue points in each sensor show the measurement positions on the transducer outer rim. The brown square indicates the position of the centre of the water tank entrance window. (b) Transducer spatial location after the CPD registration.

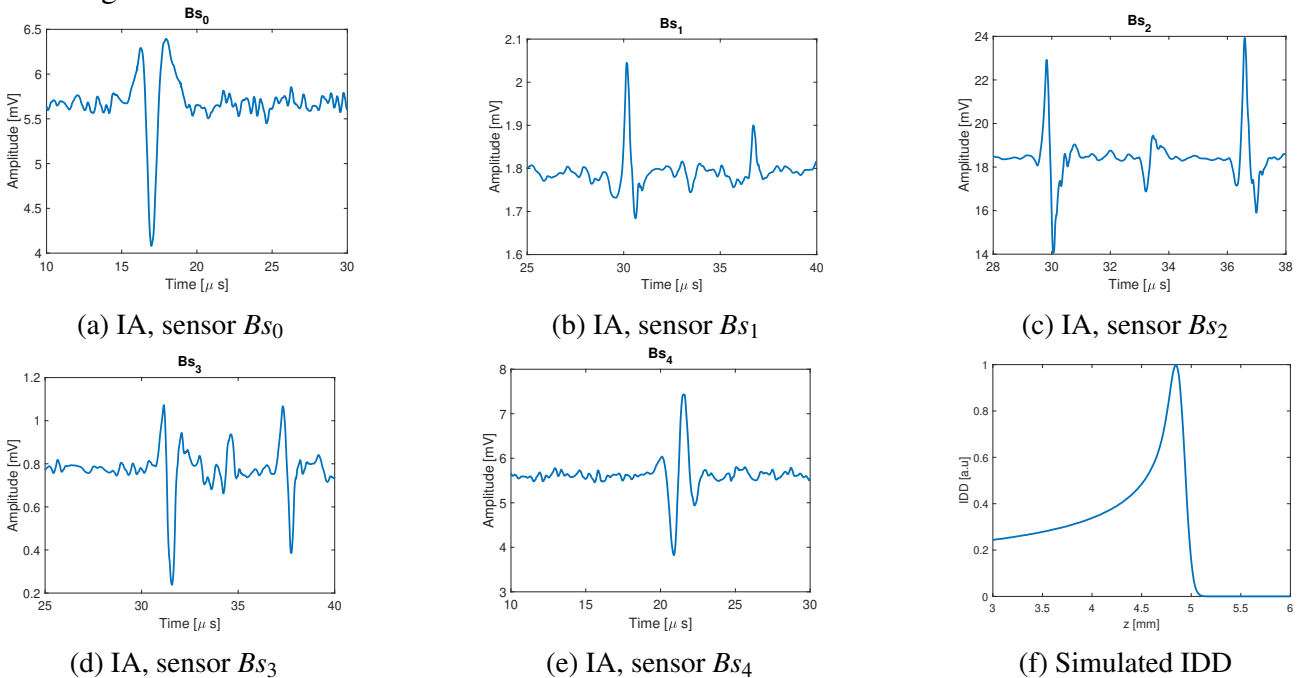


Figure 45: The recorded ionoacoustic signals were obtained from various sensor locations, as follows: (a,e) two lateral transducers (Bs_0, Bs_4); (b,d) two transducers tilted at an angle of 28° with respect to the beam axis (Bs_1, Bs_3); (c) the axial transducer. In addition, a simulated integral depth dose normalized by its maximum is shown in (f) (IDD simulation courtesy of Dr Julie Lascaud). All the recorded signals were averaged over 50 acquisitions, with a total dose of 29 Gy, figures from [150].

Table 15: The mean and standard deviation of ToF for all transducers in the network, ranging from Bs_0 to Bs_4 , were computed. The signals were averaged over 50 acquisitions. The ToF was estimated using the *max envelope* extraction method for all the recorded signals.

ToF Method	ToF, Bs_0	ToF, Bs_1	ToF, Bs_2	ToF, Bs_3	ToF, Bs_4
Max envelope	$15.57 \pm 0.19 \mu s$	$28.75 \pm 0.12 \mu s$	$28.54 \pm 0.05 \mu s$	$30.06 \pm 0.14 \mu s$	$19.81 \pm 0.13 \mu s$

For the 3D multilateration, initially, the BP was localised considering the sensor localisation illustrated in Fig.(44a), without considering the CPD registration. The results were then compared to BP localisation using sensor positions from CPD, as shown in Fig.(44b). The results of BP multilateration in 3D using TOA and TDOA for the setup depicted in Fig.(22) are presented in Figs.(46a,46b). The sensor locations were determined with particular attention, resulting in a total error in determining the 3D BP position of 1.00 ± 0.72 mm and 0.82 ± 0.23 mm for TOA and TDOA, respectively. It is essential to point out that the accuracy of the sensor localisation was further improved by performing the proposed registration step. Without this step, the BP multilateration error increases to 2.48 ± 0.30 mm for TOA and 8.82 ± 1.52 mm for TDOA. These results demonstrate the importance of accurate sensor localisation in BP multilateration, mainly when using TDOA. The proposed co-registration step can significantly improve the accuracy of the sensor positions, leading to more precise BP localisation.

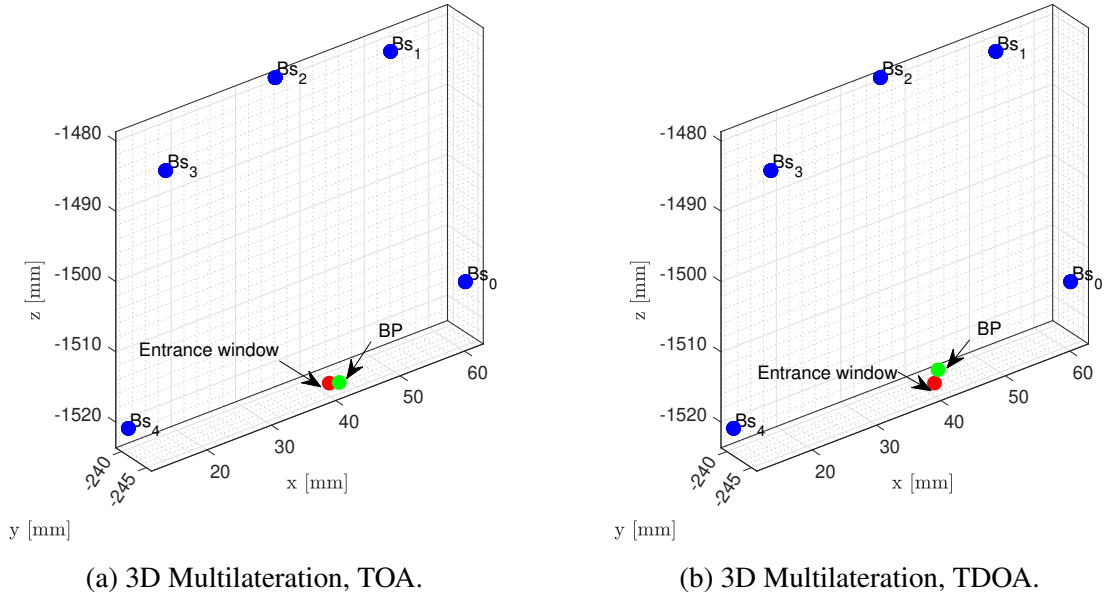


Figure 46: 3D BP Multilateration performed by the horseshoes transducer array with (a) TOA and (b) TDOA. Sensor positions are shown as blue dots (sensor positions determined with registration step). The entrance window is shown as a red dot and the BP is shown as a green dot. Figure extracted from [150].

SNR^{Bs_0}	SNR^{Bs_1}	SNR^{Bs_2}	SNR^{Bs_3}	SNR^{Bs_4}
11.60 ± 3.11	11.34 ± 4.12	41.70 ± 14.07	12.06 ± 3.98	16.81 ± 3.48

Table 16: SNR estimated from all the transducers with 50 acquisitions.

4.3.3 Improvement of the ToF extraction using a Gaussian fit

Fig.(47a) to Fig.(47e) illustrate the IA signals before and after a Gaussian fitting is applied to the signal envelope. For the sensors B_{S_0} and B_{S_4} , the phases were inverted as a matter of visualisation. However, the multilateration was performed on the initial signal. When estimating the ToF based on the *max envelope*, the estimated maximum can deviate from the expected value due to signal noise, signal distortion, and other effects (see, for instance, Fig.(47d)). As a result, the ToF estimation can either be underestimated or overestimated, depending on the maximum value observed in the signal envelope. Therefore, applying a Gaussian fitting to the signal envelope can ensure the presence of a unique signal maximum. This improves ToF estimation accuracy and enhances the detection algorithm robustness. Accordingly, the optimisation works faster due to the more reliable ToF estimation procedure. However, the Gaussian fitting is computationally expensive⁶³ especially in the presence of signal distortion and low SNR.

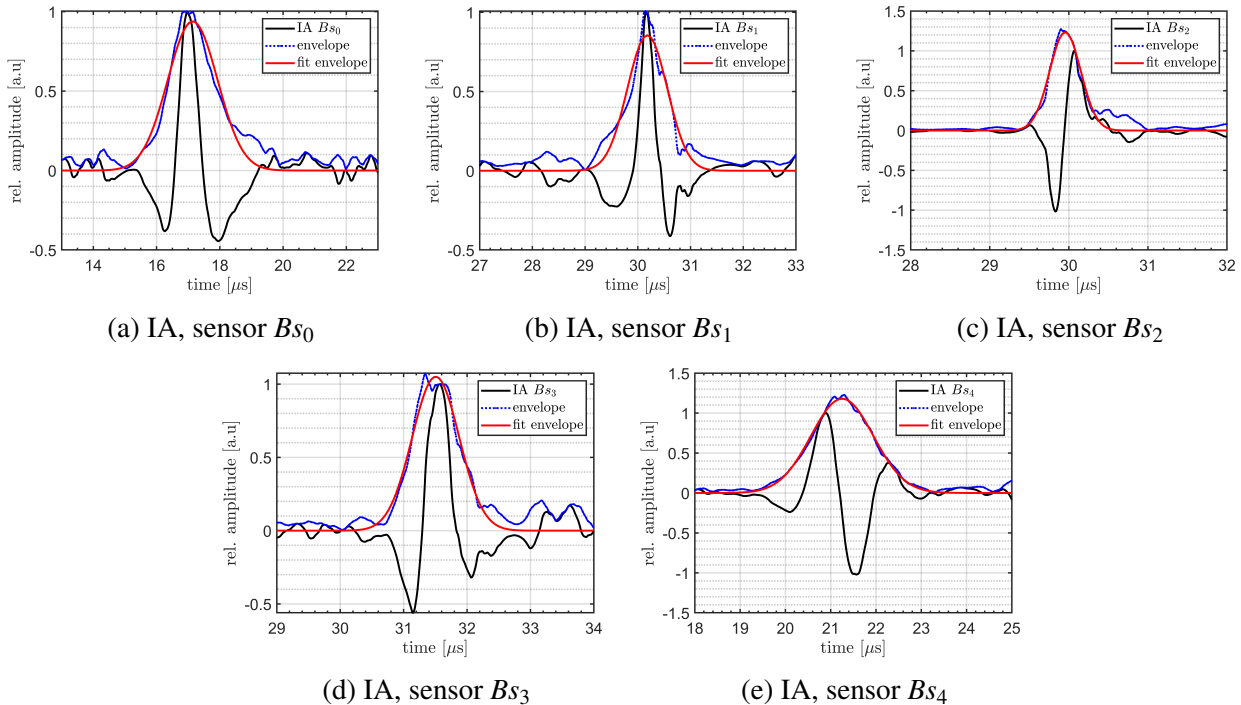


Figure 47: The recorded IA signals were obtained by averaging 1000 acquisitions. In Figures (a, b, c, d), we can observe the IA signals recorded with sensors labelled as B_{S_0} , B_{S_1} , B_{S_2} , B_{S_3} , and B_{S_4} . These figures depict the unfitted and Gaussian-fitted signal envelopes.

Initially, the BP was localised by averaging the 1000 signal acquisitions. The rationale was to decrease the random errors (which should average out with many signal averages) and increase the SNR. When localising the BP, the error in position equals 0.36 mm and 0.72 mm for TOA and TDOA, respectively, without any fitting applied to the signal envelope. Consequently, after averaging the 1000 signal acquisitions, a Gaussian fitting was applied to the envelope signals recorded with all sensors (as depicted in Fig.(47)), the error on the localised BP position reduces further to 0.12 mm and 0.67 mm for the TOA and TDOA, respectively. One reason the error in localisation is higher for the TDOA is that by increasing the signal average, random errors still remain, making TOA perform better than TDOA. The fitting procedure decreases the error to 0.24 mm and 0.05 mm for TOA

⁶³A proper numerical quantification may be required.

and TDOA, respectively. The improvement in TDOA is likely because of the fitting process, which reduces systematic errors in ToF estimation. However, due to uneven error distribution across all sensors, systematic errors may persist even when localising the BP with B_{s_1} as the reference sensor.

4.4 SIRMIO Case Study

This section focuses on localising the BP position within the context of the SIRMIO project. The primary purpose is to investigate the influence of ToF in relation to a sensor arrangement designed for the SIRMIO setup. Various proton time profiles were examined to evaluate their impact on ToF estimation and, subsequently, on the accuracy of BP position localisation. Following this, a comprehensive analysis of ToF was conducted, encompassing all previously introduced extraction methods. Subsequently, the multilateration technique was employed to assess BP position localisation for different proton time profile widths, considering the optimal ToF extraction method. Furthermore, the multilateration process was performed for various beam spatial locations with respect to the sensor arrangement to assess its effectiveness in different scenarios.

4.4.1 Error on ToF Depending on the Proton Time Profile

Fig.(48a) to Fig.(48d) demonstrate the relationship between the error in ToF for different proton time profile widths⁶⁴ compared to IVP. The comparison is made considering the *max envelope*, *min amplitude*, *max amplitude* and *zero-crossing*. In section 4.2.1, it was concluded that the *max envelope* extraction method is the optimal ToF extraction method due to the lowest error on the ToF for the lateral and axial sensors. This conclusion was reached by considering a 200 ns square pulse.

A different time profile was considered in this study because the SIRMIO setup is expected to be integrated into clinical facilities [54]. Hence, the results reported here consider a different beam energy and proton time profile (i.e., varying from 1 μs to 10 μs) compared to the one performed in section 4.2, which was a 200 ns square pulse. To keep the results concise, the analysis of the ToF error for all the extraction methods was limited to the axial sensor. This procedure is applied to the results presented in Figs. (48a,48d). The reasoning is that the error in ToF for the axial sensor depends only on the γ -wave. However, for realistic scenarios, it cannot completely be ensured that an axial sensor will always be available.

When the ToF is extracted using the *max envelope* method as illustrated in Fig.(48a), the findings show that the minimum ToF error occurs when the proton profile widths range from 3 μs to 6 μs . Moreover, for the ToF estimated using the *min* and *max amplitude* extraction methods, it can be seen that the lowest error in ToF is achieved when the proton time profile widths vary from 1 μs to 4 μs , as illustrated in Figs.(48b,48c). On the other hand, when the *zero-crossing* extraction method is employed to estimate the ToF, a lower error in ToF is obtained for proton profile widths ranging from 1 μs to 4 μs , as demonstrated in Fig.(48d). Overall, the error on ToF converted into the distance is lower if the ToF is extracted from the maximum signal envelope. Furthermore, if we consider the IVP without convolving with any proton time profile, the *zero-crossings* gives a lower error. One reason is that *zero-crossings* is less sensitive to changes in the IA signal phase.

To summarise, the error on the ToF is lower for the *max envelope* extraction method because of the spatial dose distribution. The sensors placed axially record an acoustic pressure signal, which can be estimated as the first-order derivative of the IDD. The IDD resembles a Gaussian profile at the Bragg peak region. Accordingly, the ionoacoustic signal is the first-order derivative of a Gaussian profile, giving the typical bipolar shape obtained for axial signals. Likewise, the pressure wave propagates according to the first-order derivative of the Gaussian cross-section profile for the sensors placed laterally. Since the envelope of the first-order derivative of a Gaussian signal resembles a Gaussian profile,

⁶⁴The recorded IA signals were convolved with different Gaussian's proton profile widths.

which in our case resembles either the lateral cross-section profile or the BP region of the IDD, the *max envelope* correctly estimates the ToF. Hence, for more realistic proton time profiles, we obtained a lower error on the ToF for axial and lateral sensors when the *max envelope* was used.

The error in the distance for the ToF extracted using the *max envelope* is 0.79 mm for proton profile widths within the clinical range of 3 to 6 μs , as demonstrated in Fig.(48a). However, upon examining Fig.(48b) to Fig.(48c), the error in ToF (converted into distance) estimated from the *min amplitude* is 1.22 mm, while from the *max amplitude*, it is 0.82 mm, both for a proton profile width of 1 μs . The error of 1.22 mm demonstrates that the ToF extracted from the signal *min amplitude* is more sensitive to IA signal shape, e.g., compared to the ToF extracted from the signal *max amplitude* (see section 4.2.1 and Fig.(41)). It should be noted that this proton profile width is shorter than that used in the clinical synchrocyclotron facility, which is around 3.7 μs [76]. Therefore, for the SIRMIO beamline setup, the BP will be localised only considering the ToF extracted from the *max envelope*.

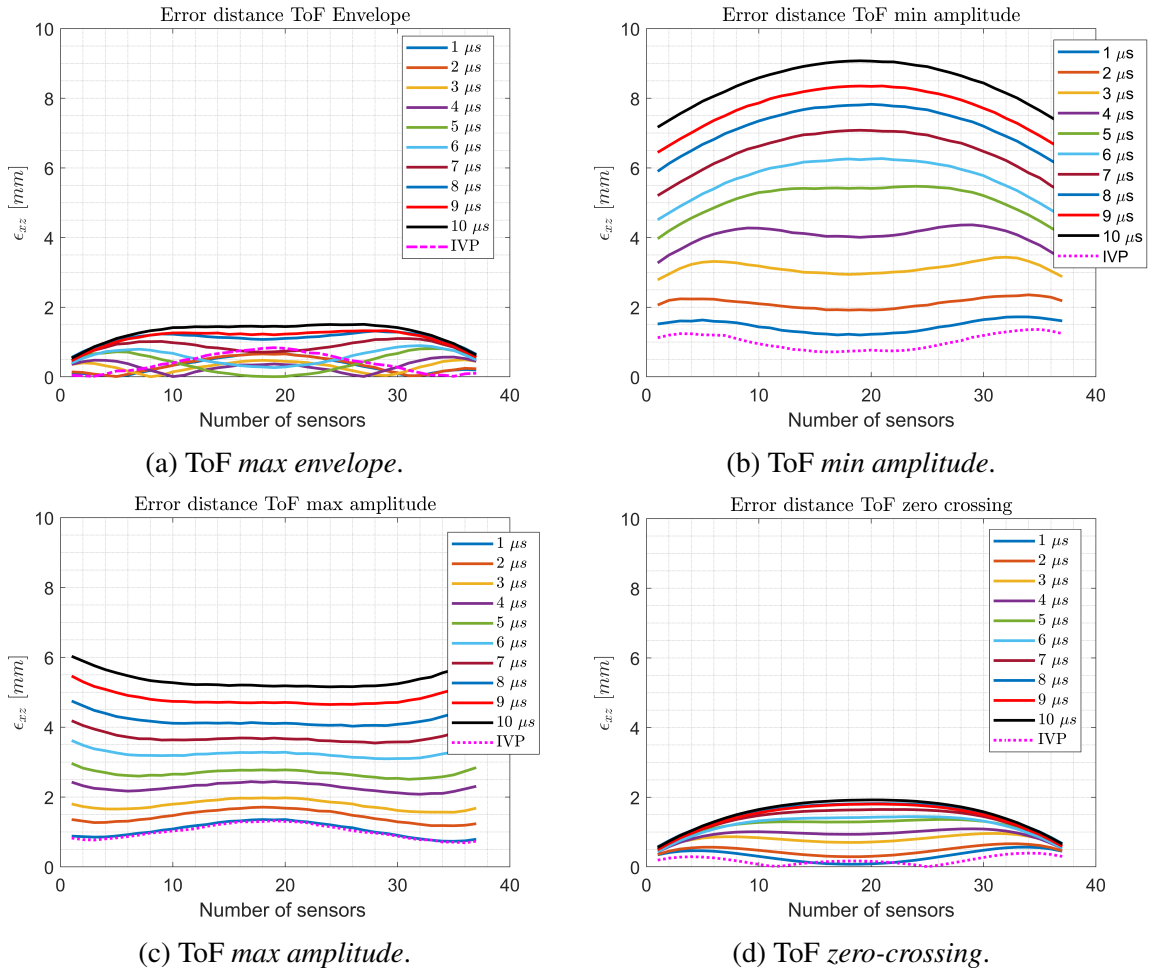


Figure 48: Error on ToF estimation (converted to distance) of the IA signal produced by a SIRMIO beam of 50 MeV stopped in water, depending on the ToF identification approach. Different proton time profiles were analysed, from 1 μs to 10 μs with a step of 1 μs , and the error in ToF was estimated taking the IVP as ground truth. (a) Error in distance ToF extracted with *max envelope* method. (b) Error in distance ToF extracted with *min amplitude* method. (c) Error in distance ToF extracted with *min amplitude* method. (d) Error in distance ToF extracted with the *zero-crossing* method. All the ToF estimations were based on the setup illustrated in Fig.(25) in chapter 3.

4.4.2 Multilateration Accuracy Depending on the Proton Time Profile

Fig.(49) shows the multilateration performed considering different time profile widths and the number of sensors. When performing the multilateration with TOA, as shown in Fig.(49a), the error in localisation is below 0.59 mm for proton pulse width varying from 1 μs to 6 μs for all sensor configurations. The multilateration performed with three sensors results in an average error of 0.37 mm, with minimum and maximum errors at time profile widths of 2 μs and 10 μs , respectively. By increasing the number of sensors, the dependency on proton pulse width increases because the error in BP localisation goes up to 2.44 mm. Fig.(49b) shows the dependency of the pulse width for multilateration performed with TDOA. The error in localisation is below 0.60 mm for pulse width varying from 1 μs to 6 μs for all sensor configurations. The minimum average error in position of 0.28 mm is achieved for a proton pulse width of 1 μs , and the maximum average error in the position is 0.70 mm for a proton pulse width of 10 μs .

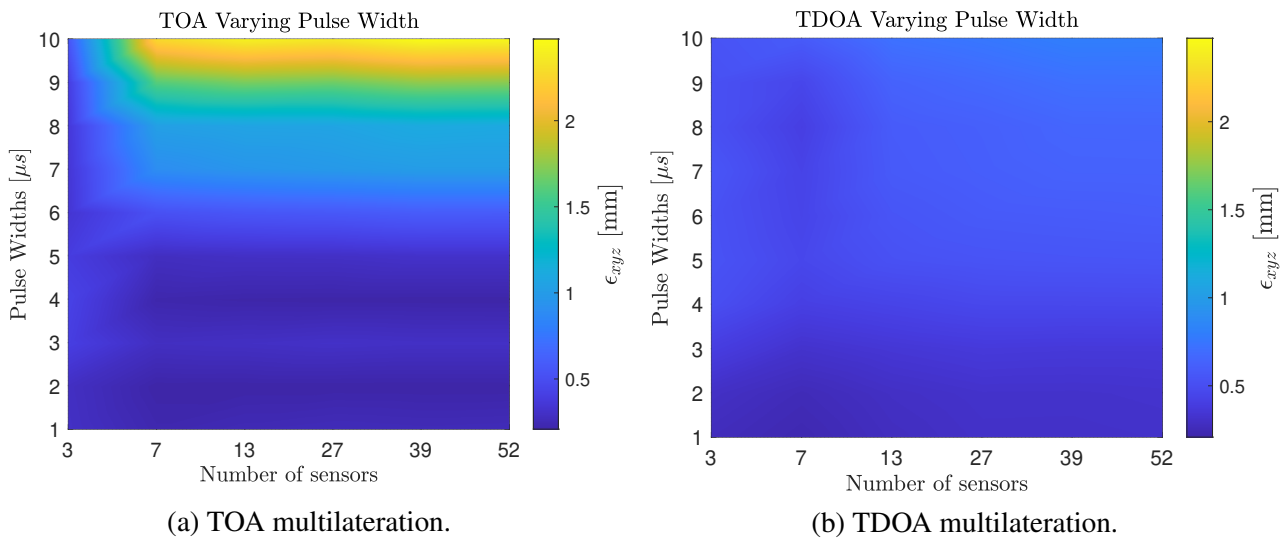


Figure 49: Error in position for TOA and TDOA multilateration. The BP localisation was performed by varying the number of sensors and proton pulse widths. (a) TOA multilateration for different sensors and proton pulse widths. (b) TDOA multilateration for different sensors and proton pulse widths. For all sensor configurations, the reference sensor was the axial one, as shown in the setup illustrated in Fig.(25) in chapter 3.

To summarise, the proton time profile affects the accuracy of BP position localisation. It was demonstrated that the accuracy of the ToF estimation depends on the proton time profile width, as discussed in section 4.4.1. Furthermore, it was found that wider proton time profiles tend to result in higher errors on the reconstructed BP position [70]. For shorter proton pulse width (i.e., proton pulse width $\leq 6 \mu\text{s}$) and the BP located in the centre of the array, the multilateration performed with TOA yields lower overall localisation errors compared to TDOA, as illustrated in Figs.(49a,49b). Furthermore, Fig.(48a) illustrates that the lowest average error in ToF is achieved when proton profile widths range from 1 μs to 4 μs . This trend is also observed for BP localisation, except for localisation with only three sensors. In addition to the proton time profile, the number of sensors used in localisation is also crucial. Table(17) highlights that the error is consistently below 0.55 mm for localisation with only three sensors for all proton time profile widths. When increasing the number of sensors from 7 to 52, the error in position is below 0.59 mm for a proton time profile varying from 1 μs to 6 μs . Moreover, when increasing the proton time profile widths from 7 μs to 10 μs , the error in position increases from approximately 1 mm to 2.47 mm. TOA resulted in being more sensitive to the proton pulse width

(e.g., for multilateration performed with $n \geq 7$, see Fig.(49a)).

When employing TDOA for multilateration, the dependence on the proton pulse width decreases. Indeed, a more homogeneous distribution of the error in position can be seen, as shown in Fig.(49b). For the TDOA, the error in localisation is consistently below 0.55 mm for all proton profile widths for the BP localised with three sensors. When increasing the number of sensors (i.e., $n \geq 7$), the error in localisation is below 0.80 mm, as reported in Table(18). Besides the proton time profile width and the number of sensors, the reference sensors also affect localisation accuracy (for more details, see Fig.(59) in appendix I). A compromise between the proton time profile width, the number of sensors, and the reference sensors is required for the TDOA algorithm. For example, having a sensor network with 7 sensors, the BP position can be localised with an error of 0.41 mm for a proton pulse of 4 μs . The sensor configuration is crucial in localising the BP in pre-clinical or clinical applications. The number of sensors used impacts the localisation accuracy, especially when comparing configurations with 7 sensors to those with 3 sensors. Notably, for shorter pulse widths, utilising 7 sensors results in diminished errors, whereas, for longer pulses, the error increases. Consequently, choosing an appropriate sensor configuration is paramount for achieving accurate localisation of the BP.

All results for the multilateration performed with TOA and TDOA depending on the proton profile width are reported in Tables(17,18). We can conclude that for wider proton profile width, it is preferable to have an ideal/optimal sensor position to reduce ToF error.

Pulse Width	$\epsilon^{n=3}$ [mm]	$\epsilon^{n=7}$ [mm]	$\epsilon^{n=13}$ [mm]	$\epsilon^{n=27}$ [mm]	$\epsilon^{n=39}$ [mm]	$\epsilon^{n=52}$ [mm]
1 μs	0.30	0.23	0.25	0.26	0.26	0.26
2 μs	0.29	0.21	0.21	0.21	0.21	0.21
3 μs	0.40	0.28	0.29	0.30	0.30	0.30
4 μs	0.43	0.22	0.21	0.21	0.21	0.21
5 μs	0.39	0.28	0.29	0.30	0.31	0.31
6 μs	0.34	0.52	0.55	0.57	0.59	0.59
7 μs	0.35	0.90	0.95	0.98	1.00	1.00
8 μs	0.36	1.02	1.06	1.06	1.11	1.10
9 μs	0.39	1.60	1.69	1.67	1.75	1.73
10 μs	0.55	2.27	2.41	2.36	2.47	2.44

Table 17: Multilateration error in BP position for different proton time profile widths using the TOA algorithm, varied from 1 μs to 10 μs . The BP is located in the centre of the sensor array. The localisation was performed with multiple sensor configurations. The sensor configuration varied from a minimum of 3 to 52 sensors. For all the cases considered, the multilateration was assessed with the *max envelope* ToF extraction method.

Pulse Width	$\epsilon^{n=3}$ [mm]	$\epsilon^{n=7}$ [mm]	$\epsilon^{n=13}$ [mm]	$\epsilon^{n=27}$ [mm]	$\epsilon^{n=39}$ [mm]	$\epsilon^{n=52}$ [mm]
1 μs	0.27	0.23	0.28	0.30	0.30	0.31
2 μs	0.30	0.25	0.29	0.32	0.32	0.32
3 μs	0.40	0.32	0.35	0.37	0.37	0.37
4 μs	0.51	0.41	0.44	0.47	0.47	0.47
5 μs	0.53	0.46	0.52	0.54	0.55	0.55
6 μs	0.53	0.45	0.55	0.58	0.59	0.60
7 μs	0.56	0.44	0.58	0.61	0.63	0.64
8 μs	0.52	0.41	0.59	0.62	0.66	0.66
9 μs	0.52	0.46	0.63	0.67	0.71	0.72
10 μs	0.54	0.59	0.72	0.76	0.80	0.80

Table 18: Multilateration error in BP position for different proton time profile widths using the TDOA algorithm, varied from 1 μs to 10 μs . The BP is located in the centre of the sensor array. The localisation was performed with multiple sensor configurations. The sensor configuration varied from a minimum of 3 to 52 sensors; the reference sensor was always the axial one. For all the cases considered, the multilateration was assessed using the *max envelope* ToF extraction method.

4.4.3 Multilateration for Different Beam Spatial Locations

Tables(19,21) display the BP error in position resulting from multiple beam offsets applied along the x, y, and z-axis, for the multilateration performed with TOA algorithm. The localisation error is determined based on the highest positive and negative beam offset applied. For the TOA algorithm, when applying the offset of ± 1 mm along the x-axis (beam axis), the localisation performed with three sensors yields an error of 0.36 mm and 0.53 mm. When the number of sensors is increased (i.e., $n \geq 7$), the localisation error remains stable and decreases to 0.21 mm for all beam offsets (all results are reported in Table(19)). When considering the beam offsets applied along the y-axis for the multilateration performed with three sensors, the same trend in the error was observed for an offset of ± 1 mm. Indeed, the error in localisation is 0.40 mm and 0.48 mm, corresponding to the maximum localisation error. It decreases in average to 0.21 mm for all beam offsets and when the number of sensors is increased (i.e., $n \geq 7$). See the results reported in Table(20). Lastly, when considering the beam offsets applied along the z-axis, the error in localisation increases to 1.23 mm and 0.86 mm for a beam offset of ± 1 mm and the BP retrieved with three sensors. For a beam offset of ± 0.5 mm, the localisation error decreases on average to 0.81 mm to 0.40 mm when increasing the number of sensors (i.e., $n \geq 7$). All results are reported in Table(21).

Tables(22,24) display the BP error in position resulting from multiple beam offsets applied along the x, y, and z-axis for the multilateration performed with the TDOA algorithm. When performing the multilateration with TDOA and considering a beam offset of ± 1 mm applied along the x-axis (beam axis), the localisation errors equal to 0.41 mm and 0.76 mm for the multilateration performed with three sensors, see Table(22). When the number of sensors increases (i.e., $n \geq 7$), the localisation error increases for all considered beam offsets. For example, considering 39 sensors, the localisation

error reaches a maximum of 0.79 mm and 0.87 mm (e.g., for a beam offset of -1 mm and -0.5 mm), respectively. For different sensor configurations and beam offsets, see Table(22). For the offset of ± 1 mm applied along the y-axis, the localisation error equals 0.56 mm and 0.48 mm for the multilateration performed with three sensors, as reported in Table(23). The error increases when the number of sensors is increased (i.e., $n \geq 7$), reaching a maximum of 0.71 mm and 0.76 mm, for a beam offset of ± 1 mm, as reported in Table(23). Finally, when the beam is moved along the z-axis, i.e., considering an offset of ± 1 mm and for the BP localised with three sensors, the localisation errors are 1.26 mm and 0.90 mm. The error increases when the number of sensors is increased (i.e., $n \geq 7$) to 1.40 mm and 1.05 mm, respectively, as reported in Table(24).

To summarise the multilateration performed with TOA, all the results are reported in Tables(19,21). It was demonstrated that the accuracy of the BP position localisation heavily depends on the direction of the beam offsets. The localisation error is consistently lower when the offsets are applied along the x-axis (beam axis) and the y-axis, compared to when the offsets are applied along the z-axis. For the multilateration performed considering offsets along the x-axis, the maximum error in position was equal to 0.48 mm. Moreover, for offsets applied along the y-axis, the maximum error in position was equal to 0.53 mm. This is likely because the y and z-axes are perpendicular to the direction of the beam, whereas the x-axis is parallel to it. The error in BP position was more sensitive for the beam offsets applied along the z-axis. The maximum error in position was equal to 1.20 mm for the multilateration performed with 7 to 52 sensors. The results also show that placing the sensors optimally and increasing the number of sensors can help compensate for the localisation error, leading to a more accurate position estimate. It is important to note that the asymmetry of the error in position observed when considering multiple offsets is not necessarily an indication of a problem with the multilateration setup. Other factors, such as the beam asymmetry, the simulation grid spacing ($200 \mu\text{m}$ in all directions) and numerical optimisation fluctuations, also contribute to the observed asymmetry on the multilateration error output given a symmetric beam offset, i.e., an offset of ± 1 mm.

Nonetheless, the results obtained from this study provide valuable insights for understanding that the error in position may be strongly dependent on the beam spatial location w.r.t the sensors. Because by moving the beam spatially (i.e., along all axes), the error on ToF increases, e.g., when considering a beam offset of ± 1 mm. Hence, the error in localising the BP position also increases.

For the multilateration performed with TDOA, higher errors were obtained compared to TOA, as reported in Tables(19,23). The lowest localisation error of 0.41 mm was obtained when moving the beam position in the x-axis for a beam offset of 1 mm. In this case, the error in ToF is equal between the two lateral sensors. Hence, the significant contribution to the localisation error depends on the reference sensor. Increasing the number of sensors increases the error on the BP localisation for different beam offsets because the error on ToF is not equally distributed when the beam is moved along the x-axis. This is also the case for the multilateration, considering the beam offsets applied along the y-axis. The error was systematically below 0.57 mm for the localisation performed with three sensors, reaching a minimum of 0.45 mm for a beam offset of 0.5 mm. For the localisation performed with three sensors, the error is equal for the two lateral sensors. Hence, lower error in position for all beam offsets. The maximum error equals 1.40 mm for the beam moving along the z-axis (localisation performed with $n \geq 7$). The accuracy of the BP localisation resulted in being sensitive to the offsets applied to the beam position. Similar to the TOA, the asymmetry of the error in position observed when considering multiple offsets does not necessarily indicate a problem with the multilateration setup. The same factors previously mentioned (i.e., beam asymmetry, grid spacing, numerical optimisation fluctuations and beam out of plane) affect the asymmetry on the localisation error. Furthermore, the reference sensor introduces another level of complexity for the TDOA algorithm.

n	$\epsilon^{Offset=-1}$ [mm]	$\epsilon^{Offset=-0.5}$ [mm]	$\epsilon^{Offset=0}$ [mm]	$\epsilon^{Offset=0.5}$ [mm]	$\epsilon^{Offset=1}$ [mm]
3	0.53	0.48	0.38	0.40	0.36
7	0.22	0.21	0.21	0.21	0.20
13	0.21	0.21	0.21	0.21	0.20
27	0.21	0.21	0.21	0.20	0.20
39	0.21	0.21	0.21	0.21	0.20
52	0.21	0.21	0.21	0.21	0.20

Table 19: TOA Multilateration of the BP position for different beam offsets along the x-axis. The given applied offset was $Offset = (-1, -0.5, 0, 0.5, 1)$ mm. The localisation and the error in position were performed using a different number of sensors. The considered proton profile width was $3.7 \mu s$. The multilateration was assessed with the *max envelope* ToF extraction method for all the cases considered

n	$\epsilon^{Offset=-1}$ [mm]	$\epsilon^{Offset=-0.5}$ [mm]	$\epsilon^{Offset=0}$ [mm]	$\epsilon^{Offset=0.5}$ [mm]	$\epsilon^{Offset=1}$ [mm]
3	0.40	0.37	0.38	0.42	0.48
7	0.20	0.20	0.21	0.23	0.25
13	0.20	0.20	0.21	0.22	0.23
27	0.20	0.20	0.21	0.22	0.22
39	0.20	0.20	0.21	0.22	0.23
52	0.20	0.20	0.21	0.22	0.23

Table 20: TOA Multilateration of the BP position for different beam offsets along the y-axis. The given applied offset was $Offset = (-1, -0.5, 0, 0.5, 1)$ mm. The localisation and the error in position were performed using a different number of sensors. The considered proton profile width was $3.7 \mu s$. The multilateration was assessed with the maximum signal envelope ToF extraction method for all the cases considered.

n	$\epsilon^{Offset=-1}$ [mm]	$\epsilon^{Offset=-0.5}$ [mm]	$\epsilon^{Offset=0}$ [mm]	$\epsilon^{Offset=0.5}$ [mm]	$\epsilon^{Offset=1}$ [mm]
3	0.86	0.52	0.38	0.86	1.23
7	0.80	0.40	0.21	0.80	1.20
13	0.80	0.40	0.21	0.80	1.20
27	0.80	0.40	0.21	0.80	1.20
39	0.80	0.40	0.21	0.80	1.20
52	0.80	0.40	0.21	0.80	1.20

Table 21: TOA Multilateration of the BP position for different beam offsets along the z-axis. The given applied offset was $Offset = (-1, -0.5, 0, 0.5, 1)$ mm. The localisation and the error in position were performed using a different number of sensors. The considered proton profile width was $3.7 \mu s$. The multilateration was assessed with the *max envelope* ToF extraction method for all the cases considered.

n	$\epsilon^{Offset=-1}$ [mm]	$\epsilon^{Offset=-0.5}$ [mm]	$\epsilon^{Offset=0}$ [mm]	$\epsilon^{Offset=0.5}$ [mm]	$\epsilon^{Offset=1}$ [mm]
3	0.76	0.66	0.47	0.47	0.41
7	0.80	0.71	0.56	0.56	0.52
13	0.86	0.77	0.66	0.57	0.57
27	0.87	0.79	0.70	0.61	0.60
39	0.87	0.79	0.73	0.61	0.60
52	0.85	0.79	0.77	0.66	0.58

Table 22: TDOA Multilateration of the BP position for different beam offsets along the x-axis. The given applied offset was $Offset = (-1, -0.5, 0, 0.5, 1)$ mm. The localisation and the error in position were performed using a different number of sensors. The considered proton profile width was $3.7 \mu s$. The reference sensor was always the axial one. The multilateration was assessed using the *max envelope* ToF extraction method for all the cases considered.

n	$\epsilon^{Offset=-1}$ [mm]	$\epsilon^{Offset=-0.5}$ [mm]	$\epsilon^{Offset=0}$ [mm]	$\epsilon^{Offset=0.5}$ [mm]	$\epsilon^{Offset=1}$ [mm]
3	0.48	0.45	0.47	0.50	0.56
7	0.58	0.57	0.56	0.57	0.62
13	0.68	0.67	0.66	0.67	0.72
27	0.72	0.72	0.70	0.70	0.75
39	0.75	0.75	0.73	0.72	0.77
52	0.76	0.73	0.77	0.77	0.71

Table 23: TDOA Multilateration of the BP position for different beam offsets along the y-axis. The given applied offset was $Offset = (-1, -0.5, 0, 0.5, 1)$ mm. The localisation and the error in position were performed using a different number of sensors. The considered proton profile width was $3.7 \mu s$. The reference sensor was always the axial one. The multilateration was assessed with the *max envelope* ToF extraction method for all the cases considered.

n	$\epsilon^{Offset=-1}$ [mm]	$\epsilon^{Offset=-0.5}$ [mm]	$\epsilon^{Offset=0}$ [mm]	$\epsilon^{Offset=0.5}$ [mm]	$\epsilon^{Offset=1}$ [mm]
3	0.90	0.58	0.47	0.90	1.26
7	0.95	0.66	0.56	0.96	1.29
13	1.02	0.75	0.66	1.02	1.33
27	1.05	0.78	0.70	1.05	1.36
39	1.07	0.80	0.73	1.07	1.37
52	1.05	0.85	0.77	1.06	1.40

Table 24: TDOA Multilateration of the BP position for different beam offsets along the z-axis. The given applied offset was $Offset = (-1, -0.5, 0, 0.5, 1)$ mm. The localisation and the error in position were performed using a different number of sensors. The considered proton profile width was $3.7 \mu s$. The reference sensor was always the axial one. The multilateration was assessed with the *max envelope* ToF extraction method for all the cases considered.

5 Discussion and Prospects

“I am because we are...”

Ubuntu

5.1 Numerical Optimisation Methods

The performance of the numerical optimisation using the NLS method should be independent of the initial guess. Similarly, the numerical optimisation method should be capable of converging to either a local or global minimum, irrespective of the initial guess condition, hence needing the employment of global optimisation methods. The convergence issues of the numerical optimisation algorithm are a classical problem in source localisation. When using NLS optimisation methods, a typical approach to overcome this problem is to modify the cost functions using weighting factors to improve the convergence for a more accurate and precise optimisation solution [110]. Regrettably, many existing algorithms designed for solving NLS problems fail to meet this requirement.

For TDOA localisation, our study shows that the Simplex algorithm exhibits higher sensitivity to the initial guess condition, resulting in an FR of 5.42% compared to 0.57% with the Levenberg algorithm. Conversely, when employing the TOA method, the Simplex algorithm yields a lower FR for source localisation of 0% compared to 0.22% using the Levenberg algorithm. Regardless of the reference sensor, the numerical optimisation performed with the Levenberg algorithm consistently yields an FR below 1.12%. On the contrary, by varying the reference sensors (i.e., Bs_1 to Bs_3 and $l^{Ref,max}, l^{Ref,min}$), the FR for the numerical optimisation performed with the Simplex algorithm reached a maximum of 10.76%. These results emphasise the superior performance of the Levenberg algorithm in precisely localising the acoustic source, regardless of the initial guess spatial location. It is essential to point out that a global solution may not be guaranteed for Levenberg.

It would be interesting to perform a comprehensive analysis that compares the Levenberg algorithm with other algorithms, such as the genetic algorithm [171], differential evolution [172] and projection onto convex sets [173]. These algorithms are well known to guarantee global solutions. Projection onto convex sets algorithm has been demonstrated to have high-speed convergence rates, which can be helpful toward real-time multilateration without losing the localisation accuracy. The numerical optimisation algorithm will play an important role when localising the BP position in pre-clinical and clinical applications. The multilateration process must be faster than one millisecond to localise the BP position in real-time during patient treatment. This requirement arises because, at facilities equipped with a synchro-cyclotron accelerator, proton pulses are typically produced at a repetition rate of 1 kHz, meaning there is a pulse every millisecond. In this work, one multilateration process takes 22 milliseconds (for more detail, see appendix G.3).

5.2 Intrinsic Performances of TOA and TDOA

When considering ideal conditions, the multilateration performed with TOA and TDOA shows equivalent performance without uncertainties, whereas TDOA is more influenced by the source's position. Generally, the source should be located within the sensor array FOV, ideally at the centre. For the given sensor configuration, which features a triangular structure with a height of 36 mm and the range of uncertainties examined, selecting the reference sensor carefully allows TDOA to achieve a lower localisation average error⁶⁵ compared to TOA, specifically 2.32 mm against 2.68 mm when both random and systematic uncertainties are present. It is important to note that TOA exhibits greater robustness under random uncertainties, with an average error of 2.19 mm and a standard deviation⁶⁶

⁶⁵For compactness, the average error here is intended as average root mean square error, previously denoted as μ_{RMSE}^{FOV} .

⁶⁶For compactness, here the standard deviation here is intended as average root mean square error standard deviation, previously denoted as σ_{RMSE}^{FOV} .

of 0.41 mm, compared to TDOA's average error of 2.32 mm with a standard deviation of 0.66 mm. In contrast, TDOA is more robust when only systematic uncertainties are considered, as the errors effectively cancel out⁶⁷, resulting in an average error of 7.8×10^{-4} mm and a standard deviation of 4.8×10^{-4} mm. In comparison, TOA reaches an average error of 1.03 mm with a standard deviation of 0.52 mm [150].

For both multilateration algorithms in 2D and 3D, their performance is influenced by geometrical factors, i.e., source location w.r.t to the sensors. Nevertheless, the dependency on geometry is less critical for the TOA compared to TDOA. Furthermore, there are additional considerations for the TDOA algorithm. Since the TDOA accuracy is highly dependent on geometry, i.e., the number of sensors, sensor placement and reference sensors, the geometry dependency can be mitigated by increasing the number of sensors and changing the array geometry. This is a typical approach used to boost the robustness of the TDOA algorithm [174, 175]. Moreover, during our studies, it was concluded that increasing the number of sensors improves the performance of the multilateration using TDOA compared to TOA. Particular attention should be paid to arranging the sensors to guarantee the source is inside the FOV. In traditional localisation techniques, the FOV limitation often poses challenges when the source is positioned beyond the sensor's observable region. A common strategy to solve this problem and achieve optimal performance from both algorithms is to employ a hybrid approach that combines TOA and TDOA into a single algorithm [176]. The hybrid algorithm can effectively estimate the source's location, even when it falls outside the FOV. Another notable advantage is achieving higher localisation accuracy than a single approach based solely on TOA or TDOA [177, 178].

5.3 Signal Acquisition Start Time

The ionoacoustic measurements performed with 20 and 22 MeV proton beams were triggered by a stable synchronisation signal from the Tandem accelerator's chopping system. The exact time difference between when the synchronisation signal was initiated and when the protons actually entered the medium was measured with a resolution finer than 0.1 ns, equivalent to under 150 nm in water. This offset was then corrected during data analysis, ensuring that the systematic error remained negligible compared to the ToF estimation. Thus, the BP localisation with TOA provided the best results, as seen in simulations. In some proton therapy facilities, a stable synchronisation signal may be unavailable, leading to potential jitters of up to 850 ns (1.3 mm in water) [76]. Alternatively, triggering can use an external detector sensing secondary emissions, which may introduce additional offsets. Multilateration using TDOA algorithm is recommended if synchronisation is uncertain or unstable [150].

5.4 Bragg Peak Localisation in Homogeneous Media

For the BP localisation using ionoacoustic signals in a homogeneous medium with a known speed of sound and the sensors placed optimally, the main uncertainties stem from the measurement starting time, particularly the systematic error in determining when the first protons enter the media and the ToF extraction error. The multilateration of the BP position performed *in-silico*, using an arc sensor arrangement, showed that the ToF error varies with the sensor position relative to the BP and is uncorrelated across the sensor array. Therefore, TOA offers more precise BP localisation, which

⁶⁷For a detailed mathematical analysis of TDOA in the presence of systematic uncertainties, refer to eqs.(4.5,4.6).

can be improved by optimising sensor positions to reduce ToF error. Simulation studies also reveal that TDOA performance depends significantly on the reference sensor. In ionoacoustic applications, localisation error can increase eightfold based on the reference sensor position and the ToF error. However, multilateration accuracy is not directly tied to the ToF error of any single reference sensor, as illustrated in Fig.(40b). The best reference sensor for TDOA is usually one with a ToF error near the average, as this helps to balance out the errors across the entire sensor array/network [150].

In section 4.2.2, it was shown that applying the threshold technique to the estimated ToF data can enhance BP localisation. The enhancement is achieved by discarding the sensors which have high errors on the ToF (i.e., error > 0.1 mm). The 0.1 mm threshold improves the localisation by decreasing the error from 0.62 mm to 6 μ m. The threshold on the ToF was chosen by considering the error in ToF depending on the sensor position (see Fig.(40a)). For pre-clinical beams, it was shown that the superimposition between the compression and rarefaction peaks affects the ToF estimation (see Figs.(40a,41b)). From a signal-processing point of view, this superimposition could be solved by “borrowing” the peak detection technique used in electrocardiogram (ECG) [179]. The IA signal obtained in water using an axial sensor exhibits a shape almost resembling the QRS⁶⁸ complex, which allows using the wave delineation approach, commonly used for QRS signal delineation based on slope information. These wave delineation approaches exhibit robustness, particularly against low-frequency noise [181, 182]. Integration with *zero-crossing* techniques further improves ToF estimation. Additionally, employing spectral analysis, similar to electroencephalogram signal segmentation, may be crucial for IA signals. This should aid in categorising and recognising IA signals based on their frequency content, facilitating differentiation from background noise. A thorough investigation in this direction is essential for a comprehensive understanding and application of these techniques in IA signals. Real-time ECG detection is already a well-developed signal processing technique. Therefore, approaches such as real-time QRS detection [183, 184] could be used or modified for IA applications, especially for ToF estimation and detection in real-time applications.

Enhancing the information extracted from the IA signals (e.g., the accuracy of the ToF estimation) for pre-clinical and clinical applications requires advanced signal processing and classification techniques. These methods are often specific to the application, such as ionoacoustics. It was already shown that Wavelet decomposition can reduce signal averaging, minimising the minimum dose delivered to the patient [185, 186]. However, a focused study exclusively for IA applications combining different signal denoise techniques (i.e., Kalman filtering⁶⁹) may be necessary. To integrate various signal denoising techniques, such as Wavelet and Kalman filters, it is paramount to assess the specific features of the IA signals. Additionally, it is recommended to apply signal threshold techniques based on factors such as the beam energy, proton pulse time structure, and any other factors that may impact the shape of the IA signal.

⁶⁸The QRS complex mirrors the hearts depolarisation of the right and left ventricles, for more see [180, p. 412-441].

⁶⁹For more detail on the Kalman filters applied to acoustic signals, see [187, 188, 189].

5.5 Bragg Peak Localisation in Heterogeneous Media

The research conducted during this work focused “solely” on irradiating a water⁷⁰ phantom, where the speed of sound remains constant at a fixed measured temperature. In contrast, *in vivo*, the speed of sound fluctuates according to tissue type (different tissues have different speed of sound), which could reduce BP localisation accuracy [150]. By assuming a conservative 5% deviation in the average speed of sound along the acoustic path, we observed that the localisation error increased by roughly 2 mm for the evaluated geometry. Thus, applying multilateration for *in vivo* range verification should incorporate sound speed aberration, akin to techniques used in wireless capsule endoscopy tracking via radio-frequency signals [91, 93]. To address this, the speed of sound might be empirically determined from pre-treatment X-ray imaging [190] or mapped using ultrasound [191] shortly before treatment. Notably, a prior *in-silico* study indicated that over- and under-estimations of the speed of sound across the propagation path generally offset each other for the clinical scenarios examined (liver and prostate), leading to comparable localisation errors whether using the sound speed in water or the average speed derived from X-ray imaging [136].

When estimating the ToF for the homogeneous case, a ToF ground truth was needed to choose the ToF threshold correctly. For *in vivo* applications, the ToF ground truth could be estimated from the treatment plan. Therefore, the threshold can be predicted by accurately knowing the setup or having reference threshold values provided by simulated data. Furthermore, the distance between the tumour and sensor elements could be assessed using the information on the tumour location obtained from real-time ultrasound imaging. With this information, a ToF threshold can be defined for the heterogeneities relevant to IA applications.

5.6 Multilateration in Small Animals

In summary, the localisation of the BP position considering a pre-clinical beam energy of 50 MeV and employing the TOA algorithm depends on factors such as the ToF estimation, proton time profile width (e.g., lower ToF error for proton time profiles from 3 μ s to 6 μ s, see Fig.(48c) and Fig.(48c)) and the sensor arrangement. Furthermore, an optimal number of sensors that minimise the error in ToF would improve the localisation performance. Performing the multilateration with TDOA would introduce another variable to localise the BP position, i.e., the reference sensor. Therefore, localising the BP position for different beam offsets would also require an optimal reference sensor. When moving the proton beam to different spatial locations (i.e., laterally along the z-axis), the error in ToF is more likely to increase for lateral (z-axis) than axial (x-axis) beam offsets, at least for the considered sensor arrangement (setup in Fig.(25)). Increasing the error in ToF leads to higher errors in the BP localisation. Therefore, for the TDOA algorithm, the optimal reference sensors would also change depending on the beam position. For more details on the localisation error due to the beam position for both algorithms (TOA and TDOA), refer to the summary reported in appendix J.

In the investigated small animal setup, the sensors have a diameter of 1 mm. Distortions on the IA signal are also expected to change for larger sensor diameters, which would translate into an over/under-estimation of the ToF and, consequently, have an impact on the BP localisation. Moreover, the setup dimensions should be considered when having different beam offsets. The main issue in SIRMIO primarily arises from the Gaussian pulse being too broad compared to the time gap between the entrance and direct signals. The setup employed in this study showed that by moving the beam

⁷⁰The experimental studies conducted with heterogeneities, we have considered as a simple heterogeneities case. Meaning no significant variation on the speed of sound.

by ± 1 mm (along the z-axis, see Fig.(25b)), the error in localisation increases considerably (i.e., 1.20 mm and 1.40 mm for TOA and TDOA, respectively. For a beam range of 16.4 mm). This is because the signal shape differs in the near field (i.e., when the sensor is close to the source) from that in the far field, hampering the time-of-flight analysis. Accordingly, the sensors should not be placed too close to the beam during the BP localisation. For instance, when the beam is moved considering offsets along y/z-axes equal to ± 1 mm, before the multilateration, the ToF estimation algorithm should be automatised to discard those sensors' positions close to the beam position. The same approach could be applied to the axial sensors when moving the beam position along the x-axis. All in all, for the multilateration performed with TOA and TDOA, the poor localisation performance when moving the beam along the z-axis is due to the sensor arrangement. In other words, the error is strengthened by the 2D sensor arrangement, resulting in an inability to resolve the beam when offset along the z-axis. Another way to conceptualise this is that the beam falls outside the FOV.

The results presented in this work show the need for an initial evaluation based on the treatment plan (pre-treatment IA simulation) to identify the optimal sensor arrangement and proper reference sensor selection, aiming to minimise ToF estimation errors, as discussed in [150]. However, further investigation is required to refine sensor positioning, particularly regarding the stability of the optimised configuration when the BP shifts within the treatment field. This was evident in the experimental analysis of the three sensor setup (see section 4.3.1) and for the beam offsets applied for the small animal setup (see section 4.4.3), both studies aimed to mimic a treatment plan. In one case, experimentally and with only 3 sensors and in another, via simulation with 52 sensors. For the experimental case, when the BP was localised with 3 sensors, localisation errors for TOA and TDOA were similar when the proton beam shifted laterally by 5 mm, mainly due to a more significant ToF error. Therefore, determining the optimal sensor positions, number, and reference sensor for TDOA is crucial, especially for the single beams with the highest intensity in the treatment plan. This suggests that a fixed sensor array geometry may be suboptimal for multilateration. Instead, optimised for each treatment plan, a sparse detector arrangement would likely provide the most accurate BP localisation. Additionally, sensor positioning should accommodate specific treatment plan constraints, ensuring that areas where the beam enters remain free of detectors to avoid interference from high-density, high atomic number (high-Z) piezoelectric sensors. For the SIRMIO project, a sterile environment will be maintained for the small animal using a specially designed holder during irradiation [54].

For optimal SNR, IA sensors should be in direct contact with the patient⁷¹ skin, so positioning the detectors before sealing the sterile environment onto the SIRMIO platform is essential. Bulky commercial ultrasonic detectors used in this study are unsuitable for the proton imaging field-of-view due to their high water equivalent thickness (WET $\gg 1$ cm) and atomic number Z, which increase proton scattering and reduce image resolution, further limiting IA detector placement options. Alternatively, sensors with a lower material budget could be considered. Potential candidates include emerging ultrasonic transducers like micromachined transducers [73], optical hydrophones [192], and conventional piezoelectric polymers with tailored acoustic designs [193]. However, further studies are necessary to determine if these sensors are sensitive enough to detect the very low pressures (a few mPa, at least one order of magnitude lower than clinical scenarios) expected in SIRMIO after proton beam degradation [194].

⁷¹Small animal in our case.

5.7 Towards Real-time Applications

The real-time multilateration workflow could be similar to the setup described in section 3.2.3. The transducer spatial location should be ideally estimated in real-time (e.g., using an optical tracking system) to also account for possible anatomical changes. Consequently, the BP position should be retrieved in real-time. From the results of the multilateration performed with five sensors, one challenge was correctly estimating the transducer spatial location in real-time. Upon reviewing the *horseshoes* array design, we identified a 9.27 mm error between the axial sensor and the centre of the beam entrance window. The error was decreased to 0.96 mm after applying the rigid co-registration. Without improving the transducer's spatial location accuracy and the ToF estimation, the BP localisation has ranged from 0.72 mm and 0.67 mm for TOA and TDOA, respectively. Considering the improvement in the transducer's spatial location given by the CPD registration and further improving the ToF estimation (i.e., by applying the Gaussian fitting as discussed in section 4.3.3), the error in localisation decreased to values of 0.36 mm and 0.12 mm for TOA and TDOA, respectively.

It would be beneficial to use a robust self-localisation algorithm to compensate for real-time uncertainties in the sensor placement, especially to solve the patient motion during the treatment delivery (e.g., due to breathing). Self-localisation algorithms are widely implemented in robotics [195]. This approach should be similar to the one implemented for the *horseshoes* setup (see section 3.2.3). However, because of the patient motion and other artefacts, the spatial location of the sensors will change. Indeed, the correction of the transducer spatial location employing the CPD algorithm can be ideally analogous to the patient motion compensation. In other words, if the patient breathes, the transducer spatial locations are expected to change. Therefore, approaches similar to the one applied in motion compensation during *in vivo* Optical Coherence Tomography (OCT) can be used. The motion compensation approach seeks to register and align multiple OCT volume scans recorded sequentially or from various laser beam angles to estimate and correct for a given patient motion, i.e., typically during radiotherapy [196, 197], and eye or hearing surgery [198, 199]. This method can be adapted to the multilateration of the BP using IA signals. Furthermore, such approach can also be used for IA image co-registration (for more on co-registration, see [74]) and time reversal reconstruction.

5.8 IA Range Verification in Clinical Applications

Considering optimal signal acquisition synchronisation, accurate speed of sound correction, and precise sensor placement, have been extensively addressed in [150]. The primary limitation of multilateration is the ToF extraction. The previously presented results show that the IA signal shape varies with sensor position, especially at pre-clinical energies where the proton range is short compared to the propagation length. In such cases, lateral signals combine acoustic waves from the BP, plateau region, and energy discontinuities at the phantom entrance, leading to ToF errors. For clinical scenarios, the proton range increases from 4 mm at 20 MeV to 122 mm at 130 MeV in water, improving wavefront separation. Fig.(50) presents the ToF error for a 130 MeV proton beam, with a maximum error of $0.75 \mu\text{s}$ (1.11 mm), consistent with previous studies [76, 200], indicating the applicability of low-energy findings to clinical settings. Patient irradiation also generates acoustic emissions at tissue interfaces, but high spatial frequency signals are expected to be filtered out with the clinically available microsecond proton pulse. Therefore, millimetre accuracy appears achievable in areas without bones or air cavities, as confirmed by recent studies on an anthropomorphic phantom [201, 202].

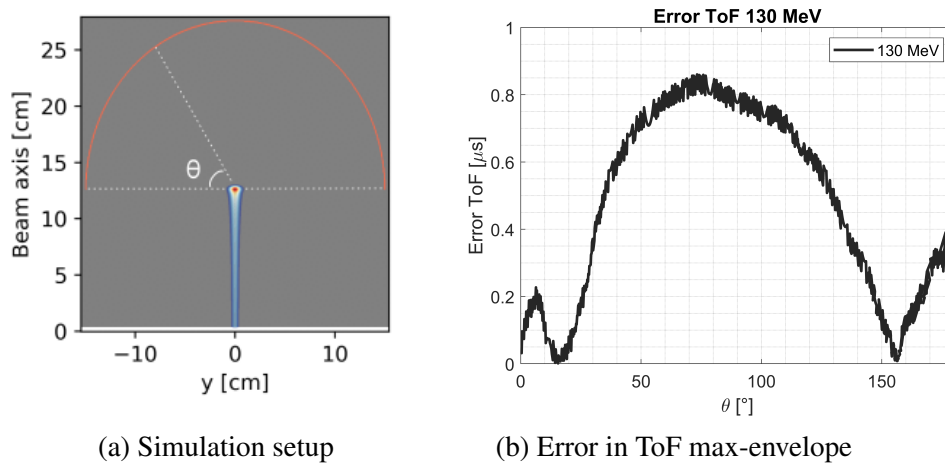


Figure 50: Evaluation of the ToF at clinical energy: (a) The simulation setup illustrates the proton beam position (colour map) in relation to the sensor arc (red line). The propagation medium's density is represented in greyscale. (b) The ToF error is determined based on the maximum of the signal envelope, varying according to the sensor position. Figure extracted from the supplementary material of [150].

5.9 Multilateration and TRR Reconstruction

As discussed in section 2.4, the TRR approach offers an alternative method for localising the BP position. This technique reconstructs the initial pressure based on the deposited dose within a given medium, similar to the back projection algorithm recently investigated for real-time dose reconstruction using IA signals [145]. Fig.(51) depicts a typical results obtained through TRR, where the initial dose is reconstructed, and the BP position is determined accordingly. The main advantage of the TRR is that it outputs the dose distribution and not just the BP position. Notably, Pratik Dash, in the context of the SIRMIO project used a similar setup in his master's thesis [148]. The author accurately reconstructed the BP position, achieving an accuracy of less than 0.5 mm in a homogeneous medium. The localisation approach using TRR was also benchmarked with experimental studies. Compared to multilateration, TRR can simultaneously output the dose distribution and the BP position. This information can later be used for dose monitoring (dosimetry) and for IA/US co-registration. The main drawback of TRR is the computation time⁷² and the number of sensors to have an accuracy below 1 mm. The impact of the number of sensors on the reconstructed BP position using TRR was investigated in [148, p. 34-35]; the number of sensors varied from 2 to 13. The best results were obtained with 13 sensors, having an accuracy of 0.8 mm after 60 iterations. Conversely, the advantage of multilateration lies in its implementation simplicity, i.e., fewer sensors, faster localisation time (i.e., 22 milliseconds⁷³) and the ability to localise the BP position in 3D with only four sensors. Furthermore, it can use absolute (TOA) or relative (TDOA) localisation approaches, which can be combined. The major drawback is that it cannot output the reconstructed dose and cannot be used for dose monitoring. While we do not intend to compare TRR and multilateration algorithms directly, both approaches can effectively localise the BP position. On the one hand, multilateration offers the advantage of localising the BP position using only three sensors, assuming they are appropriately chosen. On the

⁷²i.e., when using a CPU, the computation time is about 6 minutes, and it can be decreased to 40 seconds using a GPU.

⁷³More studies would be required to decrease this 22 milliseconds computation time by using GPU-accelerated computing.

other hand, the TRR method, in principle, can reconstruct the deposited dose distribution. By combining these two localisation approaches, we can leverage the strengths of both algorithms to achieve the highest possible accuracy in localising the BP position. For example, a routine can be created to run both algorithms simultaneously. The multilateration can output the BP position 2D/3D while the TRR outputs the reconstructed dose distribution. Furthermore, since both methods aim to localise the BP position, they can be combined as follows: first, multilateration for real-time application during treatment delivery. Second, TRR for dose reconstruction and treatment adaptation from one treatment fraction to the other.

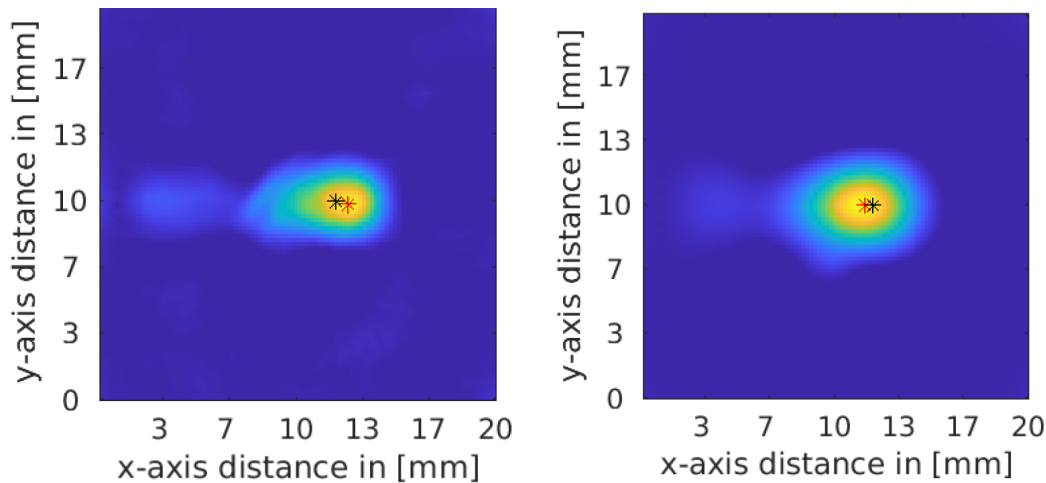


Figure 51: Dose reconstruction and BP localisation using TRR algorithm (pencil beam of 50 MeV in water). (left figure) BP localised with an error of 0.63 mm, BP ground truth indicated with a black asterisk, and reconstructed BP position indicated with a red asterisk. For this particular result, no proton time profile was considered. (right figure) BP localised with an error of 0.4 mm, BP ground truth indicated with a black asterisk, and reconstructed BP position indicated with a red asterisk. A Gaussian time profile with an FWHM of $2 \mu\text{s}$ was considered. The localised BP position is overlaid on the reconstructed dose for both cases. Figures reproduced with courtesy of Pratik Dash. They were extracted from his master's thesis [148, p. 70].

Appendices

Appendix A Heterogeneity's Silicone Setup

In this experiment, a multi-layer silicone phantom was positioned near the entrance window with a water gap of approximately 0.83 mm between them. This gap was estimated using the signal envelope to calculate the time-of-flight, with the accuracy of the estimation depending on the method used.

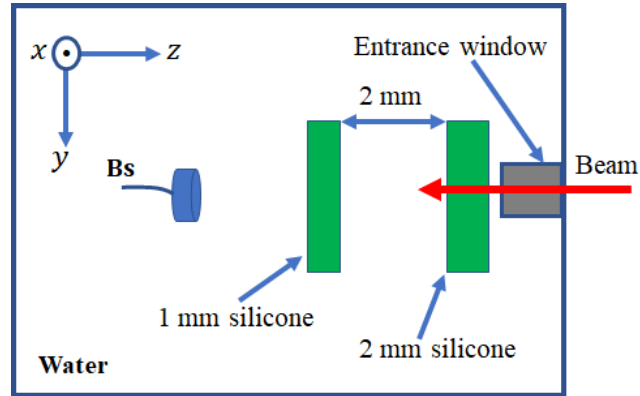


Figure 52: Initial setup showing both silicone layers positioned near the entrance window with a water gap between the entrance window and the thicker silicone layer.

Appendix B Multilateration 3D Setup

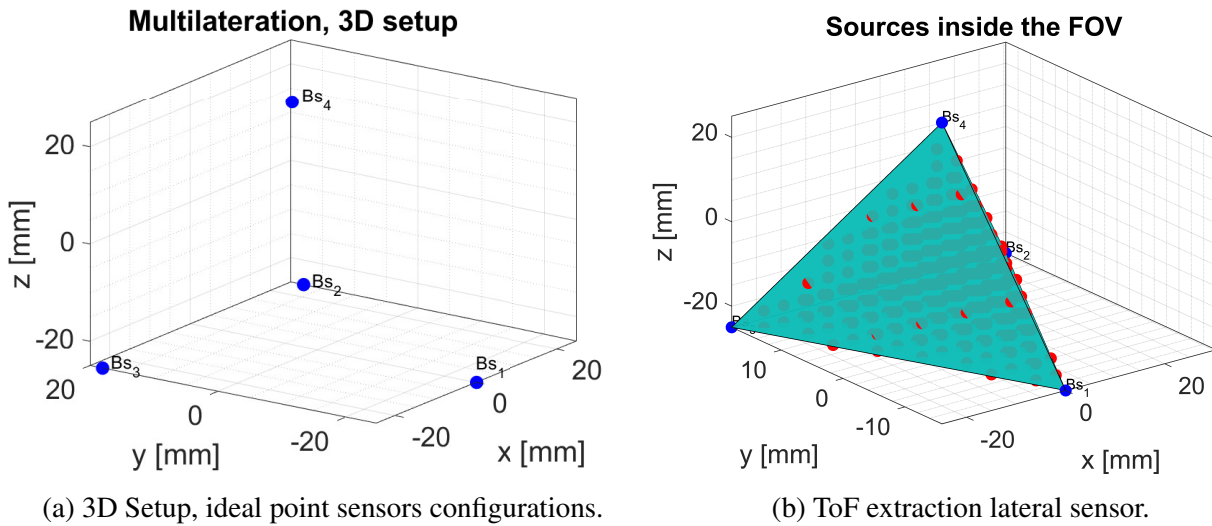


Figure 53: 3D Setup with ideal source localisation, (a) sensor Bs_1 , Bs_2 , Bs_3 and Bs_4 sensor configuration, (b) setup including all the point sources inside the FOV.

Appendix C 3D I-BEAT Experimental Setup

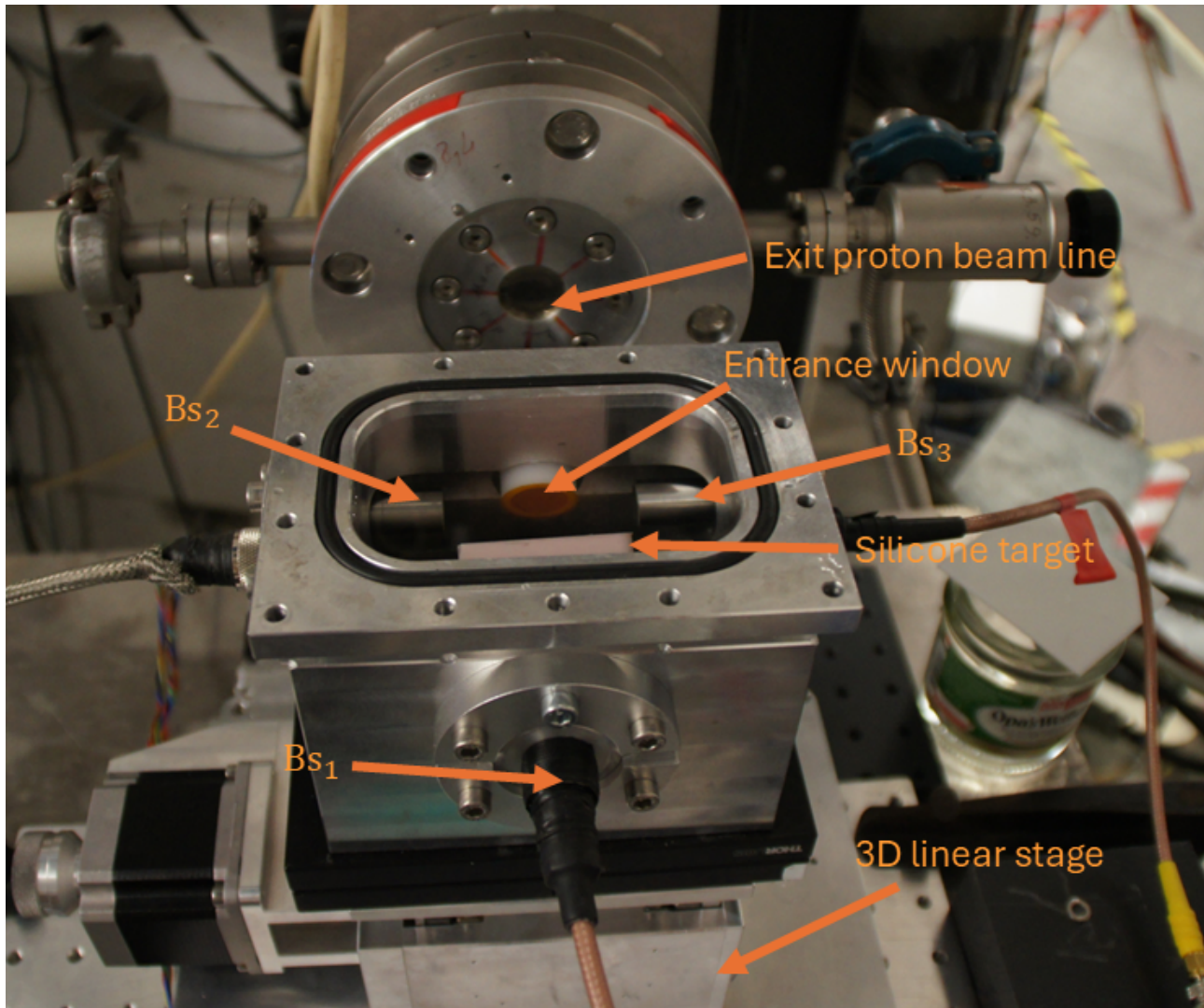
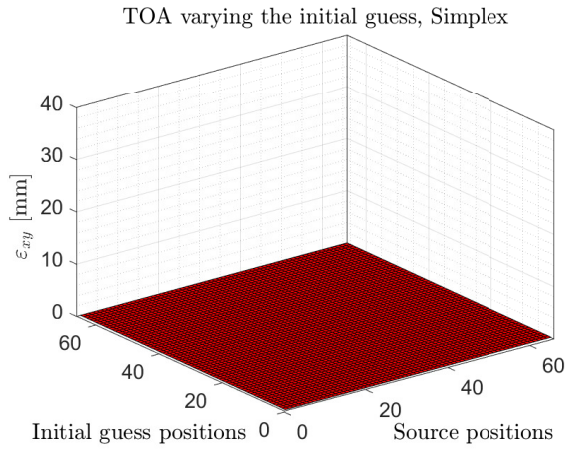
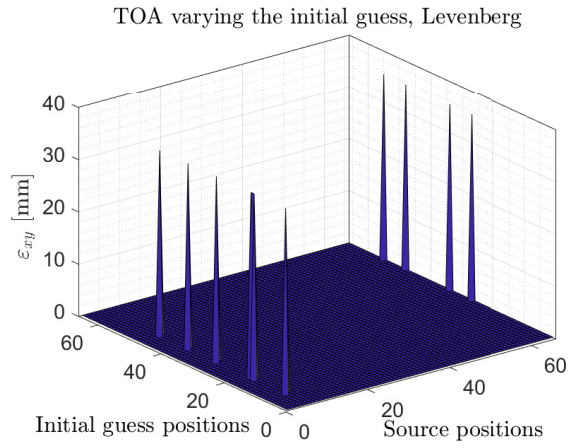


Figure 54: The experimental setup for the 3D I-BEAT detector consists of three sensors (denoted as B_{S1} , B_{S2} , and B_{S3}) and a silicon target. The silicon target was removed for the experiments discussed in this thesis, and all measurements were conducted without it. The 3D I-BEAT detector is mounted on a 3D linear stage to ensure precise and secure positioning and alignment.

Appendix D FR Simplex and Levenberg algorithms

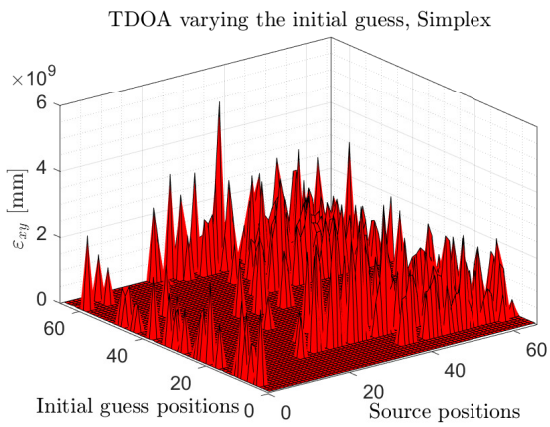


(a) TOA varying the initial guess, Simplex.

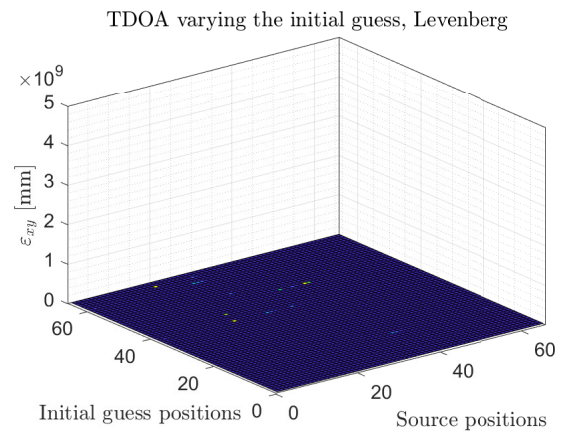


(b) TOA varying the initial guess, Levenberg.

Figure 55: FR multilateration performed with TOA method using Simplex and Levenberg algorithms.



(a) TDOA varying the initial guess, Simplex.



(b) TDOA varying the initial guess, Levenberg.

Figure 56: FR multilateration performed with TDOA method using Simplex and Levenberg algorithms.

Appendix E Multilateration and Optimisation Robustness

E.1 2D Multilateration Robustness Random Uncertainties

Multilateration Methods	Reference Sensor	μ_{RMSE} [mm]	μ_{RMSE}^{FOV} [mm]	σ_{RMSE} [mm]	σ_{RMSE}^{FOV} [mm]
TDOA	B_{S_1}	5.81	2.32	6.33	0.66
	B_{S_2}	6.50	2.32	6.33	0.68
	B_{S_3}	6.50	2.34	6.44	0.76
	$l^{Ref,max}$	5.07	2.33	4.72	0.70
	$l^{Ref,min}$	5.80	2.32	6.32	0.68
	$l^{Ref,mean}$	5.37	2.32	4.97	0.66
TOA	<i>none</i>	2.33	2.19	0.34	0.41

Table 25: Comparison of the performance of 2D multilateration using TOA and TDOA considering random uncertainties. TDOA is performed for different reference sensors such as: B_{S_1} , B_{S_2} , B_{S_3} , $l^{Ref,max}$, $l^{Ref,min}$, $l^{Ref,mean}$.

E.2 2D Multilateration Robustness Systematic Uncertainties

Multilateration Methods	Reference Sensor	μ_{RMSE} [mm]	μ_{RMSE}^{FOV} [mm]	σ_{RMSE} [mm]	σ_{RMSE}^{FOV} [mm]
TDOA	B_{S_1}	2.0×10^{-3}	7.8×10^{-4}	1.8×10^{-3}	4.8×10^{-5}
	B_{S_2}	2.4×10^{-3}	1.2×10^{-3}	2.0×10^{-3}	1.2×10^{-3}
	B_{S_3}	2.3×10^{-3}	1.1×10^{-3}	2.1×10^{-3}	8.9×10^{-4}
	$l^{Ref,max}$	1.9×10^{-3}	8.4×10^{-4}	1.5×10^{-3}	5.7×10^{-4}
	$l^{Ref,min}$	3.0×10^{-3}	1.5×10^{-3}	2.3×10^{-3}	1.3×10^{-3}
	$l^{Ref,mean}$	2.0×10^{-3}	6.9×10^{-3}	1.9×10^{-3}	3.8×10^{-3}
TOA	<i>none</i>	1.53	1.03	0.59	0.52

Table 26: Comparison of the performance of 2D multilateration using TOA and TDOA considering systematic uncertainties. TDOA is performed for different reference sensors such as: B_{S_1} , B_{S_2} , B_{S_3} , $l^{Ref,max}$, $l^{Ref,min}$, $l^{Ref,mean}$.

E.3 2D Multilateration Robustness Random and Systematic Uncertainties

Multilateration Methods	Reference Sensor	μ_{RMSE} [mm]	μ_{RMSE}^{FOV} [mm]	σ_{RMSE} [mm]	σ_{RMSE}^{FOV} [mm]
TDOA	B_{S_1}	5.37	2.32	4.97	0.66
	B_{S_2}	6.62	2.31	9.21	0.67
	B_{S_3}	5.89	2.32	6.62	0.70
	$l^{Ref,max}$	7.15	2.32	10.13	0.70
	$l^{Ref,min}$	5.81	2.31	6.38	0.67
	$l^{Ref,mean}$	5.37	2.31	4.99	0.66
TOA	<i>none</i>	3.02	2.68	0.55	0.63

Table 27: Comparison of the performance of 2D multilateration using TOA and TDOA, random and systematic uncertainties modelled simultaneously. TDOA is performed for different reference sensors such as: B_{S_1} , B_{S_2} , B_{S_3} , $l^{Ref,max}$, $l^{Ref,min}$, $l^{Ref,mean}$.

E.4 3D Multilateration Robustness Random Uncertainties

Multilateration Methods	Reference Sensor	μ_{RMSE} [mm]	μ_{RMSE}^{FOV} [mm]	σ_{RMSE} [mm]	σ_{RMSE}^{FOV} [mm]
TDOA	Bs_1	9.47	3.35	8.86	0.74
	Bs_2	10.59	3.35	13.74	0.74
	Bs_3	10.35	3.35	12.90	0.74
	Bs_4	9.03	3.35	7.74	0.75
	$l^{Ref,max}$	12.07	3.36	17.25	0.76
	$l^{Ref,min}$	9.14	3.35	7.85	0.74
	$l^{Ref,mean}$	9.05	3.35	7.72	0.74
TOA	<i>none</i>	4.03	3.14	1.03	0.42

Table 28: Comparison of the performance of 3D multilateration using TOA and TDOA considering random uncertainties. TDOA is performed for different reference sensors such as: $Bs_1, Bs_2, Bs_3, Bs_4, l^{Ref,max}, l^{Ref,min}, l^{Ref,mean}$.

E.5 3D Multilateration Robustness Systematic Uncertainties

Multilateration Methods	Reference Sensor	$\mu_{\epsilon_{RMSE}}$ [mm]	$\mu_{\epsilon_{RMSE}}^{FOV}$ [mm]	$\sigma_{\epsilon_{RMSE}}$ [mm]	$\sigma_{\epsilon_{RMSE}}^{FOV}$ [mm]
TDOA	Bs_1	3.4×10^{-3}	1.0×10^{-3}	2.7×10^{-3}	6.2×10^{-4}
	Bs_2	3.9×10^{-3}	3.9×10^{-3}	2.9×10^{-3}	1.1×10^{-3}
	Bs_3	3.7×10^{-3}	1.2×10^{-3}	2.7×10^{-3}	9.2×10^{-4}
	Bs_4	6.9×10^{-3}	1.6×10^{-3}	6.9×10^{-3}	1.3×10^{-3}
	$l^{Ref,max}$	3.5×10^{-3}	1.3×10^{-3}	2.3×10^{-3}	7.2×10^{-4}
	$l^{Ref,min}$	7.2×10^{-3}	1.3×10^{-3}	6.8×10^{-4}	7.2×10^{-4}
	$l^{Ref,mean}$	3.4×10^{-3}	9.2×10^{-4}	2.7×10^{-3}	5.4×10^{-4}
TOA	<i>none</i>	1.98	1.42	0.33	0.41

Table 29: Comparison of the performance of 2D multilateration using TOA and TDOA considering systematic uncertainties. TDOA is performed for different reference sensors such as: $Bs_1, Bs_2, Bs_3, Bs_4, l^{Ref,max}, l^{Ref,min}, l^{Ref,mean}$.

E.6 3D Multilateration Robustness Random and Systematic Uncertainties

Multilateration Methods	Reference Sensor	$\mu_{\epsilon_{RMSE}}$ [mm]	$\mu_{\epsilon_{RMSE}}^{FOV}$ [mm]	$\sigma_{\epsilon_{RMSE}}$ [mm]	$\sigma_{\epsilon_{RMSE}}^{FOV}$ [mm]
TDOA	Bs_1	9.45	3.35	8.61	0.74
	Bs_2	10.61	3.35	13.90	0.74
	Bs_3	10.28	3.35	12.35	0.75
	Bs_4	9.01	3.36	7.70	0.75
	$l^{Ref,max}$	12.05	3.36	16.98	0.76
	$l^{Ref,min}$	9.12	3.35	7.81	0.74
	$l^{Ref,mean}$	9.03	3.35	7.66	0.74
TOA	<i>none</i>	4.69	3.74	0.93	0.54

Table 30: Comparison of the performance of 3D multilateration using TOA and TDOA, random and systematic uncertainties modelled simultaneously. TDOA is performed for different reference sensors such as: $Bs_1, Bs_2, Bs_3, Bs_4, l^{Ref,max}, l^{Ref,min}, l^{Ref,mean}$.

Appendix F TOA/TDOA Cost Function Computation

```

1 function [objVal,G] = costMultilateration3D(x0,mCordTransducer,refVal,ixRefTransd,
      multilatMethods,runRef)
2 %%%%%%%%%%%%%%%%%%%%%%%%%%%%%%%%%%%%%%%%%%%%%%%%%%%%%%%%%%%%%%%%%%%%%%%%%
3 % function objVal = objectivefunctionTriangulation(x0,mCordTransducer,refVal,ixRefTransd,
      triangulaMethods)
4 %
5 %
6 %
7 % input
8 %   x0           initial guess given as the center of mass of the transducers
9 %   mCordTransducer matrix containing the transducer coordinates (x,y,z)
10 %
11 %   refVal       distances of each transducer from the source location
12 %
13 %   ixRefTransd  reference transducer for the Time Difference of Arriva(TDOA)
14 %
15 %   triangulaMethods triangulation, it a string and could be 'TOA' or 'TDOA'
16 %
17 % output
18 %   objVal       cost function for TOA or TDOA
19 %               the time index of the maximum envelop
20 % author :   Ronaldo Kalunga
21 % date   :   January 20th, 2020
22 % purpose:   Ionoacoustic source localization
23 % References :
24 % Acoustic source localization by Tribikram Kundu 2013
25 % Source Localization: Algorithms and Analysis by Reza Zekavat and R. Michael Buehrer
26
27
28 %% Triangulation approach
29
30 objVal = 0;
31 numSensor = size(mCordTransducer,1);
32
33 %% Choose the reference sensor for the time difference of arrival (TDOA)
34
35 if isempty(ixRefTransd)
36
37     % By considering the maximum distance between the source and the
38     % sensor
39
40     if contains('maxRef',runRef)
41
42         [~,ixRefTransd] = max(refVal);
43
44         % By considering the minimum distance between the source and the
45         % sensor
46
47     elseif contains('minRef',runRef)
48
49         [~,ixRefTransd] = min(refVal);
50
51         % By considering the center sensor
52
53     elseif contains('centerRef',runRef)
54
55         ixRefTransd = ceil(numel(refVal)/2);
56
57         % If none of the conditions are fullfilled then the reference sensor
58         % will always the firs sensor.
59
60     elseif contains('none',runRef)
61
62         ixRefTransd = 1;
63

```

```

64     elseif contains('meanRef', runRef)
65
66         [~,ixRefTransd] = min(abs(refVal - mean(refVal)));
67
68     elseif contains('dynamicMeanRef', runRef)
69
70         [~,ixSortDist] = sort(abs(refVal - sqrt(sum((x0.^2)))));
71         ixRefTransd = ixSortDist(end); % take the second highest distance
72
73     else
74
75         warning('The sensor has been set manually')
76         print(ixRefTransd)
77
78     end
79
80 end
81
82 %% Euclidean distance for the TOA and TDOA
83
84 euclDist = @(mDistance, x0) sqrt(sum((bsxfun(@minus, mDistance, x0).^2), 2));
85
86 objTOA = @(vRefDist, mCordTransducer, x0) sum((vRefDist - euclDist(mCordTransducer, x0)).^2);
87 objTDOA = @(vRefDist, mCordTransducer, mCordRefTransducer, x0) sum((vRefDist - euclDist(
88     mCordTransducer, x0) + euclDist(mCordRefTransducer, x0)).^2);
89
90 switch multilatMethods
91
92     case 'TOA'
93
94         % TOA implemented as TOA
95
96         objVal = objTOA(refVal, mCordTransducer, x0);
97
98         % TOA implmented from the TDOA it is more elegant but it is 1
99         % second slower.
100
101         % objVal = objTDOA(refVal, mCordTransducer, x0, x0); —> Slow
102         %% Analytical Gradient TOA
103
104         if nargin > 1
105
106             eucliDean = sqrt(sum(bsxfun(@minus, mCordTransducer, x0).^2, 2));
107
108             xComponent = (x0(1) - mCordTransducer(:, 1))./eucliDean;
109             yComponent = (x0(2) - mCordTransducer(:, 2))./eucliDean;
110             zComponent = (x0(3) - mCordTransducer(:, 3))./eucliDean;
111
112             G = -2.*[sum((refVal - eucliDean).*xComponent), sum((refVal - eucliDean).*
113                 yComponent), sum((refVal - eucliDean).*zComponent)];
114
115         end
116
117     case 'TDOA'
118
119         ixTransd = 1:numSensor;
120         ixTransd = ixTransd(ixTransd~=ixRefTransd);
121
122         vRefDiff = refVal(ixTransd)-refVal(ixRefTransd);
123         objVal = objTDOA(vRefDiff, mCordTransducer(ixTransd, :), mCordTransducer(ixRefTransd, :),
124             x0);
125
126         %% Analytical Gradient TDOA
127
128         if nargin > 1
129
130             eucliDean = sqrt(sum(bsxfun(@minus, mCordTransducer(ixTransd, :), x0).^2, 2));
131             eucliDeanRef = sqrt(sum(bsxfun(@minus, mCordTransducer(ixRefTransd, :), x0).^2, 2));
132
133             xComponent = - (x0(1) - mCordTransducer(ixTransd, 1))./eucliDean + (x0(1) -
134                 mCordTransducer(ixRefTransd, 1))./eucliDeanRef;

```

```

131     yComponent = - (x0(2) - mCordTransducer(ixTransd,2))./eucliDean + (x0(2) -
132     mCordTransducer(ixRefTransd,2))./eucliDeanRef;
133     zComponent = - (x0(3) - mCordTransducer(ixTransd,3))./eucliDean + (x0(3) -
134     mCordTransducer(ixRefTransd,3))./eucliDeanRef;
135     G =      2.*[sum(xComponent.*(vRefDiff + eucliDeanRef - eucliDean)),sum(yComponent
136     .*(vRefDiff + eucliDeanRef - eucliDean)),...
137     sum(zComponent.*(vRefDiff + eucliDeanRef - eucliDean))];
138
139     end
140
141     otherwise
142         error('does not exist')
143
144 end
145
146 end

```

Appendix G Analytical Numerical Gradient

The optimization routines from MATLAB use the numerical gradient by default based on the finite-difference approximation. Therefore, the possible issues are: computational speed.

- Computational speed. The numerical gradient can be slower compared to the analytical gradients.
- The finite-difference approximation influences the accuracy of the results. The approximation is performed using the central or forward finite difference approaches.

G.1 TOA Analytical Gradient

The analytical gradient for the TOA is computed starting from the TOA cost function. It is computed in 3D but can also be computed in 2D by cancelling the undesired coordinates. Again, the cost function can be expressed as:

$$\min_{x_s, y_s, z_s} f_{TOA}(x_s, y_s, z_s) = \min_{x_s, y_s, z_s} \sum_{i=1}^n \left(v_s \cdot (ToF_i + \Upsilon_i) - \sqrt{(x_i - x_s)^2 + (y_i - y_s)^2 + (z_i - z_s)^2} \right)^2 \quad (\text{G.1})$$

The numerical gradients are computed as follows:

$$\nabla(f_{TOA}(x_s, y_s, z_s)) = \begin{bmatrix} \frac{\partial f_{TOA}(x_s, y_s, z_s)}{\partial x} \\ \frac{\partial f_{TOA}(x_s, y_s, z_s)}{\partial y} \\ \frac{\partial f_{TOA}(x_s, y_s, z_s)}{\partial z} \end{bmatrix} = -2 \cdot \begin{bmatrix} \sum_{i=1}^n \frac{(d_{TOA,i} - \|d_i\|_2) \cdot (x_s - x_i)}{\|d_i\|_2} \\ \sum_{i=1}^n \frac{(d_{TOA,i} - \|d_i\|_2) \cdot (y_s - y_i)}{\|d_i\|_2} \\ \sum_{i=1}^n \frac{(d_{TOA,i} - \|d_i\|_2) \cdot (z_s - z_i)}{\|d_i\|_2} \end{bmatrix} \quad (\text{G.2})$$

Where $d_{TOA,i}$ and d_i are expressed as:

$$d_{TOA,i} = v_s \cdot (ToF_i + \Upsilon_i) \quad (G.3)$$

$$\|d_i\|_2 = \sqrt{(x_i - x_s)^2 + (y_i - y_s)^2 + (z_i - z_s)^2} \quad (G.4)$$

For compactness in the analytical gradient model, the calculation was computed by setting $\Upsilon_i = 0$.

G.2 TDOA Analytical Gradient

The analytical gradient for the TDOA is computed starting from the TDOA cost function. It can be expressed as:

$$\min_{x_s, y_s, z_s} f_{TDOA}(x_s, y_s, z_s) = \min_{x_s, y_s, z_s} \sum_{i=1}^n \sum_{ref \neq i} \left(v_s \cdot w - \sqrt{(x - x_s)^2 + (y - y_s)^2 + (z - z_s)^2} + \|d_{ref}\|_2 \right)^2 \quad (G.5)$$

To be noted that w is describe as:

$$w = (ToF_i + \Upsilon_i) - (ToF_{ref} + \Upsilon_{ref}) \quad (G.6)$$

Similar to the TOA, we can move from a 3D to a 2D problem by cancelling the undesired coordinates. Therefore, the analytical gradients for TDOA can be computed as follows:

$$\nabla(f_{TDOA}(x_s, y_s, z_s)) = \begin{bmatrix} \frac{\partial f_{TDOA}(x_s, y_s, z_s)}{\partial x} \\ \frac{\partial f_{TDOA}(x_s, y_s, z_s)}{\partial y} \\ \frac{\partial f_{TDOA}(x_s, y_s, z_s)}{\partial z} \end{bmatrix} = 2 \cdot \begin{bmatrix} \sum_{i=1}^n \sum_{ref \neq i} \left(\frac{-(x_s - x_i)}{\|d_i\|_2} + \frac{(x_s - x_{ref})}{\|d_{ref}\|_2} \right) \cdot R^{TDOA} \\ \sum_{i=1}^n \sum_{ref \neq i} \left(\frac{-(y_s - y_i)}{\|d_i\|_2} + \frac{(y_s - y_{ref})}{\|d_{ref}\|_2} \right) \cdot R^{TDOA} \\ \sum_{i=1}^n \sum_{ref \neq i} \left(\frac{-(z_s - z_i)}{\|d_i\|_2} + \frac{(z_s - z_{ref})}{\|d_{ref}\|_2} \right) \cdot R^{TDOA} \end{bmatrix} \quad (G.7)$$

Where R^{TDOA} and $\|d_{ref}\|_2$ and $d_{TDOA,i}$ are expressed as:

$$R^{TDOA} = d_{TDOA,i} - \|d_i\|_2 + \|d_{ref}\|_2 \quad (G.8)$$

$$d_{TDOA,i} = v_s \cdot w; \text{ where } \Upsilon_i = \Upsilon_{ref} = 0 \quad (G.9)$$

G.3 Multilateration Time Performance

Without considering the analytical gradient, the multilateration computation takes 1.2 seconds, and when considering random and systematic uncertainties, it takes 27000 seconds. The computation time is improved when the analytical gradient is considered. The multilateration time decreases to 0.022 seconds without uncertainties and increases to 495 seconds when considering random and systematic uncertainties. These values were obtained by comparing the output of the multilateration without modelling uncertainties for a single numerical optimisation with and without considering the analytical gradient for the TOA. Then, the outcome was multiplied by a different number of samples considering the random and systematic uncertainties. In other words, $t_{optimisation} = N_{syst} \times N_{rand} \times t_{ideal}$ ($N_{syst} = N_{rand} = 150$; with a total of 22500 samples for each source position. Where t_{ideal} is the time when no uncertainties are considered, equal to 1.2 seconds (without analytical gradient) and 0.022 seconds (with analytical gradient).

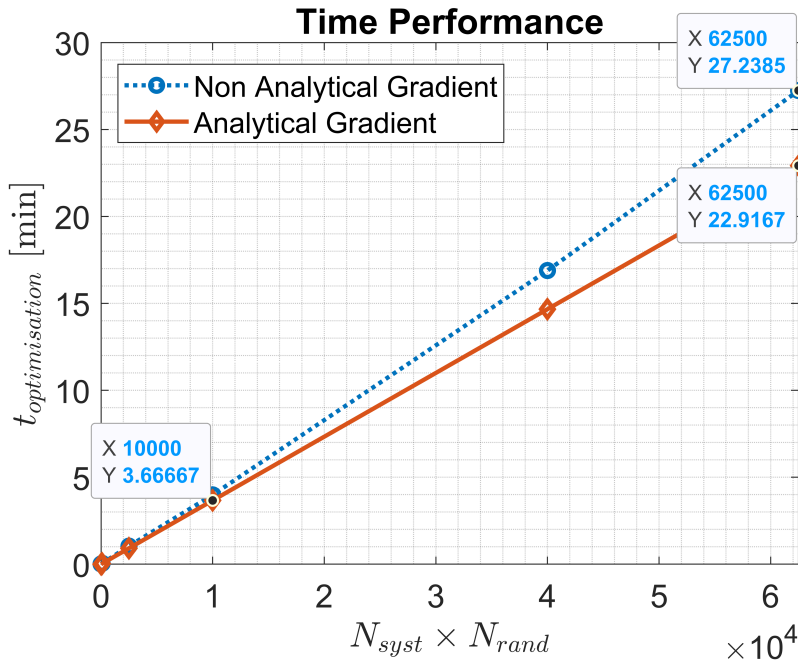


Figure 57: Multilateration performance with and without the analytical-numerical gradient.

Appendix H Pulse-echo Measurement Between the Lateral Sensors

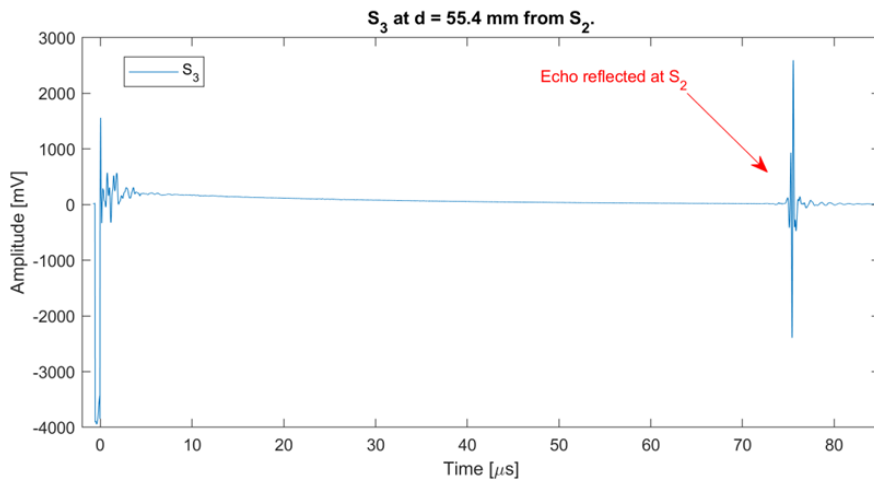
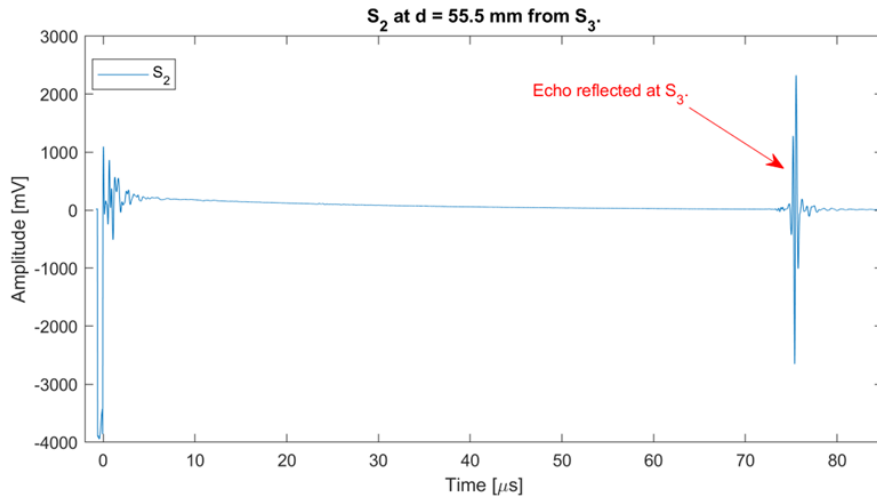


Figure 58: Misalignment between the two lateral sensors inside the 3D-IBeat. (a) Sensor B_{S_2} here denominated as (S_2). (b) Sensor B_{S_3} here denominated as (S_2). There was a misalignment between the two sensors of 0.10 mm.

Appendix I TDOA Fixed Beam Position and Varying the Reference Sensor

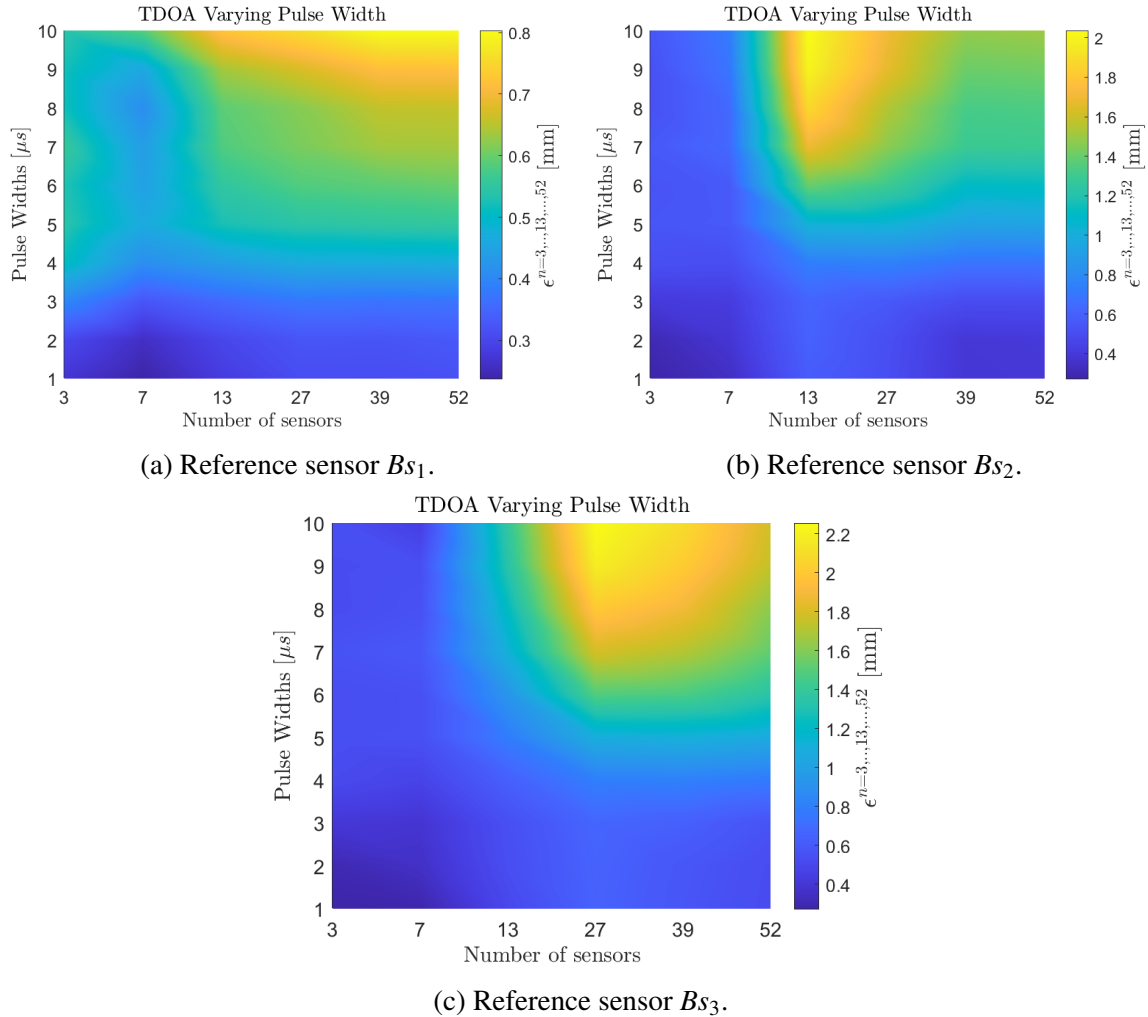
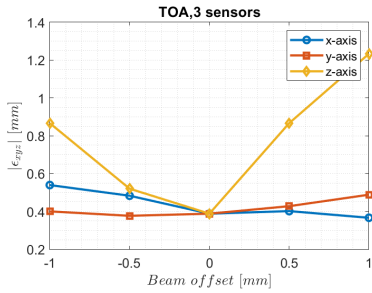
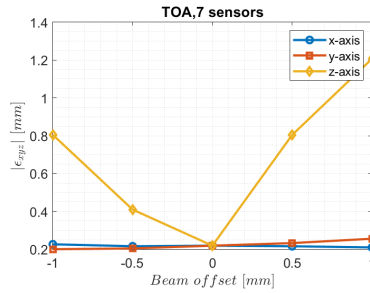


Figure 59: Multilateration using TDOA for different proton widths (i.e., 1,2,3,4,5,6,7,8,9, 10 μ s), for the beam position at $(x,y,z) = (0,0,0)$ mm. (a) TDOA with B_{S_1} as reference sensor, (b) TDOA with B_{S_2} as reference sensor, (c) TDOA with B_{S_3} as a reference sensor.

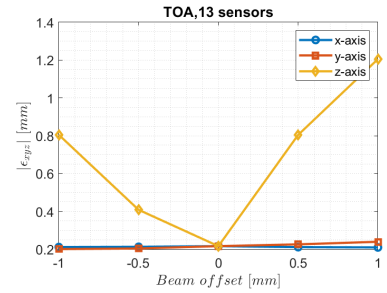
Appendix J TOA/TDOA Beam Offsets & Localisation Using Multiple Sensors



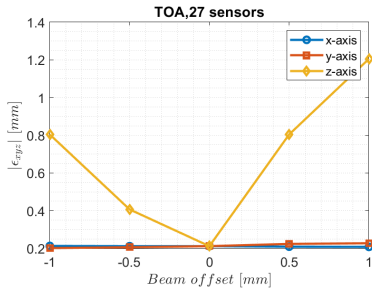
(a) Localisation with 3 sensors.



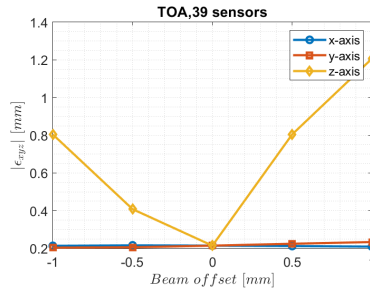
(b) Localisation with 7 sensors.



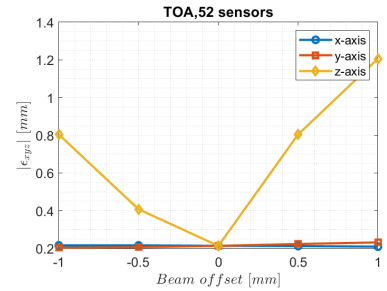
(c) Localisation with 13 sensors.



(d) Localisation with 27 sensors.

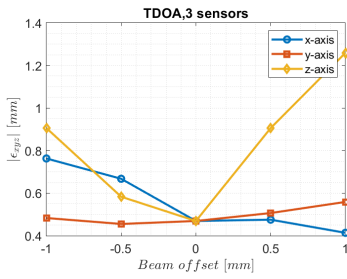


(e) Localisation with 39 sensors.

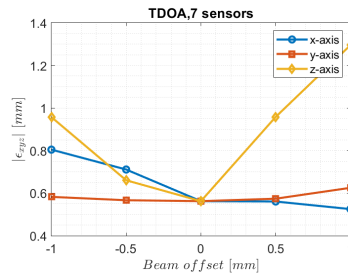


(f) Localisation with 52 sensors.

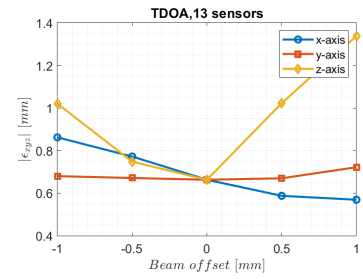
Figure 60: TOA, BP localised with multiple beam offsets. Localisation is performed with different sensor sets (3,7,13,27,39, and 52).



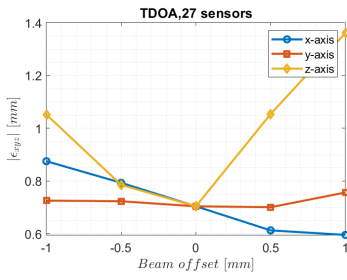
(a) Localisation with 3 sensors.



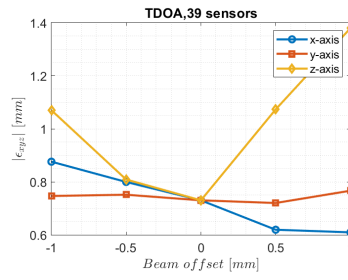
(b) Localisation with 7 sensors.



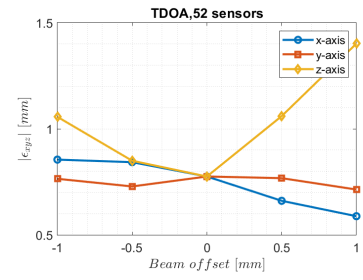
(c) Localisation with 13 sensors.



(d) Localisation with 27 sensors.



(e) Localisation with 39 sensors.



(f) Localisation with 52 sensors.

Figure 61: TDOA, BP localised with multiple beam offsets. Localisation is performed with different sensor sets (3,7,13,27,39, and 52).

List of Publications

1. **Title:** Towards a novel small animal proton irradiation platform: the SIRMIO project
Authors: K. Parodi, W. Assmann, C. Belka, J. Bortfeldt, D.A. Clevert, G. Dedes, **R. Kalunga**, S. Kundel, N. Kurichiyani, P. Lämmer, J. Lascaud, K. Lauber, G. Lovatti, S. Meyer, M. Nitta, M. Pinto, M.J. Safari, K. Schnürle, J. Schreiber, P.G. Thirolf, H.-P. Wieser, M. Würll
Journal: Acta Oncologica, 58 (10), 1470-1475
Year: 2019
2. **Title:** Investigating the accuracy of co-registered ionoacoustic and ultrasound images in pulsed proton beams
Authors: J. Lascaud, P. Dash, HP Wieser, **R. Kalunga**, M Würll, W. Assmann, K. Parodi
Journal: Physics in Medicine & Biology, 66 (18), 185007
Year: 2021
3. **Title:** Enhancement of the ionoacoustic effect through ultrasound and photoacoustic contrast agents
Authors: J. Lascaud, P. Dash, M. Würll, H.-P. Wieser, B. Wollant, **R. Kalunga**, S. Lehrack, F.S. Englbrecht, W. Assmann, A.S. Savoia, K. Parodi
Journal: Scientific Reports, 11 (1), 2725
Year: 2021
4. **Title:** Optimization of the backing material of a low-frequency PVDF detector for ion beam monitoring during small animal proton irradiation
Authors: J. Lascaud, R. Kowalewski, B. Wollant, H. Carmigniani, K. Schnürle, P. Dash, **R. Kalunga**, H.-P. Wieser, J. Bortfeldt, R. Rouffaud, A. Gérard, M. Vidal, J. Hérault, D. Certon, K. Parodi
Conference: 2021 IEEE International Ultrasonics Symposium (IUS), 1-4
Year: 2021
5. **Title:** Applicability of capacitive micromachined ultrasonic transducers for the detection of proton-induced thermoacoustic waves
Authors: J. Lascaud, **R. Kalunga**, S. Lehrack, H.-P. Wieser, F.S. Englbrecht, M. Würll, W. Assmann, A.S. Savoia, K. Parodi
Conference: 2019 IEEE International Ultrasonics Symposium (IUS), 143-146
Year: 2019
6. **Title:** On the robustness of multilateration of ionoacoustic signals for localization of the Bragg peak at pre-clinical proton beam energies in water
Authors: **R. Kalunga**, HP. Wieser, P. Dash, M. Würll, M. Riboldi, J. Schreiber, ...
Journal: Physics in Medicine & Biology, 68 (10), 105010
Year: 2023

DGMP Abstracts

7. **Title:** On the localization of the proton Bragg peak position in 3D using multilateration of ionoacoustic signals
Authors: R. Kalunga, HP. Wieser, J. Lascaud, P. Dash, AK. Schmidt, S. Gerlach, ...
Year: 2021

8. **Title:** Investigating the co-registration of ionoacoustic and ultrasound signals along with possibilities of dose reconstruction in realistic small animal models for proton irradiation
Authors: P. Dash, J. Lascaud, HP. Wieser, R. Kalunga, B. Wollant, W. Assmann, ...
Year: 2020

9. **Title:** Untersuchung des ionoakustischen Effektes in heterogenen Medien zur Minimierung der Reichweitenunsicherheit in der Partikeltherapie
Authors: HP. Wieser, J. Lascaud, S. Lehrack, R. Kalunga, M Würfl, W. Assmann, ...
Year: 2019

A Bibliography

- [1] W. Cao, H.-D. Chen, Y.-W. Yu, N. Li, and W.-Q. Chen, “Changing profiles of cancer burden worldwide and in china: a secondary analysis of the global cancer statistics 2020,” *Chinese Medical Journal*, vol. 134, no. 07, pp. 783–791, 2021.
- [2] J. Ferlay, M. Colombet, I. Soerjomataram, D. M. Parkin, M. Piñeros, A. Znaor, and F. Bray, “Cancer statistics for the year 2020: An overview,” *International journal of cancer*, vol. 149, no. 4, pp. 778–789, 2021.
- [3] Y. Xi and P. Xu, “Global colorectal cancer burden in 2020 and projections to 2040,” *Translational Oncology*, vol. 14, no. 10, p. 101174, 2021.
- [4] R. Sharma, “Mapping of global, regional and national incidence, mortality and mortality-to-incidence ratio of lung cancer in 2020 and 2050,” *International journal of clinical oncology*, vol. 27, no. 4, pp. 665–675, 2022.
- [5] F. A. Sloan, H. Gelband, *et al.*, “The cancer burden in low-and middle-income countries and how it is measured,” in *Cancer control opportunities in low-and middle-income countries*, National Academies Press (US), 2007.
- [6] C. Fitzmaurice, D. Dicker, A. Pain, H. Hamavid, M. Moradi-Lakeh, M. F. MacIntyre, C. Allen, G. Hansen, R. Woodbrook, C. Wolfe, *et al.*, “The global burden of cancer 2013,” *JAMA oncology*, vol. 1, no. 4, pp. 505–527, 2015.
- [7] S. C. Shah, V. Kayamba, R. M. Peek Jr, and D. Heimbarger, “Cancer control in low-and middle-income countries: is it time to consider screening?,” *Journal of global oncology*, vol. 5, pp. 1–8, 2019.
- [8] H. L. Guyatt and R. W. Snow, “Impact of malaria during pregnancy on low birth weight in sub-saharan africa,” *Clinical microbiology reviews*, vol. 17, no. 4, pp. 760–769, 2004.
- [9] J.-F. Trape, G. Pison, A. Spiegel, C. Enel, and C. Rogier, “Combating malaria in africa,” *Trends in parasitology*, vol. 18, no. 5, pp. 224–230, 2002.
- [10] I. O. Morhason-Bello, F. Odedina, T. R. Rebbeck, J. Harford, J.-M. Dangou, L. Denny, and I. F. Adewole, “Challenges and opportunities in cancer control in africa: a perspective from the african organisation for research and training in cancer,” *The lancet oncology*, vol. 14, no. 4, pp. e142–e151, 2013.
- [11] R. I. Anorlu, “Cervical cancer: the sub-saharan african perspective,” *Reproductive health matters*, vol. 16, no. 32, pp. 41–49, 2008.
- [12] A. L. Pillay, “Rural and urban south african women’s awareness of cancers of the breast and cervix,” *Ethnicity and Health*, vol. 7, no. 2, pp. 103–114, 2002.
- [13] V. Vanderpuye, S. Grover, N. Hammad, H. Simonds, F. Olopade, D. Stefan, *et al.*, “An update

- on the management of breast cancer in africa,” *Infectious agents and cancer*, vol. 12, no. 1, pp. 1–12, 2017.
- [14] N. N. Mthembu, Z. Mbita, R. Hull, and Z. Dlamini, “Abnormalities in alternative splicing of angiogenesis-related genes and their role in hiv-related cancers,” *HIV/AIDS (Auckland, NZ)*, vol. 9, p. 77, 2017.
- [15] P. Kanavos, “The rising burden of cancer in the developing world,” *Annals of oncology*, vol. 17, pp. viii15–viii23, 2006.
- [16] L. A. Torre, F. Bray, R. L. Siegel, J. Ferlay, J. Lortet-Tieulent, and A. Jemal, “Global cancer statistics, 2012,” *CA: a cancer journal for clinicians*, vol. 65, no. 2, pp. 87–108, 2015.
- [17] M. Medina-Rico, H. L. Ramos, M. Lobo, J. Romo, and J. G. Prada, “Epidemiology of renal cancer in developing countries: Review of the literature,” *Canadian Urological Association Journal*, vol. 12, no. 3, p. E154, 2018.
- [18] L. H. Nel, “Discrepancies in data reporting for rabies, africa,” *Emerging infectious diseases*, vol. 19, no. 4, p. 529, 2013.
- [19] D. Litzenberg, D. Roberts, M. Lee, K. Pham, A. Vander Molen, R. Ronningen, and F. Becchetti, “On-line monitoring of radiotherapy beams: Experimental results with proton beams,” *Medical physics*, vol. 26, no. 6, pp. 992–1006, 1999.
- [20] A. Herskovic, K. Martz, M. Al-Sarraf, L. Leichman, J. Brindle, V. Vaitkevicius, J. Cooper, R. Byhardt, L. Davis, and B. Emami, “Combined chemotherapy and radiotherapy compared with radiotherapy alone in patients with cancer of the esophagus,” *New England Journal of Medicine*, vol. 326, no. 24, pp. 1593–1598, 1992.
- [21] B. C. Baumann, D. E. Hallahan, J. M. Michalski, C. A. Perez, and J. M. Metz, “Concurrent chemo-radiotherapy with proton therapy: reduced toxicity with comparable oncological outcomes vs photon chemo-radiotherapy,” *British Journal of Cancer*, vol. 123, no. 6, pp. 869–870, 2020.
- [22] J. E. Leeman, P. B. Romesser, Y. Zhou, S. McBride, N. Riaz, E. Sherman, M. A. Cohen, O. Cahlon, and N. Lee, “Proton therapy for head and neck cancer: expanding the therapeutic window,” *The lancet oncology*, vol. 18, no. 5, pp. e254–e265, 2017.
- [23] M. Testa, J. M. Verburg, M. Rose, C. H. Min, S. Tang, E. H. Bentefour, H. Paganetti, and H.-M. Lu, “Proton radiography and proton computed tomography based on time-resolved dose measurements,” *Physics in Medicine & Biology*, vol. 58, no. 22, p. 8215, 2013.
- [24] W. D. Newhauser and R. Zhang, “The physics of proton therapy,” *Physics in Medicine & Biology*, vol. 60, no. 8, p. R155, 2015.
- [25] L. Magallanes, S. Meyer, C. Gianoli, B. Kopp, B. Voss, O. Jäkel, S. Brons, J. Gordon, and K. Parodi, “Upgrading an integrating carbon-ion transmission imaging system with active

- scanning beam delivery toward low dose ion imaging,” *IEEE Transactions on Radiation and Plasma Medical Sciences*, vol. 4, no. 2, pp. 262–268, 2019.
- [26] P. Palaniappan, S. Meyer, F. Kamp, C. Belka, M. Riboldi, K. Parodi, and C. Gianoli, “Deformable image registration of the treatment planning ct with proton radiographies in perspective of adaptive proton therapy,” *Physics in Medicine & Biology*, vol. 66, no. 4, p. 045008, 2021.
- [27] T. Bortfeld, “An analytical approximation of the bragg curve for therapeutic proton beams,” *Medical physics*, vol. 24, no. 12, pp. 2024–2033, 1997.
- [28] A.-C. Knopf and A. Lomax, “In vivo proton range verification: a review,” *Physics in Medicine & Biology*, vol. 58, no. 15, p. R131, 2013.
- [29] P. Andreo, “On the clinical spatial resolution achievable with protons and heavier charged particle radiotherapy beams,” *Physics in Medicine & Biology*, vol. 54, no. 11, p. N205, 2009.
- [30] H. Paganetti, “Range uncertainties in proton therapy and the role of monte carlo simulations,” *Physics in Medicine & Biology*, vol. 57, no. 11, p. R99, 2012.
- [31] R. Grün, T. Friedrich, M. Krämer, K. Zink, M. Durante, R. Engenhart-Cabillic, and M. Scholz, “Physical and biological factors determining the effective proton range,” *Medical physics*, vol. 40, no. 11, p. 111716, 2013.
- [32] NHS, “Proton beam therapy.” <http://www.england.nhs.uk/commissioning/spec-services/highly-spec-services/pbt/>, Last accessed on 2022-08-08.
- [33] H. Li, X. Zhang, P. Park, W. Liu, J. Chang, Z. Liao, S. Frank, Y. Li, F. Poenisch, R. Mohan, *et al.*, “Robust optimization in intensity-modulated proton therapy to account for anatomy changes in lung cancer patients,” *Radiotherapy and Oncology*, vol. 114, no. 3, pp. 367–372, 2015.
- [34] S. McGowan, N. Burnet, and A. Lomax, “Treatment planning optimisation in proton therapy,” *The British journal of radiology*, vol. 86, no. 1021, pp. 20120288–20120288, 2013.
- [35] J. Unkelbach and H. Paganetti, “Robust proton treatment planning: physical and biological optimization,” in *Seminars in radiation oncology*, vol. 28, pp. 88–96, Elsevier, 2018.
- [36] J. Unkelbach, T. C. Chan, and T. Bortfeld, “Accounting for range uncertainties in the optimization of intensity modulated proton therapy,” *Physics in Medicine & Biology*, vol. 52, no. 10, p. 2755, 2007.
- [37] S. Tattenberg, T. M. Madden, T. Bortfeld, K. Parodi, and J. Verburg, “Range uncertainty reductions in proton therapy may lead to the feasibility of novel beam arrangements which improve organ-at-risk sparing,” *Medical Physics*, vol. 49, no. 7, pp. 4693–4704, 2022.
- [38] M. Zhang, W. Zou, and B.-K. K. Teo, “Image guidance in proton therapy for lung cancer,”

Translational lung cancer research, vol. 7, no. 2, p. 160, 2018.

- [39] P. S. Sanghavi and B. G. Jankharia, “Applications of dual energy ct in clinical practice: A pictorial essay,” *Indian Journal of Radiology and Imaging*, vol. 29, no. 03, pp. 289–298, 2019.
- [40] N. Hudobivnik, F. Schwarz, T. Johnson, L. Agolli, G. Dedes, T. Tessonier, F. Verhaegen, C. Thieke, C. Belka, W. H. Sommer, *et al.*, “Comparison of proton therapy treatment planning for head tumors with a pencil beam algorithm on dual and single energy ct images,” *Medical physics*, vol. 43, no. 1, pp. 495–504, 2016.
- [41] K. M. Hanson, “Proton computed tomography,” *IEEE Transactions on Nuclear Science*, vol. 26, no. 1, pp. 1635–1640, 1979.
- [42] R. W. Schulte, V. Bashkirov, M. C. Loss Klock, T. Li, A. J. Wroe, I. Evseev, D. C. Williams, and T. Satogata, “Density resolution of proton computed tomography,” *Medical physics*, vol. 32, no. 4, pp. 1035–1046, 2005.
- [43] S. Meyer, J. Bortfeldt, P. Lämmer, F. S. Englbrecht, M. Pinto, K. Schnürle, M. Würll, and K. Parodi, “Optimization and performance study of a proton ct system for pre-clinical small animal imaging,” *Physics in Medicine & Biology*, vol. 65, no. 15, p. 155008, 2020.
- [44] W. Enghardt, P. Crespo, F. Fiedler, R. Hinz, K. Parodi, J. Pawelke, and F. Poenisch, “Charged hadron tumour therapy monitoring by means of pet,” *Nuclear Instruments and Methods in Physics Research Section A: Accelerators, Spectrometers, Detectors and Associated Equipment*, vol. 525, no. 1-2, pp. 284–288, 2004.
- [45] C. Richter, G. Pausch, S. Barczyk, M. Priegnitz, I. Keitz, J. Thiele, J. Smeets, F. Vander Stappen, L. Bombelli, C. Fiorini, *et al.*, “First clinical application of a prompt gamma based in vivo proton range verification system,” *Radiotherapy and Oncology*, vol. 118, no. 2, pp. 232–237, 2016.
- [46] K. Parodi, H. Paganetti, E. Cascio, J. B. Flanz, A. A. Bonab, N. M. Alpert, K. Lohmann, and T. Bortfeld, “Pet/ct imaging for treatment verification after proton therapy: a study with plastic phantoms and metallic implants,” *Medical physics*, vol. 34, no. 2, pp. 419–435, 2007.
- [47] A. Knopf, K. Parodi, H. Paganetti, E. Cascio, A. Bonab, and T. Bortfeld, “Quantitative assessment of the physical potential of proton beam range verification with pet/ct,” *Physics in Medicine & Biology*, vol. 53, no. 15, p. 4137, 2008.
- [48] A. Knopf, K. Parodi, T. Bortfeld, H. A. Shih, and H. Paganetti, “Systematic analysis of biological and physical limitations of proton beam range verification with offline pet/ct scans,” *Physics in Medicine & Biology*, vol. 54, no. 14, p. 4477, 2009.
- [49] X. Zhu and G. El Fakhri, “Proton therapy verification with pet imaging,” *Theranostics*, vol. 3, no. 10, p. 731, 2013.
- [50] A. Wrońska *et al.*, “Prompt gamma imaging in proton therapy-status, challenges and devel-

- opments,” in *Journal of Physics: Conference Series*, vol. 1561, p. 012021, IOP Publishing, 2020.
- [51] S. Kurosawa, H. Kubo, K. Ueno, S. Kabuki, S. Iwaki, M. Takahashi, K. Taniue, N. Higashi, K. Miuchi, T. Tanimori, *et al.*, “Prompt gamma detection for range verification in proton therapy,” *Current applied physics*, vol. 12, no. 2, pp. 364–368, 2012.
- [52] L. Kelleter, A. Wrońska, J. Besuglow, A. Konefał, K. Laihem, J. Leidner, A. Magiera, K. Parodi, K. Rusiecka, A. Stahl, *et al.*, “Spectroscopic study of prompt-gamma emission for range verification in proton therapy,” *Physica Medica*, vol. 34, pp. 7–17, 2017.
- [53] Y. Hayakawa, J. Tada, N. Arai, K. Hosono, M. Sato, T. Wagai, H. Tsuji, and H. Tsujii, “Acoustic pulse generated in a patient during treatment by pulsed proton radiation beam,” *Radiation Oncology Investigations*, vol. 3, no. 1, pp. 42–45, 1995.
- [54] K. Parodi, W. Assmann, C. Belka, J. Bortfeldt, D.-A. Clevert, G. Dedes, R. Kalunga, S. Kundel, N. Kurichiyani, P. Lämmer, *et al.*, “Towards a novel small animal proton irradiation platform: the sirmio project,” *Acta oncologica*, vol. 58, no. 10, pp. 1470–1475, 2019.
- [55] R. Mohan and D. Grosshans, “Proton therapy—present and future,” *Advanced drug delivery reviews*, vol. 109, pp. 26–44, 2017.
- [56] S. Gerlach, M. Pinto, N. Kurichiyani, C. Grau, J. Herault, M. Hillbrand, P. Poulsen, S. Safai, J. M. Schippers, M. Schwarz, *et al.*, “Beam characterization and feasibility study for a small animal irradiation platform at clinical proton therapy facilities,” *Physics in Medicine & Biology*, vol. 65, no. 24, p. 245045, 2020.
- [57] N. Kurichiyani, M. Pinto, T. Rösch, S. Kundel, M. Würfl, F. S. Enghbrecht, J. Schreiber, and K. Parodi, “Design of an adaptable permanent-magnet quadrupole triplet for refocusing of energy degraded proton beams for small animal irradiation,” *Medical Physics*, no. 6, 2019.
- [58] G. Lovatti, M. Nitta, M. J. Safari, C. Gianoli, M. Pinto, G. Dedes, A. Zoglauer, P. G. Thirolf, and K. Parodi, “Design study of a novel geometrical arrangement for an in-beam small animal positron emission tomography scanner,” *Physics in Medicine & Biology*, vol. 68, no. 23, p. 235005, 2023.
- [59] L. E. Kinsler, A. R. Frey, A. B. Coppens, and J. V. Sanders, *Fundamentals of acoustics*. John Wiley & sons, 2000.
- [60] Y. Zhou, J. Yao, and L. V. Wang, “Tutorial on photoacoustic tomography,” *Journal of biomedical optics*, vol. 21, no. 6, pp. 061007–061007, 2016.
- [61] R. S. Cobbold, *Foundations of biomedical ultrasound*. Oxford university press, 2006.
- [62] L. V. Wang and H.-i. Wu, *Biomedical optics: principles and imaging*. John Wiley & Sons, 2012.

- [63] S. Lehrack, *Investigating accuracy and precision of ionoacoustics for range determination of ion beams in water*. PhD thesis, lmu, 2018.
- [64] E. Grüneisen, “Theorie des festen zustandes einatomiger elemente,” *Annalen der Physik*, vol. 344, no. 12, pp. 257–306, 1912.
- [65] S. Hickling, L. Xiang, K. C. Jones, K. Parodi, W. Assmann, S. Avery, M. Hobson, and I. El Naqa, “Ionizing radiation-induced acoustics for radiotherapy and diagnostic radiology applications,” *Medical physics*, vol. 45, no. 7, pp. e707–e721, 2018.
- [66] B. Cox and B. Treeby, “Effect of sensor directionality on photoacoustic imaging: a study using the k-wave toolbox,” in *Photons Plus Ultrasound: Imaging and Sensing 2010*, vol. 7564, pp. 123–128, SPIE, 2010.
- [67] B. Cox and P. C. Beard, “Modeling photoacoustic propagation in tissue using k-space techniques,” in *Photoacoustic Imaging and Spectroscopy*, pp. 25–34, CRC Press, 2017.
- [68] V. Albul, V. Bychkov, S. Vasil’Ev, K. Gusev, V. Demidov, E. Demidova, N. Krasnov, A. Kurchanov, V. Luk’yashin, and A. Y. Sokolov, “Measuring the ultrasonic field generated in water upon the deceleration of a proton beam,” *Instruments and Experimental Techniques*, vol. 47, no. 4, pp. 502–507, 2004.
- [69] K. Jones, A. Witztum, C. Sehgal, and S. Avery, “Proton beam characterization by proton-induced acoustic emission: simulation studies,” *Physics in Medicine & Biology*, vol. 59, no. 21, p. 6549, 2014.
- [70] K. C. Jones, F. Vander Stappen, C. M. Sehgal, and S. Avery, “Acoustic time-of-flight for proton range verification in water,” *Medical physics*, vol. 43, no. 9, pp. 5213–5224, 2016.
- [71] W. Assmann, S. Kellnberger, S. Reinhardt, S. Lehrack, A. Edlich, P. Thierolf, M. Moser, G. Dollinger, M. Omar, V. Ntziachristos, *et al.*, “Ionoacoustic characterization of the proton bragg peak with submillimeter accuracy,” *Medical physics*, vol. 42, no. 2, pp. 567–574, 2015.
- [72] J. B. Farr, M. F. Moyers, C. E. Allgower, M. Bues, W.-C. Hsi, H. Jin, D. N. Mihailidis, H.-M. Lu, W. D. Newhauser, N. Sahoo, *et al.*, “Clinical commissioning of intensity-modulated proton therapy systems: Report of aapm task group 185,” *Medical physics*, vol. 48, no. 1, pp. e1–e30, 2021.
- [73] J. Lascaud, R. Kalunga, S. Lehrack, H.-P. Wieser, F. S. Englbrecht, M. Würfl, W. Assmann, A. S. Savoia, and K. Parodi, “Applicability of capacitive micromachined ultrasonic transducers for the detection of proton-induced thermoacoustic waves,” in *2019 IEEE International Ultrasonics Symposium (IUS)*, pp. 143–146, IEEE, 2019.
- [74] J. Lascaud *et al.*, “Investigating the accuracy of co-registered ionoacoustic and ultrasound images in pulsed proton beams,” *Physics in Medicine & Biology*, vol. 66, no. 18, p. 185007, 2021.

- [75] K. C. Jones, F. Vander Stappen, C. R. Bawiec, G. Janssens, P. A. Lewin, D. Prieels, T. D. Solberg, C. M. Sehgal, and S. Avery, "Experimental observation of acoustic emissions generated by a pulsed proton beam from a hospital-based clinical cyclotron," *Medical physics*, vol. 42, no. 12, pp. 7090–7097, 2015.
- [76] S. Lehrack, W. Assmann, D. Bertrand, S. Henrotin, J. Herault, V. Heymans, F. Vander Stappen, P. G. Thirolf, M. Vidal, J. Van de Walle, *et al.*, "Submillimeter ionoacoustic range determination for protons in water at a clinical synchrocyclotron," *Physics in Medicine & Biology*, vol. 62, no. 17, p. L20, 2017.
- [77] Y. Ye *et al.*, *Bounds on RF cooperative localization for video capsule endoscopy*. PhD thesis, Worcester Polytechnic Institute, 2013.
- [78] P. Ara, K. Yu, S. Cheng, E. Dutkiewicz, and M. C. Heimlich, "Human abdomen path-loss modeling and location estimation of wireless capsule endoscope using round-trip propagation loss," *IEEE Sensors Journal*, vol. 18, no. 8, pp. 3266–3277, 2018.
- [79] A. S. Bjørnevik, "Localization and tracking of intestinal paths for wireless capsule endoscopy," Master's thesis, NTNU, 2015.
- [80] R. Chávez-Santiago, A. Khaleghi, I. Balasingham, and T. A. Ramstad, "Architecture of an ultra wideband wireless body area network for medical applications," in *2009 2nd International Symposium on Applied Sciences in Biomedical and Communication Technologies*, pp. 1–6, IEEE, 2009.
- [81] S. Li, Y. Geng, J. He, and K. Pahlavan, "Analysis of three-dimensional maximum likelihood algorithm for capsule endoscopy localization," in *2012 5th International Conference on BioMedical Engineering and Informatics*, pp. 721–725, IEEE, 2012.
- [82] I. Dove, "Analysis of radio propagation inside the human body for in-body localization purposes," Master's thesis, University of Twente, 2014.
- [83] J. Xu, M. Ma, and C. L. Law, "Aoa cooperative position localization," in *IEEE GLOBECOM 2008-2008 IEEE Global Telecommunications Conference*, pp. 1–5, IEEE, 2008.
- [84] G. Zanca, F. Zorzi, A. Zanella, and M. Zorzi, "Experimental comparison of rssi-based localization algorithms for indoor wireless sensor networks," in *Proceedings of the workshop on Real-world wireless sensor networks*, pp. 1–5, 2008.
- [85] W. Suzhe and L. Yong, "Node localization algorithm based on rssi in wireless sensor network," in *2012 6th International Conference on Signal Processing and Communication Systems*, pp. 1–4, IEEE, 2012.
- [86] X. Li, Z. D. Deng, L. T. Rauchenstein, and T. J. Carlson, "Contributed review: Source-localization algorithms and applications using time of arrival and time difference of arrival measurements," *Review of Scientific Instruments*, vol. 87, no. 4, p. 041502, 2016.

- [87] M. A. Stuchly and S. S. Stuchly, "Coaxial line reflection methods for measuring dielectric properties of biological substances at radio and microwave frequencies-a review," *IEEE Transactions on instrumentation and measurement*, vol. 29, no. 3, pp. 176–183, 1980.
- [88] W. Kuang and S. Nelson, "Low-frequency dielectric properties of biological tissues: a review with some new insights," 1998.
- [89] M. Guardiola, S. Buitrago, G. Fernández-Esparrach, J. M. O'Callaghan, J. Romeu, M. Cuatrecasas, H. Córdova, M. Á. González Ballester, and O. Camara, "Dielectric properties of colon polyps, cancer, and normal mucosa: Ex vivo measurements from 0.5 to 20 ghz," *Medical physics*, vol. 45, no. 8, pp. 3768–3782, 2018.
- [90] M. Zhou and K. Pahlavan, "On the accuracy of in-body toa ranging inside the gastrointestinal tract using carrier frequency," in *2015 Wireless Telecommunications Symposium (WTS)*, pp. 1–5, IEEE, 2015.
- [91] A. S. Mohan, A. Boddupalli, M. D. Hossain, F. Gozasht, and S. S. Ling, "Techniques for rf localization of wireless capsule endoscopy," in *2016 International Conference on Electromagnetics in Advanced Applications (ICEAA)*, pp. 856–859, IEEE, 2016.
- [92] M. Särestöniemi, M. Hämäläinen, and J. Iinatti, "An overview of the electromagnetic simulation-based channel modeling techniques for wireless body area network applications," *IEEE Access*, vol. 5, pp. 10622–10632, 2017.
- [93] U. Khan, Y. Ye, A.-U. Aisha, P. Swar, and K. Pahlavan, "Precision of em simulation based wireless location estimation in multi-sensor capsule endoscopy," *IEEE journal of translational engineering in health and medicine*, vol. 6, pp. 1–11, 2018.
- [94] W. Marczak, "Water as a standard in the measurements of speed of sound in liquids," *the Journal of the Acoustical Society of America*, vol. 102, no. 5, pp. 2776–2779, 1997.
- [95] T. E. Lavelle, *Temperature-Related Effects on the Speed of Sound in Bovine Liver*. PhD thesis, 2017.
- [96] R. L. Moses, D. Krishnamurthy, and R. M. Patterson, "A self-localization method for wireless sensor networks," *EURASIP Journal on Advances in Signal Processing*, vol. 2003, no. 4, pp. 1–11, 2003.
- [97] R. Lee, M.-S. Kang, B.-H. Kim, K.-H. Park, S. Q. Lee, and H.-M. Park, "Sound source localization based on gcc-phat with diffuseness mask in noisy and reverberant environments," *IEEE Access*, vol. 8, pp. 7373–7382, 2020.
- [98] L. Cong and W. Zhuang, "Hybrid tdoa/aoa mobile user location for wideband cdma cellular systems," *IEEE Transactions on Wireless Communications*, vol. 1, no. 3, pp. 439–447, 2002.
- [99] A. Pages-Zamora, J. Vidal, and D. H. Brooks, "Closed-form solution for positioning based on angle of arrival measurements," in *The 13th IEEE international symposium on personal, indoor*

and mobile radio communications, vol. 4, pp. 1522–1526, IEEE, 2002.

- [100] R. Engelbrecht, “Passive source localization from spatially correlated angle-of-arrival data,” *IEEE transactions on acoustics, speech, and signal processing*, vol. 31, no. 4, pp. 842–846, 1983.
- [101] B. Ananthasubramaniam and U. Madhow, “Cooperative localization using angle of arrival measurements in non-line-of-sight environments,” in *Proceedings of the first ACM international workshop on Mobile entity localization and tracking in GPS-less environments*, pp. 117–122, 2008.
- [102] N. H. Nguyen and K. Doğançay, “Closed-form algebraic solutions for angle-of-arrival source localization with bayesian priors,” *IEEE Transactions on Wireless Communications*, vol. 18, no. 8, pp. 3827–3842, 2019.
- [103] N. Patwari and A. O. Hero III, “Using proximity and quantized rss for sensor localization in wireless networks,” in *Proceedings of the 2nd ACM international conference on Wireless sensor networks and applications*, pp. 20–29, 2003.
- [104] H. C. So and L. Lin, “Linear least squares approach for accurate received signal strength based source localization,” *IEEE Transactions on signal processing*, vol. 59, no. 8, pp. 4035–4040, 2011.
- [105] H.-L. Song, “Automatic vehicle location in cellular communications systems,” *IEEE Transactions on Vehicular Technology*, vol. 43, no. 4, pp. 902–908, 1994.
- [106] V. Chandrasekhar, W. K. Seah, Y. S. Choo, and H. V. Ee, “Localization in underwater sensor networks: survey and challenges,” in *Proceedings of the 1st ACM international workshop on Underwater networks*, pp. 33–40, 2006.
- [107] A. Benslimane, “Localization in vehicular ad hoc networks,” in *2005 Systems Communications (ICW’05, ICHSN’05, ICMCS’05, SENET’05)*, pp. 19–25, IEEE, 2005.
- [108] S. Hara and D. Anzai, “Experimental performance comparison of rssi-and tdoa-based location estimation methods,” in *VTC Spring 2008-IEEE Vehicular Technology Conference*, pp. 2651–2655, IEEE, 2008.
- [109] H. P. Mistry and N. H. Mistry, “Rssi based localization scheme in wireless sensor networks: A survey,” in *2015 Fifth International Conference on Advanced Computing & Communication Technologies*, pp. 647–652, IEEE, 2015.
- [110] T. Kundu, “Acoustic source localization,” *Ultrasonics*, vol. 54, no. 1, pp. 25–38, 2014.
- [111] R. Zekavat and R. M. Buehrer, “Handbook of position location: Theory, practice, and advances,” 2019.
- [112] J. Smith and J. Abel, “Closed-form least-squares source location estimation from range-

- difference measurements,” *IEEE Transactions on Acoustics, Speech, and Signal Processing*, vol. 35, no. 12, pp. 1661–1669, 1987.
- [113] K. W. Cheung, H.-C. So, W.-K. Ma, and Y. T. Chan, “Least squares algorithms for time-of-arrival-based mobile location,” *IEEE transactions on signal processing*, vol. 52, no. 4, pp. 1121–1130, 2004.
- [114] L. Lin, H.-C. So, and Y. T. Chan, “Accurate and simple source localization using differential received signal strength,” *Digital Signal Processing*, vol. 23, no. 3, pp. 736–743, 2013.
- [115] J. D. Carroll and P. Arabie, “Multidimensional scaling,” *Measurement, judgment and decision making*, pp. 179–250, 1998.
- [116] H.-C. So and F. K. Chan, “A generalized subspace approach for mobile positioning with time-of-arrival measurements,” *IEEE transactions on Signal Processing*, vol. 55, no. 10, pp. 5103–5107, 2007.
- [117] F. K. Chan and H.-C. So, “Efficient weighted multidimensional scaling for wireless sensor network localization,” *IEEE Transactions on Signal Processing*, vol. 57, no. 11, pp. 4548–4553, 2009.
- [118] B. Saez-Mingorance, A. Escobar-Molero, J. Mendez-Gomez, E. Castillo-Morales, and D. P. Morales-Santos, “Object positioning algorithm based on multidimensional scaling and optimization for synthetic gesture data generation,” *Sensors*, vol. 21, no. 17, p. 5923, 2021.
- [119] M. L. Johnson and S. G. Frasier, “[16] nonlinear least-squares analysis,” in *Methods in enzymology*, vol. 117, pp. 301–342, Elsevier, 1985.
- [120] P. Teunissen, “Nonlinear least squares,” 1990.
- [121] P. E. Gill and W. Murray, “Algorithms for the solution of the nonlinear least-squares problem,” *SIAM Journal on Numerical Analysis*, vol. 15, no. 5, pp. 977–992, 1978.
- [122] R. I. Jennrich and R. H. Moore, “Maximum likelihood estimation by means of nonlinear least squares,” *ETS Research Bulletin Series*, vol. 1975, no. 1, pp. i–36, 1975.
- [123] T. Amemiya, “The maximum likelihood and the nonlinear three-stage least squares estimator in the general nonlinear simultaneous equation model,” *Econometrica: Journal of the Econometric Society*, pp. 955–968, 1977.
- [124] T. J. Ypma, “Historical development of the newton–raphson method,” *SIAM review*, vol. 37, no. 4, pp. 531–551, 1995.
- [125] P. B. Ryan, R. L. Barr, and H. D. Todd, “Simplex techniques for nonlinear optimization,” *Analytical Chemistry*, vol. 52, no. 9, pp. 1460–1467, 1980.
- [126] J. C. Meza, “Steepest descent,” *Wiley Interdisciplinary Reviews: Computational Statistics*,

- vol. 2, no. 6, pp. 719–722, 2010.
- [127] J. J. Moré, “The levenberg-marquardt algorithm: implementation and theory,” pp. 105–116, 1978.
- [128] M. H. Loke and T. Dahlin, “A comparison of the gauss–newton and quasi-newton methods in resistivity imaging inversion,” *Journal of applied geophysics*, vol. 49, no. 3, pp. 149–162, 2002.
- [129] L. Rui and K. Ho, “Efficient closed-form estimators for multistatic sonar localization,” *IEEE Transactions on Aerospace and Electronic Systems*, vol. 51, no. 1, pp. 600–614, 2015.
- [130] J. Arora, O. Elwakeil, A. Chahande, and C. Hsieh, “Global optimization methods for engineering applications: a review,” *Structural optimization*, vol. 9, no. 3, pp. 137–159, 1995.
- [131] J. Nocedal and S. J. Wright, *Numerical optimization*. Springer, 1999.
- [132] R. H. Bartels and G. H. Golub, “The simplex method of linear programming using lu decomposition,” *Communications of the ACM*, vol. 12, no. 5, pp. 266–268, 1969.
- [133] H. Schjaer-Jacobsen and K. Madsen, “Algorithms for worst-case tolerance optimization,” *IEEE Transactions on Circuits and Systems*, vol. 26, no. 9, pp. 775–783, 1979.
- [134] S. Wright, J. Nocedal, *et al.*, “Numerical optimization,” *Springer Science*, vol. 35, no. 67-68, p. 7, 1999.
- [135] S. K. Patch, D. E. Hoff, T. B. Webb, L. G. Sobotka, and T. Zhao, “Two-stage ionoacoustic range verification leveraging monte carlo and acoustic simulations to stably account for tissue inhomogeneity and accelerator–specific time structure—a simulation study,” *Medical physics*, vol. 45, no. 2, pp. 783–793, 2018.
- [136] K. C. Jones, W. Nie, J. C. Chu, J. V. Turian, A. Kassae, C. M. Sehgal, and S. Avery, “Acoustic-based proton range verification in heterogeneous tissue: simulation studies,” *Physics in Medicine & Biology*, vol. 63, no. 2, p. 025018, 2018.
- [137] H. Liu, H. Darabi, P. Banerjee, and J. Liu, “Survey of wireless indoor positioning techniques and systems,” *IEEE Transactions on Systems, Man, and Cybernetics, Part C (Applications and Reviews)*, vol. 37, no. 6, pp. 1067–1080, 2007.
- [138] R. N. Bracewell and R. N. Bracewell, *The Fourier transform and its applications*, vol. 31999. McGraw-Hill New York, 1986.
- [139] J. Otero, I. Felis, M. Ardid, and A. Herrero, “Acoustic localization of bragg peak proton beams for hadrontherapy monitoring,” *Sensors*, vol. 19, no. 9, p. 1971, 2019.
- [140] J. Otero, I. Felis, A. Herrero, J. A. Merchán, and M. Ardid, “Bragg peak localization with piezoelectric sensors for proton therapy treatment,” *Sensors*, vol. 20, no. 10, p. 2987, 2020.

- [141] C. Knapp and G. Carter, “The generalized correlation method for estimation of time delay,” *IEEE transactions on acoustics, speech, and signal processing*, vol. 24, no. 4, pp. 320–327, 1976.
- [142] Y. Yu, Z. Li, D. Zhang, L. Xing, and H. Peng, “Simulation studies of time reversal-based protoacoustic reconstruction for range and dose verification in proton therapy,” *Medical physics*, vol. 46, no. 8, pp. 3649–3662, 2019.
- [143] C. Freijo, J. L. Herraiz, D. Sanchez-Parcerisa, and J. M. Udias, “Dictionary-based protoacoustic dose map imaging for proton range verification,” *Photoacoustics*, vol. 21, p. 100240, 2021.
- [144] Z. Jiang, L. Sun, W. Yao, Q. J. Wu, L. Xiang, and L. Ren, “3d in vivo dose verification in prostate proton therapy with deep learning-based proton-acoustic imaging,” *Physics in Medicine & Biology*, 2022.
- [145] S. Wang, G. Gonzalez, L. Sun, Y. Xu, P. Pandey, Y. Chen, and S. Xiang, “Real-time tracking of the bragg peak during proton therapy via 3d protoacoustic imaging in a clinical scenario,” *npj Imaging*, vol. 2, no. 1, p. 34, 2024.
- [146] M. Fink, “Time-reversal mirrors,” *Journal of Physics D: Applied Physics*, vol. 26, no. 9, p. 1333, 1993.
- [147] M. Fink, “Time reversed acoustics.,” *Physics today*, vol. 50, no. 3, pp. 34–40, 1997.
- [148] P. K. Dash, “Feasibility Study of Ionoacoustics-based Dose Reconstruction for Small Animal Proton Irradiation Monitoring,” Master’s thesis, Ludwig Maximilian University of Munich, Munich, 2020.
- [149] Y. Yu, P. Qi, and H. Peng, “Feasibility study of 3d time-reversal reconstruction of proton-induced acoustic signals for dose verification in the head and the liver: A simulation study,” *Medical Physics*, vol. 48, no. 8, pp. 4485–4497, 2021.
- [150] R. Kalunga, H.-P. Wieser, P. Dash, M. Würfl, M. Riboldi, J. Schreiber, W. Assmann, K. Parodi, and J. Lascaud, “On the robustness of multilateration of ionoacoustic signals for localization of the bragg peak at pre-clinical proton beam energies in water,” *Physics in Medicine & Biology*, vol. 68, no. 10, p. 105010, 2023.
- [151] H. Wieser *et al.*, “Experimental demonstration of accurate bragg peak localization with ionoacoustic tandem phase detection (itpd),” *Physics in Medicine & Biology*, vol. 66, no. 24, p. 245020, 2021.
- [152] A. Ferrari, J. Ranft, P. R. Sala, and A. Fassò, *FLUKA: A multi-particle transport code (Program version 2005)*. No. CERN-2005-10, Cern, 2005.
- [153] T. Böhlen, F. Cerutti, M. Chin, A. Fassò, A. Ferrari, P. G. Ortega, A. Mairani, P. R. Sala, G. Smirnov, and V. Vlachoudis, “The fluka code: developments and challenges for high energy and medical applications,” *Nuclear data sheets*, vol. 120, pp. 211–214, 2014.

- [154] J. Lascaud *et al.*, “Enhancement of the ionoacoustic effect through ultrasound and photoacoustic contrast agents,” *Scientific reports*, vol. 11, no. 1, pp. 1–15, 2021.
- [155] B. E. Treeby and B. T. Cox, “k-Wave: MATLAB toolbox for the simulation and reconstruction of photoacoustic wave fields,” *Journal of Biomedical Optics*, vol. 15, no. 2, 2010.
- [156] S. Gerlach, F. Balling, A. Schmidt, F. Brack, F. Kroll, J. Metzkes-Ng, M. Reimold, U. Schramm, M. Speicher, K. Zeil, *et al.*, “Three-dimensional acoustic monitoring of laser-accelerated protons in the focus of a pulsed-power solenoid lens,” *High Power Laser Science and Engineering*, pp. 1–9.
- [157] S. Lim, C. Jun, D. Chang, D. Petrisor, M. Han, and D. Stoianovici, “Robotic transrectal ultrasound guided prostate biopsy,” *IEEE transactions on biomedical engineering*, vol. 66, no. 9, pp. 2527–2537, 2019.
- [158] V. Chaplin, M. Phipps, S. V. Jonathan, W. A. Grissom, P. Yang, L. M. Chen, and C. F. Caskey, “On the accuracy of optically tracked transducers for image-guided transcranial ultrasound,” *International journal of computer assisted radiology and surgery*, vol. 14, no. 8, pp. 1317–1327, 2019.
- [159] G. Darmani, T. Bergmann, K. B. Pauly, C. Caskey, L. de Lecea, A. Fomenko, E. Fouragnan, W. Legon, K. Murphy, T. Nandi, *et al.*, “Non-invasive transcranial ultrasound stimulation for neuromodulation,” *Clinical Neurophysiology*, 2021.
- [160] M. Ayat, M. B. Shamsollahi, B. Mozaffari, and S. Kharabian, “Ecg denoising using modulus maxima of wavelet transform,” in *2009 Annual International Conference of the IEEE Engineering in Medicine and Biology Society*, pp. 416–419, IEEE, 2009.
- [161] Ç. P. Dautov and M. S. Özerdem, “Wavelet transform and signal denoising using wavelet method,” in *2018 26th Signal Processing and Communications Applications Conference (SIU)*, pp. 1–4, Ieee, 2018.
- [162] G. Baldazzi, G. Solinas, J. Del Valle, M. Barbaro, S. Micera, L. Raffo, and D. Pani, “Systematic analysis of wavelet denoising methods for neural signal processing,” *Journal of Neural Engineering*, vol. 17, no. 6, p. 066016, 2020.
- [163] E. A. Vallicelli, M. Corona, M. Dell’Acqua, A. Baschiroto, and M. De Matteis, “Denoising for enhancing signal-to-noise ratio in proton sound detectors,” pp. 1–4, 2021.
- [164] A. Myronenko and X. Song, “Point set registration: Coherent point drift,” *IEEE transactions on pattern analysis and machine intelligence*, vol. 32, no. 12, pp. 2262–2275, 2010.
- [165] M. Würfl, F. S. Enghbrecht, S. Lehrack, C. Gianoli, F. H. Lindner, T. F. Rösch, D. Haffa, F. Olivari, M. Petasecca, M. L. Lerch, *et al.*, “Time-of-flight spectrometry of ultra-short, polyenergetic proton bunches,” *Review of Scientific Instruments*, vol. 89, no. 12, p. 123302, 2018.
- [166] M. A. A. Caballero, A. Rosenthal, A. Buehler, D. Razansky, and V. Ntziachristos, “Optoacous-

- tic determination of spatio-temporal responses of ultrasound sensors,” *IEEE transactions on ultrasonics, ferroelectrics, and frequency control*, vol. 60, no. 6, pp. 1234–1244, 2013.
- [167] K. A. Wear and S. M. Howard, “Correction for spatial averaging artifacts in hydrophone measurements of high-intensity therapeutic ultrasound: An inverse filter approach,” *IEEE transactions on ultrasonics, ferroelectrics, and frequency control*, vol. 66, no. 9, pp. 1453–1464, 2019.
- [168] M. Johansson, “The hilbert transform,” *Mathematics Master’s Thesis. Växjö University, Suecia. Disponible en internet: http://w3.msi.vxu.se/exarb/mj_ex.pdf*, vol. 19, 1999.
- [169] J. Schauer, H.-P. Wieser, Y. Huang, H. Ruser, J. Lascaud, M. Würfl, A. Chmyrov, M. Vidal, J. Herault, V. Ntziachristos, *et al.*, “Proton beam range verification by means of ionoacoustic measurements at clinically relevant doses using a correlation-based evaluation,” *Frontiers in Oncology*, vol. 12, p. 5055, 2022.
- [170] A. D. Wiles, D. G. Thompson, and D. D. Frantz, “Accuracy assessment and interpretation for optical tracking systems,” in *Medical Imaging 2004: Visualization, Image-Guided Procedures, and Display*, vol. 5367, pp. 421–432, SPIE, 2004.
- [171] J. J. Grefenstette, “Optimization of control parameters for genetic algorithms,” *IEEE Transactions on systems, man, and cybernetics*, vol. 16, no. 1, pp. 122–128, 1986.
- [172] A. Malgoezar, M. Snellen, R. Merino-Martinez, D. G. Simons, and P. Sijtsma, “On the use of global optimization methods for acoustic source mapping,” *The Journal of the Acoustical Society of America*, vol. 141, no. 1, pp. 453–465, 2017.
- [173] D. Blatt and A. O. Hero, “Energy-based sensor network source localization via projection onto convex sets,” *IEEE Transactions on Signal Processing*, vol. 54, no. 9, pp. 3614–3619, 2006.
- [174] G. Shen, R. Zetik, and R. S. Thoma, “Performance comparison of toa and tdoa based location estimation algorithms in los environment,” in *2008 5th Workshop on Positioning, Navigation and Communication*, pp. 71–78, IEEE, 2008.
- [175] M. Sadeghi, F. Behnia, and R. Amiri, “Optimal geometry analysis for tdoa-based localization under communication constraints,” *IEEE Transactions on Aerospace and Electronic Systems*, vol. 57, no. 5, pp. 3096–3106, 2021.
- [176] R. I. Reza, *Data fusion for improved TOA/TDOA position determination in wireless systems*. PhD thesis, Virginia Tech, 2000.
- [177] M. Laaraiedh, L. Yu, S. Avrillon, and B. Uguen, “Comparison of hybrid localization schemes using rssi, toa, and tdoa,” in *17th European Wireless 2011-Sustainable Wireless Technologies*, pp. 1–5, VDE, 2011.
- [178] R. Fujiwara, K. Mizugaki, T. Nakagawa, D. Maeda, and M. Miyazaki, “Toa/tdoa hybrid relative positioning system using uwb-ir,” in *2009 IEEE Radio and Wireless Symposium*, pp. 679–682,

IEEE, 2009.

- [179] P. Laguna, R. Jané, and P. Caminal, “Automatic detection of wave boundaries in multilead ecg signals: Validation with the cse database,” *Computers and biomedical research*, vol. 27, no. 1, pp. 45–60, 1994.
- [180] L. Sörnmo and P. Laguna, *Bioelectrical signal processing in cardiac and neurological applications*, vol. 8. Academic press, 2005.
- [181] F. Gritzali, G. Frangakis, and G. Papakonstantinou, “Detection of the p and t waves in an ecg,” *Computers and Biomedical Research*, vol. 22, no. 1, pp. 83–91, 1989.
- [182] R. Braojos, G. Ansaloni, D. Atienza, and F. J. Rincón, “Embedded real-time ecg delineation methods: A comparative evaluation,” in *2012 IEEE 12th International Conference on Bioinformatics & Bioengineering (BIBE)*, pp. 99–104, IEEE, 2012.
- [183] J. Pan and W. J. Tompkins, “A real-time qrs detection algorithm,” *IEEE transactions on biomedical engineering*, no. 3, pp. 230–236, 1985.
- [184] R. Gutiérrez-Rivas, J. J. Garcia, W. P. Marnane, and A. Hernández, “Novel real-time low-complexity qrs complex detector based on adaptive thresholding,” *IEEE Sensors Journal*, vol. 15, no. 10, pp. 6036–6043, 2015.
- [185] J. Wang, J. J. Sohn, Y. Lei, W. Nie, J. Zhou, S. Avery, T. Liu, and X. Yang, “Deep learning-based protoacoustic signal denoising for proton range verification,” *Biomedical Physics & Engineering Express*, vol. 9, no. 4, p. 045006, 2023.
- [186] R. van Bergen, L. Sun, P. K. Pandey, S. Wang, K. Bjegovic, G. Gonzalez, Y. Chen, R. Lopata, and L. Xiang, “Discrete wavelet transformation for the sensitive detection of ultrashort radiation pulse with radiation-induced acoustics,” *IEEE Transactions on Radiation and Plasma Medical Sciences*, 2023.
- [187] L. Angrisani, A. Baccigalupi, and R. S. L. Moriello, “Ultrasonic time-of-flight estimation through unscented kalman filter,” *IEEE Transactions on Instrumentation and Measurement*, vol. 55, no. 4, pp. 1077–1084, 2006.
- [188] L. Streeter, “Time-of-flight range image measurement in the presence of transverse motion using the kalman filter,” *IEEE Transactions on Instrumentation and Measurement*, vol. 67, no. 7, pp. 1573–1578, 2018.
- [189] Z.-J. Yao, Q.-H. Meng, and M. Zeng, “Improvement in the accuracy of estimating the time-of-flight in an ultrasonic ranging system using multiple square-root unscented kalman filters,” *Review of scientific instruments*, vol. 81, no. 10, 2010.
- [190] T. D. Mast, “Empirical relationships between acoustic parameters in human soft tissues,” *Acoustics Research Letters Online*, vol. 1, no. 2, pp. 37–42, 2000.

- [191] R. Rau, D. Schweizer, V. Vishnevskiy, and O. Goksel, “Speed-of-sound imaging using diverging waves,” *International journal of computer assisted radiology and surgery*, vol. 16, no. 7, pp. 1201–1211, 2021.
- [192] S. Sueyasu, T. Takayanagi, K. Miyazaki, Y. Kuriyama, Y. Ishi, T. Uesugi, M. B. Unlu, N. Kudo, Y. Chen, K. Kasamatsu, *et al.*, “Ionoacoustic application of an optical hydrophone to detect proton beam range in water,” *Medical Physics*, 2022.
- [193] J. Lascaud *et al.*, “Optimization of the backing material of a low frequency pvdf detector for ion beam monitoring during small animal proton irradiation,” in *2021 IEEE International Ultrasonics Symposium (IUS)*, pp. 1–4, IEEE, 2021.
- [194] J. Lascaud, P. Dash, K. Schnürle, J. Bortfeldt, K. Niepel, J. Maas, M. Würll, M. Vidal, J. Hérault, G. Landry, *et al.*, “Fabrication and characterization of a multimodal 3d printed mouse phantom for ionoacoustic quality assurance in image-guided pre-clinical proton radiation research,” *Physics in Medicine & Biology*, vol. 67, no. 20, p. 205001, 2022.
- [195] A. Ledergerber, M. Hamer, and R. D’Andrea, “A robot self-localization system using one-way ultra-wideband communication,” in *2015 IEEE/RSJ International Conference on Intelligent Robots and Systems (IROS)*, pp. 3131–3137, IEEE, 2015.
- [196] A. Maslennikova, M. Sirotkina, A. Moiseev, E. Finagina, S. Ksenofontov, G. Gelikonov, L. Matveev, E. Kiseleva, V. Zaitsev, E. Zagaynova, *et al.*, “In-vivo longitudinal imaging of microvascular changes in irradiated oral mucosa of radiotherapy cancer patients using optical coherence tomography,” *Scientific reports*, vol. 7, no. 1, p. 16505, 2017.
- [197] T. Inoue, N. Masai, R.-J. Oh, H. Shiomi, and N. Hashida, “Adaptive replanning intensity-modulated radiotherapy for choroidal metastasis of breast cancer using optical coherence tomography,” *Journal of Radiation Research*, vol. 55, no. 3, pp. 502–508, 2014.
- [198] M. F. Kraus, B. Potsaid, M. A. Mayer, R. Bock, B. Baumann, J. J. Liu, J. Hornegger, and J. G. Fujimoto, “Motion correction in optical coherence tomography volumes on a per a-scan basis using orthogonal scan patterns,” *Biomedical optics express*, vol. 3, no. 6, pp. 1182–1199, 2012.
- [199] B. Braaf, K. V. Vienola, C. K. Sheehy, Q. Yang, K. A. Vermeer, P. Tiruveedhula, D. W. Arathorn, A. Roorda, and J. F. de Boer, “Real-time eye motion correction in phase-resolved oct angiography with tracking slo,” *Biomedical optics express*, vol. 4, no. 1, pp. 51–65, 2013.
- [200] K. C. Jones, C. M. Seghal, and S. Avery, “How proton pulse characteristics influence protoacoustic determination of proton-beam range: simulation studies,” *Physics in Medicine & Biology*, vol. 61, no. 6, p. 2213, 2016.
- [201] S. K. Patch, C. Nguyen, D. Dominguez-Ramirez, R. Labarbe, G. Janssens, D. Cammarano, J. Lister, C. Finch, J. Lambert, J. Pandey, *et al.*, “Thermoacoustic range verification during pencil beam delivery of a clinical plan to an abdominal imaging phantom,” *Radiotherapy and Oncology*, vol. 159, pp. 224–230, 2021.

- [202] J. Schauer, H.-P. Wieser, J. Lascaud, Y. Huang, M. Vidal, J. Hérault, V. Ntziachristos, G. Dollinger, and K. Parodi, “Range verification of a clinical proton beam in an abdominal phantom by co-registration of ionoacoustics and ultrasound,” *Physics in Medicine & Biology*, vol. 68, no. 12, p. 125009, 2023.



LUDWIG-
MAXIMILIANS-
UNIVERSITÄT
MÜNCHEN

Dekanat Medizinische Fakultät
Promotionsbüro



Affidavit

Kalunga, Ronaldo Dos Anjos Macondo

Surname, first name

I hereby declare, that the submitted thesis entitled:

**Investigations on Multilateration of Ionoacoustic Signals
for Localisation of the Bragg Peak in Pre-clinical Research**

is my own work. I have only used the sources indicated and have not made unauthorised use of services of a third party. Where the work of others has been quoted or reproduced, the source is always given.

I further declare that the dissertation presented here has not been submitted in the same or similar form to any other institution for the purpose of obtaining an academic degree.

Munich, 02.05.2025

Place, Date

Kalunga, Ronaldo

Signature doctoral candidate



LUDWIG-
MAXIMILIANS-
UNIVERSITÄT
MÜNCHEN

Dekanat Medizinische Fakultät
Promotionsbüro



**Confirmation of congruency between printed and electronic version of the
doctoral thesis**

Kalunga, Ronaldo Dos Anjos Macondo

name, first name

I hereby declare that the electronic version of the submitted thesis, entitled:

**Investigations on Multilateration of Ionoacoustic Signals
for Localisation of the Bragg Peak in Pre-clinical Research**

is congruent with the printed version both in content and format.

Munich, 02.05.2025

Place, Date

Kalunga, Ronaldo

Signature doctoral candidate

Acknowledgements

This incredible journey began in the vibrant streets of Luanda, where I learned the true power of knowledge, even when resources were scarce. It started as a dream—to explore different cultures, places, and realities. That’s how I approached life, with insatiable curiosity, even when uncertainty surrounded basic necessities. “To the children who walked countless kilometres to reach school, thank you; you are my heroes. Imagine what we could have achieved with the luxury of learning without hunger”.

In Luanda, I made lifelong friends and found brilliant minds, especially at the Simione Mucune Institute. Prof. Sara, thank you for those unforgettable Maths lectures wherever you are. To my family in Luanda, “um xi coração para todos”—a heartfelt embrace to each of you. To my parents, Verónica Cahalo Macondo and José Bernardo Kalunga, thank you for your unwavering support, love, and belief that we could turn the “impossible” into “possible”. My grandmother, Maria Luísa Muovoluoca, thank you for teaching me the art of business and much more (Amor eterno). Hildebrando, Mãe Marta, Tia Sambita, Tio Elias, and the Monteiro, Mufinda, and Xtragados families—thank you for staying connected all these years; with you, it feels as though I never left.

From Luanda, my journey took me to Italy/Rome. Daje! There, I learned to walk alone and pursue my dreams. Rome will always be HOME. Deep thanks to Alfredo Catalfo, Tavinha, Jocelyne, Francesca Mariani, Atanasio, Dr. Issau Agostinho, Prof. Alessandro Savoia, and all my friends from Roma Tre University. I extend special gratitude to Prof. Luca Cabibbo. You had a huge impact on my academic career, especially on the art of coding!

Roma Ostiense (Biblioteca) and Statuto 44 will always be among the best memories ever. Our paths intersected there, and we combined the passion of pushing towards the marvellous universe of “learning and exploring”. Thank you for everything, Dr.(Corazon) Cristina Sanz Martin.

One of the chapters led me to Spain for an unforgettable Erasmus year in Zaragoza. Thank you, Prof. Pablo Laguna, for introducing me to biomedical signal processing. Spain will always hold a special place in my heart, as it taught me different ways to persevere. Thank you, Encarni, Carlos, German and Darwin, for those cherished moments of writing by the mountains and waterfalls of Cabuérniga in Cantabria. Thank you for cheering up all my professional and academic achievements (from the Bachelor’s to the PhD!).

During my adventures, I had to stop in Germany/Munich. Where I got this amazing opportunity to start my PhD journey. During my PhD, I interacted with colleagues and friends who shared the journey’s highs and lows. My deepest thanks go to my colleagues Juliana, Katrin, Franz, Jannis, Sebastian Lehrack (I still have your book!), Andreas, Sonja, Pratik (always a pleasure, my friend), Giulio, Prasanna (it is time to print!), Zé, Mune, Leonard, Bea, Mambo and Giovanni.

A special thanks to “Andrea Leintaler”—you’ll be deeply missed. I had the best support I could had during my PhD adventure at the chair. Whatever I needed, you were there to support your management, and dynamism is something that I took note of!

This work was also made possible thanks to PD. Dr Walter Assmann, who introduced me to Munich’s working culture. I would also love to thank all the past and new members of the SIRMIO project.

To the other senior people, a special thanks go to Dr Chiara Gianoli, Dr Matthias Würfl, Dr Jonathan Bortfeldt, Prof. Dr Marco Riboldi, Prof. Dr Jörg Schreiber, PD. Dr George Dedes, Dr Marco Pinto and Prof. Dr Peter Thirolf.

To Dr. Julie Lascaud, it was a pleasure to work and learn from you. It was a long journey for both of us, and I firmly believe we learned a lot along the way. Thank you for your insights, support, and hard work. Without you, this work wouldn't have been possible (*merci beaucoup!*). To Dr Hans-Peter Wieser, your passion for what you do will always be an inspiration. Thank you for all the support and extra motivation to never give up on the academic journey!

Sometimes, the PhD adventure also involves friends and work colleagues. To you all: Angel, Claudia, Tommaso, Sebastian Wittmeier, Ali, Khaleel, ilB< 4, Pedro Manuel and Simon, I am grateful for all your support in this journey.

The SIRMIO project was a school for me in all aspects. While working on the project, I learned transversal things that will be invaluable even for my future projects. One of these “soft skills” is the art of management. I express my gratitude to you, Prof. Dr Katia Parodi, for the opportunity to be part of your team and learn from you. It was never easy, but you always had this leadership approach, which makes complicated things easy. Your futuristic and innovative way of approaching things is something truly inspirational. Words won't be enough to express my feelings (*grazie di cuore!*).

“I am because we are...”